Spring 1998

Experimental Geometry Optimization Techniques for Multi-Element Airfoils

Drew Landman
Old Dominion University

EXPERIMENTAL GEOMETRY OPTIMIZATION TECHNIQUES FOR MULTI-ELEMENT AIRFOILS

by

Drew Landman
B.S.M.E., June 1983, Lehigh University
M.S.M.E., December 1984, Lehigh University

A Dissertation submitted to the Faculty of Old Dominion University in Partial Fulfillment of the Requirement for the Degree of

DOCTOR OF PHILOSOPHY

AEROSPACE ENGINEERING

OLD DOMINION UNIVERSITY
May 1998

Approved by:

_____
Colin Britcher (Director)

_____
Ponnampalam Balakumar (Member)

_____
Oktay Baysal (Member)

_____
John Lin (Member)

_____
Natalia Alexandrov (Member)

ABSTRACT

EXPERIMENTAL GEOMETRY OPTIMIZATION TECHNIQUES
FOR MULTI-ELEMENT AIRFOILS.

Drew Landman
Old Dominion University, 1998
Director: Dr. Colin P. Britcher

A study is reported on geometry optimization techniques for high-lift airfoils. A modern three-element airfoil model with a remotely actuated flap was designed, tested, and used in wind tunnel experiments to investigate optimum flap positioning based on lift. All the results presented were obtained in the Old Dominion University low-speed wind tunnel. Detailed results for lift coefficient versus flap vertical and horizontal position are presented for two airfoil angles-of-attack: 8 and 14 degrees. Three automated optimization simulations, the method of steepest ascent and two variants of the sequential simplex method, were demonstrated using experimental data. An on-line optimizer was demonstrated with the wind tunnel model which automatically seeks the optimum lift as a function of flap position. Hysteresis in lift as a function of flap position was discovered when tests were conducted with continuous flow conditions. It was shown that optimum lift coefficients determined using continuous flow conditions exist over an extended range of flap positions when compared to those determined using traditional intermittent conditions.

This work is dedicated to my wife, Katherine Landman, who has been my partner and best friend and made my life fuller than I ever thought possible. A very special thanks to my parents Dirk and Laura Landman, and to my brothers Hank and Todd Landman, for their unbridled support, enthusiasm, and understanding.

ACKNOWLEDGMENTS

The author sincerely thanks Dr. Colin P. Britcher for his guidance and support as academic advisor. This work was partially funded by two ASEE summer faculty fellowships at the NASA Langley Research Center (LaRC) with the Experimental Flow Physics Branch (EFPB) (now the Flow Modeling and Control Branch) and the Subsonic Aerodynamics Branch (SAB). Additional funding was received from NASA LaRC task orders, one from EFPB and a second from the Multi-Disciplinary Design and Optimization Branch (MDOB). Specifically, the author wishes to acknowledge the help of Dr. Steve Robinson, Mike Walsh, Dr. John Lin, and Dr. Steve Klausmeyer of the EFPB, as well as Ed Waggoner and Harry Morgan, of the SAB and Floyd Backley for his expertise in manufacturing the wind tunnel model. In addition, a special thanks to Dr. John Otto and Dr. Tom Zang of the MDOB for their support and interest.

TABLE OF CONTENTS

Page

Page

Page

LIST OF TABLES

LIST OF FIGURES

Figure Page

Figure Page

NOMENCLATURE

A	Aspect Ratio
A-O-A	Angle-of-Attack
B	Best Response Vertex
C	Airfoil Chord Length
C_d	Profile Drag Coefficient
C_D	Wing Drag Coefficient
C_l	Profile Lift Coefficient
C_L	Wing Lift Coefficient
Cl_{max}	Maximum Profile Lift Coefficient
C_m	Moment Coefficient
C_p	Pressure Coefficient
C_R	Contracted Vertex for Favorable R Response
C_W	Contracted Vertex for Unfavorable R Response
D	Drag
d	Landing Distance, Take-Off Distance
E	Expanded Vertex
FG	Flap Gap
FO	Flap Overhang
h	Total Head
L	Lift
m_T	Mass Flow of Wind Tunnel
m_v	Mass Flow of Wind Tunnel Venting System

M	Mach Number
M_∞	Mach Number of Freestream
N	Next Best Response Vertex
OH	Overhang
p	Static Pressure
p_n	First Auxiliary Face Increment
P	Centroid of Sequential Simplex B-N Face
P_{ref}	Reference Pressure
q	Dynamic Pressure
q_n	Second Auxiliary Face Increment
Re_C	Reynolds Number Based on Airfoil Chord
r/c	Airfoil Leading Edge Radius to Chord Ratio
S	Wing Area, Edge Length
s	Unit Vector
S_o	Initial Step Size
S_{max}	Maximum Step Size
s/c	Airfoil Slot Width to Chord Ratio
T	Thrust
t/c	Airfoil Thickness to Chord Ratio
tol	Triangle Reference Length
u	Local Velocity Component in the x Direction
U_{ref}	Reference Velocity
v	Local Velocity Component in the y Direction

V_∞	Freestream Velocity
W	Weight, Worst Response Vertex
w	Local Velocity Component in the z Direction
x	Horizontal (Chordwise) Spatial Coordinate, Design Variable
x^j	Simplex Vertex Design Variable Pair
x_i	Element of Column Vector x
X1	Design Variable
y	Vertical Spatial Coordinate
Y_w	Wake Rake Survey Width
α	Angle-of-Attack, Step Size
β	Conjugate Gradient Step Size, Contraction Scaling Factor for Sequential Simplex
$\Delta\alpha_{maxLE}$	Increase in Stall Angle-Of-Attack due to Slat
$\Delta Cdmin_{LE}$	Increment of Minimum Profile Drag Coefficient due to Leading-Edge Slat
$\Delta Cdmin_{TE}$	Increment of Minimum Profile Drag Coefficient due to Trailing-Edge Flap
ΔClp_{LE}	Increment of Minimum Drag Profile Lift Coefficient due to Leading-Edge Slat
ΔClp_{TE}	Increment of Minimum Drag Profile Lift Coefficient due to Trailing-Edge Flap
ΔCL_{TE}	Increment of Wing Lift Coefficient due to Trailing-Edge Flap
δ_f	Flap Deflection Angle
δ_s	Slat Deflection Angle
δ_v	Vane Deflection Angle

σ	Density Ratio, $\rho/\rho_{sea\ level}$
γ	Climb Angle, Expansion Scaling Factor for Sequential Simplex

1 INTRODUCTION

Modern designers rely on sophisticated high-lift devices to meet the severe design challenges inherent to aircraft which must operate between high subsonic cruise speeds and the lower speeds required for take-off and landing. A large transport wing is typically designed for optimum cruise, a flight regime which is characterized by high speed, low lift coefficient (C_l) and low drag coefficient (C_d) [Nelson, 1995]. These design goals are met with a thin swept wing of small area [Butter, 1984]. Conversely, the landing flight regime requires the wing to generate high lift and drag for the lowest approach speed, the steepest approach angle, and the shortest rollout. During take-off, high lift is required for minimum take-off distance, wheras maximum climb angle is achieved with maximum lift-to-drag ratio. These bipolar design constraints have traditionally led designers to provide a mechanical alteration of the wing section on at least the inboard portion of the wing [McCormick, 1995].

1.1 The Importance of High-Lift Systems

During take-off, the rolling distance is principally a function of the take-off maximum lift coefficient (Cl_{max}), while the climb angle is a function of lift-to-drag ratio (L/D) [Butter, 1984; Hale, 1994]. A system for generating more lift, supplementary to that of the cruise defined wing geometry, is a necessity for modern transports; this system is known as the *high-lift system*. Consider the

---

The model journal for this document is Applied Mechanics Reviews.

take-off, to a first order, the take-off distance d can be shown to be [Butter, 1984]

$$d \propto \frac{W}{T}\frac{W}{S}\frac{1}{\sigma C l_{max}} \qquad (1.1\text{-}1)$$

Here W is the aircraft weight, T the thrust, S the wing area and σ the density ratio. T/W is known as the *thrust-to -weight ratio* and W/S as the *wing loading*. The landing distance depends on the same variables with the omission of thrust. Again, to a first order the landing distance d can be shown to be [Butter, 1984]

$$d \propto \frac{W}{S}\frac{1}{\sigma C_l} \qquad (1.1\text{-}2)$$

Typically, an aircraft will be designed with a compromise thrust loading and wing loading to meet all design constraints while in flight. This leaves the alteration of the wing C_l as the primary free variable to achieve acceptable landing and take-off performance. Several alternatives arise for increasing C_l, of which the most common may be to increase wing camber, to increase effective wing area, to use circulation control, or to use boundary layer control to delay stall [Nelson, 1995; McCormick, 1967 and 1995; Kohlman, 1981].

Historically, retractable devices were developed due to the desire to improve landing and take-off performance by increasing Cl_{max}. Retractable devices can be deployed at lower speeds to increase wing area and retracted

for high-speed flight conditions. Small improvements in the high-lift system can have dramatic effects on the aircraft performance. As an example, a 5% improvement in maximum lift coefficient (Cl_{max}) at landing allows a 25% increase in payload [Butter, 1984].

Transport aircraft are normally configured with leading-edge devices known as *slats* or *leading-edge flaps* and one or more trailing-edge devices known as *flaps* to provide typical cruise C_l values near 0.5 and maximum C_l values (Cl_{max}) of 2.4 [Nelson, 1995; Butter, 1984; McCormick, 1995]. Figure 1.1 shows some of the many variations of mechanical flaps and slats in use on aircraft today [McCormick, 1995]. The blown flap and jet flap can outperform the mechanical flaps but require a continuous supply of air from sources such as the aircraft engine. The blown and jet flap are extreme examples of increasing lift by circulation control.

The pure jet flap employs a jet of air only at the trailing edge, deflected downward, whereas the blown flap utilizes a sheet of air blown over its upper surface [Kohlman, 1981; McCormick, 1967]. The behavior of the two flaps is similar, stemming from the sheet of high momentum air that is directed downward from the trailing edge which results in increased circulation. The pure jet flap causes a reaction lift due to the vertical component of the jet stream as well as an effective increase in wing area. Also, a favorable pressure gradient develops on the airfoil so that boundary layer separation is delayed allowing a higher angle-of-attack to be reached before stall occurs.

The blown flap benefits from the same phenomena with the addition of the increased area of the physical flap leading to even higher circulation.

For engine-out safety reasons, civil transports currently employ only passive mechanical high-lift systems [Nelson, 1995]. System reliability decreases with increasing mechanical complexity, while weight and cost increase. Hence designers seek configurations with the fewest airfoil elements. The Fowler flap and extensible slat increase the local chord length (and wing area) as well as the camber. Figure 1.2 shows a contemporary three-element airfoil typical of the more simplified approach to high-lift design now in vogue with major aircraft manufacturers which employ the Fowler flap with the extensible slat [Nelson, 1995]. In figure 1.3, the relative positions of the airfoil elements of a multi-element high-lift system are shown for each corresponding flight regime [Woods, 1988].

The discussion so far has focussed on maximum lift, which is the most important factor in the landing and take-off distances. Upon leaving the ground following the take-off roll, regulating authorities require aircraft to maintain a positive climb angle with one engine out [Nelson, 1995; McCormick, 1995; Dillner, 1984]. The climb angle, γ, for small angles is shown in equation 1.1-3 where D is the aircraft drag [Hale, 1984]

$$\gamma = \frac{T - D}{W} = \frac{T}{W} - \frac{D}{L} \qquad (1.1\text{-}3)$$

Clearly, the climb angle is critically dependent on the L/D and for this reason the high-lift system must be optimized accordingly.

1.2 Current Design Tools for High-Lift Airfoils

The aerodynamics of high-lift airfoils are extremely complex including confluent boundary layers, transonic regions and local flow separations [Kuethe and Chow, 1986; Smith, 1974]. Computational design and analysis is fraught with difficulty, so that experimental validation is an essential part of the research and development process.

At the initial design stage a data base is often employed which is based on correlations of experimental results around a theoretical framework [Wedderspoon, 1986; Nelson, 1995]. This empirical tool provides the basis for sizing high-lift devices for a new aircraft design based on past experience. The flow field around an aircraft with a high-lift system deployed is so complex that an accurate three-dimensional viscous solver has not been demonstrated successfully to date. The computational modeling of high-lift systems is primarily performed with two-dimensional (2D) viscous flow solvers, that give wing section data in conjunction with three-dimensional (3D) surface singularity methods, which reveal only the inviscid flow field. In addition, some aircraft manufacturers employ a quasi-3D viscous method. One approach joins the two methods by coupling a normalized mid-span pressure distribution, calculated with the 2D viscous solver, with a non-uniform distribution over the whole wing calculated by a 3D panel method [Wedderspoon, 1986].

The methods discussed can provide a reasonable prediction of the lift forces for the 3D aircraft model and a more accurate prediction of the lift forces for the 2D airfoil. In contrast, the drag forces are relatively poorly predicted. In the 2D case the computer codes suffer from poor modeling of turbulence and other flow field features such as transition, confluent boundary layers and wakes, laminar separation bubbles, and compressibility effects. In the 3D case the quasi-3D model provides drag results which suffer from the inherent compromises of the code's design. While great advances in computational design tools have occurred in recent years, it is clear that wind tunnel testing is still a necessity in the design process.

1.3 Multi-Element Airfoil Nomenclature

A multi-element airfoil possesses many geometric degrees of freedom. The main element has an angle-of-attack which is associated with the entire high-lift system. Each auxiliary element such as a slat or flap has a relative angle-of-attack with respect to the main element. In addition, the relative positions of the auxiliary elements with respect to the main element are defined in terms of gap and overhang. Nomenclature for describing the relative positions of the elements is shown in figure 1.4. Slat and flap deflection angles are measured from a reference chord line defined in the airfoil's stowed configuration. A *gap* is the shortest distance from the trailing edge of a forward element to an aft element. *Overhang* is defined as the chordwise overlapping distance between two elements. Overhang is positive

if elements overlap and negative if they are a distance apart [Klausmeyer and Lin, 1997; Lin, 1995].

1.4 Wind Tunnel Testing Issues and Procedures

In addition to the geometric degrees of freedom there are fluid parameters to consider which include Reynolds number and Mach number. The wind tunnel testing of a given multi-element airfoil model over a range of values for all the possible degrees of freedom is virtually impossible. As an example, consider a simple airfoil consisting of a main element and flap. If one fluid condition is chosen (Reynolds and Mach number) and the four geometric parameters (flap gap and overhang, flap deflection, and angle-of-attack) are each evaluated for ten values, a test matrix of 10,000 points is needed. Typically, researchers test new designs over an extremely sparse test matrix which is chosen based on experience and computational results [Nelson, 1995; Valarezo, 1991]. Optimization of multi-element configurations first requires individual element optimization while other elements are in a "conservative" setting, followed by entire system optimization to find the highest performance possible [Lin and Dominik, 1995; Ljungström, 1973a].

Wind tunnel models most often used for high-lift testing are of three main types: two-dimensional wing sections, three-dimensional half wing models, and full 3D aircraft models [Wedderspoon, 1986]. In most cases, fixed brackets are used to position the auxiliary elements with respect to the main element, requiring the tunnel to be shut down between each geometry

change. Technicians will typically gage angles, gap, and overhang settings manually between each test run [Lin, 1993].

The testing objective can be to optimize lift, minimize drag, or find the best lift-to-drag ratio (L/D). To properly optimize a real multi-element airfoil high-lift system the model should be tested at Reynolds numbers and Mach numbers that approach flight conditions since significant differences in maximum lift coefficient have been measured due to variation in these parameters [Valarezo et al., 1993]. It is generally not practical to obtain full-scale Reynolds numbers by using a full-scale model; however, there are methods of increasing the Reynolds number with a reduced scale model. One popular method is to pressurize the wind tunnel [Rae and Pope, 1984]. A second approach is to use a different working fluid with a higher density, such as Freon 12. This fluid can increase the Mach number and the Reynolds number for a given power input when compared to air. A third approach is to cool the fluid - a cryogenic tunnel [Rae and Pope, 1984].

1.5 Dissertation Objective

This research seeks to demonstrate the practicality of experimental optimization of multi-element airfoils. In other words, methods will be developed permitting the remote adjustment of the airfoil geometry in the wind tunnel. To demonstrate the practicality of remote geometry adjustment for multi-element airfoils, a unique model with actuators capable of moving while enduring forces associated with wind tunnel testing, must be designed, constructed and tested. A modern three-element airfoil model with a remotely

actuated flap will be used in wind tunnel tests to explore the possibility of in situ optimization of flap position for best lift using automated optimization algorithms. Specifically, the response to be optimized is lift coefficient (C_l) with flap vertical and horizontal motion as design variables (C_l=f{x,y}). This study will also investigate any unknown flow physics associated with this unique application of optimization, such as inherent hysteretic effects in geometry dependent lift measurements which are thought to influence optimum rigging.

The current research expands the existing sparse data base for variation of lift with flap gap and overhang changes and is unique in that geometry optimization using continuous flow conditions had not previously been published. The proposed benefits of this study are focused on experience with optimization methodology as applied to the experimental testing of high-lift systems which can be transferred to production facilities. It is hoped that the knowledge gained from this preliminary 2D investigation may be extended to 3D testing and ultimately benefit vehicle high-lift system design.

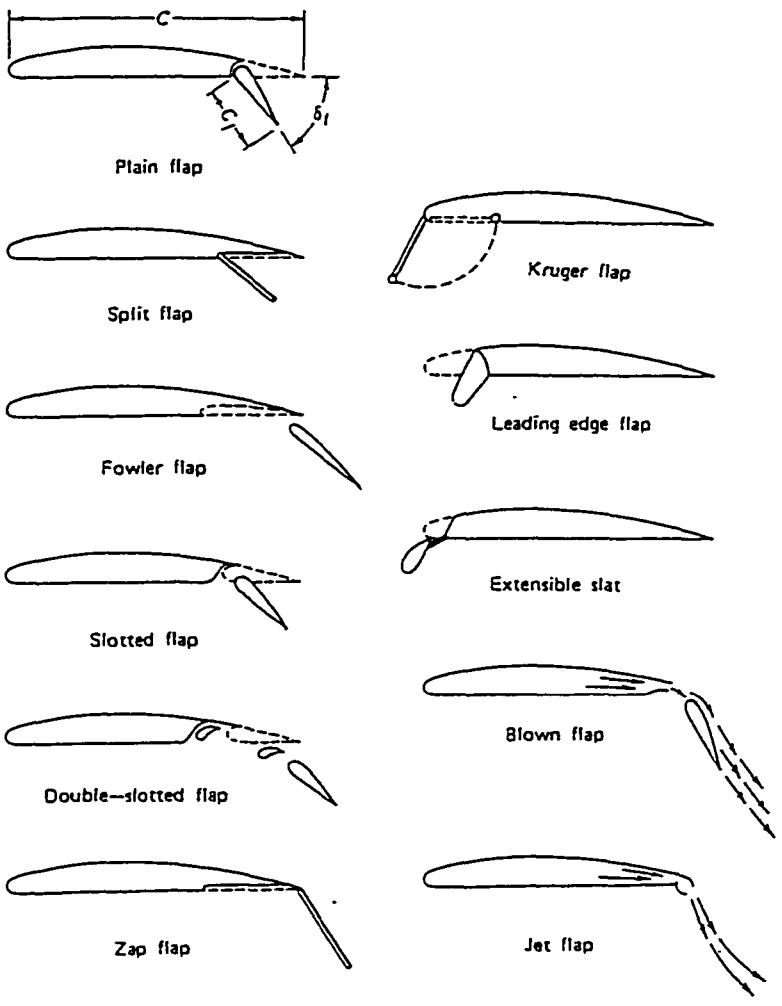

Figure 1.1 Variation in Flap and Slat Designs

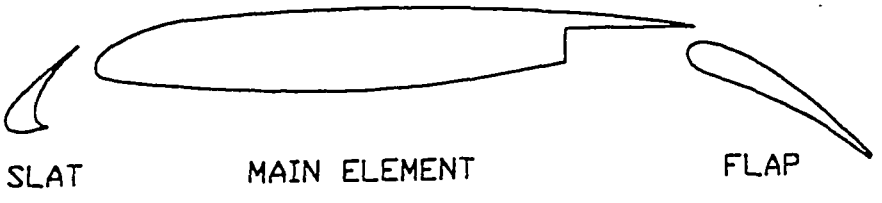

Figure 1.2 Modern Three-Element Airfoil

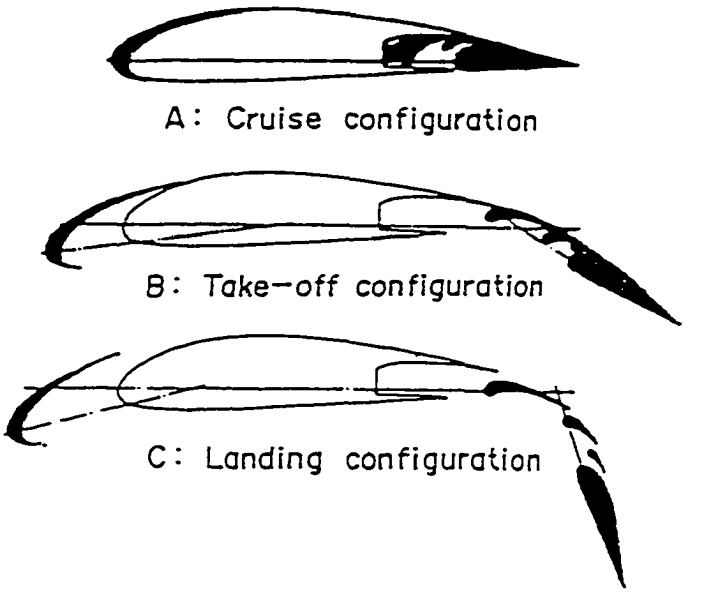

Figure 1.3 Relative Positions of Multi-Element Airfoil Elements for Three Flight Regimes

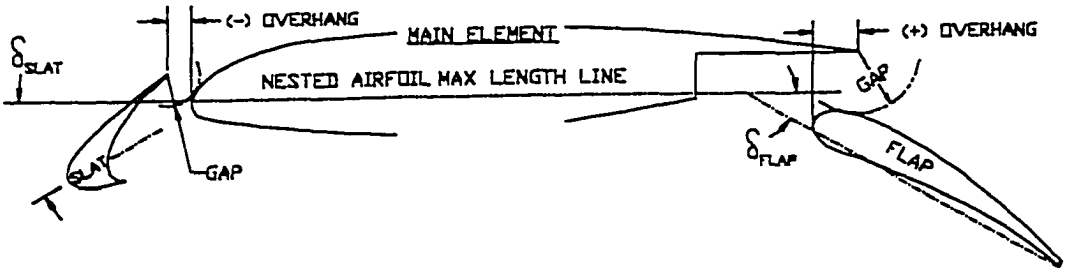

Figure 1.4 Multi-Element Airfoil Nomenclature

2 MULTI-ELEMENT AIRFOIL AERODYNAMICS

In order for subsequent experiments to be properly configured and to assist in the interpretation of experimental results, this section will review the following: (1) the flow physics associated with multi-element high-lift airfoils, (2) current wind tunnel procedures as they apply to multi-element airfoil testing, and (3) the state of the art in relevant computational methods.

The flow field of a multi-element airfoil presents challenges to both experimental and computational analysis in that it is dominated by complex viscous flow phenomena. The flow field, as illustrated in figure 2.1 includes laminar and turbulent boundary layers, confluent (merging) boundary layers, and often local separations and separation bubbles, all requiring finesse in modeling and experimental measurement techniques [Brune and McMasters, 1990; Nakayama et al., 1990; Olson and Orloff, 1981; Braden, 1986; Adair and Horne, 1988a and 1988b]. Airflow near the leading-edge slat can be accelerated to transonic velocities, requiring that compressibility effects be included in an analysis. The large pressure gradients make it difficult to achieve spanwise uniformity in a two-dimensional testing program due to wind tunnel wall boundary layer interactions with the model [Paschal et al., 1991]. In this section, an overview of the flow field features is presented first, followed by a review of current methods for computational analysis and description of experimental methods as they apply to multi-element airfoils.

2.1 Two-Dimensional Multi-Element Airfoil Flow Field Features

2.1.1 Forces - The Effect of Leading and Trailing-Edge Devices

The overall effects on the aerodynamic forces due to the deflection of leading and trailing-edge devices can best be described by considering each element separately. Deploying a trailing-edge flap causes an upward displacement of the lift curve (C_l vs α) while the lift curve slope remains relatively constant [Hoerner, 1985; Katz and Plotkin, 1991]. For example, consider a plain flap as shown in figure 2.2, a 20% chord flap on a NACA 66(215)-216 profile. As the deflection angle (δ) is increased the lift is seen to increase while the angle-of-attack (α) at maximum lift is slightly reduced. If a thin turbulent boundary layer is maintained over the aft portion of the wing section (as is the case with a largely laminar airfoil design), small deflections of the flap do not cause separation, with corresponding large increase in drag. Rather, they shift the range of lift coefficients for which low drag is obtained [Abbott and Von Doenhoff, 1959]. Figure 2.3 shows results from a 2D wind tunnel model of a NACA 2419 airfoil with a 30% chord Fowler flap [Hoerner, 1985]. From this figure, it is seen that the deflection of the flap produces the same change in the lift curve, however the lift increment is greater than with the plain flap in part due to the increased effective chord and camber. In addition, choice of gap and overhang are important; minute movements have a profound effect on the maximum lift coefficient (Cl_{max}). Figure 2.4 shows contours of Cl_{max} as a function of flap location with respect to the main element trailing edge for a NACA 23012 airfoil with a 25% chord flap

deflected at 50 degrees [Abbott and Von Doenhoff, 1959]. It is worth noting that the optimum configuration positions the flap with a small positive overhang and gap - found to be a typical rigging.

Deploying a leading-edge flap or slat causes an extension of the lift curve (Cl vs α) while the lift curve slope remains relatively constant [Hoerner, 1985; Nelson,1995]. A simple example is depicted in figure 2.5 where a plain Clark Y airfoil is fitted with a slotted leading edge [Hoerner, 1985]. A slot differs from a slat only in that the exterior geometry is fixed [Hoerner, 1985]. Here the fundamental effect of a leading-edge device is clearly shown - delay of stall by extension of the lift curve. In this case the angle-of-attack at stall increased approximately 10 degrees. The minimum profile drag for the slat and airfoil is increased with the deflection of the slat [Abbott and Von Doenhoff, 1959].

Consider now forces on a three-element airfoil with a slat, main element and trailing-edge Fowler flap compared to the plain airfoil with high-lift devices retracted. Figure 2.6 summarizes the changes in the lift and profile drag. Using the notation of the figure, the wing lift coefficient increases by $\Delta C_{L_{TE}}$ due to the trailing-edge flap while the angle-of-attack before stall is increased by $\Delta\alpha_{max_{LE}}$ by the slat [Nelson, 1995]. The profile drag coefficient is increased from its minimum value by the deployment of the slat and the flap by $\Delta Cdmin_{LE}$ and $\Delta Cdmin_{TE}$ respectively. The corresponding minimum drag profile lift coefficient increments due to the same geometry changes are given as ΔClp_{LE} and ΔClp_{TE}.

2.1.2 Boundary Layer Structure

A general understanding of the pressure distribution and boundary layer structure surrounding a multi-element airfoil is provided by figure 2.7 [Kuethe and Chow, 1986]. This configuration incorporates two trailing-edge devices located in succession with the nomenclature vane (C1) and flap (C2) respectively. The boundary layer that develops on the suction side of the slat (A) is initially laminar and typically transitions to turbulent before forming a confluence with the layer from the underside of the slat and the boundary layer formed on the suction side of the main element (B). On the pressure side of the slat, a separated region may exist with recirculation, followed by boundary layer growth [Brune and McMasters, 1990; Nakayama et al., 1990; Nelson, 1995]. This pattern is broadly repeated for each subsequent downstream element. It should be noted that laminar separation bubbles are often found at the leading edge of the flap(s) and main element. Separation and recirculation can occur on the bottom surface of the main element in configurations where the flap cove (the open area where the flap is stowed in cruise configuration) is poorly faired [Brune and McMasters, 1990; Nakayama et al., 1990; Nelson, 1995; Lin, 1992]. It is interesting to examine the wake, which carries a "history" of the upstream elements in the form of a velocity deficit for each element. Note also that the shear layers over the flap become curved and thick (true especially at high angles-of-attack), leading to a static pressure variation across the shear layer [Nakayama et al., 1990].

Recent experimental work has focused on careful measurement of flow field quantities such as mean velocities, turbulent stresses and static pressures [Nakayama et al., 1990; Olson and Orloff, 1981; Braden et al., 1986; Adair and Horne, 1988a and 1988b]. Figure 2.8 shows the mean velocity vector plot from hot-wire data for a three-element airfoil [Nakayama et al., 1990]. Clearly shown are overall velocity profiles defining the shear layers, flow curvature in the near wake, and the flow in the flap cove area. The static pressure within the shear layers of this high-lift system was found to vary by as much as 10% of the dynamic pressure, which the authors note as typical for a multi-element high-lift system. They attribute this variation to the large pressure difference between the upper and lower surfaces as well as the thick confluent shear layers. Turbulent stress profiles often provide more detailed representations of merging shear layers than mean velocity profiles [Nakayama et al., 1990; Adair and Horne, 1988b]. Figure 2.9 shows the level of detail possible with a hot-wire survey.

Nakayama et al. give an excellent written characterization of the various boundary layers of a three-element airfoil tested at a Reynolds number of three million for two cases: (A) $\alpha = 10°$, $\delta_{flap} = 15°$, $\delta_{slat} = 30°$ and (B) $\alpha = 18°$, $\delta_{flap} = 30°$, $\delta_{slat} = 30°$ both at near optimum gap and overhang settings [Nakayama et al., 1990]. In both cases no separation was noted except for separation bubbles in the flap cove and on the underside of the slat. The shear flows on the bottom of the surfaces were termed "negligibly thin" compared to those of the top surface and the wake.

The wake of the slat was found to be very small and even difficult to identify for case A while in case B it was more significant. This was thought to be related to the slat loading, which is much higher for case B. The slat wake is the only additional flow phenomena present on the main element versus a plain airfoil with boundary layer. Nakayama et al. (1990) believe the shear layer interaction between these two flows was weak but not negligible.

The flow around the flap is, of course, the most complex; here three separate shear layers interact and merge over the leading edge. The distinct layers were characterized as an outermost layer composed of the wake of the main airfoil combined with the slat, a jet-like accelerated middle layer from the gap with a much lower static pressure compared to the outer layer, and an inner boundary layer with a strong favorable pressure gradient and convex curvature, tending to remain thin and laminar. By the time the flow reaches the flap trailing edge, all of these layers have had time to interact with the strongest influence in terms of mean velocity and turbulent stress being the wake of the main element. Figure 2.10 shows the turbulent stress profiles for case A revealing the distinct regions discussed above. The mean velocity profile for the jet region in the gap adjacent to the flap leading edge was captured in another study by Adair and Horne which involved only a flap and airfoil [Adair and Horne, 1988a]. Figure 2.11 shows the mean velocity vector plot in the area, note the higher velocity flow and sharp inflections to the velocity profile when compared to the flow elsewhere over the flap.

Nakayama et al. (1990)describes the "near wake" and "intermediate wake" as the region where most of the smoothing of the velocity profiles and flow turning takes place. Here the contributions of separate shear layers may still be identified, however their effect is attenuated. The near wake was found to be very thick with large curvature visible in the mean velocity vectors of figure 2.12 [Nakayama et al., 1990]. Here it is clear that the confluent boundary layers, visible as the multiple velocity deficit regions, blend into a large wake with a single velocity deficit. A similar wake structure was found to exist on a two-element system consisting of a main airfoil and flap by Olson and Orloff [Olson and Orloff, 1981]. The distinct shear layers merged in the near wake and eventually formed a velocity profile with a single velocity deficit.

An understanding of the shear layers and their interaction coupled with a knowledge of the pressure distribution led to the identification of several characteristic effects inherent to multi-element airfoils. This work was first published in a landmark paper presented by A.M.O Smith in August 1974 and is the subject of the next section [Smith, 1974].

2.1.3 Characteristic Aerodynamic Effects of High-Lift Systems

Five primary effects due to gaps in multi-element airfoils were originally discussed by A.M.O. Smith. Reviewing the pressure distribution of figure 2.7a high suction peak is noted on the slat which coincides with very high velocities. The flow over the slat of a multi-element airfoil can therefore become supercritical with freestream Mach numbers as low as 0.2 [Brune and

McMasters, 1990; Nakayama et al., 1990; Butter, 1984]. The slat actually reduces the suction peak on the main element as compared to the main element acting alone. This effect was given the name "slat effect" by Smith (1974) and it can be summarized as follows: velocities associated with circulation on an upstream element tend to reduce the pressure peak on a downstream element [Smith, 1974]. Smith (1974) used a simple example which is repeated as figure 2-13 to illustrate the effect. If a line vortex is positioned near the leading edge of an airfoil it simulates the circulation present around a slat. It can be seen that the velocities induced on the airfoil by the vortex are counter to those from the airfoil alone, hence the pressure peak is reduced.

Examining the pressure distribution of figure 2.7 again, it is noted that the pressure at the trailing edge of the main element is elevated as compared to an airfoil acting alone. This effect has been termed the "circulation effect" by Smith (1974) and it can be stated as: a downstream element causes the trailing edge of an adjacent upstream element to be in a region of increased velocity inclined to the mean line at the rear of the forward element. The trailing edge is effectively at a higher angle-of-attack and therefore to satisfy the Kutta condition, circulation on the upstream element must increase. As a demonstration, Smith (1974) used an airfoil as the upstream element and a line vortex to represent the downstream element. Figure 2.14 is a reproduction of Smith's (1974) original demonstration.

The multi-element arrangement allows a fresh boundary layer to form beginning at the leading edge of each separate element. When compared to a single-element airfoil of the same chord, the boundary layers of the multi-elements are thinner, and thinner boundary layers can withstand stronger adverse pressure gradients, delaying separation. Smith (1974) calls this effect the "fresh boundary layer effect".

When the boundary layer of a forward element is discharged from the trailing edge into the region of higher velocity flow caused by a downstream element, Smith (1974) terms this the "dumping effect". The higher discharge velocity helps attenuate the pressure rise impressed on the boundary layer, hence providing increased lift or avoiding separation problems. In addition, these same boundary layers decelerate without contact with a solid wall. This "off the surface pressure recovery", as termed by Smith (1974) is an efficient method. Although an adverse pressure gradient magnifies the velocity defect and flow reversal can occur, off the surface pressure recovery is still more effective than any alternative in a boundary layer flow which contacts a wall [Smith, 1974].

2.2 Two-Dimensional Multi-Element Experimental Aerodynamics

By definition, two-dimensional (2D) airfoil models are constant chord airfoil elements positioned in a wind tunnel so as to maintain a uniform spanwise flow. Force measurements and boundary layer flow diagnostics are the most common measurements on 2D models. This discussion will focus on the methods for measuring forces, verification of flow uniformity, and

configuration optimization. In addition, an introduction to the effects of Mach and Reynolds number scaling is reviewed as they apply to multi-element optimization.

2.2.1 Force Measurements

Aerodynamic forces on the model can be indirectly calculated using integrated pressures from the model, or the tunnel walls, and from a wake survey or rake [Pankhurst and Holder, 1965; Rae and Pope, 1984; Ljungström, 1973a and 1973b]. Currently, the most popular method for determining lift forces is to integrate surface pressures [Lin, 1992; Papadakis, 1997; Innes et al., 1995; Wentz, 1976; Lin and Dominik, 1995; Valarezo et al., 1991]. Pressures are sampled from orifices located on the model surface, usually at the mid-span, upper and lower surfaces on all elements. Static pressure taps should be kept small so as not to interfere with the flow, particularly where boundary layer transition is of interest [Rae and Pope, 1984; Lynch, 1992]. If they are kept to a diameter of 1/32 of an inch or less it has been reported that there is negligible difference between drilling them perpendicular to the surface or perpendicular to the chord when used on typical low-speed airfoil models [Rae and Pope, 1984]. However, the taps should always be flush with the surface. One method to assure this is to drill holes from the outside of a metal model and join annealed stainless steel tubing to the hole by press fitting the tube into a small counterbore on the inside [Backley, 1994; Pope and Goin, 1978]. Pressure orifices are clustered near the leading edge where the pressure gradients are steeper; Rae and

Pope recommend as a minimum, locations at 0, 1.25, 2.5, 5, 10, 15, 20, 30, 40, 50, 60, 70, 80, 90, 95, and 100% chord. This clustering provides better resolution for integration of forces. While many investigators report the details of their measurement methods, it is difficult to find any mention of the integration method. The NASA Langley Low Turbulence Pressure Tunnel (LTPT) staff use a simple trapezoidal integration rule for their force data reduction [Walker, 1994]. This method can be justified by comparing resulting forces from integrations of a known continuous pressure distribution versus using discrete points (at the pressure orifice locations) from the pressure distribution with a trapezoidal approximate integration. Appendix A.2 details the method used in this work for determining the lift coefficient from pressure data for a multi-element airfoil model. Two recent studies help quantify uncertainty in lift coefficient measurements using integrated pressures. Lin reports an uncertainty of ±0.02 for maximum lift coefficient (Cl_{max}) using 140 pressure taps [Lin, 1992] while Anderson reported ±0.03 for lift coefficients using 146 pressures during his recent study [Anderson and Bonhaus, 1993]. Both studies were conducted in LTPT using three-element high-lift models.

While forces derived from integrated surface pressures, resolved normal to the freestream direction, provide accurate and repeatable measurements for lift, integrating pressures and resolving forces in a direction parallel to the freestream will not give the total drag, since skin friction is not included [Paschal et al., 1991; Rae and Pope, 1984]. Instead, the well established momentum deficit method, which relates momentum loss in the

wake to airfoil drag, is most often used [Lin, 1992; Rae and Pope, 1984; Ljungström, 1973a; Papadakis, 1997; Lin and Dominik, 1995]. The derivation of this method is not presented here but figure 2.15 summarizes the results [Ljungström, 1973a]. In the figure, static pressure, dynamic pressure, and total head are denoted by p,q, and h respectively and Y_w is the total wake rake survey width. Ljungström shows two standard deviations in drag to be about 2.7% with the rake positioned one chord length downstream using a 2-D insert in a low-speed tunnel. Lin chose 1.35 chord lengths and quotes an uncertainty of ±2.5% for the drag coefficient for recent tests in LTPT [Lin, 1992]. The static pressure at these downstream locations does not vary significantly across the wake compared to the reference static pressure upstream of the model (P_{ref} in figure 2.15) [Nakayama, 1990; Ljungström, 1973a]

A more direct method of determining forces is to mount the model on a balance [Ljungström, 1973b]. For two-dimensional testing the balance system usually supports the model through both sidewalls with the model spanning the tunnel (or insert) [Paschal et al., 1991; Biber and Zumwalt, 1992 and 1993]. The LTPT balance is representative of a modern sidewall balance for two-dimensional testing [Stainback, 1986]. Figure 2.16 shows the general configuration [Paschal et al., 1991]. The airfoil model is held between two circular endplates that are attached to an inner drum. A motor driven, externally mounted pitch mechanism provides attitude control by rotating the inner drums within the outer drums. The outer drums are attached to the yoke

arm which is connected to the force balance platform. The force balance is a three component strain gage configuration with load limits of 18,000 pounds in lift and 550 pounds in drag and is accurate to within 0.1% of design load limits. When comparing typical force measurements with the balance versus momentum deficit methods (drag) or integrated pressures (lift), the balance is generally inferior. One reason is that the entire flow field must be two-dimensional requiring careful sidewall boundary layer control. Pressure methods require only that the centerline flow field be representative of the two-dimensional flow field. In addition, there is often uncertainty (typically reported ±0.5°) in the mean flow direction leading to further error [Paschal, 1991, et al.; Ljungström, 1973a and 1973b].

2.2.2 Maintenance of Uniform Spanwise Flow

Large pressure gradients induced by high-lift airfoils can cause the wind tunnel sidewall boundary layers to separate in the test section and reduce the lift generated. Reviewing the pressure distribution in figure 2.7 reveals steep suction peaks at the leading edges of the airfoils which can turn the sidewall boundary layer towards the upper surface of the model near the model/wall juncture. This process will tend to cause the sidewall boundary layer to separate leading to an irregular three-dimensional flow pattern which contaminates the flow over the low aspect ratio model resulting in reduced lift [Paschal et al., 1991; Meyers and Hepner, 1984; Schieman and Kubendran, 1988; Kornilov and Kharitonov, 1984; Kobashi et al., 1982]. Separation is particularly likely at high angles-of-attack where the pressure gradients are

the steepest [Innes, 1995; Paschal et al., 1991]. Control of flow two-dimensionality is generally accomplished by one of three methods: sidewall blowing, sidewall suction, and the use of model endplates (2D insert), or a combination of these methods [Nakayama, 1990; Braden, 1986; Innes et al., 1995; Wentz, 1976; Valarezo, 1991].

A boundary layer control system (BLC) utilizing the blowing technique as used in LTPT is shown in figure 2.17 [Paschal et al., 1991]. Note the profound increase in lift when the blowing system is used, particularly for the lower Reynolds numbers at high angles-of-attack. Tangential blowing slots were positioned at the leading edge of the slat, top surface of the main element and flap, and just upstream of the flap cove region. These slots were fed with pressurized air through plenum chambers. The mass flow rate of the injected air is controlled through valves and tunnel pressure is held constant by removing air downstream of the test section. [Paschal et al., 1991; Morgan et al., 1987].

Wall suction involves the removal of the boundary layer through porous walls or suction slots. This can require that a vacuum system be installed in the case of a test section at atmospheric pressure, or achieved simply by venting the walls of a pressurized tunnel [Paschal et al., 1991; Ljungström 1973b; Wedderspoon, 1986]. In figure 2.18 a cross section of the current LTPT BLC system using ventilated walls is depicted. Air from the porous endplates vents through ducts which are instrumented with total pressure probes, static wall taps, and a thermocouple [Paschal et al., 1991]. The mass

flow rate of the exiting air is automatically calculated using compressible flow equations [Stainback, 1986]. An auxiliary compressor, controlled by a feedback loop, is used to make up the lost air. Results for various endplate perforation patterns for a typical four-element high-lift model are shown in figure 2.19, where m_V/m_T is the ratio of vent and test section mass flow rates. The spanwise pressure distributions are "fuller" and more uniform with the BLC system operating.

A more simplified approach to boundary layer control is the use of endplates on a model which are displaced from the tunnel sidewall [Olson and Orloff, 1981; Innes et al., 1995; Wentz, 1976; Biber and Zumwalt, 1992 and 1993]. Figure 2.20 shows the use of circular endplates with a high-lift model in the NASA Ames 7 x 10 foot wind tunnel [Olson and Orloff, 1981]. The gap between the endplate and the tunnel wall reduces the interaction of the model pressure gradient with the tunnel sidewall since the end plate boundary layer is fresh and thin. A recent report by Innes contains an example of a hybrid method for sidewall boundary layer control [Innes et al., 1995]. Here a tangential blowing slot was incorporated into the end plate to control separation of the end plate boundary layer and reduce flow three-dimensionality. If a full span model is used, fences can be installed slightly inboard of the tunnel sidewall to act as endplates [Adair and Horne, 1988b].

Verification of flow two-dimensionality is accomplished using spanwise pressure measurements and flow visualization. The study summarized by figure 2.19 shows the use of pressure data. The level of spanwise uniformity

considered acceptable varies among experimenters. As discussed earlier, the use of a force balance demands the utmost regard for uniform flow. Paschal et al. (1990) were able to control all spanwise pressure coefficients to within ±0.1 for a given spanwise location which represented roughly 0.5% of the leading-edge suction peaks typically seen at maximum lift [Paschal, 1991]. Nakayama, Kreplin, and Morgan report an acceptable level of spanwise uniformity as less than 5% of the total pressure coefficient variation over the whole model [Nakayama et al., 1990].

The most common flow visualization method used to verify uniform flow is tufts or "minitufts", attached to the surface [Nakayama et al., 1990; Paschal et al., 1991; Crowder, 1977]. The entire model can be tufted with fluorescent monofilament nylon line (minitufts) and viewed with an ultraviolet light to show overall local flow directions and separation [Rae and Pope, 1984]. Separating flow will cause a tuft to lift off and twirl while attached flow will force the tuft to lay on the surface and align with the local flow direction. Tufts can of course also be used to investigate stall and separation patterns due to configuration changes or changes in angle-of-attack [Wentz, 1976].

Tempera and kerosene were used by Biber to investigate the flow character near the wall juncture of a high-lift model [Biber and Zumwalt, 1993]. Oil flow was successfully used by Ljungström to check flow uniformity and also allowed the identification of laminar separation bubbles, natural transition and turbulent separation [Ljungström , 1973b].

2.2.3 Optimization of Multi-Element Airfoils at High Reynolds Numbers

To truly optimize the geometry of a multi-element airfoil high-lift system the model should be tested at near flight Reynolds and Mach numbers; this constraint severely limits the number of facilities available for high-lift testing [Nelson, 1995; Butter, 1984; Lynch, 1992; Valarezo, 1993]. Significant differences in maximum lift coefficient have been measured due to variation in Mach and Reynolds numbers [Valarezo, 1991 and 1993; Woodward, 1988]. For most aircraft, it is not generally practical to obtain full-scale Reynolds numbers in wind tunnel testing by using a full-scale model; however, it is often possible with a reduced scale model. Pressurized and cryogenic tunnels provide the increased density and/or the decreased viscosity required to raise the Reynolds number [Rae and Pope, 1984].

Rigging geometry optimization of multi-element configurations requires individual element optimization first while other elements are kept in a "conservative setting", meaning a choice of gap and overhang that, based on experience, is thought to provide adequate slot flow without risking separation. This is followed by whole system optimization to find the highest performance possible [Nelson, 1995; Lin and Dominik, 1995; Valarezo, 1991]. Certain parameters must be chosen before testing can begin. The variables include: baseline slat and flap gap and overhang, slat and flap deflection, angle-of-attack, and freestream Mach and Reynolds number. The number of variables, the economics of tunnel occupancy, and development time restraints realistically dictate the development of a sparse test matrix. As a

relevant example of a modern optimization consider the recent work of Valarezo et al. in LTPT [Valerezo, 1991]. The study focused on obtaining maximum lift coefficients of 4.5 and 5.0 respectively for two advanced transport high-lift landing configurations, the first a three-element, and the second a four-element configuration as shown in figure 2.21. Testing began by first measuring Cl_{max} for the cruise configuration wing (high-lift devices stowed) as a function of Reynolds number at a Mach number of 0.2. These results served as a baseline for investigating Reynolds number effects on the high-lift configuration and showed that Cl_{max} is relatively constant (cruise configuration) for Reynolds numbers above 5 million. Unfortunately this Reynolds number insensitivity was not repeated for the high-lift configurations. It was decided to choose 9 million and 0.2 for the Reynolds and Mach number so as to best represent full-scale flow over the stall critical section of the wing, which is simply the first spanwise location on the wing to encounter stall. Next, the four-element configuration's flaps were installed and set at 35° and 15° deflection (35° deflection for main flap, 50° for the auxiliary flap) with conservative gap and overhang settings.

A slat optimization was now performed using three slat deflection angles : 25°, 30°, and 35° and several gap and overhang values. The results are shown as figure 2.22, where each point (a single geometry) can represent as much as two hours tunnel occupancy due to the use of a pressurized facility in conjunction with manual adjustment and gaging of elements [Lin, 1993]. The maximum lift coefficient occurs with the 30° slat deflection. The

two higher deflections were shown to load the slat, even past the angle-of-attack where the main element stalled. Having chosen the deflection angle, the slat gap and overhang were varied further as the grid in figure 2.22 shows. An optimum rigging was chosen for a Reynolds number of 5 million and the test was run again at 9 million - results are shown in figure 2.23. The difference in optimum slat gap settings with overhang held constant was 0.7%C, a significant difference. The most significant Mach number effect on the slat is the limiting of the peak pressure attained as shown in figure 2.24 which occurred at 0.26 Mach number. The flap optimization was conducted subsequent to the slat studies. Using the optimum slat setting, a Reynolds number of 9 million, and the two segment flap, seven gap and overhang riggings were chosen for the same deflection settings as were used in the slat optimization. The effect of Mach number on the four-element airfoil is shown in figure 2.25. Focussing now on the single element flap at two deflection angles; 30° and 35°, the rigging choices and Cl_{max} results are shown in figure 2.26. What is not evident in the lift plots is the large separation at low angles-of-attack in the 35° flap deflection case leading to the choice of the 30° deflection as optimum. The pressure distribution on the flap for the two deflections shows the distinctive droop in the upper surface plot of the 35° case of figure 2.27 indicating that separation has begun in this region. The investigators rejected the rigging which allowed flow separation at low angle-of-attack due to the noise that would have been created on the actual airplane while approaching the airport.

This study and other recent studies in LTPT provide insight into the testing of multi-element airfoils and the importance of testing at representative Mach and Reynolds numbers particularly while choosing optimum rigging geometry for slats and flaps.

2.3 Two-Dimensional Multi-Element Computational Aerodynamics

The purpose of this section is to briefly review some popular computational fluid dynamics (CFD) methods as they apply to the analysis of 2D multi-element airfoils. The discussion in the previous sections detailed the complex flow physics associated with the viscous flow over the airfoil. In particular, even at the time of this writing, code developers have had difficulty modeling merging shear layers, separated flow, and boundary layer transition. This is due in part to the fact that experimentalists do not fully understand the flow physics [Nelson, 1995; Brune and McMasters, 1990].

Only recently have computational tools been available that partially deal with the separated flows and viscous interactions of high-lift systems. [Brune and McMasters, 1990]. In the beginning, inviscid panel codes were used for analysis. A natural evolution was the coupling of a boundary layer solution to the panel code. Later these codes were adapted to include small scale separation and later massive separation. The most recent tool developed has been the use of algorithms which solve the Reynolds-averaged Navier-Stokes equations (RANS) directly using a turbulence model for closure [Brune and McMasters, 1990; Nelson, 1995].

Recent progress is perhaps best summarized, with respect to this study, by the results of the "High-Lift Workshop CFD Challenge", held in May 1993 at the NASA Langley Research Center [Klausmeyer and Lin, 1997]. This meeting was a pseudo-contest where competitors were asked to compute aerodynamic force coefficients, pressure and velocity distributions using a Douglas three-element airfoil at given flow conditions without prior knowledge of experimental results taken in LTPT. It is the purpose of the following sections to provide an overview of some current methods used for analysis, while focusing on comparisons to experimental results. The most popular modern codes (excluding airfoil optimization and design) can be broadly grouped into two categories: coupled inviscid-viscous and Navier-Stokes methods.

2.3.1 Coupled Inviscid - Viscous Flow Methods

In general, these methods are less expensive to run than Navier-Stokes (N-S) solvers and have simplified grid requirements. In comparison, the biggest disadvantage is that the flow physics are not as accurately represented. The codes must provide a model for separation regions, wakes and confluences [Nelson, 1995].

Modern coupled codes model large separated regions as well as boundary layers and small separation bubbles. The method of Cebeci is representative of a modern methodology which uses a panel method loosely coupled to boundary layer equations [Cebeci, 1992]. The interactive sequence of calculations begins by solving for the external inviscid velocity

field using a panel method which provides the edge velocity for the boundary layer on the airfoil elements, with the exception of troublesome areas such as the flap cove region. The Falkner-Skan transformation is used to transform the boundary layer equations which are solved next, beginning on the top surfaces, progressing from the stagnation point, through the regions of laminar, transitional, and turbulent flow to the trailing edge. The bottom surface boundary layer solution progresses in a similar manner. With velocity distributions on both surfaces known at the trailing edge, calculations are extended into the wake. A displacement thickness is now available and the panel method is again invoked; iteration continues until convergence. One advantage to this method is that the required grid is restricted to the surface. The turbulence model employed is that of Cebeci and Smith [Cebeci and Smith, 1974].

MSES is an extremely fast and robust code developed by Drela and Giles which is currently in use for research and production [Drela, 1990 and 1993]. The Euler equation is solved on an H-grid simultaneously with the integral boundary layer equations using a Newton solver. The inner grid boundary is displaced by the calculated boundary layer displacement thickness and the wake trajectory is determined implicitly. Boundary layer transition is said to occur when the amplitude of the most unstable Tollmien-Schlichting wave in the boundary layer has grown by a factor of e^9 (~8100). This code has been proven to handle large-scale separation and asymmetric

wakes; results for a three-element configuration are presented in section 2.3.3 [Nelson, 1995; Klausmeyer and Lin, 1997].

2.3.2 Navier-Stokes Methods

Navier-Stokes methods are perhaps best characterized by the choice of grid, flow solver, and turbulence model. Multi-element grids can be patched together from smaller structured grids generated around each element which share common points at their boundaries. Alternately, structured grids may be generated around each element and randomly overlapped, or unstructured grids surrounding the entire model can be used [Nelson, 1995; Klausmeyer and Lin, 1997].

Grids are often described by their overall shape. An example of a C-grid is a grid which forms a doubly connected region beginning at the upper surface trailing edge (or in the wake) of an airfoil and wraps around the leading edge until the endpoint is coincident with the start point. When a slender body, such as an airfoil, is inserted into a surrounding grid, it is represented as a slit in the computational domain, and this doubly connected region is known as an H-grid.

Patched or multi-block grids split the domain into patches with common boundaries. A grid which is point-wise continuous is generated for each individual patch which shares common boundaries with neighboring patches. Typically C-grids are used around each element and the domain is patched together with other C or H-grids. An example of a multi-block grid is shown for a three-element airfoil in figure 2-28 [Vatsa et al., 1994]. This 97 block

grid was generated using GridPro™/az3000 software and has approximately 50,000 grid points.

Overset or Chimera grids randomly overlap body-fitted grids for each element and have the advantage of not requiring prior knowledge of the flow field [Renze et al., 1992, Nelson, 1995; Benek et al., 1986]. In the Chimera method, individual grids receive information from each other in the form of interpolated quantities.

Unstructured grid methods offer geometric flexibility and naturally lend themselves to the complex geometry and flow physics of multi-element configurations [Marcum, 1995; Barth and Linton, 1995; Nelson, 1995]. Also, unstructured grids offer the potential to adapt the grid to improve the computational accuracy. Unstructured grids typically rely on geometric triangulation algorithms which distribute a stretched mesh over the domain, clustering points near the body surfaces to provide resolution in the flow field where the influence of viscosity is greatest.

The multiblock grid shown in figure 2.28 was used with a finite volume, central difference code originally developed for three-dimensional applications called TLNS3D-MB. The Spalart-Allmaras turbulence model [Spalart and Allmaras, 1992] was chosen over the Baldwin-Lomax model [Baldwin and Lomax, 1978] by comparing computed velocity profiles to experimental data using both methods. Results from this code and others for a three-element airfoil are compared with experimental data in the next section.

A Chimera grid was used in a comparative study of two popular turbulence models used with a multi-element model [Renze et al., 1992]. The Baldwin-Lomax [Baldwin and Lomax, 1978] and Baldwin-Barth [Baldwin and Barth, 1990] algebraic turbulence models were used with a code called OVERFLOW to solve the thin-layer N-S equations [Buning et al., 1991]. OVERFLOW uses a three factor, diagonalized, central difference scheme, purposefully designed to process Chimera overset grids.

An unstructured grid was used by Anderson and Bonhaus to solve the RANS equations for flow around a three-element airfoil [Anderson and Bonhaus, 1993]. An upwind, implicit, node based solver, using a linearized backward-Euler formulation, known as FUN2D was used with both the Baldwin-Barth [Baldwin and Barth, 1990] and Spalart-Allmaras [Spalart and Allmaras, 1991] turbulence models. Results including comparison to experimental data are included in the next section.

2.3.3 Modern CFD Multi-Element Airfoil Methods Compared

The data presented in this section is a result of a cooperative agreement between the Douglas Aircraft Company and the NASA Langley Research Center (LaRC). At the LaRC "High-Lift Workshop CFD Challenge," twelve invited researchers shared computed results for flows over a Douglas three-element airfoil [Klausmeyer and Lin, 1997]. The participant's computed results were found with no prior knowledge of experimental results obtained in the LTPT. The overall geometry is a three-element configuration based on a 11.55%C thick supercritical airfoil, with slat and flap chords of 14.48%C and

30%C, respectively based on the nested airfoil chord (C). Results shown are for the landing configuration which is designated 30P30N meaning a 30° slat deflection, and 30° flap deflection. The "P" refers to the slat rigging where the slat gap is 2.9%C and the slat overhang is -2.5%C. The "N" refers to the flap rigging, although two flap rigging configurations were tested leading to some confusion concerning the nomenclature; results will be presented for configuration "A" which defines the flap gap as 1.27%C, flap overhang as 0.25%C [Anderson and Bonhaus; Nelson, 1995]. Figure 2.29 shows the geometry for the A configuration in solid lines including the numbered chordwise stations. Table 2.1 summarizes the codes and participants used in the high-lift workshop blind calculations. Note the column marked "legend key" which identifies the participant's results in the following figures. Figures 2.30 and 2.31 present the lift, drag, and pitching moment coefficient data. Clearly, all the methods have difficulty in accurately predicting the drag polar. Collectively, the RANS methods appear to better predict the lift curve and pitching moment polar than the coupled methods, although Drela's and Amirchoupani's routines perform favorably. In figures 2.32 and 2.33 some representative velocity profiles are shown for chordwise station 1 (on the main element, x/c = 0.45) and station 3 (on the flap, x/c =0.8982) of figure 2.29. Problems can be seen in accurately modeling the slat wake region and a generally wide variation in velocity magnitude between the codes is noted. A pressure distribution representative of typical RANS solvers used at the CFD challenge, is given in figure 2.34 [Anderson and Bonhaus, 1993].

Comparatively, the coupled methods produced more scatter in the pressure distribution results than the RANS methods [Klausmeyer and Lin, 1997]. In summary, Rogers listed the most important findings of the workshop: (1) it is best to include wind-tunnel walls in the computational model when comparing to experimental data, (2) most grid approaches showed they could handle the three-element geometry, (3) grid resolution studies were important, (4) there is a need for solution adaptation of the grid for shear layers and wakes, (5) there are no reliable transition models, and (6) for 2D modeling it is only important to identify trends, not absolute levels [Nelson, 1995].

In conclusion, it is apparent that there is a very real requirement for experiments. In general, CFD methods as applied to multi-element airfoils are not fully capable of modeling the associated complex flow physics, and therefore they do not predict forces and moments with sufficient accuracy. Nevertheless, one of the primary benefits to using computational methods in developing high-lift airfoils is to predict the effects of gap and overhang changes and the scaling effect of Reynolds number to reduce wind tunnel occupancy time during configuration optimization [Klausmeyer and Lin, 1997].

Legend Key	Person	Affiliation	Program	Type	Grid	Modeling Notes
Kyle	Anderson/ Bonhaus	Langley	FUN2D	RANS	Unstructured	Without point vortex farfield corrections
Kyleff	Anderson/ Bonhaus	Langley	FUN2D	RANS	Unstructured	With point vortex farfield corrections
jones	Jones	Langley	CFL3D	RANS	Structured-Chimera	
bied	Biedron	Langley	CFL3D	RANS	Structured-Eiseman multi-block	
vatsa	Vatsa	Langley	TLNS3D	RANS	Structured-Eiseman multi-block	
dod	Dodbele	Langley	MCARF	Coupled	-	
mavk	Mavriplis/ Klausmeyer	Langley	NSU2D	RANS	Unstructured	
stusb	Rogers	Ames	INS2D	RANS	Structured-Chimera	Baldwin/Barth turbulence model
stusa	Rogers	Ames	INS2D	RANS	Structured-Chimera	Spalart/Allmaras turbulence model
stuso	Rogers	Ames	INS2D	RANS	Structured-Chimera	k-ω turbulence model
drela	Drela	MIT	MSES	Coupled	Structured	
hawk	Hinson/ Hawke	Learjet	MEAFOIL	Coupled	-	
wood	Woodson	Cessna	MCARF	Coupled	-	
caobb	Cao/ Kusunose	Boeing	INS2D	RANS	Structured	Baldwin/Barth turbulence model
caoba	Cao/ Kusunose	Boeing	INS2D	RANS	Structured	Spalart/Allmaras turbulence model
amir	Amirchoupani	Boeing		Coupled	-	Free transition
amirt	Amirchoupani	Boeing		Coupled	-	Fixed transition

Table 2.1 High-Lift Workshop CFD Challenge Participants

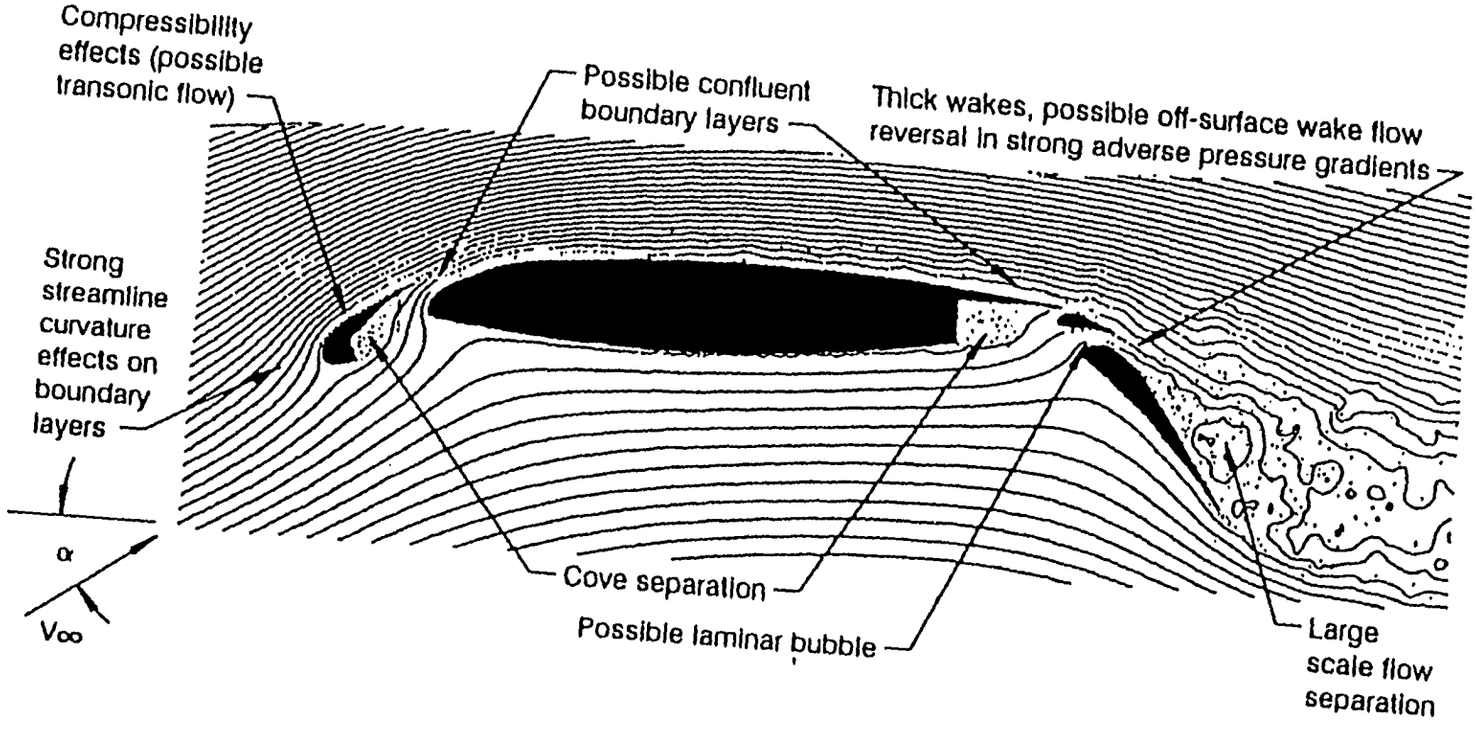

Figure 2.1 Multi-Element Airfoil Flow Field Features

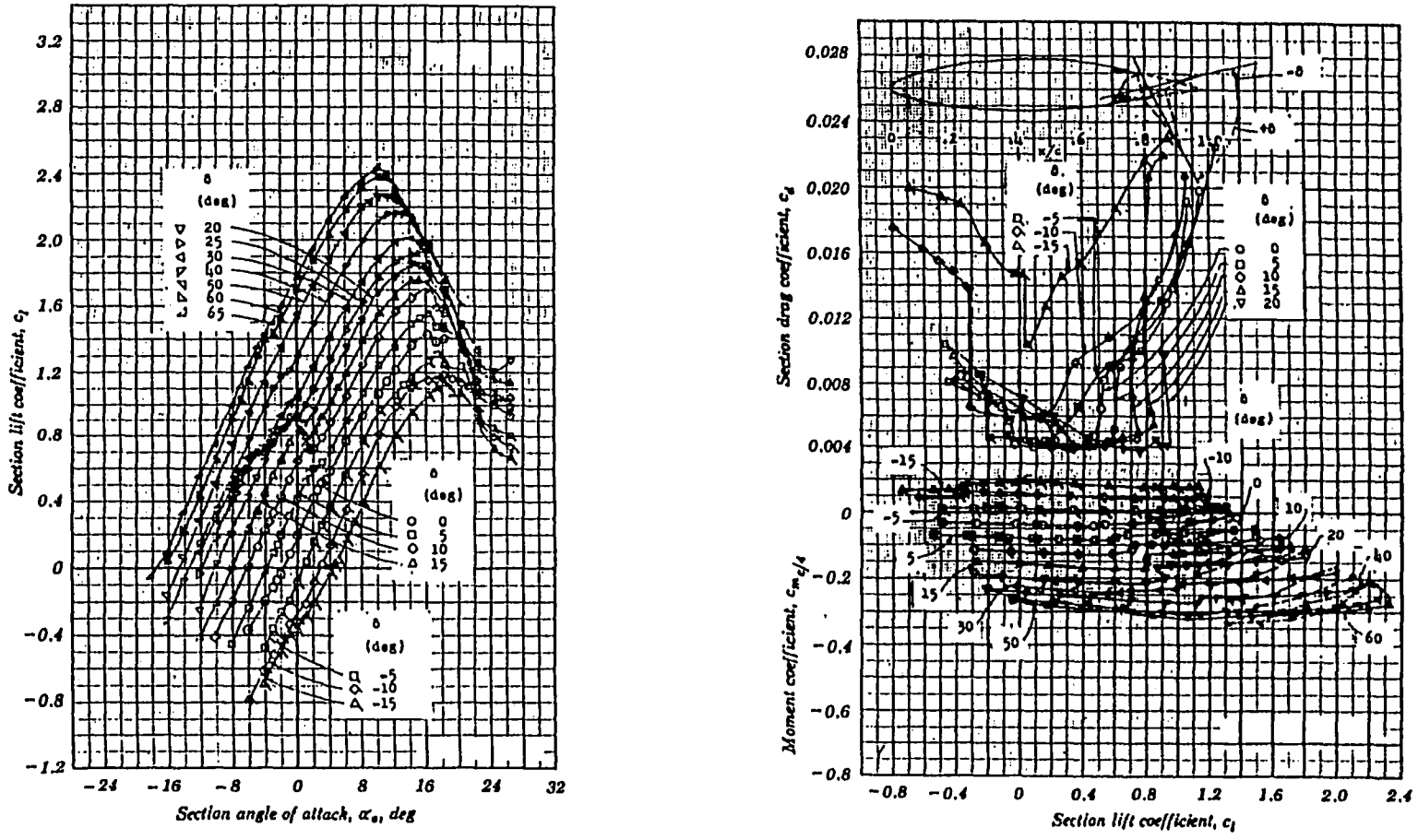

Figure 2.2 Force and Moment Coefficients for a NACA 66(215)-216 Airfoil with a 20% Chord Plain Flap

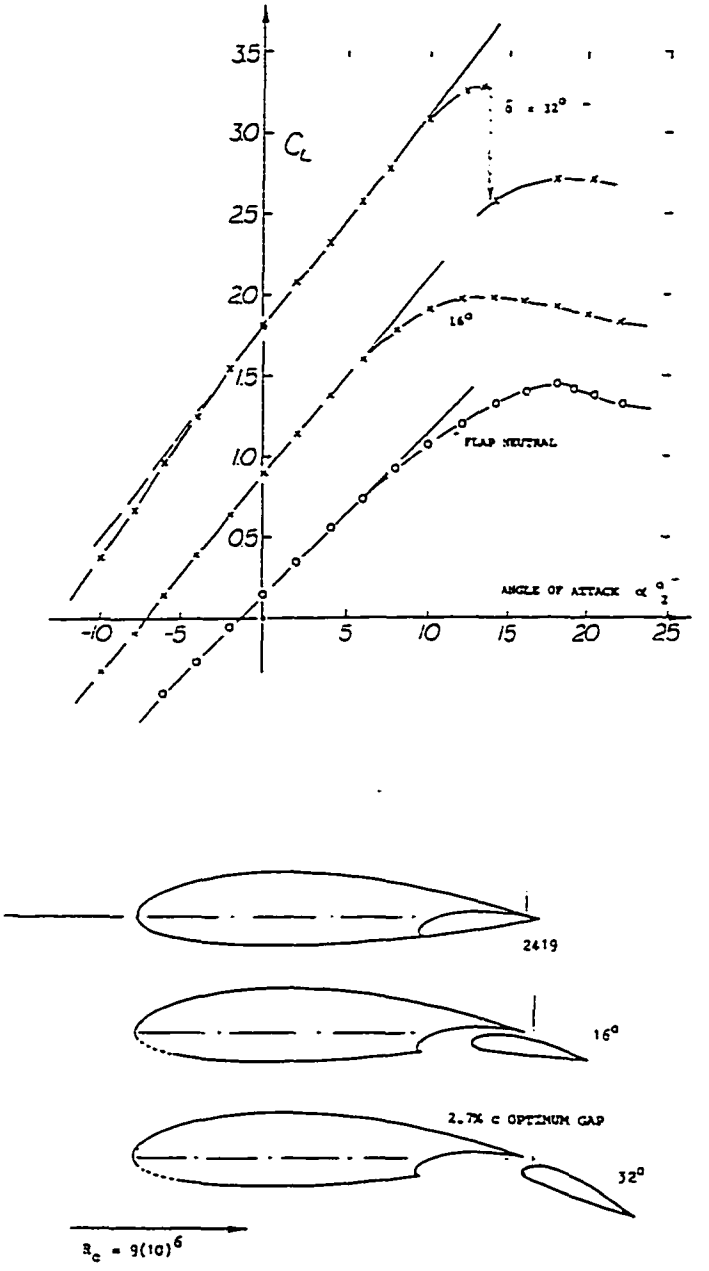

Figure 2.3 Lift Curves for a NACA 2419 Airfoil with 30% Chord Fowler Flap

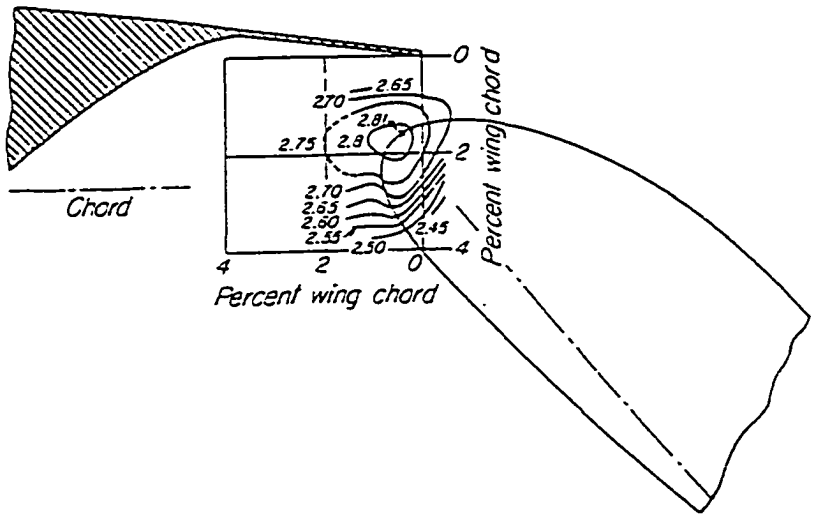

Figure 2.4 Contours of Maximum Lift Coefficient as a Function of Flap Position for NACA 23012 with 25% Chord Flap Deflected at 50°

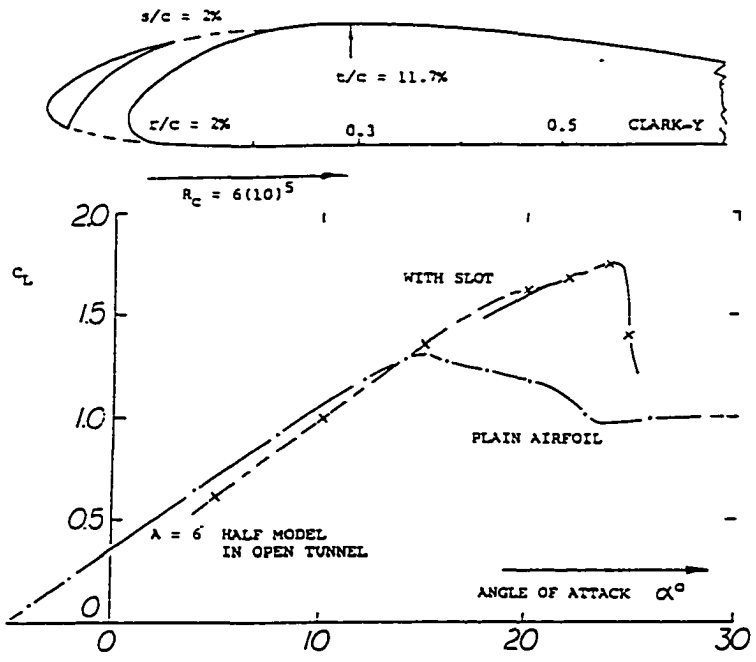

Figure 2.5 Effect of Fixed Slot on Clark-Y Airfoil

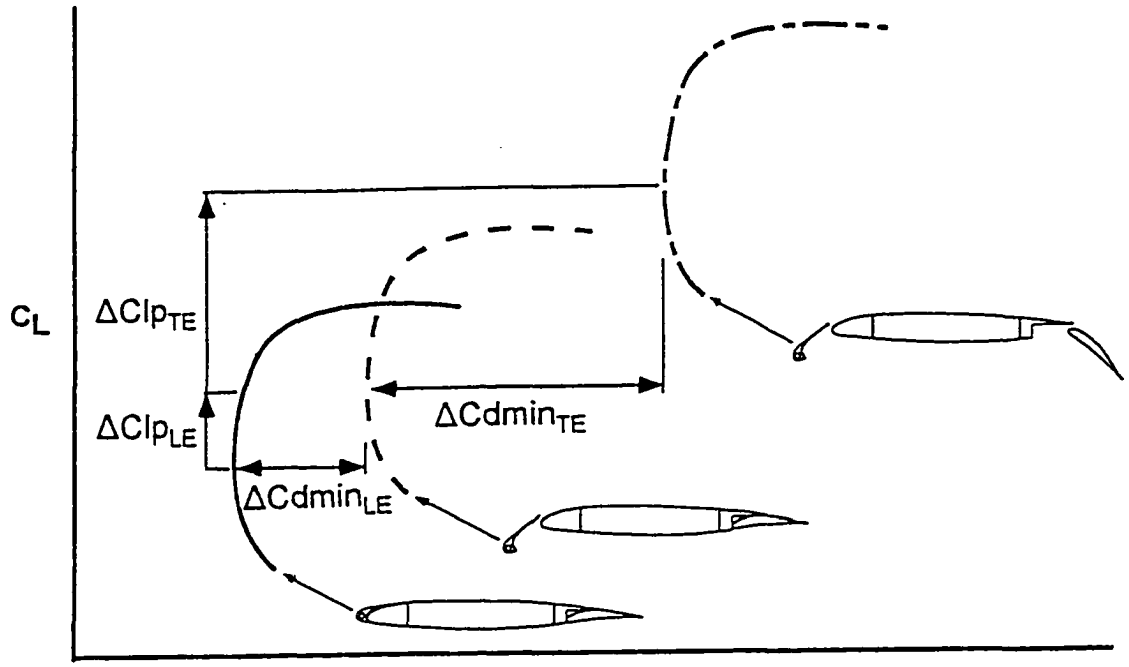

$$C_d = C_D - \frac{C_L^2}{\pi AR}$$

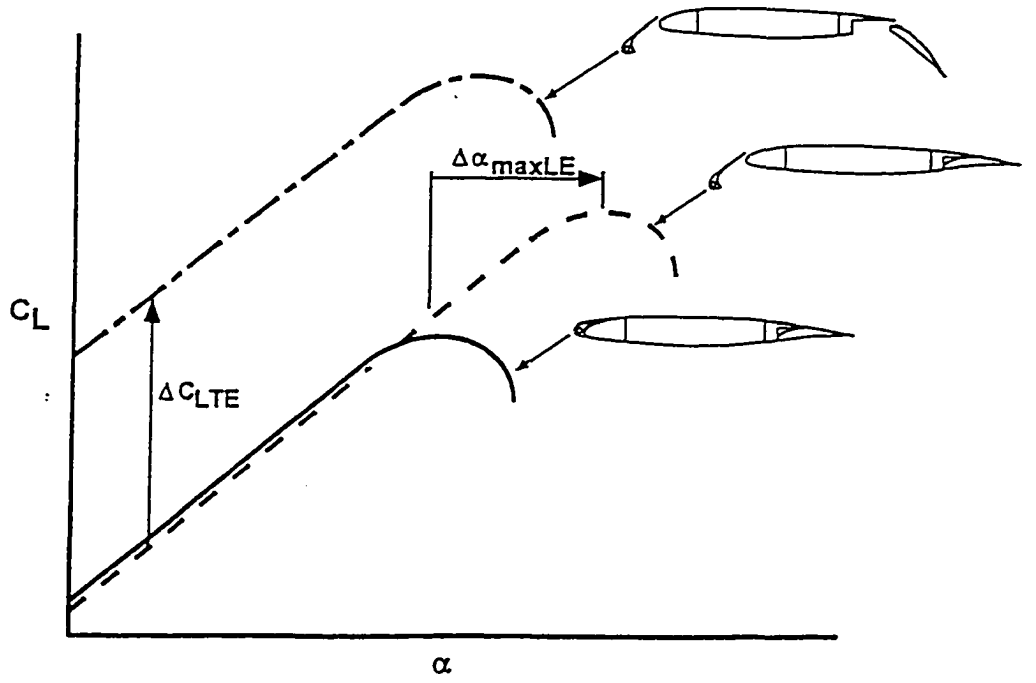

Figure 2.6 Effect of High-Lift Devices on Airfoil Lift Curve and Drag Polar

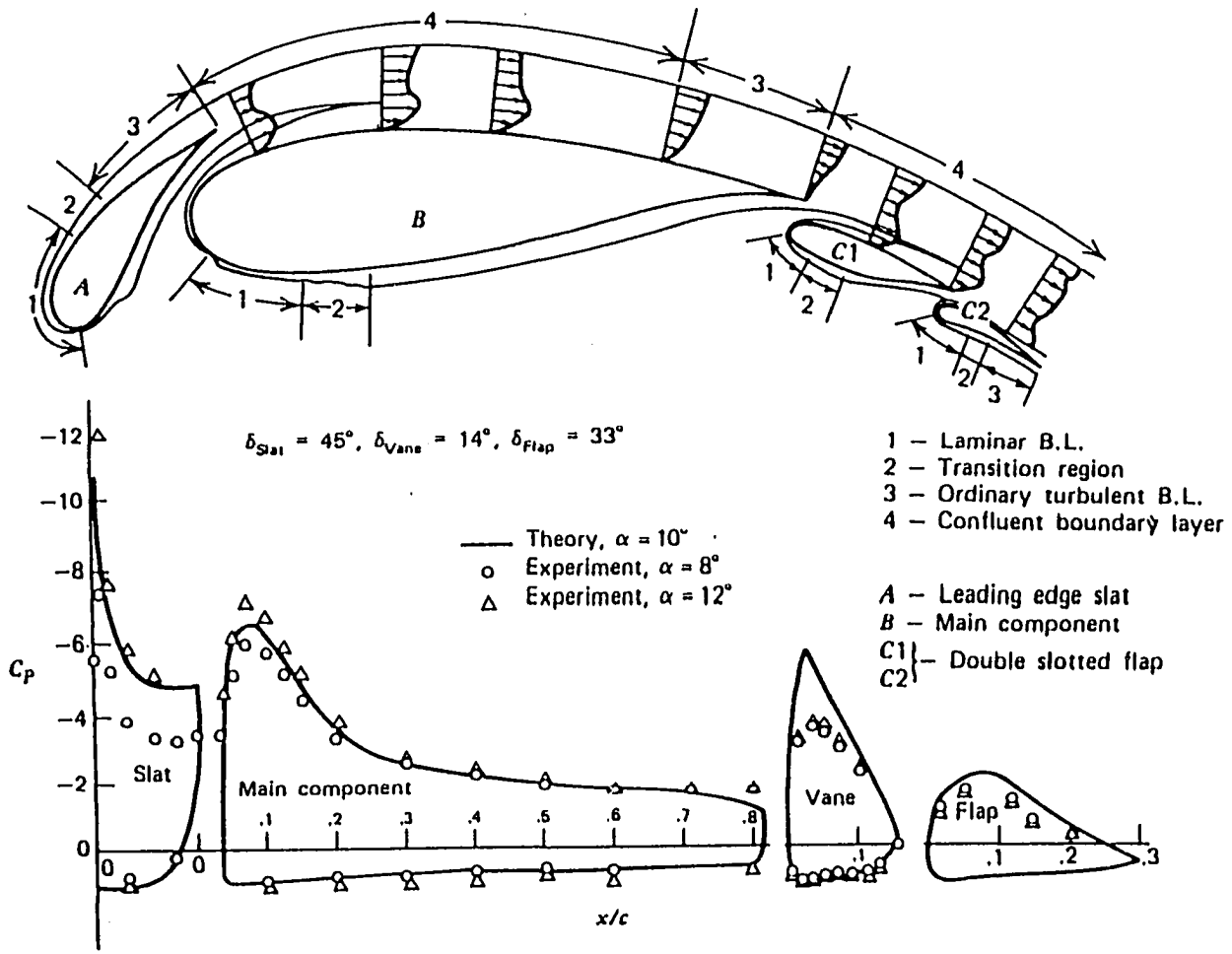

Figure 2.7 Multi-Element Airfoil Boundary Layer Development and Pressure Distribution

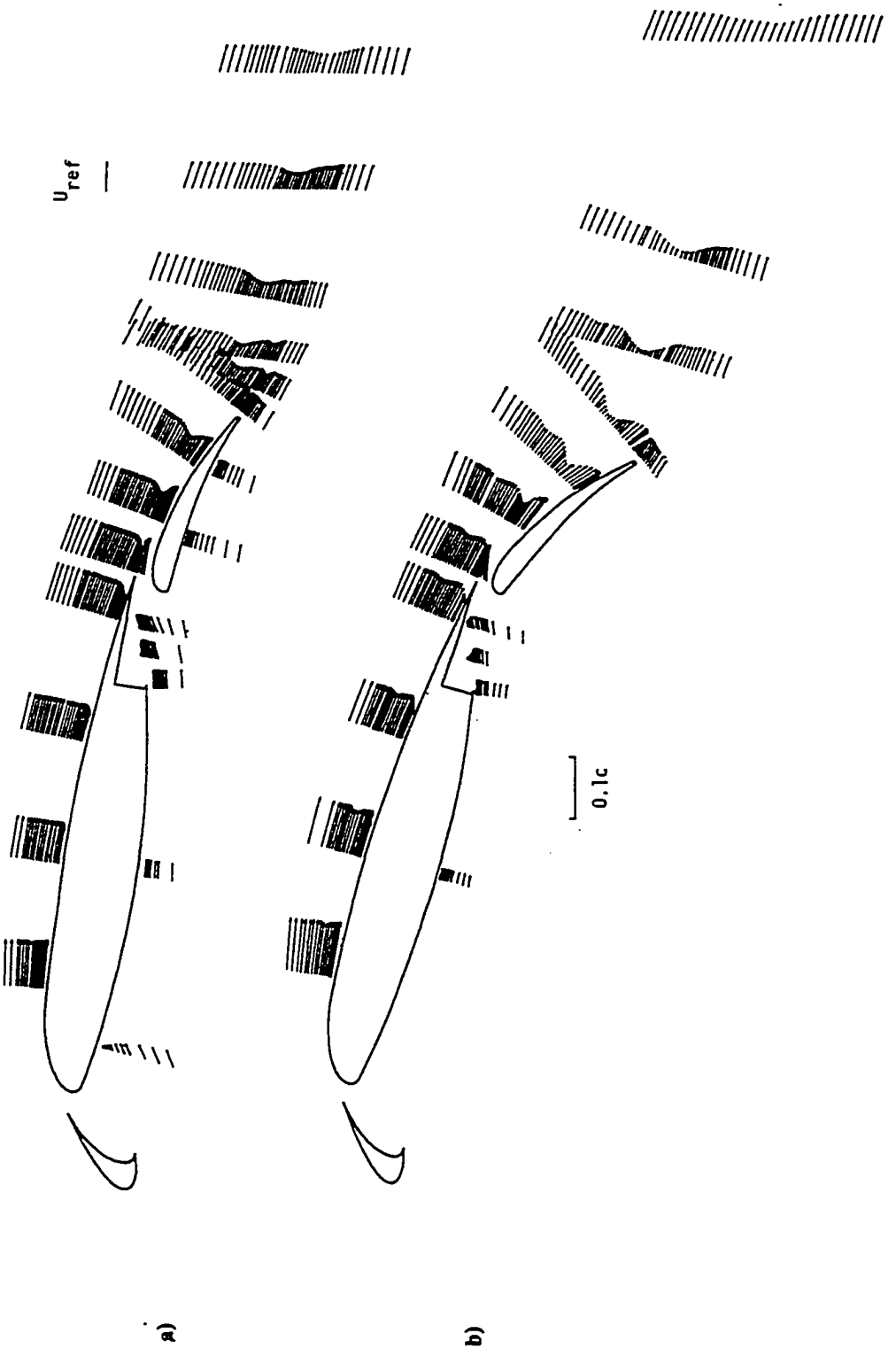

Figure 2.8 Mean Velocity Vectors from Hot-Wire Measurements for a Three-Element Airfoil

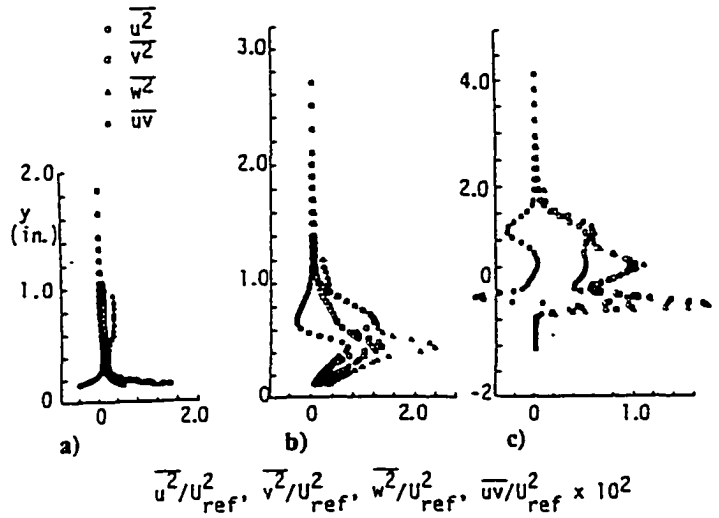

Figure 2.9 Representative Turbulent Stress Profiles for Case A of the model of Nakayama et al.; a) Main Element Upper Surface, x/c=0.4, b) Flap Upper Surface, x/c=0.8 c) Wake, x/c=1.05

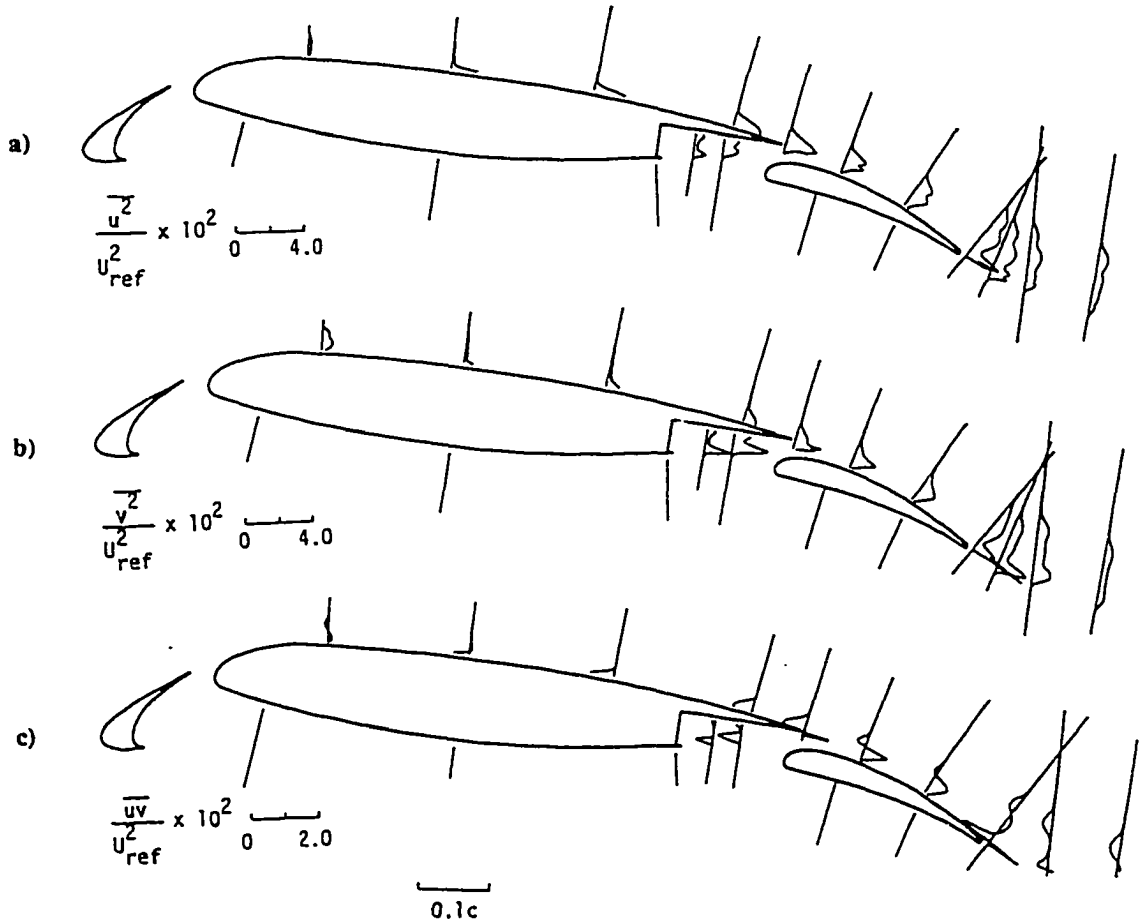

Figure 2.10 Turbulent Stresses for the Three-Element Model of Nakayama et al.

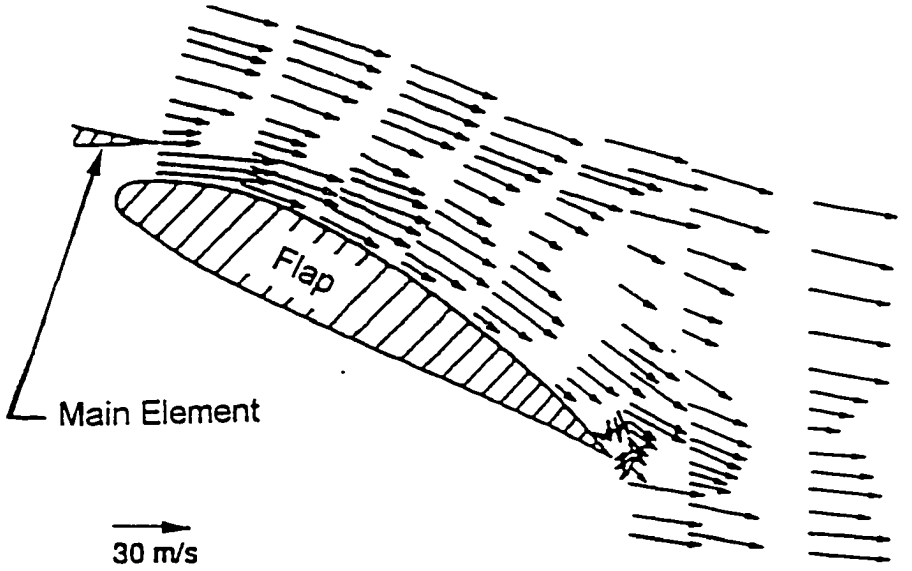

Figure 2.11 Mean Velocity Vectors Showing Recirculation Region on Flap

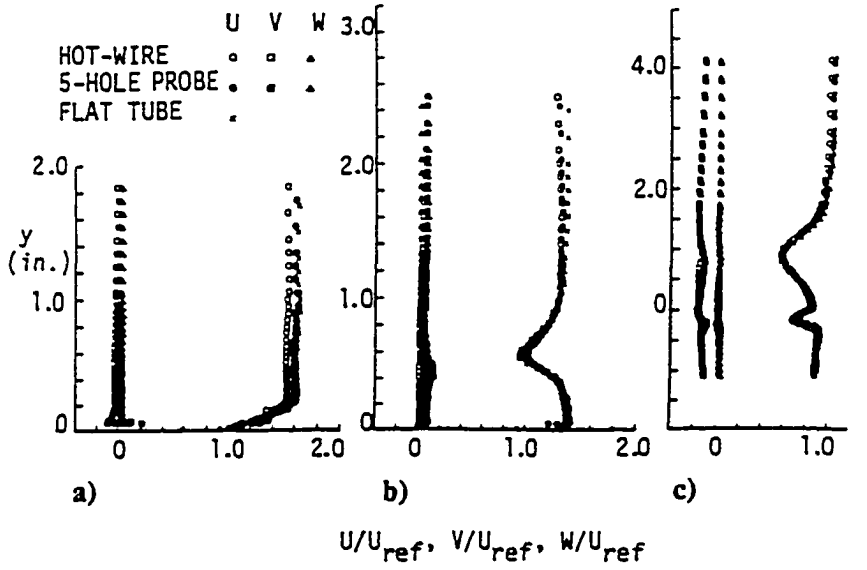

Figure 2.12 Representative Mean Velocity Profiles for Case A of the Model of Nakayama et al.; a) Main Element Upper Surface, x/c=0.6, b) Flap Upper Surface, x/c=0.8, c) Wake, x/c=1.5

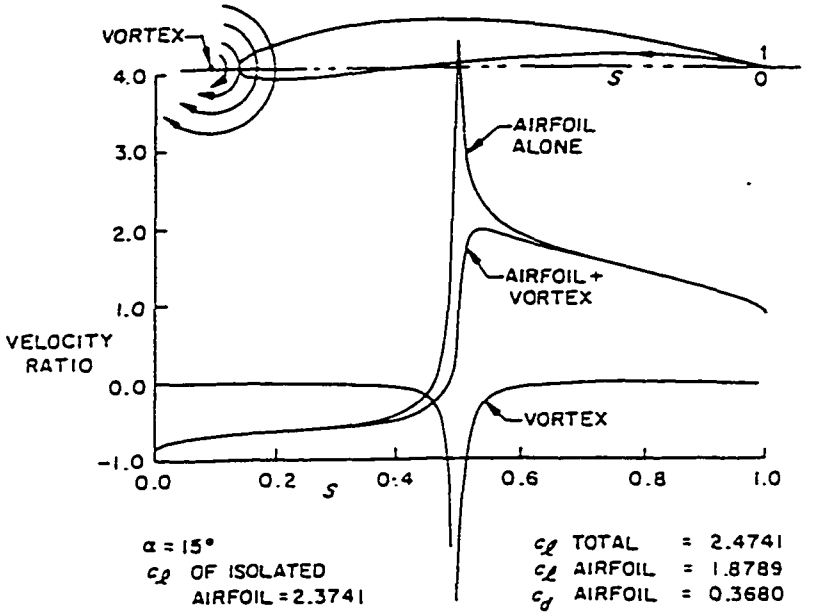

Figure 2.13 Velocity Distributions on an Airfoil with a Vortex Located Near the Leading Edge Illustrating the *Slat Effect*

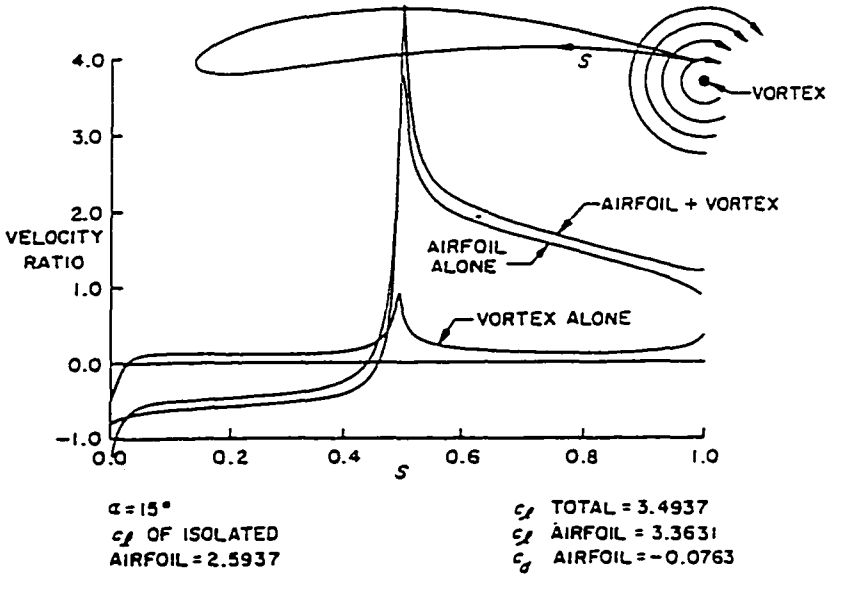

Figure 2.14 Velocity Distributions on an Airfoil with a Vortex Located Near the Trailing Edge Illustrating the *Circulation Effect*

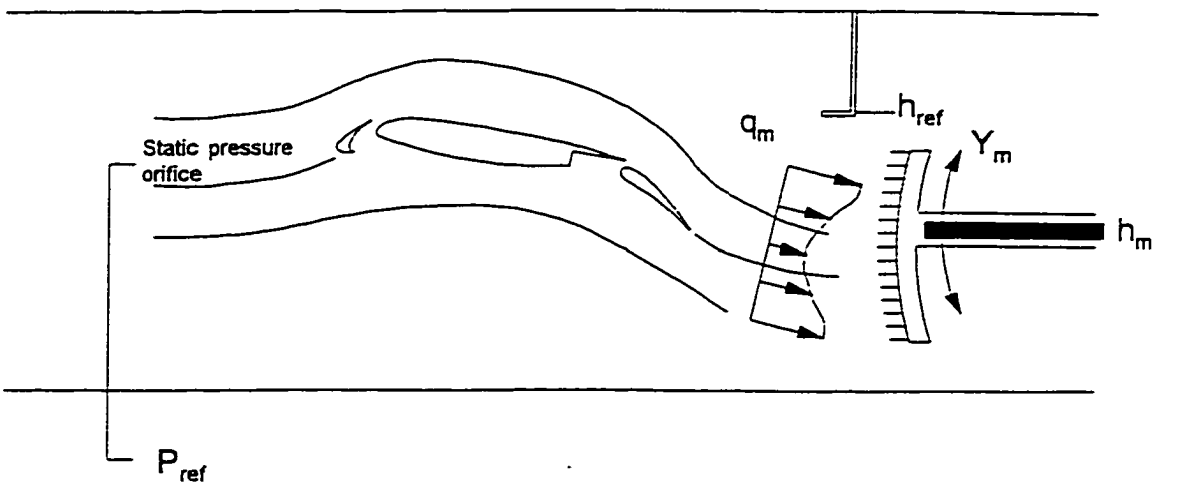

$$C_d = \frac{2}{C}\int_0^{Y_m}\left[\sqrt{\frac{q_m}{q_{ref}}}-\frac{q_m}{q_{ref}}\right]dy \qquad q_m = h_m - P_{ref} \qquad q_{ref} = h_{ref} - P_{ref}$$

Figure 2.15 Airfoil Drag Measurement using the Momentum Deficit Method (adapted from Ljungström, 1973a)

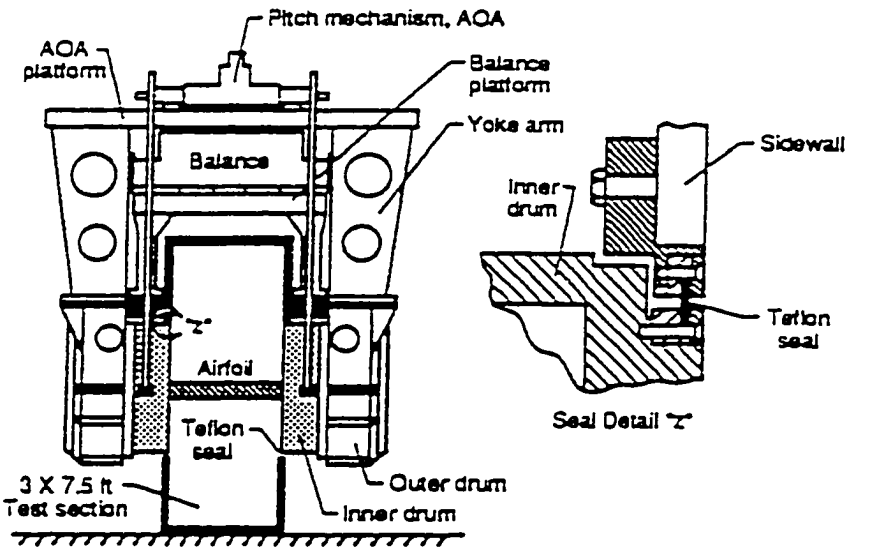

Figure 2.16 Force Balance of the Langley Low Turbulence Pressure Tunnel

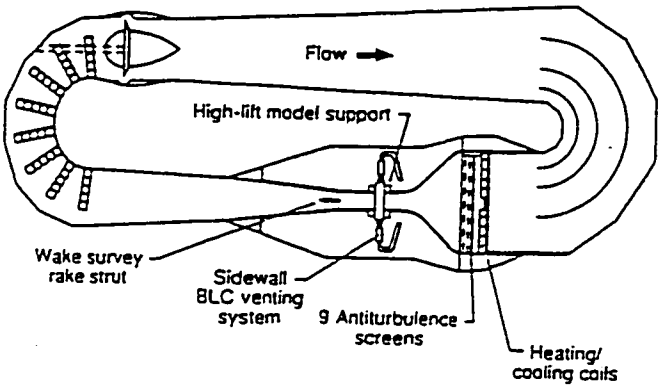

(a) BLC system location in LTPT

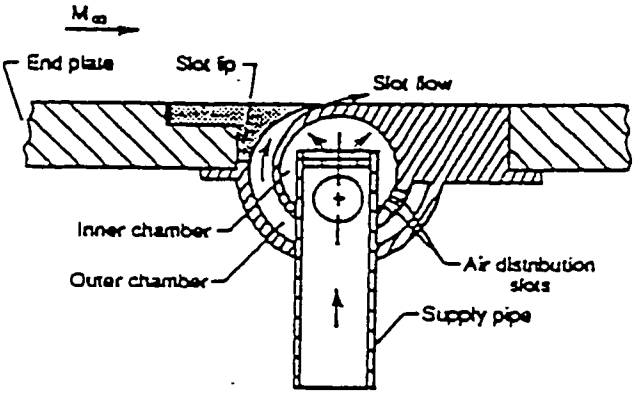

(b) Detail of Blowing Slot

Figure 2.17 Sidewall Boundary Layer Control by Tangential Blowing

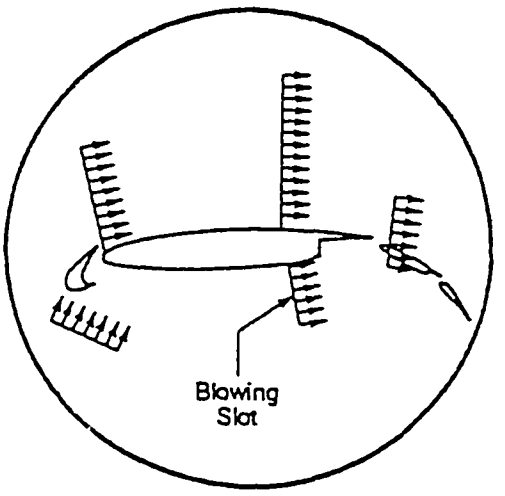

(c) Blowing Slot Locations

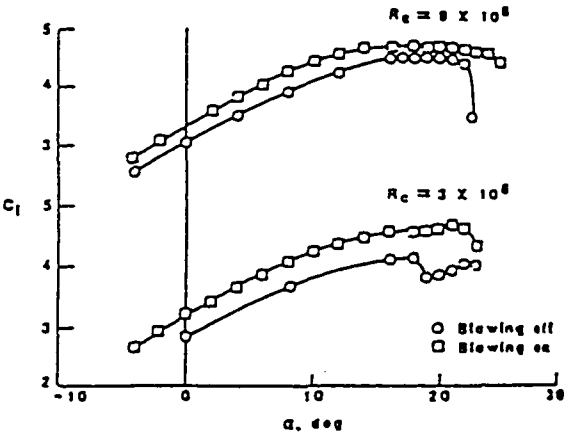

(d) Effect of Blowing on C_l for Typical High-Lift model

Figure 2.17 Concluded

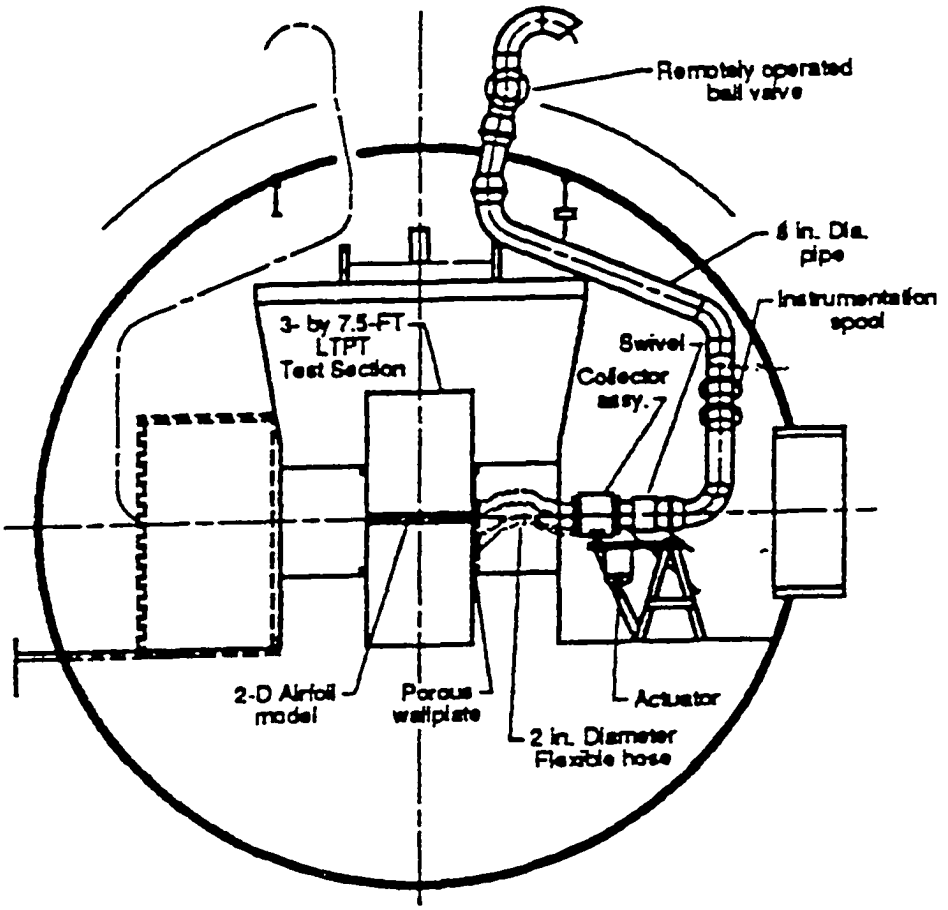

Figure 2.18 Langley Low Turbulence Pressure Tunnel Venting System for Sidewall Boundary Layer Control

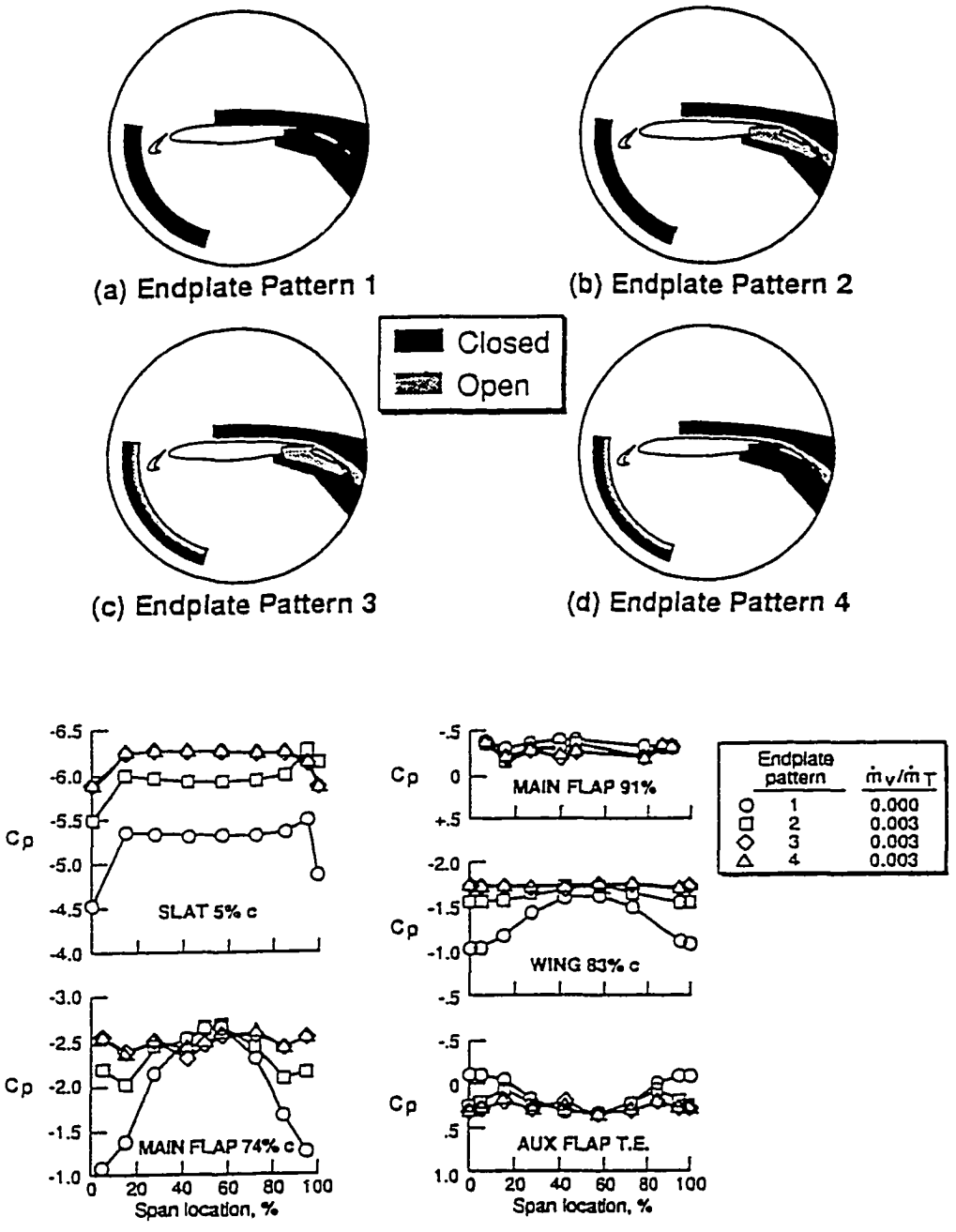

Figure 2.19 Spanwise Pressure Distributions for Four Porous Endplate Configurations with a Four-Element Airfoil Model using the System of Figure 2.18

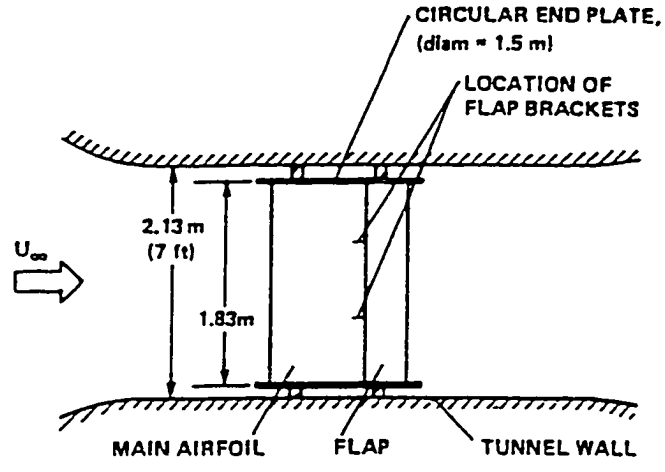

a) VIEW FROM SIDE

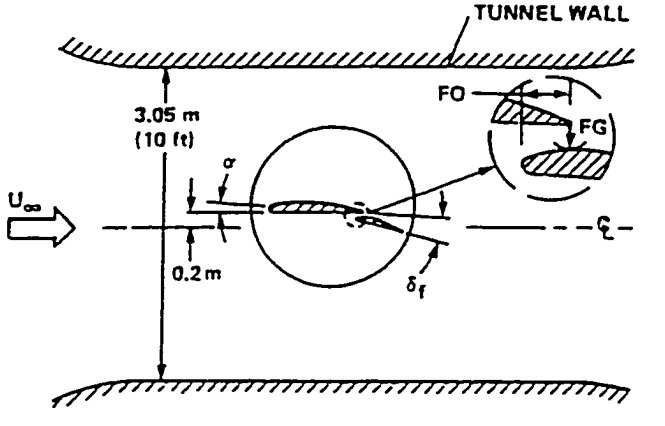

b) VIEW FROM TOP

Figure 2.20 Wind Tunnel Installation of Airfoil and Flap Model using Endplates

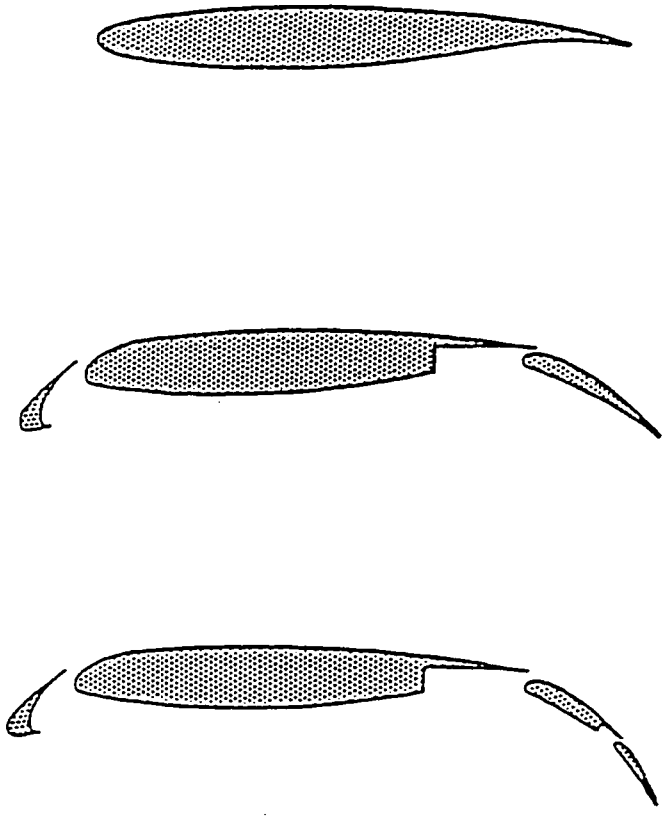

Figure 2.21 Airfoil Configurations Tested by Valarezo et al.

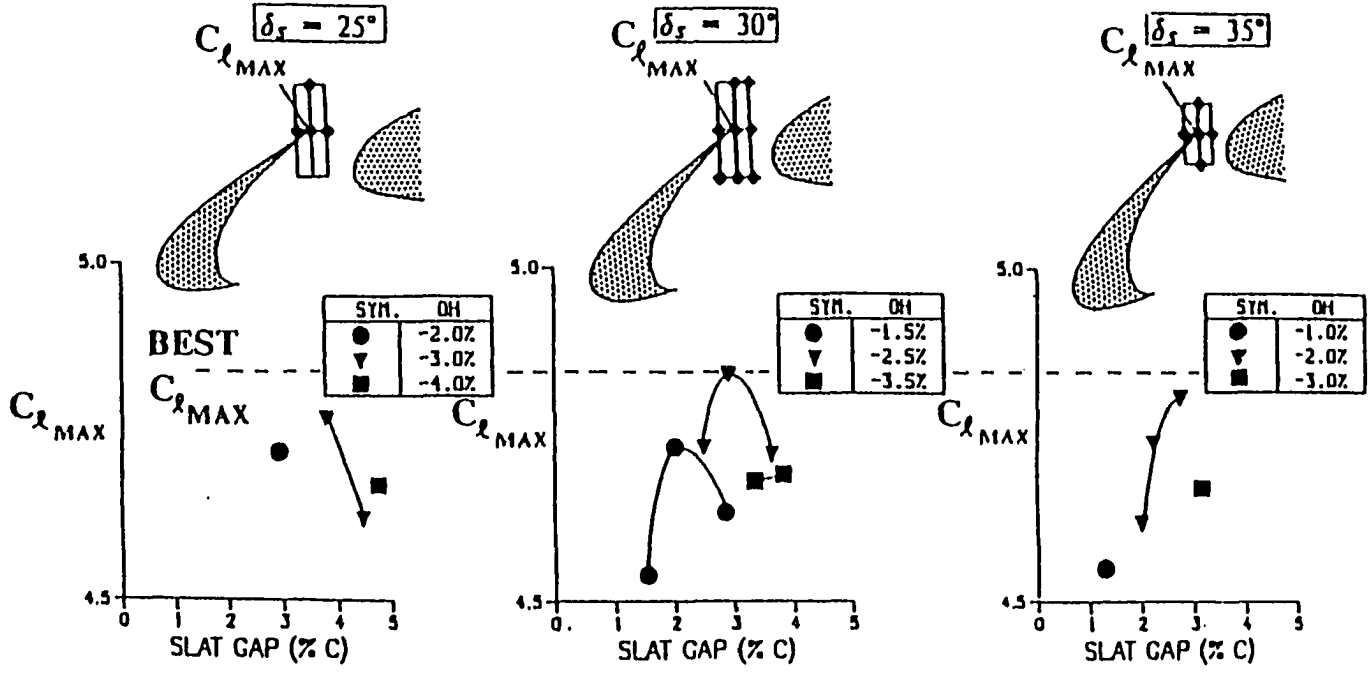

Figure 2.22 Results of Slat Optimization Study by Valarezo et al.

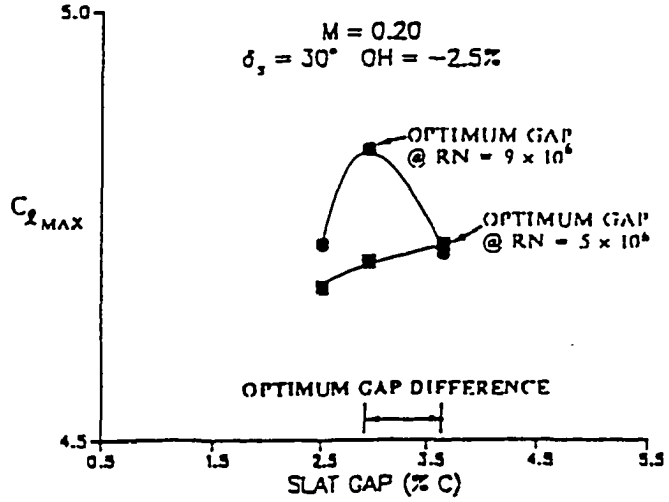

Figure 2.23 Effect of Reynolds Number on Optimum Slat Gap

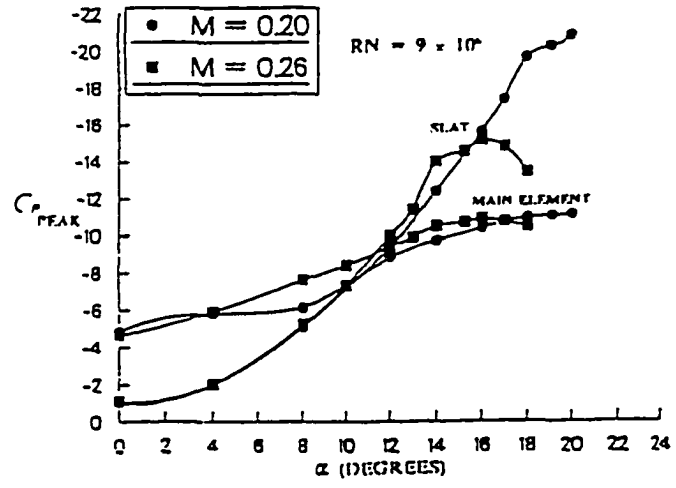

Figure 2.24 Effect of Mach Number on Peak Pressure Coefficient

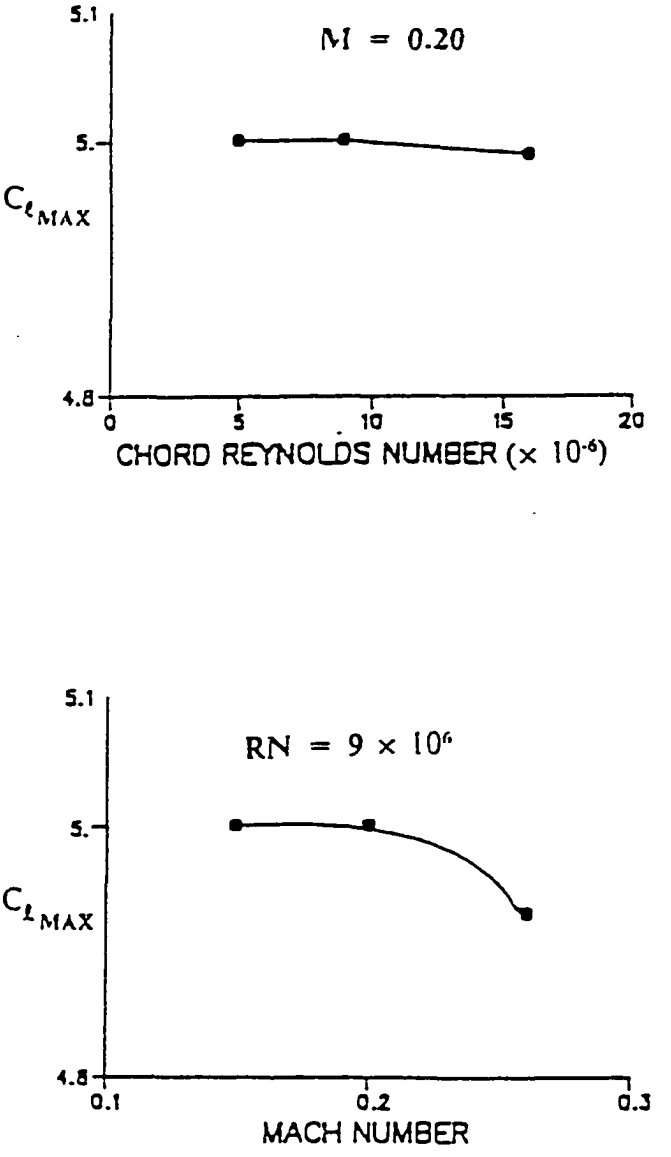

Figure 2.25 Reynolds and Mach Number Effects on Maximum Lift

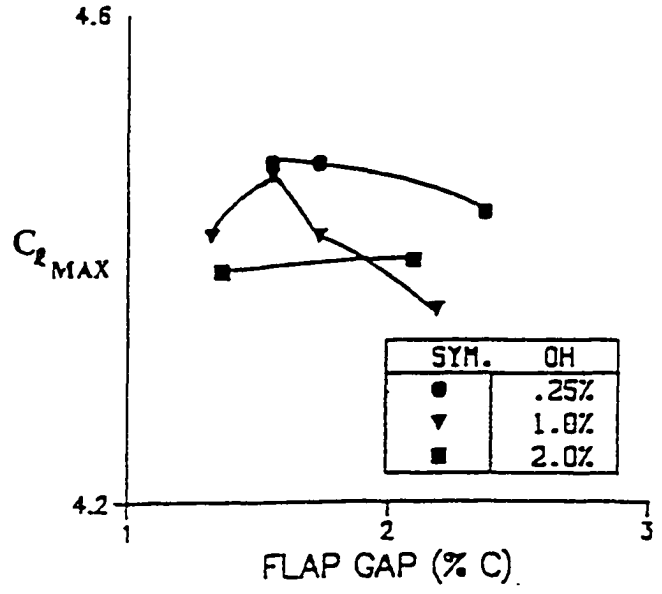

Single-Segment Flap Optimization ($\delta_f = 30°$)

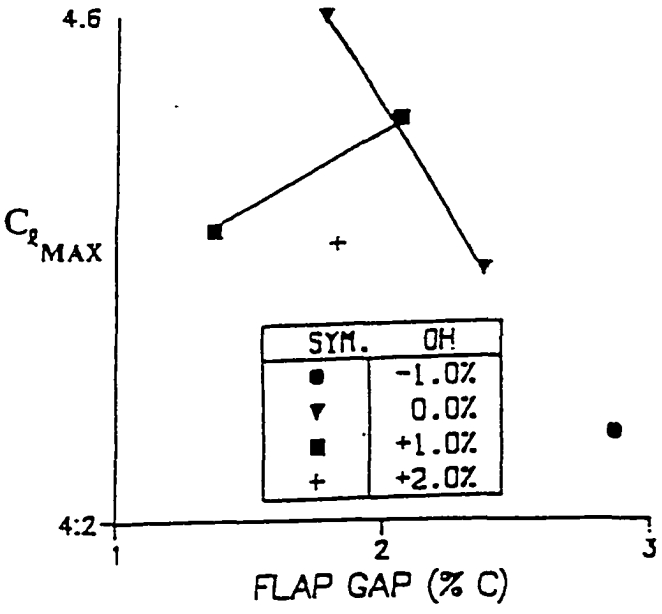

Single-Segment Flap Optimization ($\delta_f = 35°$)

Figure 2.26 Results of Flap Optimization Study by Valarezo et al.

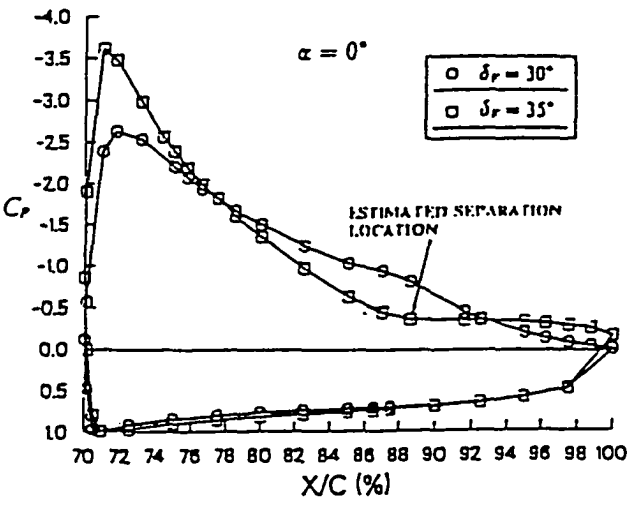

Figure 2.27 Surface Pressures on Single Element Flap at an Approach-Like Condition

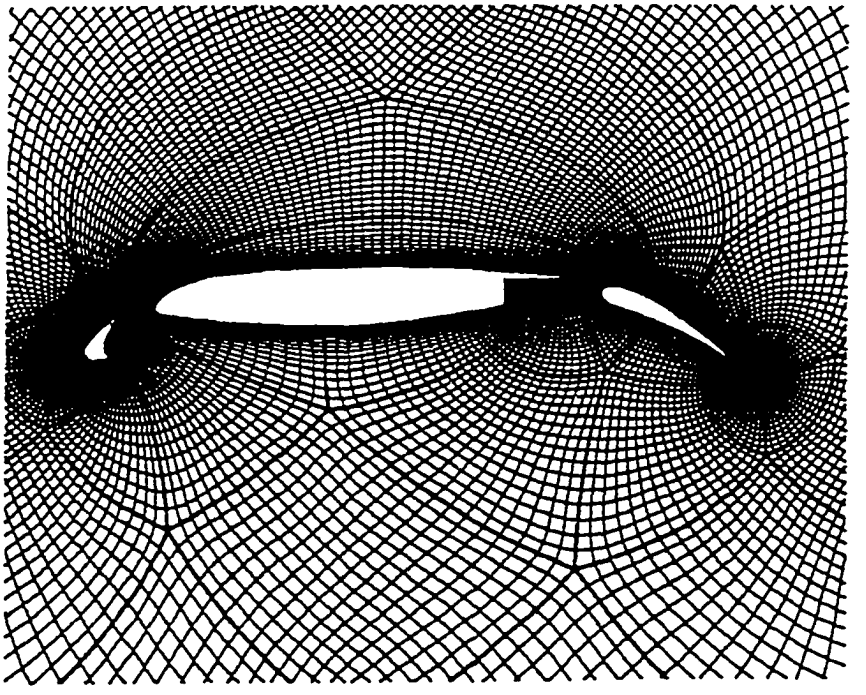

Figure 2.28 Partial View of 97-Block Grid for Three-Element Airfoil by Vatsa et al.

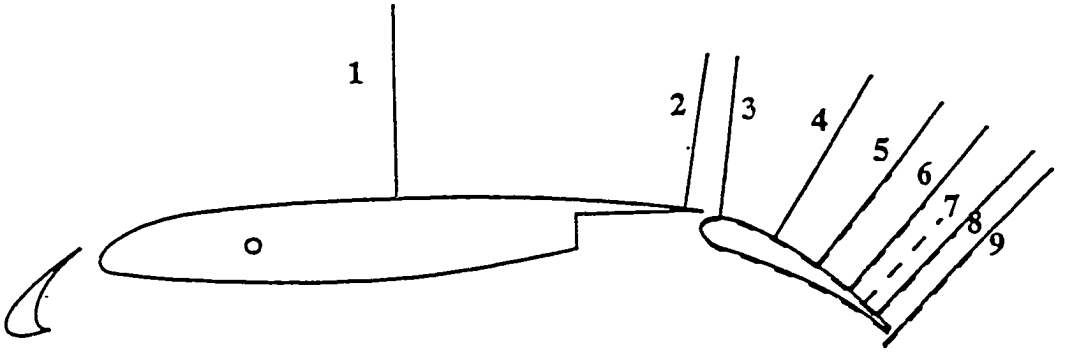

Figure 2.29 High-Lift Workshop Douglas Three-Element Airfoil with Chordwise Stations

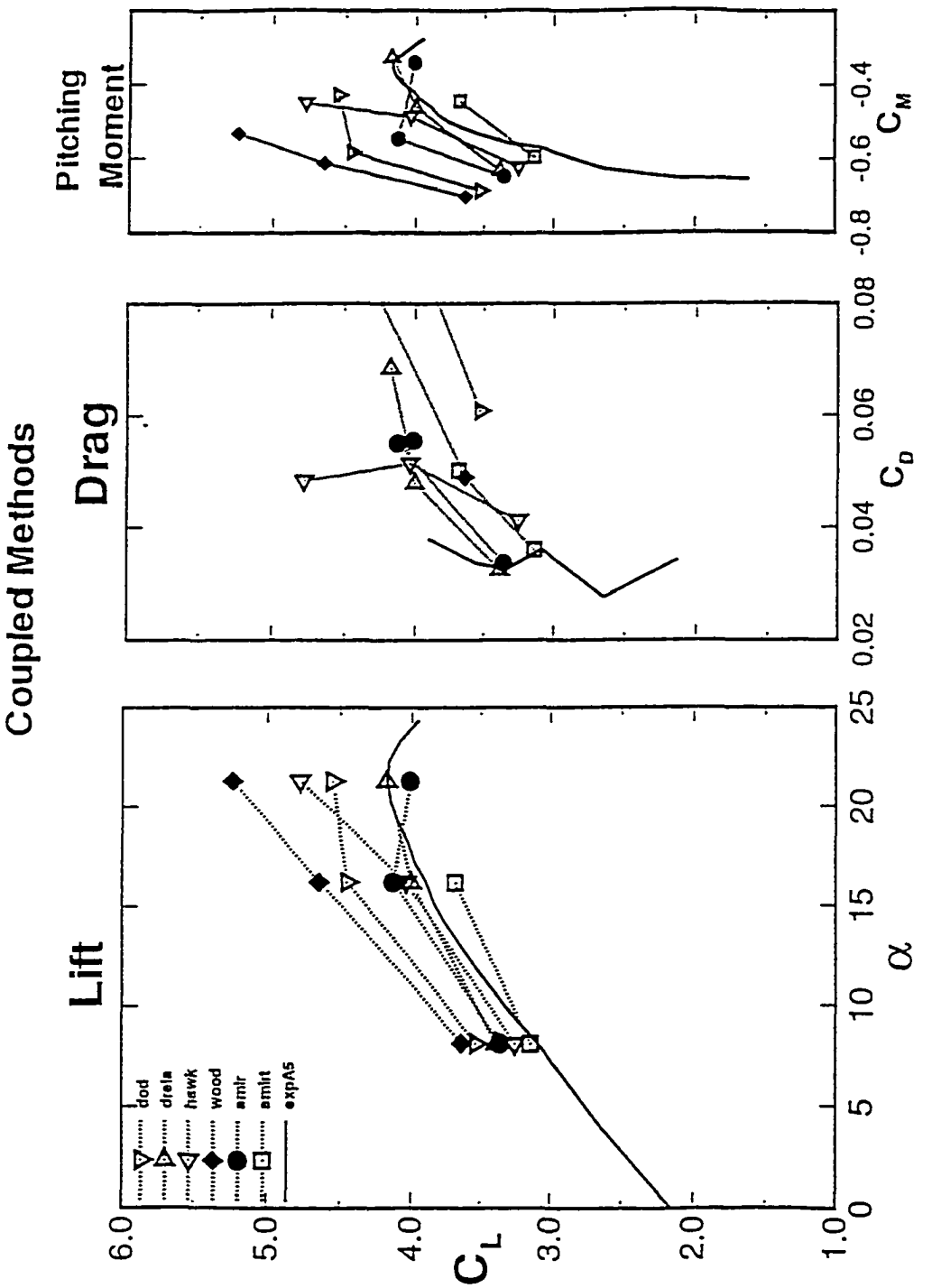

Figure 2.30 Results for Coupled Methods, Force and Moment Coefficients, Re_c=5 x 10^6, Geometry A

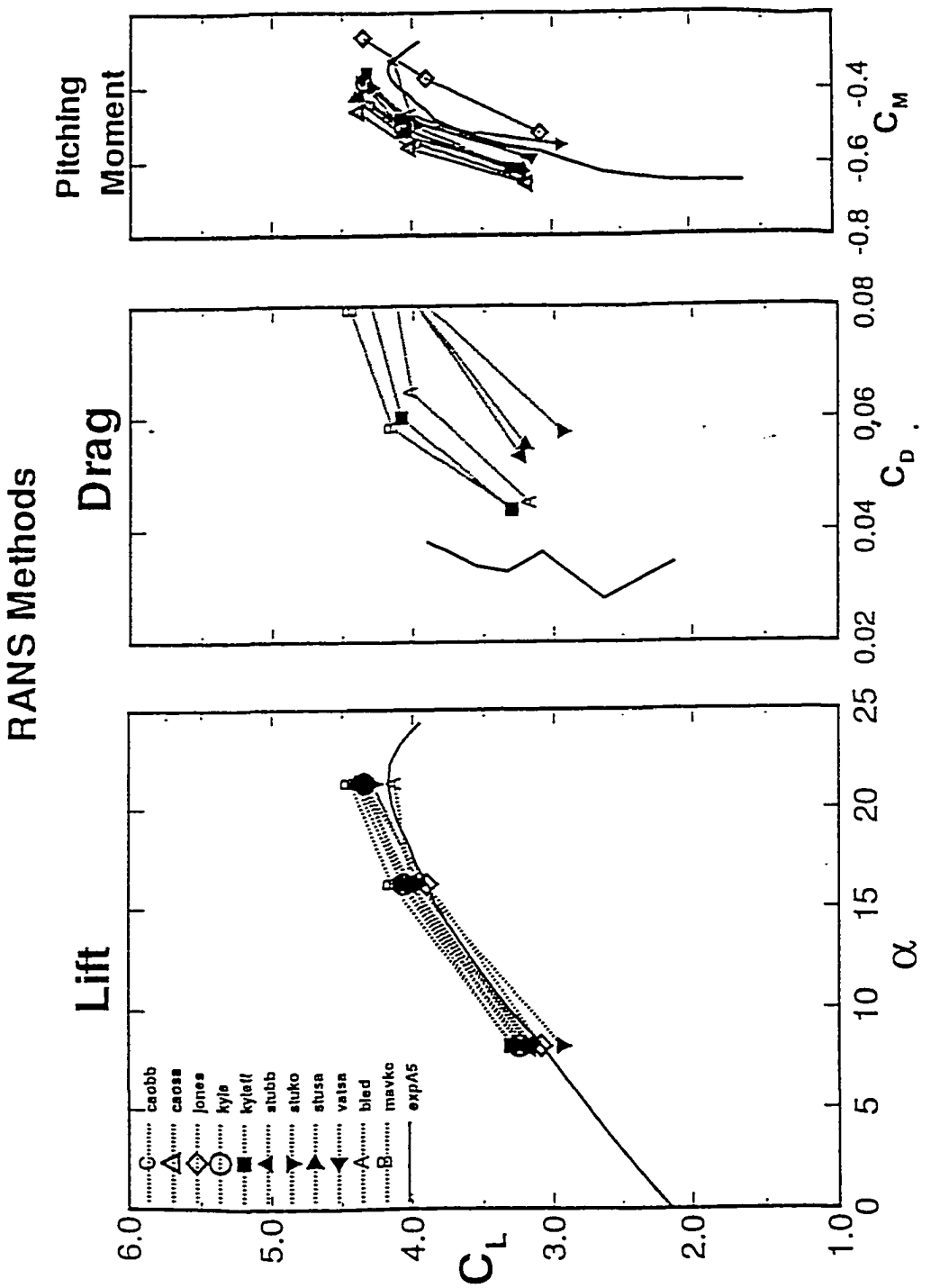

Figure 2.31 Results for RANS Methods, Force and Moment Coefficients, $Re_c=5 \times 10^6$, Geometry A

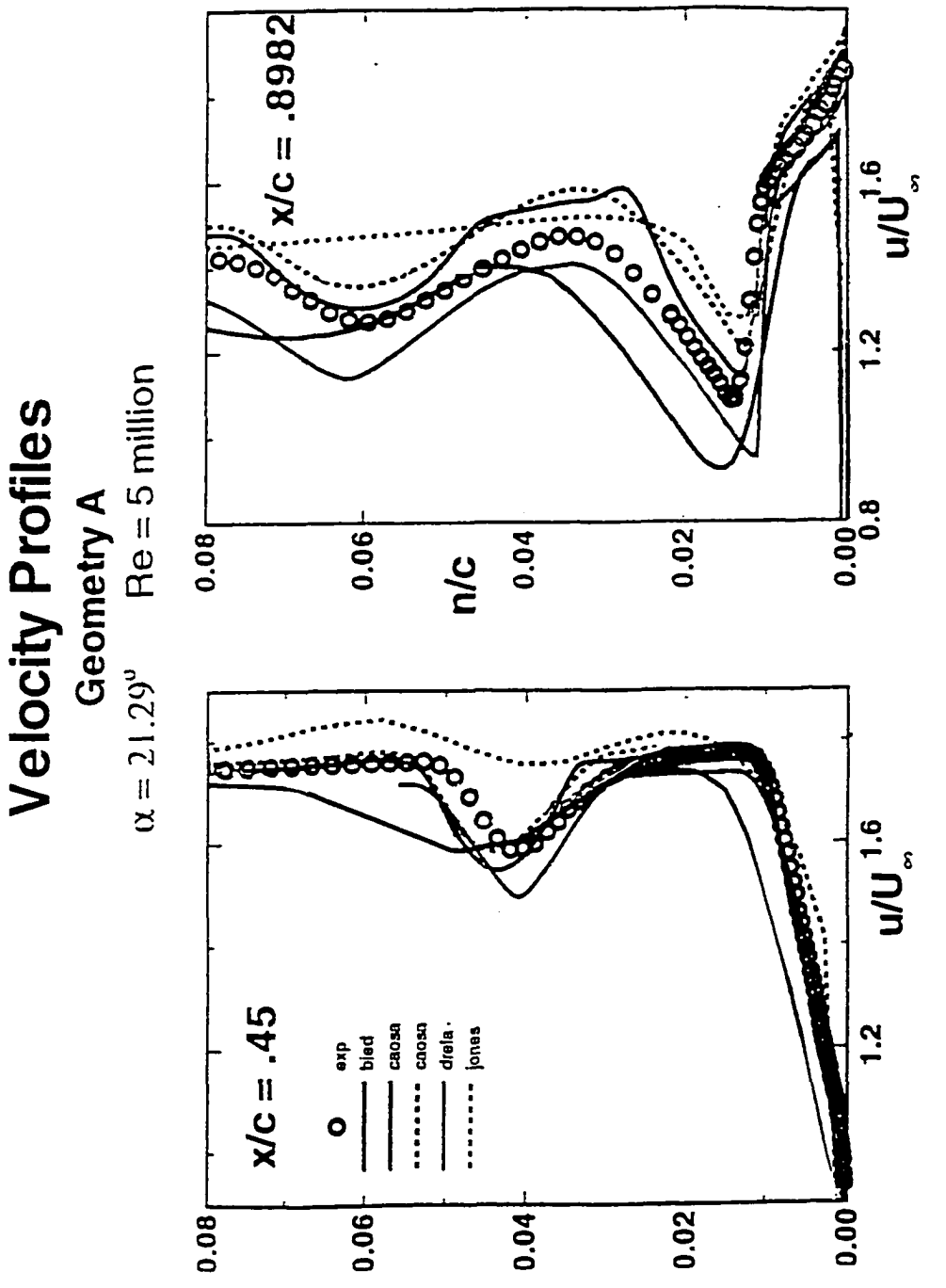

Figure 2.32 Results for Coupled Methods, Velocity Profiles, Re_c=5 x 10^6, Geometry A

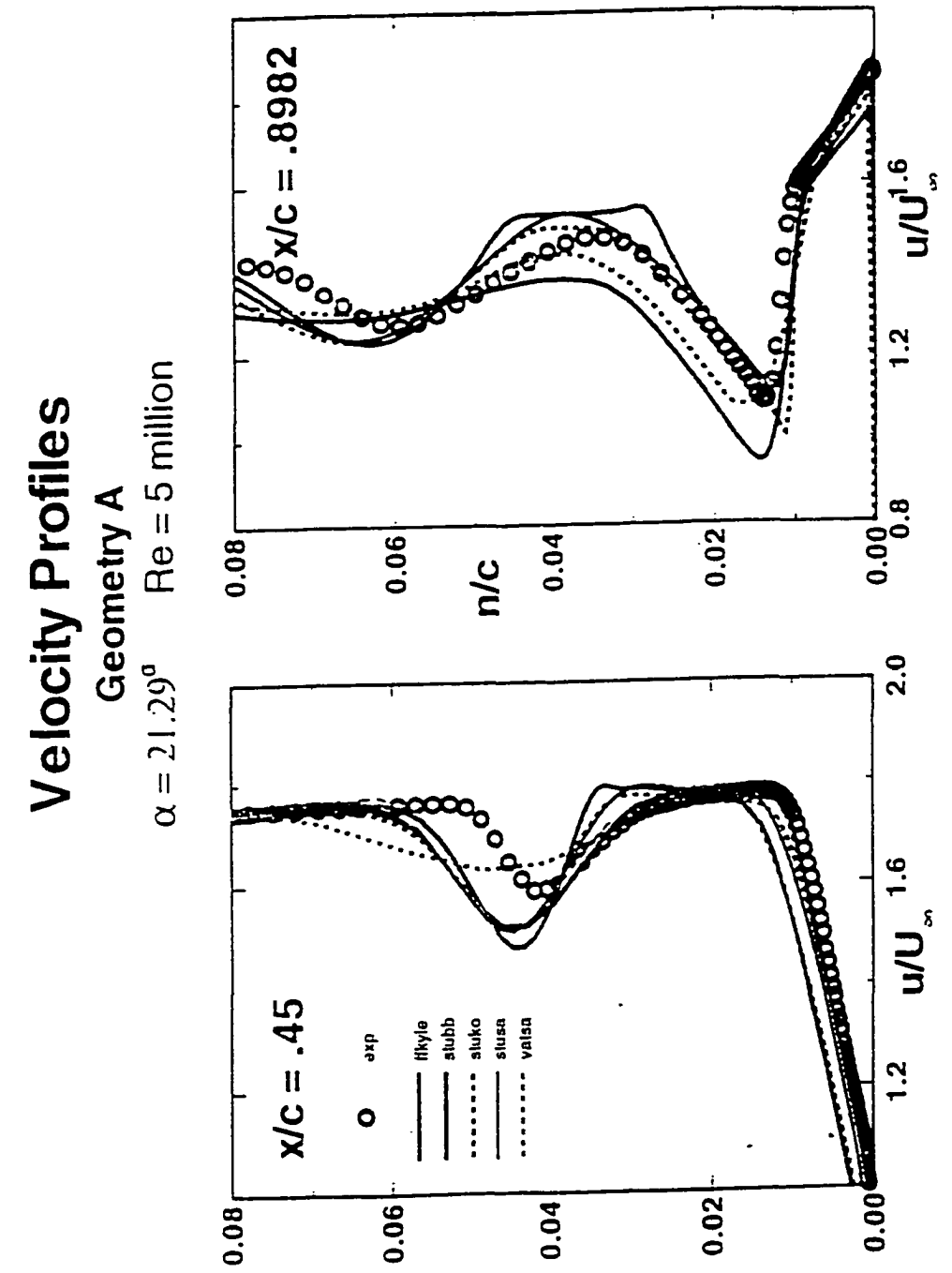

Figure 2.33 Results for RANS Methods, Velocity Profiles, Re_c=5 x 10^6, Geometry A

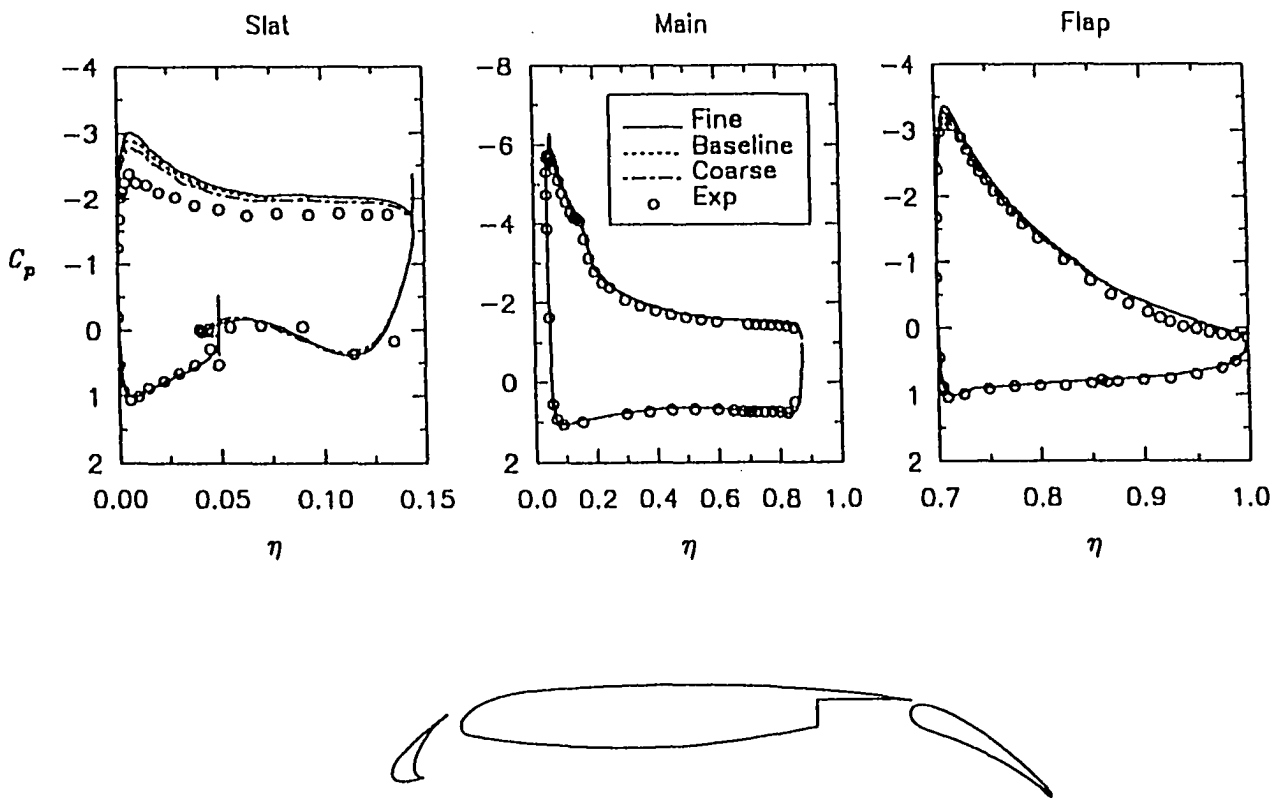

Figure 2.34 Computed and Experimental Pressure Distributions for 30P-30N, Re_c=9 x 10^6, M=0.2, A-O-A=8.23^0 Results of Anderson and Bonhaus

3 EXPERIMENTAL OPTIMIZATION

Optimization can be defined in the broadest sense as the collective process of finding the set of conditions required to achieve the best result from a given situation [Beveridge, 1970]. If an optimum is sought on the basis of experimental results, this process is called *experimental optimization.* In a complementary fashion, optimization is often used to design efficient experiments to help extract data and physical insight from an experiment. This process is known as *optimization of experimental design* [Scott and Haftka, 1995].

Experimental optimization methods can be grouped into two approaches: on-line and off-line. On-line methods are often called "direct insertion" methods since they are embedded into the experiment, allowing optimization in real time [Yesilyurt, to be published; Otto et al.,1995]. In off-line methods, the experiment is invoked only to construct a simple input-output model (a surrogate or response surface) from experimental data; this model then serves as a simulation in subsequent design studies [Otto, 1995; Yesilyurt, 1995]. Comparing the two approaches, the off-line approach to optimization offers several advantages [Otto et al., 1996; Landman and Britcher, 1996]. First, the number of appeals to the experiment for a desired confidence level can be specified beforehand. Second, the model is flexible, in that different optimization methods may be studied with the same model, without rerunning the experiment. Third, the model approach offers a natural means to add data from other sources. With regards to disadvantages, a

new source of error is introduced by the model. On-line approaches often require less data points, a distinct advantage; however, most on-line methods rely on a serial progression towards an optimum, a process inherently unforgiving of a poor data point.

To describe optimization, it is first necessary to define some terms. These definitions are consistent with the literature but some variation in strict meaning is found among authors [Fox, 1971; Box and Draper, 1987; Scott and Haftka, 1995, Haftka and Gürdal, 1992]. The numerical quantities for which values are to be varied are called *design variables* or *factors*. The numerical quantity for which a best value is desired is referred to as the *response*; moreover, *noise* is defined as the uncertainty associated with the response. Strictly speaking, the function to be optimized which governs the dependent relationship between response and design variables is called the *objective function*. In this study, the measured response is airfoil lift coefficient (C_l), and the design variables are flap movement in the vertical (y), and horizontal (x) direction. An analytical objective function in this case is unknown; an experiment will take its place. *Design constraints* are the restrictions that must be satisfied to permit an acceptable design. In this study, design constraints are the extreme limits of motion for the flap. *Design space* is a term given to the n-dimensional space defined by the range of continuous design variables [Fox, 1971, Haftka and Gürdal, 1992]. A *design point* is a point in design space defined by a unique set of design variables [Scott and Haftka, 1995]. A *response surface* is a simple function such as a

linear or quadratic polynomial, used to describe response in a small neighborhood of the design space [Box and Draper, 1987]. The term has been used more loosely to represent any surface describing a response in the entire design space, whether analytically generated or fitted from experimental data.

3.1 Experimental Optimization Methods

When using a mathematical function for the objective function, different optimization methods offer different strategies for obtaining sequences of points which will lead to the optimum design. In experimental optimization these same methods may be employed with the response provided by an experiment.

In a recent publication, which reviewed optimization methods as they apply to experiments, one of the strongest deciding factors listed in the selection of methods was the cost of each experiment [Scott and Haftka, 1995]. Another major factor was whether a method required derivatives of the objective function. Sometimes approximations for derivatives (i.e. finite differences) will be satisfactory if the noise level is low; alternately, one can seek methods in which derivatives are not required [Scott and Haftka, 1995]. In the following sections, a variety of techniques will be presented. Later, the more promising techniques for this work are selected and discussed in more detail.

Relatively expensive experiments require efficient methods in order to minimize the number of experiments required. One reported efficient method

is called *Evolutionary Operation* [Box and Draper,1987; Cornell,1990]. In this method, a response surface is fitted to the results of the experiments and used to perform a local optimization. Each local optimization is called a *design cycle* and involves a small portion of the design space. A second design cycle is subsequently performed in the region of the first optimum, and the process continues. This method has been very successful in optimizing chemical and biological processes [Villen,1992; Banarjee, 1993; King and Buck, 1991]. Taguchi methods, which offer techniques for choosing design points as well as a comprehensive method of optimization are ideally suited to expensive experiments [Beck and Arnold, 1977; Gardner, 1991; Kaufman and Stone, 1987]. In the Taguchi method a response surface is generated using products of linear polynomials in each design variable. Other methods suitable to expensive experiments include the D-Optimal criterion and Box-Hunter methods [Villén et al., 1992]. The D-Optimal criterion in its most rudimentary form is sometimes called a parametric study or interactive method. Using this method, the ranges of the experimental design variables are determined first. Next, the objective function is calculated using a limited number of design points chosen by incrementing each design variable uniformly. The design space is then reduced based on the initial calculations, centered on the estimated optimum, divided again in smaller increments, and an objective function is again calculated. The process is repeated until convergence on an optimum is achieved [Scott and Haftka, 1995]. Variations of this algorithm have been used successfully in problems as diverse as

optimizing the placement of sensors on space structures [Bayard, 1988] to determination of the optimum test for "nitrogen washout" in the human lung [Lewis et al., 1982].

Unless an objective function is convex, no optimization algorithms can distinguish local and global optima. The most simplistic approach to seeking the global optima is to restart the optimization at randomly selected initial points to seek other solutions. While this may be practical for simple problems, problems with many variables may require an excessive number of runs. Genetic algorithms use techniques analogous to biological processes, mimicking Darwin's theory of "survival of the fittest" [Holland, 1975; Haftka and Gürdal, 1992]. One advantage to this method is that it is easy to program, and has a high probability to reach the global optimum [Krottmaier, 1993]. Combinations of the design variables are represented by bit strings which are analagous to chromosomes in nature. The method seeks to minimize the objective function which is quantified by the combinations in the strings. The optimization problem involves three commonly used genetic operations: reproduction, crossover, and mutation. At the onset, the population size is chosen and each variable in the string is assigned a random value. The next step, reproduction, involves forming a new population of strings with good objective function values determined by the initial search. Now the members of the new population are paired off randomly for crossover. Crossover involves choosing a random point in the bit string where the values of 0's of each bit are replaced by 1's and vice

versa. These transformed strings are known as offspring. At this point it may be possible to have a population made up of multiple copies of an optimal string. To avoid this, mutation is periodically implemented by randomly changing one value in the bit string. No derivatives are required, an advantage when using experiments. A disadvantage may be the typically high number of required objective function evaluations. The genetic algorithm is summarized in figure 3.1 [Haftka, and Gürdal, 1992].

A minority of problems fall into the category of inexpensive experiments. Experiments which are easily performed and/or are suited to rapid data acquisition are often inexpensive. If the noise is also found to be low, then this type of problem lends itself to more simplistic optimization methods originally developed for use with an analytic objective function. Adaptive control problems, such as adjusting chemical process variables on-line, are possibly the most common examples of inexpensive, low noise, experimental optimization problems [Scott and Haftka, 1995]. Gradient methods are often used in these problems [Sameness and Lim 1990; Jacoby et al.,1972; Fox, 1971]. These methods have in common the use of gradients of the objective function, or in the case of experiments, approximations to the gradient. All gradient methods seek the set of design variables that minimize the gradient of the objective function, which is a measure of the rate of change of the response [Fox, 1971]. The method of steepest ascent (or descent) seeks the greatest magnitude of the gradient, for a given set of design variables, and moves in that direction progressively, stepping towards

a local optimum. The magnitude of the gradient in previous steps is retained and used to scale the step size [Fox, 1971; Beveridge and Schecter, 1970; Jacoby et al., 1972]. This method is detailed in section 3.2.

The sequential simplex method is one of the oldest search methods for optimization [Spendley, 1962]. This method has been used successfully with many problems, particularly those optimizing chemical processes [Khummongkol, 1992; Walters, 1991]. The basic premise is to use a geometric figure with responses as vertexes to define an object in the design space. The responses are then ranked and the figure is translated and transformed until it surrounds the optimum region. A major advantage to this direct search procedure is that no derivatives of the objective function are required. The sequential simplex is most often used with problems involving few design variables [Scott and Haftka, 1995; Jacoby et al., 1972; Walters, 1991]. A major disadvantage is that no information is retained beyond two step cycles, often resulting in a less efficient path towards the optimum [Jacoby et al., 1972]. Two variations of this method are presented in sections 3.3 and 3.4.

If optimization is performed based on a simple response surface, there is a need to validate the results. Validation can be as simple as rechecking some of the design points after achieving an optimum, using any method, or a more rigorous mathematical approach can be implemented which provides statistical bounds to the accuracy of the method. For example, Kaufman and Stone reported the use of additional experiments for validation of an optimum

lap shear bond strength [Kaufman and Stone, 1987]. Fox and Lee describe the use of a "signal-to-noise ratio" calculation for each design variable used in optimizing a metal injection process using the Taguchi method [Fox and Lee, 1990]. A recent method for optimization including validation has emerged using *Bayesian-Validated Surrogates* [Yesilyurt and Patera, 1995]. The method was originally demonstrated using noisy computer simulations [Otto, Landman, Patera, 1995; Yesilyurt et al., to appear] and has now been successfully utilized with experimental data [Otto et al., 1996]. In this method, surrogates are analogous to response surfaces, constructed by fitting surfaces to a finite grid of experimental design points, but over the entire design space. In addition, a number of randomly generated design points are used to statistically validate the optimization. The entire data set is taken at one time and all optimization and validation operations are performed off-line and "a posteriori".

3.1.1 Experimental Optimization in Aerodynamics

There has been very little published work on the subject of experimental optimization methods applied to aerodynamics. While multi-element airfoils have always required wind tunnel testing to determine optimal gap and overhang rigging, the methods used to obtain these settings have been trial and error with a matrix of test values typically generated from computational results [Valarezo, W. O. et al., 1993; Klausmeyer and Lin, 1997].

The objective of the present study was to optimize lift coefficient (C_l) as a function of flap position (x,y). Initial evaluations of the response using the experiment revealed very low noise (discussed later), while the use of automatic positioning and data acquisition equipment classified the experiment as inexpensive. This rare combination permitted the choice of relatively simple methods more often reserved for use with closed form functions. The following methods were chosen as candidates for an on-line optimization routine. The final choice of method was based on results from simulations which modeled the response and noise of the experiment.

The primary objective in this study was to demonstrate the practicality of experimental optimization using multi-element airfoils. A simple gradient based method and pattern search technique were chosen as representative of numerous more refined methods suitable to this type of problem. While algorithm efficiency was of interest, demonstration of the viability of in-situ optimization was of prime concern during this study.

3.2 The Method of Steepest Ascent

The method of steepest ascent falls under the broad category of optimization methods known as gradient methods [Fox, 1971; Beveridge, 1970]. These methods depend on the evaluation of a function's gradient at a given point [Jacoby et al., 1972]. Gradient methods can be used to find local optimum points (maxima or minima) in a design space by invoking a sequential algorithm which, starting at a given point, will progress through intermediate points toward a local optimum (i.e. maximum of F). The method

depends on an evaluation of the gradient of the response starting with a given point (design variable set), chooses a direction to move which is based on successive gradient magnitudes and a scaling factor (often obtained from experience), and moves until the optimum response is attained [Beveridge, 1970].

3.2.1 The Method of Steepest Ascent - Analytical Background

For a function $F=F(\bar{x})$, where $\bar{x}$ is a column vector of design variables (x_1, x_2, x_3 ...), the vector ∇F, *the gradient of F*, lies in the direction of the greatest rate of change of F and has the rate of change as its magnitude [Shenk, 1979]. The direction given by ∇F is known as the direction of steepest ascent; similarly the direction of steepest descent is given as $-\nabla F$ [Fox, 1971]. In a given design space, a starting point $\bar{x}_k$ can be chosen to begin a minimization process; at the kth iteration the next point is obtained as

$$\bar{x}_{k+1} = \bar{x}_k + \alpha \bar{s} \qquad (3.2.1\text{-}1)$$

Here $\bar{s}$ is the unit vector in the direction of steepest descent and α is chosen so F is minimized. The unit vector $\bar{s}$ is found to be

$$\bar{s} = -\frac{\nabla F}{|\nabla F|} \qquad (3.2.1\text{-}2)$$

If the function F to be minimized is quadratic, it may be written as

$$F = \frac{1}{2} x^T Q x + b^T x + c \qquad (3.2.1\text{-}3)$$

where Q is known as the Hessian matrix. The step length, α can be determined directly by substituting equation 3.2.1-1 into 3.2.1-3 for the k+1 iteration followed by a minimization of F with respect to α which yields α^*, a value for α that minimizes F [Haftka and Gürdal, 1992; Fox, 1971]

$$\alpha^* = -\frac{(x_k^T Q + b^T) s}{(s^T Q s)} \qquad (3.2.1\text{-}4)$$

The performance of the steepest descent method (using 3.1.2-1) depends on the condition number of the Hessian matrix. The condition number of a matrix is the ratio of the largest to smallest eigenvalue, where a large condition number implies that the contours of the function form an elongated design space, causing the method to proceed at a very slow pace. For large condition values, the design variables may be rescaled to approach a condition number of unity, avoiding the slow zig-zag progression known as *hemstitching* [Haftka and Gürdal, 1992].

For most multivariable function minimizations, it is not easy to determine an appropriate scaling of variables to assure a rapid convergence. An alternative method is provided by Fletcher and Reeves, which is guaranteed to minimize quadratic functions without scaling the design variables [Fletcher and Reeves, 1964]. The minimization process is begun in

the same manner given above: an arbitrary point $\bar{x}_0$ is chosen and the function F is minimized along the steepest descent direction, $\bar{s}_0 = \nabla F(\bar{x}_0)$, then using equations 3.2.1-3 and 3.2.1-6 the next iterate $\bar{x}_1$ is found. Subsequent steps toward the minimum may be found using

$$\bar{x}_{k+1} = \bar{x}_k + \alpha_{k+1}\bar{s}_k \qquad (3.2.1\text{-}5)$$

such that F is minimized with respect to α and

$$\beta_k = \frac{|\nabla F_k|^2}{|\nabla F_{k-1}|^2} \qquad \bar{s}_k = -\nabla F_k + \beta_k \bar{s}_{k-1} \qquad (3.2.1\text{-}6)$$

Unfortunately, in experimental optimization the behavior of the objective function is often unknown and subject to noise, very often rendering this analytical approach to determining step size infeasible. Nonetheless, this method provides a background for developing step sizes based on the magnitude of the gradient. In the next section a method of steepest ascent is presented which has been developed by this author using some of the concepts discussed previously.

3.2.2 The Method of Steepest Ascent - Optimizer Algorithm

In the earlier general discussion, a gradient is calculated assuming a function exists for the input-output relation. In this application, the input - output relationship is known only through an experiment . In particular, lift coefficient (C_l) is defined as a function of flap position, or $C_l=C_l(x,y)$. To evaluate the gradient, this method relies on sampling three closely spaced

points (the minimum number possible), which form an equilateral triangle. The gradient is then calculated from the plane defined by the triangle and a move is made in the direction of the gradient (steepest slope) to a new point, where the process is repeated. The response at the location of the centroid of the triangle, formed by the three points, is used to determine convergence on the optimum. This procedure is depicted graphically in figure 3.2, where the gradient vectors for successive points are shown at the centroidal points of each triangular grouping of points. The level curves form a contour plot of the response; the ordinate and abscissa mark the two design variables. Borrowing from the method of Fletcher and Reeves, the magnitude of the gradients for the 2 successive calculations is then used to scale the distance moved to the next point [Landman and Britcher, 1996; Fletcher and Reeves, 1964]. In figure 3.2 the gradient vector for the first point (0) has a larger magnitude than the second point indicating a steeper local gradient and resulting in a larger step to the second point than the following step to the third point. The choice of the step size is important since it directly influences the number of points used to reach an optimum. The calculation proceeds until a local maximum is attained within a desired tolerance. The algorithm is explained in detail below and is known as the method of steepest ascent, the name reflecting the dependence of the method on the positive value of the gradient, leading to a maximized objective function [Beveridge, 1970].

In general the equation for a plane through 3 points of the C_l versus x,y surface is given by

$$C_l = a + bx + cy \qquad (3.2.2\text{-}1)$$

The gradient defines the direction of steepest slope for the plane formed by the three points. The coefficients a, b and c are found by simultaneous solution of equation 3.2.1-1 using the coordinates of each of the triangle's vertexes. The unit direction for the plane formed by the first three points is easily shown (using subscript "0") to be [Shenk, 1979]

$$P_0 = \frac{b_0\, i + c_0\, j}{\sqrt{b_0^2 + c_0^2}} \qquad (3.2.2\text{-}2)$$

The centroid of the first three points (x_o, y_o) is the starting point for the optimization. Using a fixed scaling factor S_o, determined by experience, the next centroidal point (x_1,y_1) is calculated [Fox, 1971]:

$$x_1 = x_0 + S_0 \frac{b_0}{\sqrt{b_0^2 + c_0^2}} \qquad y_1 = y_0 + S_0 \frac{c_0}{\sqrt{b_0^2 + c_0^2}} \qquad (3.2.2\text{-}3)$$

Now three points about x_1, y_1 can be used to calculate the gradient for the new location. Subsequent points are computed in the same manner but using a scaling factor based on the local slope and the distance between previous points [Fox, 1971]:

$$x_{i+1} = x_i + S_i \frac{b_i}{\sqrt{b_i^2 + c_i^2}} \qquad y_{i+1} = y_i + S_i \frac{c_i}{\sqrt{b_i^2 + c_i^2}} \qquad (3.2.2\text{-}4)$$

where the scaling parameter (described below) is

$$S_i = \left[\frac{\sqrt{b_i^2 + c_i^2}}{\sqrt{b_{i-1}^2 + c_{i-1}^2}} \right]^M \sqrt{(x_i - x_{i-1})^2 + (y_i - y_{i-1})^2} \qquad (3.2.2\text{-}5)$$

Since the actual objective function is unknown, S_i can be limited by a maximum value to prevent extreme moves (overshoot) in areas of steep gradients [Jacoby et al., 1972]. Now the algorithm can be reapplied until C_I satisfies some convergence criterion. This will be discussed in section 6.5.

The choice of a theoretically optimal scaling factor would require an analytical model of the objective function. In practice, the choice of scaling factors is often a result of experimentation and it has been found (particularly in the case of inexpensive experiments) that it is better to choose a smaller than optimal step size (and hence scaling factor) [Jacoby et al., 1972; Semones and Lim, 1989].

In this work, an experimental response surface was first constructed to investigate the nature of the objective function (discussed in section 6.5.1) for the purpose of choosing a scaling factor with global applicability. As can be seen in figure 3.3 the surface is composed of steep nearly linear regions bordering relatively flat "plateaus" with some regions of locally higher response. The design space encompasses this entire region including the sharply defined transition regions where the slopes are essentially discontinuous.

sharply defined transition regions where the slopes are essentially discontinuous.

The simplified scaling method shown was successfully invoked with a steepest ascent optimizer using the fitted experimental data in a simulated experiment. The exponent of the gradient magnitude ratio, M was varied through trials with the optimizer until the final value of ½ was selected as a good compromise between convergence rate and stability. Since the focus of this work was to demonstrate the practicality of experimental optimization in a particular setting rather than develop the most efficient optimization routine, no further effort was expended toward increasing algorithm efficiency.

3.3 Fixed-Size Sequential Simplex Optimization

The fixed-size sequential simplex method was originally conceived by Spendley, Hext, and Himsworth [Spendley et al., 1962]. Since the design space of this study involved two dimensions, the remaining discussion will be focussed on the two design variable case which means each simplex is a triangle. Each vertex of the triangle represents a set of experimental conditions and for visualization purposes solid lines are drawn between vertexes.

Each of the three responses to the pair of design variables at each vertex of a simplex can be ranked in descending order. The responses are sorted from "best" to "worst" with the center response called "next to best". Adopting the notation of Walters et al., the abbreviations for these responses are B, N, and W where B always has the highest numerical response value, N

has the next highest, and W has the lowest numerical response value of the three [Walters et al., 1991]. Each vertex represents a pair of design variables. For example a vertex B is located at [x1,x2] and has response Y (see figure 3.4).

If a vertex is removed, what remains is called a face [Walters et al., 1991]. If the W vertex of the simplex is removed (i.e. by discarding the worst response), the centroid of the remaining face is given the symbol P. The coordinates of P are found by averaging the coordinates of B and N, one design variable at a time.

$$P = \frac{1}{2}(N + B) \qquad (3.3\text{-}1)$$

The fixed-size simplex optimization algorithm is very simple. An initial simplex is chosen, the responses are evaluated, and the best and next best vertex are retained for use as vertexes in the next simplex. The third vertex for the second simplex comes from a reflected vertex called R. The term reflection describes the process of taking the mirror image of the W vertex about the line formed by the B and N vertexes. Now the only other rule to follow is to force the N vertex of the previous simplex to become the W vertex of the next sequential simplex. This last rule serves two purposes, it will eliminate the possibility of a simplex getting stuck on a "ridge" in design space, and the sequential simplex structure will "circle" the optimum. This means that only the initial simplex requires all three responses to be ranked in descending

order. All subsequent simplexes will require only the ranking of the B and N vertex, the W vertex having already been chosen as the previous N vertex.

Figure 3.4 illustrates a simplex in a design space with design variables X1 and X2. A reflected vertex, called R, is defined as a point found by reflecting the worst response (W) about the simplex face. R is found to be

$$R = 2P - W \tag{3.3-2}$$

The fixed-size sequential simplex algorithm is known as a direct search method; the movement of the simplex toward the optimum is facilitated by comparison of responses of the objective function. There is no need to evaluate gradients of the objective function either directly (as in the case of an analytical function) or indirectly (using finite differences for instance). When the optimizer is in the neighborhood of the optimum the simplexes will circle the optimum region.

Choice of size of the simplex is related to the desired accuracy in locating the region of local maxima and the noise level in the response [Walters et al., 1991; Jacoby et al., 1972; Spendley et al., 1962]. These criteria must be established on an individual problem basis through experience and may require trial and error. For relative spacing of the initial simplex vertexes used with a variable-size simplex method, Jacoby, Kowalik, and Pizzo suggest using two auxiliary values, p_n and q_n with a scaling factor S, to define the n+1 simplex vertexes for a simplex with edge length S [Jacoby et al., 1972].

$$p_n = \frac{\sqrt{n+1} - 1 + n}{n\sqrt{2}} S \qquad q_n = \frac{\sqrt{n+1} - 1}{n\sqrt{2}} S \tag{3.3-3}$$

Restricting the simplex to two dimensions (n=2), the vertexes (x^1,x^2,x^3) corresponding to design variables x and y are found to be

$$\begin{aligned} x^1 &= (x_{start}, y_{start}) \\ x^2 &= (x_{start} + p_n, y_{start} + q_n) \\ x^3 &= (x_{start} + q_n, y_{start} + p_n) \end{aligned} \tag{3.3-4}$$

The author found this method useful for finding the spacing of the vertexes using the fixed-size method as well as the initial simplex for the variable-size simplex method. The choice of the scaling factor(s) is still required and was determined by trial and error.

At some point the sequential simplex development must be halted. The convergence criteria can be based on changes in response or on changes to the design variables; however, none of the methods are foolproof and their performance is degraded as noise levels increase [Walters et al., 1991]. One method is to calculate the standard deviation of the responses for the three vetexes, and halt development when this value is below a prescribed threshold [Nelder and Mead, 1965]. A simple method useful for the two-dimensional fixed-size simplex algorithm when used in a design space with very little noise is to identify the first instance of two successive

new reflected vertexes overlapping previous vertexes - development is now halted, since the simplexes are "circling".

3.4 Variable-Size Sequential Simplex Optimization

The fixed-size sequential simplex algorithm was later modified by Nelder and Mead (1965) to yield the variable-size sequential simplex method [Nelder and Mead, 1965]. It is related to the fixed-size method with the addition of two basic modifications which allow the simplex to expand in directions that are favorable and contract in directions that are unfavorable [Walters et al., 1991; Nelder and Mead, 1965]. The new contracted and expanded vertexes are calculated as given by Walters et al. and found to be

$$\begin{aligned} E &= R + \gamma (P - W) \\ C_R &= P + \beta (P - W) \\ C_W &= P - \beta (P - W) \\ \gamma &= 1.0 \quad \beta = 0.5 \end{aligned} \tag{3.4-1}$$

The possible moves of the variable-size simplex with labeled vertexes are shown in figure 3.4. Choosing a small initial simplex size is not as important as with the fixed-size method, since the subsequent simplexes will contract and expand dependent on the responses. Convergence criterion are difficult, if not impossible, to define, especially in a noisy experiment [Walters et al., 1991; Khummongkol, 1992]. The variable-size sequential simplex method is outlined below [Walters et al., 1991].

1) Rank the vertexes of the first simplex in decreasing order of response from best to worst (i.e. B, N, W).

2) Calculate the location of the reflected vertex R and evaluate the response:

A) if $N \leq R \leq B$, use simplex B N R, go to step 3)

B) if $R > B$, calculate an expanded point, E. Evaluate the response.

i) If $E \geq B$, use simplex B N E, go to step 3)

ii) If $E < B$, use simplex B N R, go to step 3)

C) If $R < N$:

i) if $R \geq W$, calculate a contracted point C_R, evaluate response, and use simplex B N C_R, go to step 3)

ii) If $R < W$, calculate contracted point C_W, evaluate response, and use simplex B N C_W, go to step 3)

3) Never use the current simplex vertex W in the next sequential simplex. Always use the current N vertex as the W vertex for the next simplex. Rank the remaining retained vertexes in order of decreasing response and go to step 2). Repeat until convergence criteria are satisfied.

Convergence is usually judged by comparing the computed standard deviation in the response of the vertexes to a given threshold [Walters et al., 1991].

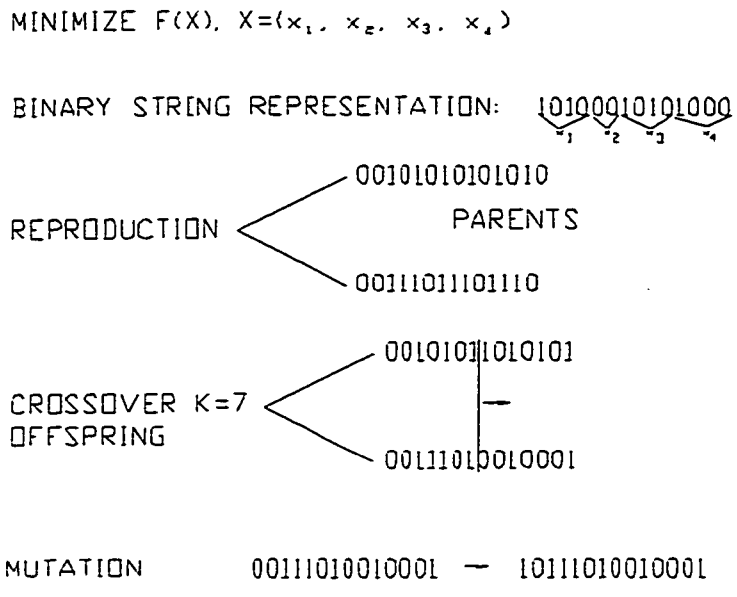

Figure 3.1 Operations of the Genetic Algorithm

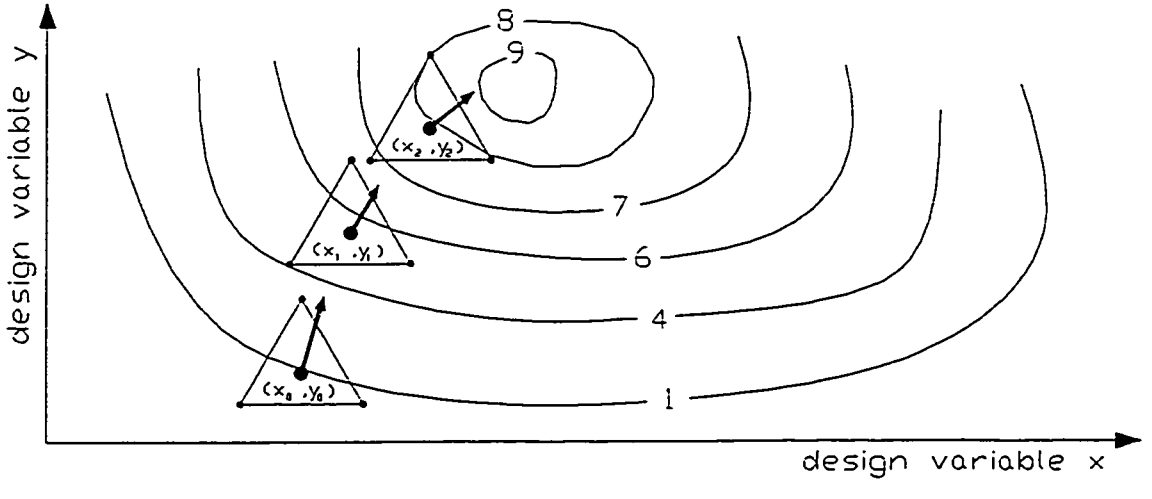

Figure 3.2 The Method of Steepest Ascent

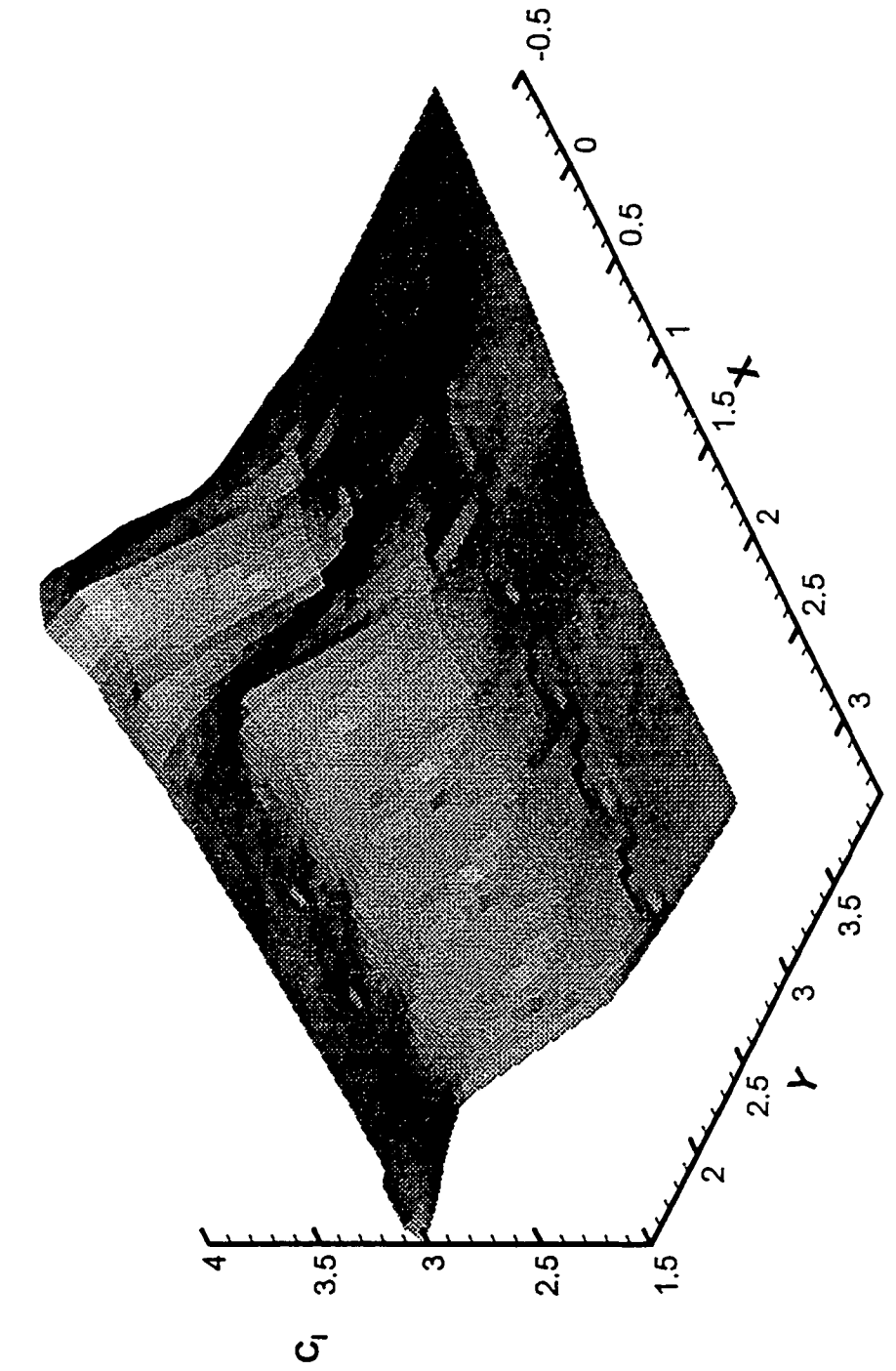

Figure 3.3 Response Surface, C_l=f(x,y)

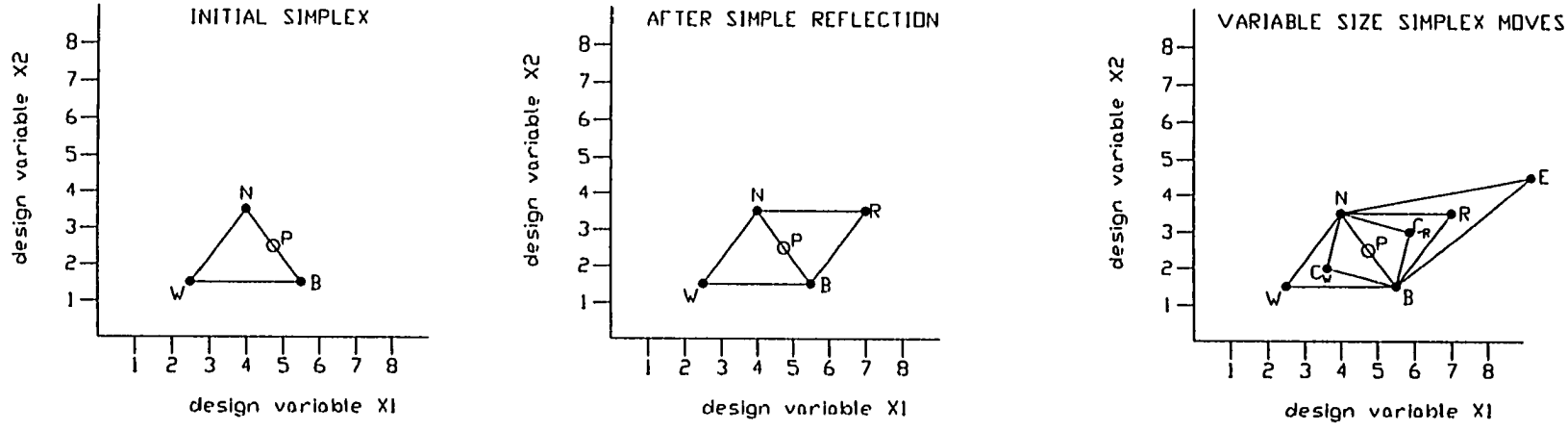

Figure 3.4 Sequential Simplex Examples

4 INTERNAL ACTUATORS FOR MULTI-ELEMENT TESTING

Remotely actuated high-lift devices on wind tunnel models serve to increase wind tunnel productivity by providing quick configuration changes [Landman and Britcher, 1995 and 1996; Otto et al., 1996]. By these means they promote the use of larger data sets for determining optimum riggings and facilitate unique opportunities to study the path dependent effects of device deployment. While the benefits of remote actuators are clearly recognized, their design and implementation is complicated by such design criteria as small available space, large loads, positional accuracy, and tolerance to temperature changes.

4.1 Control Surface Actuators on Wind Tunnel Models

Historically, remote actuation of control surfaces has been employed principally in 3D models at low dynamic pressures [Pope and Goin, 1978]. The extremely high loads caused by testing at full-scale flight Reynolds numbers makes design of actuators more difficult, particularly for a high-lift system. Since it is now believed that attaining near flight Reynolds numbers is crucial to optimizing a high-lift system, actuators must be designed to accommodate the higher loads [Lynch, 1992]. Some representative examples of wind tunnel testing incorporating control surface actuation include free-flight testing and static tests investigating control effectiveness.

Free-flight testing was performed in the NASA Langley Full-Scale Tunnel (FST) until its decommissioning in 1995. A large number of tests were conducted with this technique on aircraft ranging from general aviation, to

fighter, to large military transports. As one example, aircraft longitudinal stability and trim characteristics of upper surface blown flap transport models were investigated in the FST using free-flight models [Johnson and Phelps, 1974, Parlett 1977]. Engine thrust was simulated using compressed air supplied to the aircraft via an "umbilical" which also carried signals to command control surface inputs through pneumatic actuators. A typical test setup in the FST is depicted in figure 4.1. The models tested used control actuators on the rudder, ailerons, and elevator and were equipped with a throttle to set the thrust. Most of these free-flight tests were used to probe the area of dynamic stability and control for problems which might not show up in static testing. The control surface actuators were simple bang-bang air cylinders which allowed the control surface to reside at either of two extreme positions [Phelps, 1997]. A safety cable was used to prevent flyaway accidents resulting in wind tunnel fan damage.

The aeroelastic effects of active control surfaces have been investigated using reduced scale wind tunnel models with control surface actuators. P.A. van Gelder described the use of a dynamic wind tunnel model with active ailerons, tailplane, spoilers, and rudder used in a low-speed tunnel [van Gelder, 1986]. Primary control was commanded by use of the ailerons or spoilers with the tailplanes and rudder used for rigid body mode control. Random gusts could be generated in the tunnel which helped to perfect the governing control laws through optimization methods.

A novel method to generate and control separated vortices from the leading edge of a delta wing model was demonstrated using pneumatically actuated leading edge flaps [Karagounis et al., 1989]. This model is shown in figure 4.2 and allows the leading edge flap to move from a position of being folded on the upper surface to a position perpendicular to this surface. Surface pressure measurements were carried out for both flap static positions and rapidly opening and closing flaps. The flap actuator consisted of a push-pull pneumatic cylinder, linked to a sliding rack, which is tied to connecting rods and finally, to the flaps through control horns (see figure 4-2).

Servo-electric actuators are typically used on aircraft control surfaces for free-flight testing by researchers in the Transonic Dynamics Tunnel at NASA Langley Research Center. Typical tests involve critical aeroelasticity studies of fighter aircraft wings and tails. The models are controlled through a cable (as described above for the FST) which supplies power to the actuators [Hanson, 1998]. Control surface actuators are used to maintain the aircraft position in the tunnel while supplemental devices excite vibrations in the aircraft structure in question.

4.2 Justification for the Use of Remote Actuation

In section 2, it was shown that the optimum rigging of leading and trailing edge devices has been historically determined using a very sparse matrix of test results. This is due in large part to the extended occupancy time required to change and gauge model bracket settings manually, and in the case of cryogenic or pressurized facilities, to wait for the fluid properties of the

test section to cycle between ambient and operational values. An automated method for rigging changes to explore fully the available gap and overhang ranges is highly desirable [Lin, 1993; Nelson, 1995].

Experience in choosing probable optimum settings becomes a requirement when the number of test points is limited. Limitations can stem from wind tunnel availability, economics, or design schedules. This approach may work for traditional configurations but becomes more difficult with flow modifiers and novel configurations, for example the use of vortex generators or Gurney flaps. The increasing demand for high Reynolds number high-lift data and the limited number of facilities means that wind tunnel productivity must be increased [Lynch, 1992; Nelson, 1995].

4.3 Internal versus External Actuators for Two-Dimensional Multi-Element Airfoil Flap Movement

When faced with the prospect of designing a remotely actuated 2D high-lift airfoil model, the designer will typically have two choices: use internally mounted actuators or build actuators into the tunnel sidewall. These two basic configurations are illustrated in figure 4.3.

Concentrating on flap actuation, the internal design requires flap brackets to connect the flap to drive stages buried in the main element. The bracket's intrusion in the flowfield is a disadvantage, but they can be placed in such a way as to minimize spanwise flap deflection under load. The available space in the main element can be limiting and certainly requires the use of complex miniature components such as servomotors, gear trains and linear

bearings. The load capacity of the internal actuators will be inferior to the endmount configuration due to space constraints. Two further advantages of this approach are the portability of the model and the ease of installation in multiple facilities.

The sidewall configuration allows the flap to be end mounted and driven through the wall. The biggest advantage to this design approach is the larger space available for high powered actuators. There is no flow interference from brackets; however, the spanwise distortion due to the loading of the flap is increased compared to the bracket supported configuration. The flap acts as a prismatic beam under the influence of a uniformly distributed load. If the flap is simply supported (i.e. reactive forces only at each end) the deflection tends to be large and of course, greatest at the midspan. Conversely, if the ends of the flap are preloaded with restoring moments, the midspan deflection can be adjusted to zero.

These design approaches may be compared by calculating the flap deflection under load. Consider three examples using a 36 inch span steel model with a nested chord of 22 inches and a 30% chord flap. The lift force on the flap is chosen as 3000 pounds and is based on typical lift coefficients from previous experiments with high-lift models at near flight Reynolds numbers in the Low Turbulence Pressure Tunnel (LTPT) at NASA Langley [Stainback, 1986; Lin and Dominick, 1995].

First, consider the deflection of a flap which is simply supported at each end; the deflection at the center (midspan) is 0.65 inches -

unacceptable. If restoring moments are added to each end of the flap, the deflection at the midspan can be adjusted to zero, but the calculations show that the flap deflection range over the entire span is 0.034 inches and more importantly, approximately 0.025 inches over the center 18 inches of the flap. This spanwise variation over the center half is about 0.11% of the airfoil chord - significant, since gap and overhang are often optimized in smaller increments. Now consider a flap which is supported by brackets positioned at a distance of 1/4 span from each end. A conservative calculation shows that the deflection range between brackets is 0.008 inches - considerably less than the end supported case. The deflection of the flap with brackets and with restoring end moments is shown in figures 4.4 and 4.5 respectively. It should be noted that the calculation for the bracket supported flap included no end restraints, resulting in unrealistically high deflections at the ends. In reality, the brackets would resist bending moments, and the ends could be configured for a guided boundary condition rather than the free condition shown, both reducing the deflection at the flap ends. The calculations used for the three examples are included as appendix A.3.

4.4 Hysteretic Effects

Aerodynamic hysteresis is known to occur in airfoil behavior, with at least the following causes and results: (1) interaction between the inviscid pressure field and boundary layer separation, giving rise to stall hysteresis [Hoerner, 1985], (2) interaction between the inviscid pressure field and laminar/turbulent reattachment giving rise to separation bubble-induced

hysteresis, principally noticed in drag measurements [Mueller and Batill, 1982; Selig, 1996], and (3) due to an interaction between the pressure field and the overall flow structure, particularly the wake [Biber and Zumwalt, 1993]. In the multi-element airfoil case this might be anticipated if different attachment behaviors are possible for the wake impinging on one element from those upstream. Hysteresis loops in the lift curve have been shown by Biber and Zumwalt to depend on gap and overhang setting on a flap/airfoil model [Biber and Zumwalt, 1993]. Hysteretic effects due to flap position at a fixed angle-of-attack are anticipated in this study, and can only be detected if the flap can be moved while the flow is on.

It should be emphasized here that the effects being considered are fundamentally steady flow phenomena. In other words they do not arise from the dynamics of geometric adjustment.

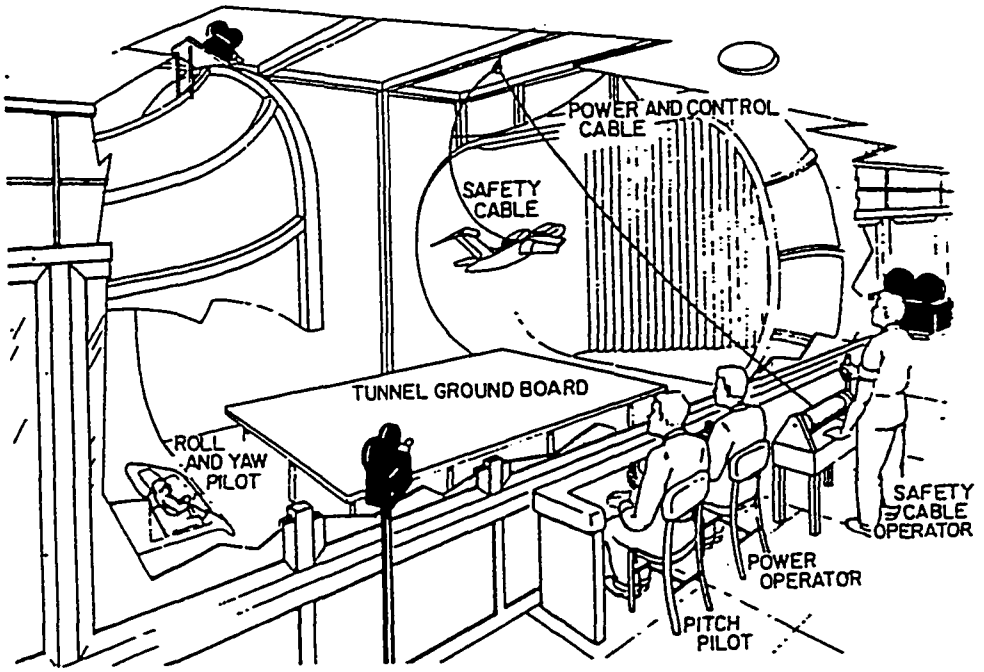

Figure 4.1 Test Setup for Free-Flight Testing in the Langley Full Scale Tunnel

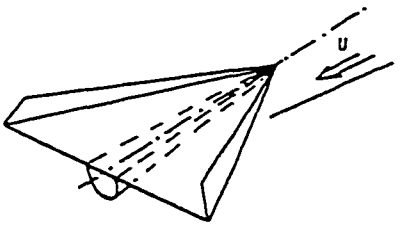

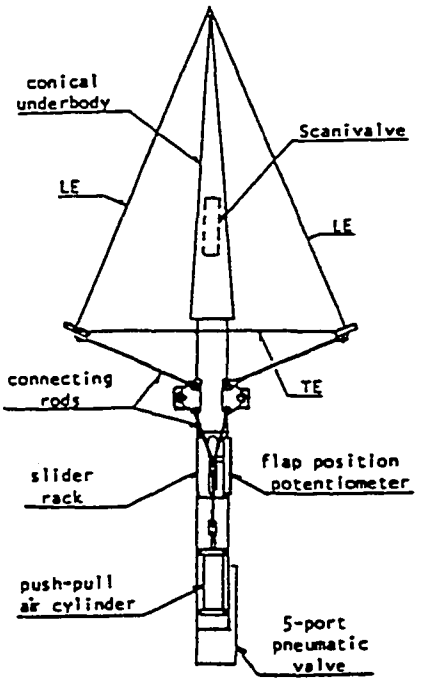

Figure 4.2 Delta Wing Model with Leading-Edge Flap Actuators of Karagounis et al.

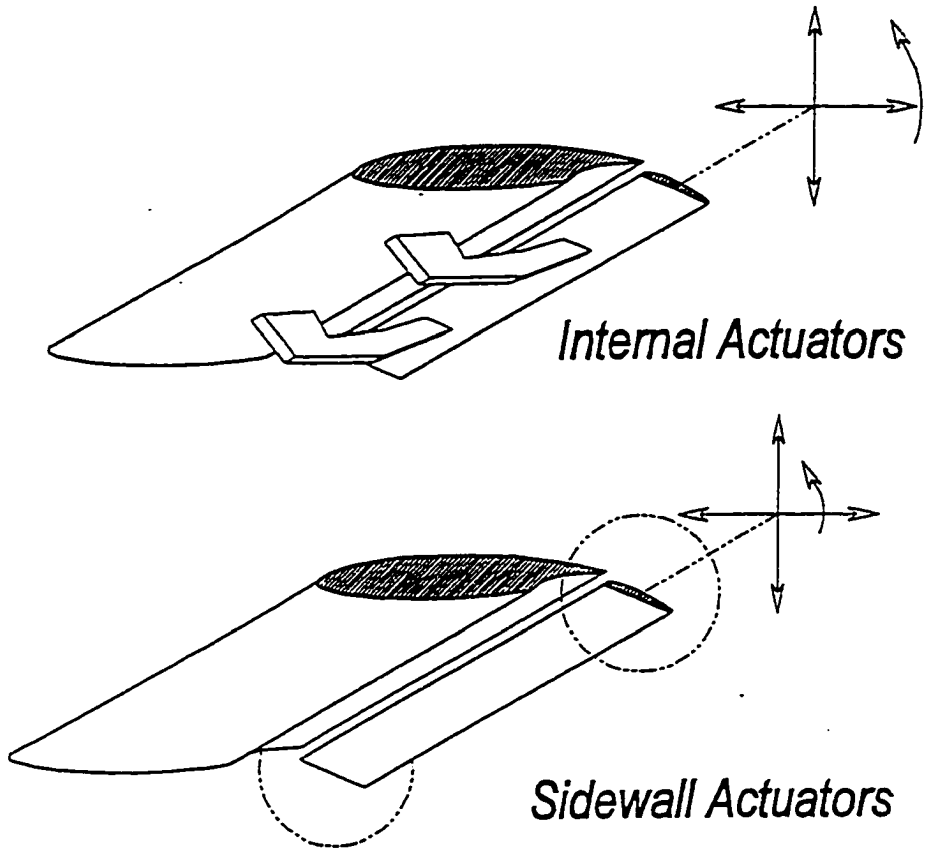

Figure 4.3 Actuator Configurations for Wind Tunnel Airfoil Models

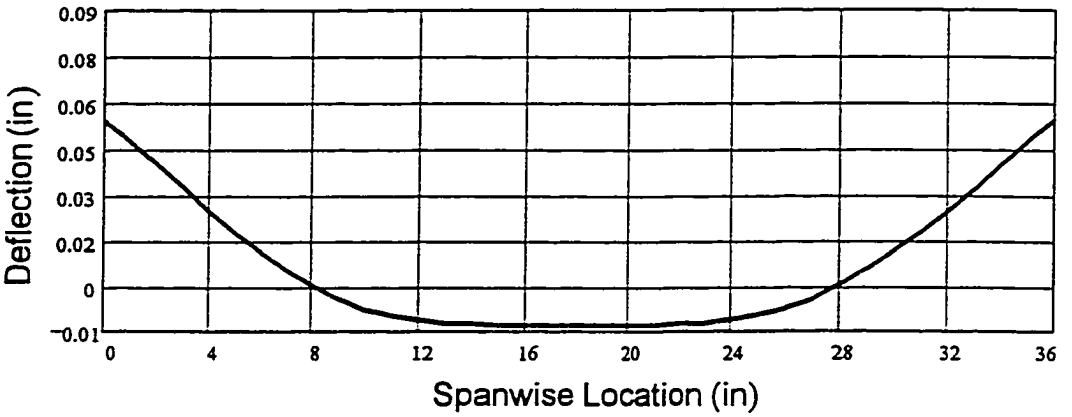

Figure 4.4 Flap Deflection for Wind Tunnel Model with Two Support Brackets Located a Distance of 1/4 Span from the Ends

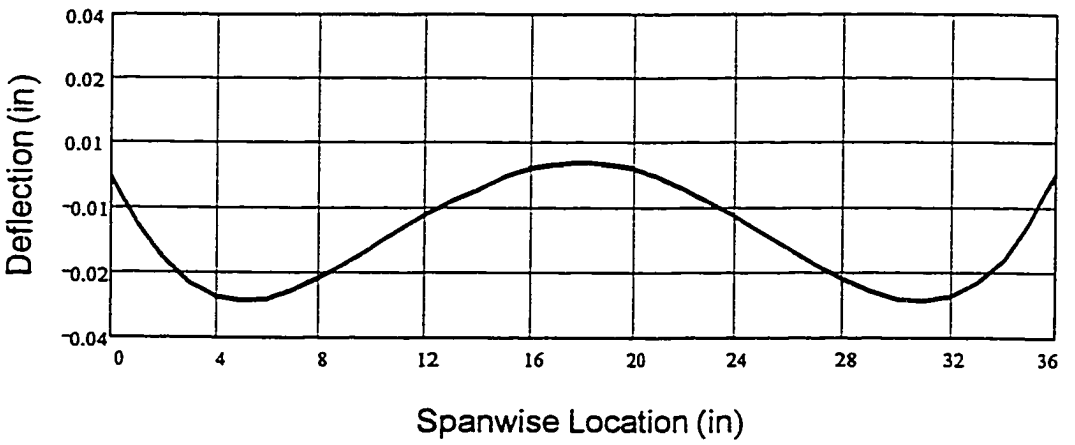

Figure 4.5 Flap Deflection for Wind Tunnel Model with End Moments

5 EXPERIMENTAL DETAILS

This study was performed in the Old Dominion University (ODU) 4-foot by 3-foot low-speed wind tunnel shown in figure 5.1. In all cases the model was mounted vertically in the test section spanning the 3 foot dimension. All lift forces were calculated from integrated pressure data measured from the mid-span pressure orifices located on the upper and lower side of all three airfoil elements. An overview of the experiment and related instrumentation is provided in figure 5.2.

5.1 Wind Tunnel Model

A unique model, shown in figure 5.3, was specially designed by the author for use in this study. The airfoil geometry is representative of a modern civil transport and was provided to NASA and other researchers by the Douglas Aircraft Company through a special agreement (this airfoil was used in the CFD Challenge mentioned in section 2.3). The coordinates are considered proprietary and are therefore unpublished. This three-element model has a nested chord of 18 inches and a span of 36 inches, where this ratio of span to chord is a standard to assure reasonable two-dimensionality [Pankhurst and Holder, 1965]. The entire model was designed using Autocad© computer aided drafting software starting with only slat bracket dimensions and the airfoil coordinates. The actuator stages were built first and tested by applying static loads of 1.5 times the expected wind tunnel testing loads. Detailed engineering drawings of the model can be found in appendix B, while the main features are shown in figure 5.3. The airfoil name

of 30P30N was originally used to describe the optimal landing rigging (see section 2.3.3). While this description requires a fixed slat and flap rigging, in lieu of any other designation the model in this study is referred to as the 30P30N, even if the rigging does not match that of the original design.

5.1.1 General Specifications

The slat and main element were numerically machined from solid aluminum stock while the flap was machined from stainless steel. All elements were hand finished to within 0.005 inches of the true profile which was verified by a numerical coordinate measuring machine. All machining was performed by the Fabrication Division of the Aerodynamics Research Equipment Section of NASA Langley Research Center. All the elements were designed to have a seamless upper surface with chordwise pressure orifices located at the mid-span. Each orifice measured 0.02 inches in diameter at the surface. Annealed stainless steel tubes were pressed into a counterbore in the backside of the orifice and routed through milled channels in the lower surface to an exit point at the left end of each element. The channel voids were then filled with epoxy resin and thickening agent, then re-profiled. Orifice locations for all elements are included in appendix B.

The slat is attached by four stainless steel brackets located on the underside of the main element and is set for a deflection angle of 30 degrees. The vertical position is varied by placing metal shims between the bracket bases and their mounting holes in the main element, while slots in the bracket base provide for fore and aft movement. The deflection angle of the slat may

changed by exchanging slat brackets which are machined for a different fixed angle.

5.1.2 Flap Actuator Design and Control

The flap is designed for a positional gap range of 1.38% to 4.4% chord (based on the nested chord of the entire model) and an overhang range of -1.38% to 3.63% chord. These values were chosen based on industry recommendations and insure that the flap can be moved to positions ranging from optimum to well off optimum, with fully separated flow over the flap.

The flap is driven by four servomotors located in the main element, arranged in two degree of freedom stages, two motors to a stage, as shown in figure 5.3 and 5.4. The main element was bored on either end to allow the insertion of the drive motor/cam units. Areas on the lower surface were relieved to provide room for the actuation stages. The motors have integral planetary gear drives providing a gear reduction ratio of 1526 to 1 and a rear mounted magnetic position encoder with 16 poles which yields a resolution of 24416 counts per revolution of the output shaft. The motor manufacturer is Micromo™ and the model number is 2842SO24C+30/1.1526:1+HEM2842S16 +x0608C+X0436A. The servomotors drive cam followers mounted on eccentric drivers that ride in slots to provide linear motion in two directions (X,Y). Limit switches provide a safety shut-off in the event that motor control is lost. The flap used in this study was deflected 30 degrees and travels on 2 brackets which are free to slide vertically on dual pins, and horizontally on machined dovetails. The brackets were designed for minimal deflection to

assure a constant gap between the flap and the main element. An interchangeable final stage on the bracket allows for a different deflection angle to be set by exchanging ends. A National Aperture™ (NA - now National Instruments), four axis servomotor control system was chosen to control the flap motors. An NA pcControl-4 card is located in an expansion slot of the personal computer and wired to an NA MC-3SA amplifier module. The amplifier drives all four motors and also provides eight channels of digital five volt level output. This feature was exploited by building a custom relay which interfaced to the tunnel motor control, allowing on/off control of flow through software.

5.2 Pressure Measurements

The stainless steel pressure tubes from each element exit the tunnel at the bottom of the test section. The flap was fitted with a thin aluminum disk that formed an endplate to seal over a hole in the floor of the tunnel. This allowed the flap to move and still provided resistance to air leakage through the floor of the test section. All stainless tubes were plumbed to scanivalves and later to the PSI 9010 modules using vinyl tubing. Each tube was leak tested using a water manometer attached to the pressure transducer side of the tube; the ports were sealed with adhesive tape and a vacuum was drawn on the manometer.

The spanwise flow uniformity was evaluated in two ways. First, the model was fitted with minitufts and run at the design Reynolds number through an angle-of-attack sweep. The tufts were monitored to look for flow

separation and spanwise flow with particular attention to tufts near the wall-model interface [Nakayama et al., 1990, Morgan et al., 1987]. Second, the spanwise pressure variation was monitored on the flap and main element through 6 orifices on each element positioned near the trailing edge. The flow was considered acceptably two-dimensional if the spanwise variation in pressure coefficient was less than 5% of the difference between the maximum and minimum value of pressure coefficient for the entire airfoil [Nakayama et al., 1990]. No sidewall boundary layer control was employed such as blowing or suction [Paschal, 1991] but rather the maximum angle-of-attack was limited to 14 degrees to maintain acceptably uniform flow across the span.

5.3 Boundary Layer Transition

The majority of the tests were conducted with free transition, meaning that there were no added surface roughness elements or tripping devices on the airfoil. Near the end of the study, during the hysteresis sweeps, it was supposed that laminar bubbles [Mueller and Batill, 1982; Selig, 1996] may be at least partially responsible for lift hysteresis due to flap position. In order to eliminate the possibility of bubble formation it was decided to force turbulent transition using strips of roughness elements. Forcing transition is a traditional method for simulating high Reynolds number flow with a model subject to low Reynolds numbers [Rae and Pope, 1984; Pankhurst and Holder, 1965]. An additional benefit to using the roughness elements was the ability to compare reference data at higher Reynolds numbers to the data of this study. A number 30 grit abrasive particle was chosen (see calculations in

appendix A.1) as just larger than the minimum size to assure transition [Braslow and Knox, 1958] . The choice of a slightly oversize particle can cause a small increase in drag, but since lift was the only force measured, this was not a major issue. All results shown are free transition measurements unless they are marked "forced transition".

5.4 Software for Automated Lift Coefficient Measurements

All of the data acquisition and control tasks were carried out automatically by various programs written by the author in the LabView™ graphical programming language. Many of the subprograms (i.e. subroutines) were common to the various programs. The software listings are cumbersome due to the graphical nature of the coding and hence the description here will be limited to the program logic using flow charts. appendix C contains examples of subprogram listings should the reader require more detail.

5.4.1 Program for Baseline Lift Coefficient Measurements

This program automatically samples pressures on the top and bottom side of all the airfoil elements, integrates for lift using a trapezoidal routine [Walker, 1994] and then calculates the lift coefficient. User inputs include a file with a matrix of flap locations (x,y) and a value for atmospheric pressure read from a barometer in the wind tunnel laboratory. All data are stored in an output file and displayed on the computer screen for immediate review.

Figure 5.5 shows a typical display from the computer and figure 5.6 is the flowchart for the program called "Matrix". A description of the operation

follows. First, the model is kept in a known "home" position after power shutdown, therefore every time the computer is powered up the motors must be initialized to reference the known home position. The PSI 9010 pressure transducers also require a call to a routine to zero each module. Second, coordinates (x,y) for the desired flap locations are read into memory and the motors are commanded to move to the first location with a feedback loop from the encoders providing verification of position. Third, the tunnel flow is turned on and a time delay is built in to allow the flow and orifice pressures to reach a steady state value. Fourth, all data is read at this point and the tunnel is turned off. Fifth, lift coefficient calculations are performed and data is displayed on the screen and written to an output file. At this point the program reaches the bottom of the loop and repeats the second through fifth steps for the remaining points in the input file.

5.4.2 Program for Hysteresis Sweeps

A modified version of the Matrix program of section 5.5.1 was used to perform the hysteresis sweeps - the only difference being a provision for leaving the tunnel flow on during the movement of the flap. Points in the input file were chosen to provide a path of flap motion that always began with fully attached flow on the flap, moved the flap to an extremum that guaranteed fully detached flow on the flap, and then traversed the same path in reverse order.

5.4.3 Program for On-Line Optimization

The method of steepest ascent is discussed in section 3.2; the algorithm given was programmed in LabView for in-situ use with the

experiment. Figure 5.7 provides a flowchart for the overall program and for the largest subprogram. The subprogram (Point C_l) differs only slightly from the core of the Matrix routine. Here again, starting with an x,y pair for the desired flap position, the program computes the lift coefficient for the individual elements, as well as the total lift coefficient. All of the output data associated with the Matrix program is again stored, not for immediate use by the optimizer, but rather for diagnostic purposes should any part of the instrumentation fail.

A description of the Steepest Ascent Program follows; details of the optimizing method may be found in section (3.2.2). The optimizer program is started by inputting an x,y pair for an initial point which the program immediately evaluates (experimentally) using the call to the Point C_l subprogram. Next, the three neighboring points which form a triangle about the initial point are evaluated. These three points are used to calculate a gradient which, in turn, provides the new direction in which the optimizer will progress. A new x,y pair is generated, lift coefficient evaluated, triangle points evaluated, and gradient calculated. The program now proceeds until the operator executes a stop command. At this point, the program has stored data for each point as shown in the Point C_l subprogram, and stored an optimizer path consisting of the lift coefficients at the triangle centroidal points and their x,y coordinates.

5.5 ODU 4-foot by 3-foot Low-Speed Wind Tunnel

The ODU 4-foot by 3-foot low-speed wind tunnel is a closed return, fan driven, atmospheric pressure tunnel using a 125 horsepower electric motor to provide speeds in excess of 130 mph. Figure 5.1 shows a pictorial view of the tunnel. The freestream turbulence intensity in this facility does not exceed 0.2% [Alcorn, 1993]. For the current study, the Reynolds number, based on the model nested chord (all high lift devices in the retracted position), was held close to 1,000,000 at all times.

Wind tunnel dynamic pressure (q) was determined by measuring the pressure differential across the contraction cone using a 10-torr MKS™, Model 310 differential pressure transducer in conjunction with a Model 170 amplifier. The calibration equation used to determine q is shown at the top of figure 5.2. The accuracy of these two units used in combination is given as less than 0.08% of reading plus less than 0.005% of full scale. Test section temperatures were measured with a Type-J thermocouple. Output voltages were acquired by a Hewlett Packard 3497A Data Acquisition and Control Unit, which has 6.5 digit accuracy, then read by a Gateway™ 486 personal computer using a GPIB expansion card and cable. Data acquisition programs were written using LabView™ software as previously described in section 5.4. The test section calibration equation was derived from previous work [Alcorn, 1993]. The equation is shown along with a schematic of the experimental set-up in figure 5.2 .

Pressures on the model were recorded in the early phase of the study using twelve Datametrics™ model 570D-100T-2A1-V (100 torr Barocell) pressure transducers with type 525 thermal base units in conjunction with type 1015 signal conditioning units powered through model 699 power supplies. These instruments were calibrated before use and were proven to have a minimum accuracy of ± 0.37% of reading plus 0.01% of full scale. A group of twelve multiport Scanivalves™, were employed to allow twelve pressures to be read simultaneously. The voltages from the Barocells were read by the Hewlett Packard 3497A Data Acquisition and Control Unit and then converted to pressures using a LabView™ software program.

Later in the study a bank of five, Pressure Systems Incorporated (PSI) model 9010 pressure transducers (with 16 channels each) were used to acquire pressures from the model. This reduced the time to acquire one data point by a factor of 5, while providing a higher level of reliability due to the lack of moving parts and the fewer tubing connections required. The PSI 9010 units digitize the pressure transducer voltages internally by taking 256 samples in 0.1 seconds and have a minimum accuracy of ±0.15% of full scale. Pressures are returned to a LabView™ program via the computer serial port and a LabView™ driver.

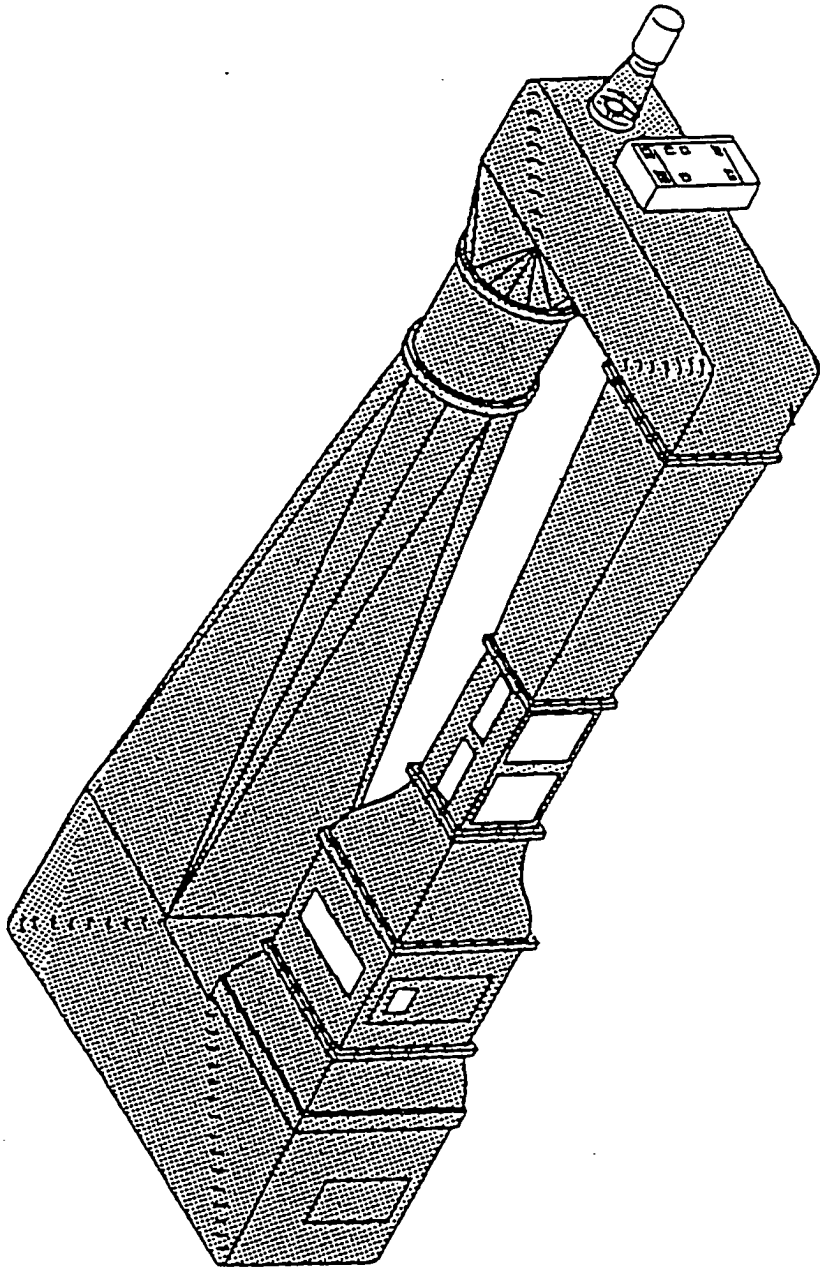

Figure 5.1 ODU Low-Speed Wind Tunnel

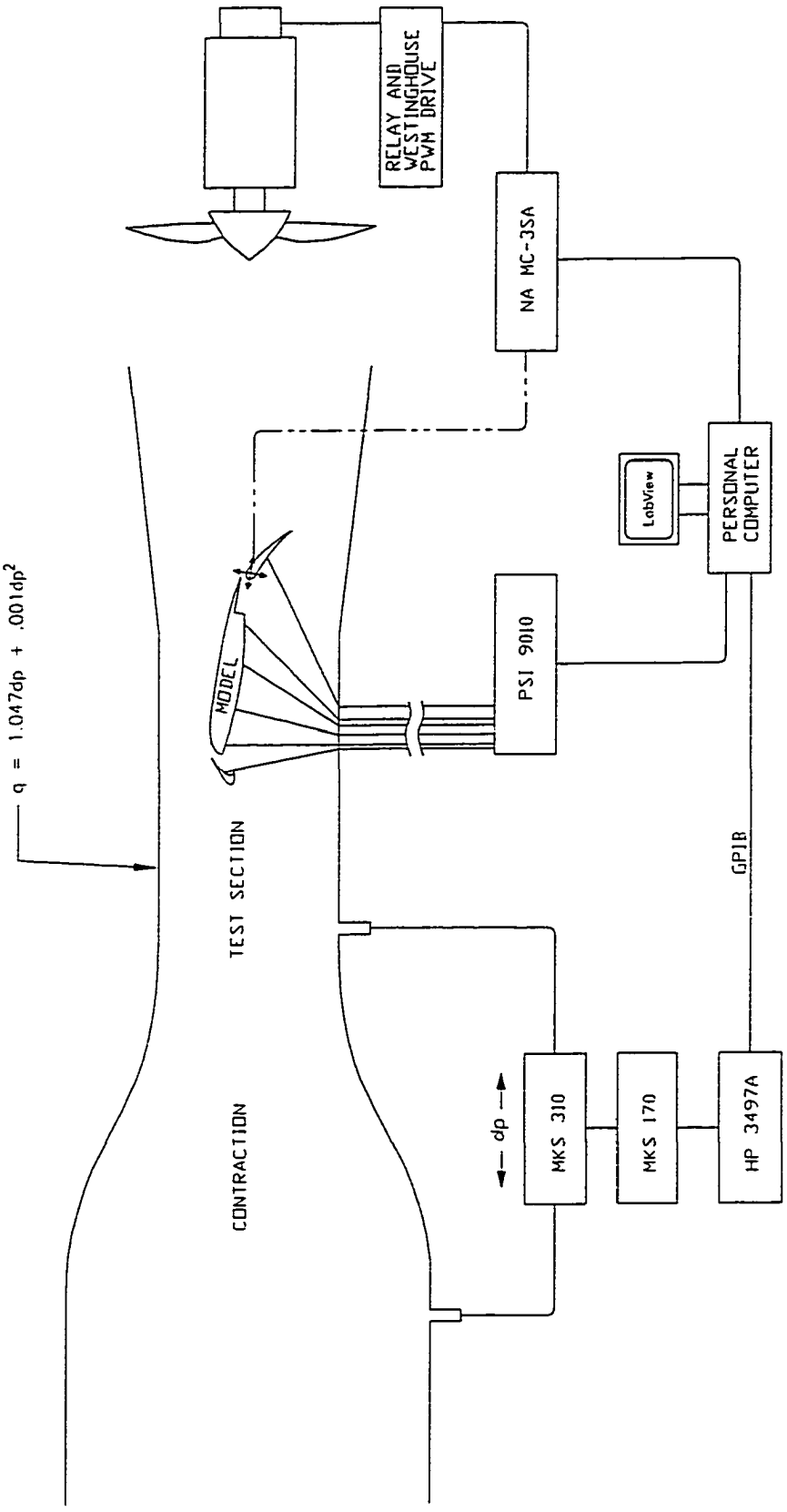

Figure 5.2 Experimental Set-Up

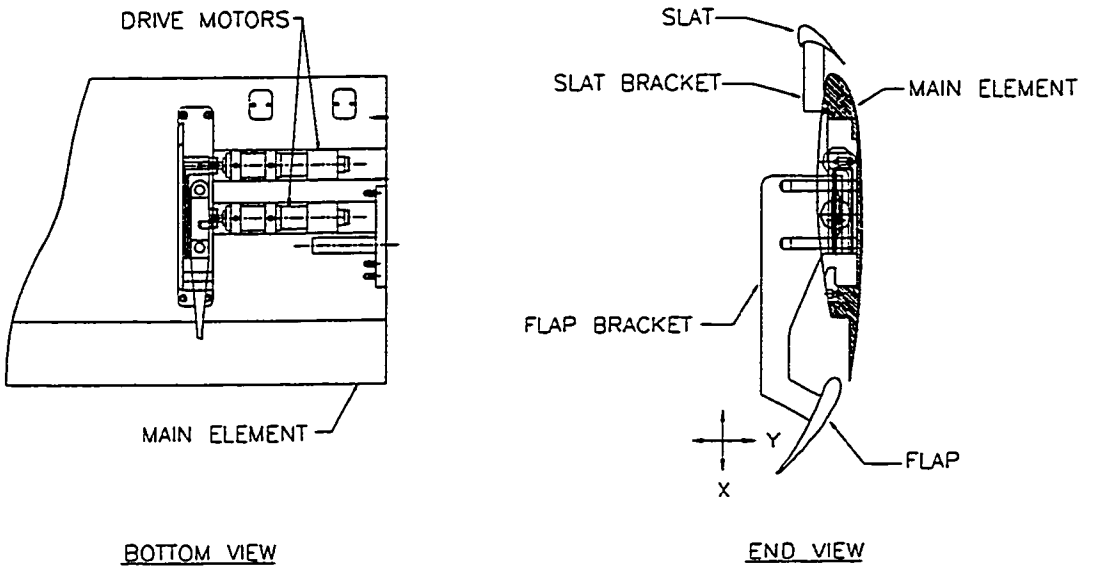

Figure 5.3 30P30N Three-Element Model

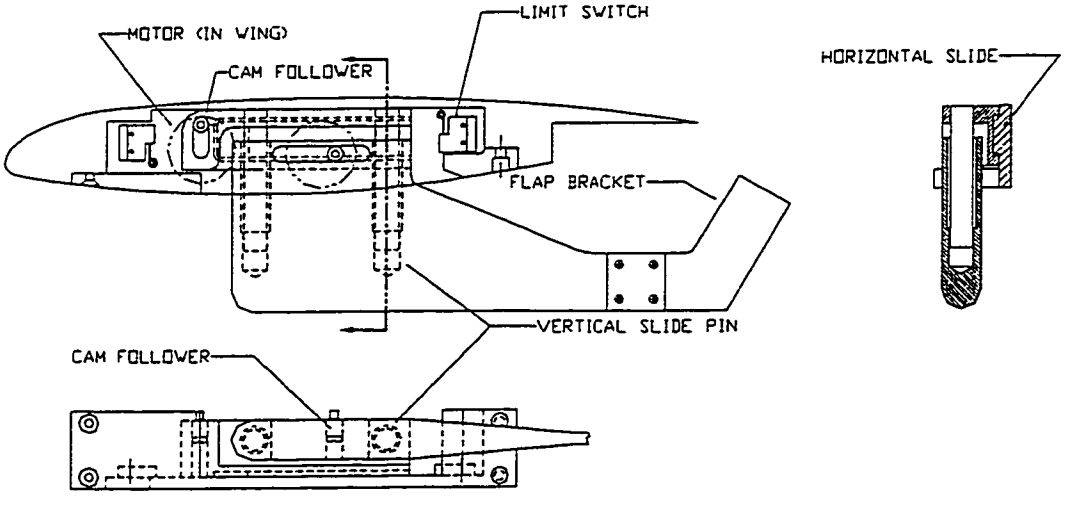

Figure 5.4 Model Flap Actuator Design

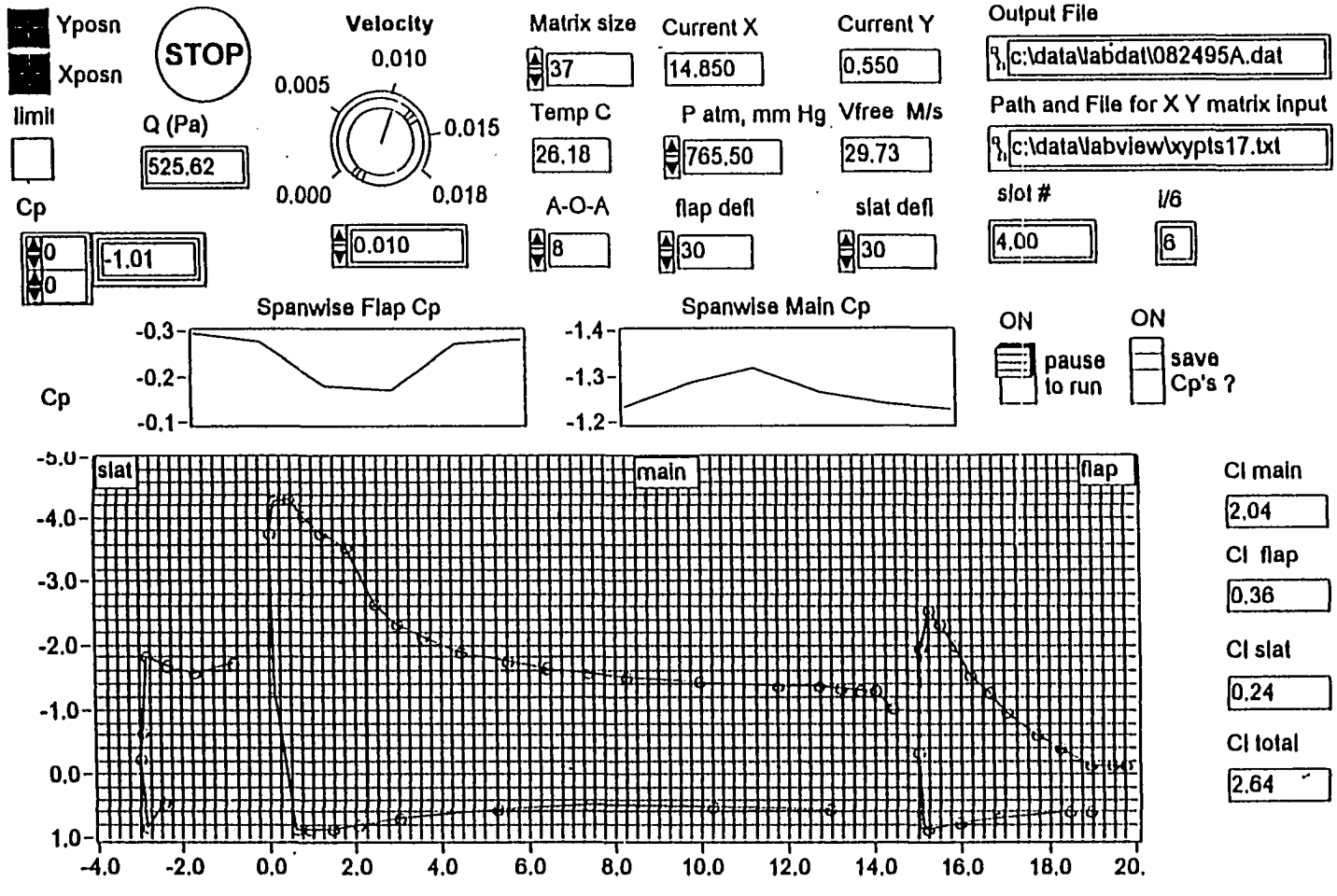

Figure 5.5 Typical Experiment Control Panel

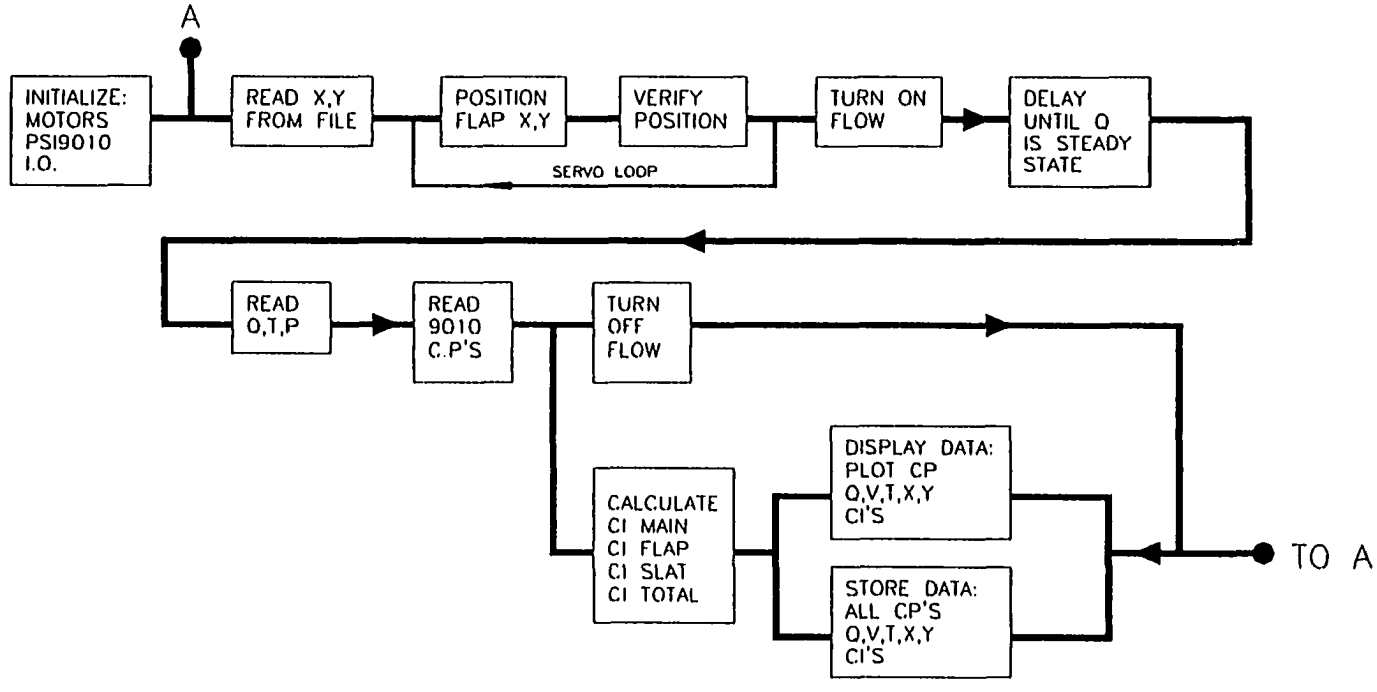

Figure 5.6 Flowchart of Program for Sampling Data and Computing Lift Coefficients for Flap Locations

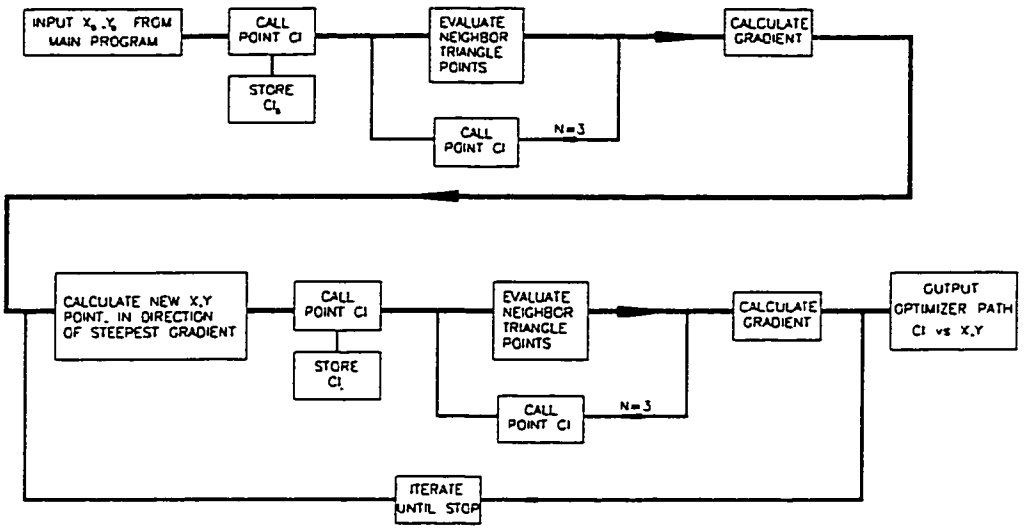

Figure 5.7a Flowchart for Program for On-Line Optimizer

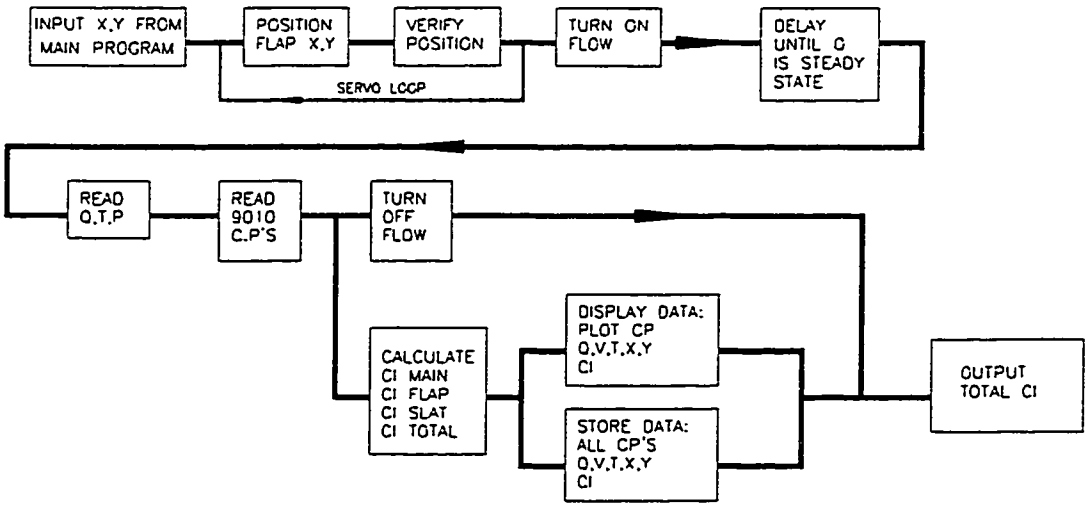

Figure 5.7b Flowchart for Sub-Program for Calculating Lift Coefficients

6 RESULTS

All tests were performed in the Old Dominion University 4-foot by 3-foot low-speed wind tunnel. All reported results are presented without corrections for boundary effects. The model, facility, instrumentation, software and experimental setup were described in detail in section 5. It is important to recall that both the flap and slat deflection angle were fixed at 30° for the entire study. Two slat settings were used; setting A had a 3.03%C gap and a -2.46%C overhang and setting B used a 2.17%C gap and a -1.46%C overhang. All distances reported as %C are based on the percentage of nested chord (18 inches). The airfoil model boundary layers were allowed to freely transition when data is notated as *free transition*; the notation *forced transition,* refers to boundary layers which were tripped by distributed roughness elements (as described in section 5). The experimental optimization algorithms referred to in this section were described in section 3.

6.1 Comparisons to Reference Data

A model of the 30P30N airfoil was tested by McDonnell Douglas (now part of Boeing Corporation) in the Low Turbulence Pressure Tunnel (LTPT) at NASA Langley Research Center. Force and moment data and pressure distributions from these tests were published in recent literature at two Reynolds numbers: 5 and 9 million [Nelson, 1995; Anderson and Bonhaus, 1993; Valarezo and Mavriplis, 1993; Klausmeyer and Lin, 1997].

Figure 6.1a shows the correlation of lift data from this study to the data from the LTPT; both data sets are uncorrected for boundary effects. Lift

coefficient from the LTPT study is plotted as a function of Reynolds number and angle-of-attack for a flap gap and overhang setting equivalent to a flap position of x=14.94" and y=0.58". Both the 8° and 14° angle-of attack case being compared from the current study are very close in flap and slat gap and overhang settings to the reference rigging (actual values noted in figures 6.1b and 6.1c) and were obtained with free transition. The current data (ODU $Re_c = 1 \times 10^6$) is shown with LTPT data that has been adjusted for the lower Reynolds number and sidewall boundary layer control (BLC). The Reynolds number scaling was obtained from the linear fit shown in figure 6.1a. The BLC correction was made using representative data presented by Paschal et al., [Paschal et al., 1991]. Figure 2.17d illustrates a similar effect.

Figure 6.1b and 6.1c show a comparison of the reference pressure distributions (uncorrected) for two cases from this study. While the actual values of the pressure coefficients are not identically duplicated for the two cases when compared to the reference, the trends are reproduced reasonably well. The lower values of the current study were again attributed to the lack of sidewall boundary layer control, small differences in gap and overhang, the reduced number of pressure taps, and the lower Reynolds number of the test condition [Paschal et al., 1991]. The key features of the reference pressure distribution appear to be captured by the less densely tapped surfaces of the current model. In particular, the suction peak of the main element, the inflection point on the upper surface of the main element (~ 15%C where the trailing edge of the slat would nest in the cruise configuration), and the flap

suction peak are well represented. The sparse tap distribution on the slat somewhat reduces the detail but was found to be adequate for resolving small changes in overall airfoil lift coefficient. The slat suction peak is attenuated, probably due to the sensitivity to the lower Reynolds number. A sample of raw data from a pressure distribution is included in appendix D.

6.2 Pressure Distributions - Element Stall

The remotely actuated flap was used to vary flap gap and overhang both with the tunnel flow on continuously, and with the flow restarting between successive data points (hereafter called intermittently). In both cases, for fixed slat riggings, excessive flap gap settings led to separation on the flap progressing from the trailing edge and moving forward as the gap was increased. This separation trend was identified by the constant pressure region at the trailing edge of the flap and verified using tufts [Adair and Horne, 1988; Biber and Zumwalt, 1993]. As an example considering figure 6.1c, the pressure distribution of the current study shows some separation evident over the last 8-10% of the flap which is visible as a constant pressure region.

The nature of the progression of flap stall was found to be both path dependent and dependent on whether the tunnel was being operated continuously or intermittently. Four paths taken by the flap were used to study stall progression and are illustrated in figure 6.2a. Each path represents motion in one degree of freedom while the second degree of freedom is fixed (i.e. changing gap with fixed overhang). Figure 6.2b reviews the nomenclature for this study. The arrows show the direction in which the

flap was moved. The underlying contours show the distribution of airfoil lift coefficient, derived from integrated pressure data, taken with intermittent flow conditions.

Pressure distributions for the points of the intermittent flow paths in figure 6.2 are shown in figure 6.3. The flow over the flap in figure 6.3a is completely attached for y=0.59" and y=0.55" but completely separates somewhere between y=0.55" and y=0.45" as the flap is moved downward in the vertical direction. The full separation is evidenced by the nearly constant pressure over the entire upper surface of the flap. A similar trend is observed in figure 6.3b which shows the stall progression as the flap is moved aft under intermittent run conditions. The interaction of the three elements can be seen in the deleterious effect the flap has on the lift of the two upstream elements, as the flap approaches stall. The decreased circulation on the flap results in a reduced suction pressure (top surface) at the trailing edge of the main element and, in turn, a lower circulation on the main element due to the *circulation effect* as discussed in section 2.1.3 [Smith, 1974; Nelson, 1995]. The now lower circulation on the main element reduces the circulation of the slat which can be seen primarily as reduced slat suction pressures. The effect of increasing gap on flap stall is well illustrated in figure 6.3b and 6.3c. In figure 6.3b the flap leading edge is at all times under the trailing edge of the main element resulting in a relatively constant gap, hence nearly identical pressure distributions. As the flap leading edge moves towards the main element trailing edge (x=14.95") the airfoil lift coefficient rises with the

increasing gap until a local maximum, and then the flap quickly stalls when the gap grows too large.

The jet flow issuing through the flap gap plays a pivotal role in dictating the maximum airfoil lift coefficient. A small (sub-optimal) gap limits the size of jet flow accelerating through the slot and limits the amount of turning possible over the flap leading edge [Nelson, 1995; Nakayama, 1990; Adair and Horne, 1988]. An optimal gap allows a high-speed potential jet to develop which creates a favorable pressure gradient on the upper surface of the flap, promoting a thin laminar boundary layer over the top surface of the flap [Nelson, 1995; Nakayama, 1990]. As the gap enlarges beyond the optimal size, the slot flow velocity is reduced, the flap boundary layer thickens and transitions to a turbulent boundary layer and the point of confluence with the wake of the main moves forward. With continued increased gap size, there is increased turbulent mixing between the wake and flap and eventually the confluent boundary layer separates [Biber and Zumwalt, 1993].

All of the results discussed so far have been for the model with free transition (i.e. no trips or added roughness elements), and it could be argued that the test Reynolds number is relatively low. To reduce the possibility of ambiguous results due to low Reynolds number effects, such as laminar separation bubbles, roughness strips were used to force transition in later tests (as discussed in section 5.4). No significant differences between free and forced transition tests were noted. However, airfoil lift coefficients were slightly lower with forced transition, presumably due to the thicker turbulent

boundary layers caused by the addition of roughness strips [Braslow and Knox, 1958]. One of the most important influences of Reynolds number is on Cl_{max}, due to changes in the boundary layer. This could not be investigated in this study.

The results shown in figure 6.4 differ from figure 6.3 in two ways: the flow was continuous, and forced transition was used. The points chosen for figure 6.4 show slightly greater differences in the pressure distribution between successive points, and the point at which stall occurs is delayed in the case of both the vertical and horizontal sweeps. This difference in stall position will be addressed in the discussion of hysteretic effects in section 6.7. What is interesting to observe is that the mechanism for stall remains the same for intermittent or continuous flow conditions, namely that the flow separates on the upper surface of the flap beginning at the trailing edge. This can be seen in figure 6.4b as the flap pressure distribution progressively flattens near the trailing edge as the flap moves from x=15" through x=15.15". In comparing this sequence to figure 6.3b, note that the increments in x are reduced, yielding greater detail such as x=15.05" which shows the flow over the flap separated for about 60% of the flap chord.

6.3 Lift Coefficient Versus Flap Position - Baseline

With the goal of on-line automatic optimization of airfoil lift coefficient in mind, test runs were initiated to measure lift coefficient over the available flap positional range to serve as a baseline, and to use in computer simulations utilizing optimizing algorithms. Two angles-of-attack were chosen as relevant:

8°, representative of an approach angle-of-attack, and 14°, the highest angle-of-attack with acceptable spanwise flow (see section 5.3). The results of figure 6.5 were compiled first using the A and B slat setting for the 8° case with free transition using 44 and 48 data points per plot respectively. The broad optimum area evident in both plots is located in approximately the same region, appears to be insensitive to slat setting, and is adequately represented by the number of points chosen. The steep gradient in C_l occurs where the flow separates over the flap as discussed in section 6.2. The 14° case of figure 6.6 revealed a C_l distribution with a more defined optimum, more sensitive to slat setting, and more sensitive to the density of data points. The "B" slat was run first with 40 data points followed by the "A" slat with 48 data points. Both runs showed 2 small regions with local maximums: one near a 2%C vertical position and 1.0% overhang position, the second near the extreme limits of vertical positioning and the 0.25% overhang position. It was reasoned that more detail may be present if the grid size was reduced in the area of the local maxima, and for efficiency in using available tunnel occupancy time, the large separated region below a vertical position of about 3%C were omitted. These tests used 120 points each and are presented as figure 6.7. Interestingly, the local maximum visible at the extreme vertical position is a very small region and corresponds to the optimum position chosen by Lynch for this airfoil [Nelson, 1995]. A raw data sample is included in appendix D for the 14°, slat A case of figures 6.6 and 6.7.

6.4 Uncertainty Assessment

Having found the baseline lift distributions, the next tests were aimed at quantifying the collective experimental error in the measurement of the lift coefficient, including the effects of pressure instrumentation and positioning. The first test used the positioning program to sample a grid of 29 points for an 8° angle-of-attack using slat A. The tunnel was restarted between each point and the entire run was repeated. The error in C_l between the two runs averaged 0.71% with a standard deviation of 0.75%. The error distribution is graphically displayed in figure 6.7c as a contour plot of the difference in C_l between fitted surfaces from each of the data sets. Next, two points were chosen at an angle-of-attack of 14° using slat setting B: a point where the flow was fully attached on the flap at a near optimum C_l, and a point in the fully separated region with a low C_l. These points were felt to be representative of flow conditions encountered over the domain of flap positions. Each point was evaluated by first moving the flap to a reference point and then back to the evaluation point. The tunnel was restarted before every evaluation and the test was repeated 30 times for each point. The results are included in appendix A and showed that the standard deviation of C_l for the separated case was 0.004 (0.16%) and 0.0118 (0.36%) for the attached case. While the difference in the results between separated versus attached flow conditions was counter-intuitive, this may be explained by several factors. Firstly, fully separated flow on the flap can be a more stable state when viewed in terms of the influence of the tunnel sidewall boundary

layer. The high suction pressures on the flap in the attached case tend to introduce unsteady three-dimensional effects (such as corner vortices) at or near the end regions of the flap, whose influence may be felt at the midspan pressure tap location. The upper surface of the fully stalled flap is characterized by a constant higher pressure region which has comparatively less effect on the sidewall boundary layer. Secondly, the integration of the pressures over the sparsely tapped slat may also introduce some error if a suction peak lies alternately coincident with, and then adjacent to, a tap location. Differences in the results between the grid of points versus the individual point evaluations may stem from the assumption that the two points picked are completely representative of the entire domain. The results of these two tests, while not exhaustive from a standpoint of statistically justifying error for a particular absolute C_l, provided a good benchmark for the choice of an optimizing algorithm with regards to noise level. The noise level was found to be relatively low from the standpoint of optimization, which permitted the use of simplified algorithms usually only suited to analytical problems.

6.5 Optimization for Maximum Lift

The baseline lift coefficient results provided an ideal database for use in a simulated experiment. By using a multivariate regression, a simulated response surface was generated using the discrete points from the baseline studies. This response surface was coupled with simulated experimental error (noise) using a random number generator. Using the simulated

experiment, three optimizing algorithms were tried: a fixed-size sequential simplex, a variable-size sequential simplex, and a method of steepest ascent. Ultimately, the most promising candidate for use on-line appeared to be the method of steepest ascent. Therefore an on-line optimizing program using the method of steepest ascent was written in LabView and tested for both the 8° and 14° case.

6.5.1 Simulation

Due to the wealth of statistical utilities and excellent graphic output capabilities available, all the simulation programs were written using MathCad©. The listings are included in appendix E. In all cases a multivariate regression fit was used to fit a surface to the experimental data points. The method employed linear combinations of locally fitted second order polynomials to represent the response surface [Mathsoft, 1995]. This response surface was augmented with a simulated experimental error by using a random number generator bounded by a standard deviation in C_l chosen as 0.017 (~0.6% based on the 8° case). This value was somewhat higher than the measured value of the worst case test (from the 30 repetitive points) of section 6.4 and was chosen so as to help guarantee the development of a robust on-line routine. The method used for the regression fit slightly influenced the data and shifted the optimum when compared to the original data, which became important when simulation results were compared to contour plots of the baseline data. To account for the affected response, the regressed response surface was output and plotted beneath

the paths of the simulated optimizations. Two sets of data were chosen for all the simulations, the data of figure 6.6a (14°, slat A) and the data of figure 6.5b (8°, slat B). The smaller data sets were chosen for computational efficiency when using the regression fits.

6.5.1.1 Simulation of the Fixed-Size Simplex Optimization

The theory behind the fixed-size simplex algorithm was discussed in section 3.3 and the listing for the simulation is included in appendix E. The runs were begun by choosing a starting point in the portion of the design space where flow was separated over the flap, then proceeded by letting the optimizer progress to a local lift coefficient maximum. The ideal size of the simplex was found by trial and error to be S=0.035". A larger size might progress to the optimum more often (more reliably), but provide less resolution of the optimum, and a smaller size would be less successful in finding the optimum, but provide better resolution. A typical trial of 30 runs for the 8° case, using 27 simplexes each, starting at x=14.85", y=0.35", resulted in all the paths passing into the optimum region of C_l=2.74 at some time. Choosing the center of the "circling" simplex lattice as the optimum brought the optimizer within 1% of the maximum C_l each time. Figure 6.8a shows a typical simplex lattice with the sequential simplexes labeled from the starting simplex A and progressing in alphabetical order. All subsequent sequential simplex figures will follow this nomenclature. Figure 6.8a shows a typical problem attributed to noise; instead of the algorithm converging to a single circle, multiple circles with offset centers are found. In addition, direction

reversals can be seen by following the alphabetical progression of the simplexes. One convergence method described in the literature suggests trapping the simplex after it completes the first circle [Spendley et al., 1962; Walters et al., 1991]. This proved to be ineffective (in this study) as the first circle was not always the true optimum. A second starting point, farther forward and lower (x=14.55", y=0.25"), yielded slightly poorer results for a trial of 30 runs; however, the optimum circle center was within 1.5% of the maximum C_l for the worst case (1 run) and within 1% of the optimum for the remaining 29 runs. A typical run is shown in figure 6.8c with the worst case run shown in figure 6.8b. Trials using the 14° data were less successful. Using the same starting points, simplex size, and trials of 30 runs, the aft starting point worked well, but the forward starting point led to some problems. The aft point gave 30 successful runs in 30 attempts using 27 simplexes per run with all circle optimum points within 1% of the design space maximum C_l. Two typical runs are shown in figure 6.9: figure 6.9a shows a near perfect run, and figure 6.9b illustrates the effect of noise in shifting the optimum circle. The aft starting point caused the algorithm difficulty which seems to stem from the shallow gradients of C_l in the region. Figures 6.10a-b illustrate the problems between consecutive runs using 27 simplexes per run. Adjusting the simplex size was ineffective in combatting the problems with noise.

Following these initial tests, it was decided that the fixed-size sequential simplex method, while fairly effective, was not entirely robust. The

variable-size simplex method was tried next as a refinement to the fixed-size method.

6.5.1.2 Simulation of the Variable-Size Simplex Optimization

Initially, the variable-size algorithm was tried for 30 runs using the same starting points as with the fixed-size simplex method using the 14° case. While the aft point worked well, the forward point was unacceptable. The simplex would either "walk off" or expand beyond the borders of the design space due to the comparatively shallow gradients and the relatively high noise level which resulted in 15 failures out of 30 runs. It was found that changing the vertical coordinate to y=0.35" (2.789%C vertical position) provided the necessary spatial buffer to allow for errors at the start. Results for 30 runs using 27 simplexes each are tabulated for the two starting points in table 6.1 and 6.2. The mean and standard deviation were calculated from the lift coefficients of the last simplex (three points). The percent difference refers to the difference between the simulated optimum (C_l) found for the run with the known optimum value from the data set (with no allowance for noise). Both data sets required choosing an expansion scaling factor (γ) of 0.6. This was found by trial and error after starting with a value of 0.5 suggested by Nelder and Mead [Nelder and Mead, 1965]. The results are promising with two points with a percent difference over 1.0% for the forward point, and seven for the more difficult forward starting point. Reasonable convergence was felt to occur on every trial as suggested by the standard deviation results. An ideal run is illustrated in figure 6.11a where the path of the optimizer

encircles the optimum region and slowly collapses on the maximum. A rectangle is used to highlight the final simplex and the first few simplexes in the lattice are shown with letters (in the same manner as used previously for the fixed-size simplex) followed by a line which joins a single vertex of each sequential simplex. Since the simplex may contract, the size of the initial simplex may be chosen as relatively large; S=0.06" was found to be ideal. Problems with the forward starting point are shown in figure 6.11b as the simplexes wander in the separated flow region and then recover to miss the optimum and converge slightly forward of the true optimum.

Turning now to the 8° case, it was found that the scaling factor value of 0.6 (γ) would not work reliably, forcing the simplexes out of the design space in 16 out of 30 runs. Through trial and error it was found that a value of 0.3 was favorable as is illustrated by the results in table 6.3 and 6.4. Here, owing partly to the shallow slope of the response surface, the results show standard deviations indicative of convergence, and final responses in all cases are less than 1% different from the known optimal value. Typical runs from the fore and aft starting points are depicted in figure 6.12.

While the sequential simplex method performed favorably when the scaling factors were adjusted individually for each case, it was felt that a single compromise value should be sought after, if the algorithm were to be invoked in an experiment where the response was unknown. Several trials using 30 runs for the 14° case with a scaling value of 0.3 were tried with less than satisfactory results. As can be seen in table 6.5, when the path

remained in the design space, the results were much like those with the 0.6 scaling factor; the only problem was that on occasion the algorithm failed completely by choosing a vertex outside the design space.

6.5.1.3 Simulation of the Steepest Ascent Optimization

For comparison purposes the same starting points as used previously were used with the method of steepest ascent and a mean and standard deviation for C_l, based on the response of the three points of the last triangle (notation used in tables is "last tri") used to calculate the gradient was computed. This method does not produce results that are entirely equivalent to those used in the variable-size simplex but does provide some means of comparison. The variable-size simplex method tends to converge (spatially contracting) on a final point whereas it will be shown that the method of steepest ascent tends to "map" the region of the optimal response by wandering back and forth across the boundaries. Although the last iteration is not necessarily the best value due to the deleterious effects of noise, rather than relying on incompletely proven convergence criteria, calculations were reserved for the last points. Since the triangle of data points used for gradient calculations remains constant in size (in fact, limited to a minimum size), a response (with error) from the centroidal coordinate was calculated in order to help judge performance.

The method of steepest ascent (as described in section 3.2) provides three parameters to control its progress, which were adjusted by trial and error to allow the algorithm to work with both angle-of-attack cases, from both

starting points. An initial step size (So) of 0.07" was used, maximizing the size of the first move while not pushing the path out of the design space boundary should noise cause a false move. A maximum limiting step size for all subsequent moves (Smax) was chosen as 0.05" and the reference size of the triangle (tol) was chosen as 0.06".

Identical trials for the four cases used for the variable simplex method were conducted using 27 moves. Results for the four cases are shown in tables 6.6 - 6.9. Perhaps more telling are the plots of the optimizer paths shown in figure 6.13 (14°) and 6.14 (8°) which were limited to 22 moves, each starting at the point in the path which is circled. Figure 6.13a illustrates the rapid progression toward the optimum region possible using this method (the first five moves here) and the "ridge walking" characteristic, where the path of the optimizer zig-zags into and out of the optimum region. Figure 6.13b and 6.13c show how robust the method is, even when starting at the forward point. In the first figure the path progresses to the maximum with a minimum of lost moves and in the second the noise is ultimately overcome as the path progresses toward the maximum region, needing only a few more moves to complete the optimization. The plots presented in figure 6.14 reveal the same characteristics for the 8° case as found in the 14° case.

6.5.1.4 Choosing a Method for Experimental Optimization

It was decided to choose one method for use on-line with a wind tunnel experiment. The method of steepest ascent was seen to have two major advantages: it very quickly progressed to the optimal region, in many cases

with as few as four steps, and it could be used with one set of parameters (i.e. So, Smax, and tol) for both test cases. A rapid progression was advantageous, particularly when instrument reliability was in question. An instrument failure encountered during a circuitous path, more common with the sequential simplex method, would most likely require a restart of the run. A failure with the steepest ascent routine may occur while the optimizer has already approached the optimum region. Since it was desirable to use the optimizer on blind cases, with no prior knowledge of the baseline data, the flexibility of the steepest ascent method was welcome, when compared to the sequential simplex method which required adjustment of the expansion scaling parameter.

With regards to convergence to the local optimum, both methods were closely matched, even when using the last points of the method of steepest ascent for comparison, a choice which clearly biased the results in favor of the variable-size simplex. Results are tabulated in table 6.10 for the previously discussed trials. In all cases the difference between the known local optimum and the optimizer is less than 0.7% and the standard deviation is on the order of the error which was added to the simulated experimental response (0.017). While both methods were certainly candidates, in the end the method of steepest ascent was chosen as the on-line experimental optimizer.

6.5.2 Experimental Optimization - Method of Steepest Ascent

Using the scaling values chosen during the simulation, and the identical algorithm for the method of steepest ascent, six trials were conducted using an angle-of-attack of 8° with both the A and B slat setting. All six runs were successful as can be seen in figure 6.15a and 6.15b, where the optimizer start point (circled on plots) is always in the region of lowest response and the contours are from the baseline measurements. The optimizing runs were performed during a separate tunnel entry at a later date than the baseline runs, and in general all lift coefficients measured during this entry were on the order of 2.5% higher than the baseline values. Two reasons may account for this difference: the method for setting the angle-of-attack on the model was rather crude yielding an accuracy of ±0.3°, and in the interim a traversing mechanism located just downstream of the model was removed from the test section. These small differences in C_l did not appear to effect the optimizer paths and all the runs were self-consistent when their responses were compared. Due to the limited availability of the tunnel, this pattern of self-consistent runs being compared to baseline data of previous entries was repeated throughout the test program. The forward test point (overhang of ~2.25%) did not cause as much difficulty as was evident in some of the simulator runs. This may be accounted for by noting that the noise was actually measured to be lower for points in the fully separated region of the design space than for points in the attached region whereas the simulator used the highest noise level for both regions. The convergence history for the

3 runs of figure 6.15a is tabulated in table 6.11 and plotted in figure 6.15c. With regards to the effect of slat rigging, no significant differences were noted between the A and B configuration in either the baseline study or the optimizer study.

For a 20-point optimizing run, 79 lift coefficients had to be calculated which took about 7 hours of tunnel time. Intermittent instrumentation problems developed, first in the barocells, and then in the motor positioning hardware which required many restarts of the optimizer. Seven trials were eventually recorded for the 14° case which demonstrated the viability of the optimization routine. Due to persistent equipment problems, and in the interest of maximizing the utility of the remaining available tunnel occupancy time, the trials were conducted using fewer points than the 8° cases presented previously. Figure 6.16 presents the results plotted over the baseline studies and figure 6.16c plots the convergence history. In table 6.12 the convergence history is tabulated for the five runs of figure 6.16. In the first trial, the path can be seen to "ridge walk" as discussed for the 8° case, where the path zig-zags across the optimal region. Trial 2 was cut short by an equipment failure and was repeated as trial 3. It is worth noting that the path of trial 3 is nearly identical to trial 2 over the first 4 points, and then begins to move on into the optimum region. Figure 6.16b illustrates more ridge walking where the path beginning at the aft start point quickly moves directly into the maximum region and then walks back and forth over the ridge. The path of the more forward start point appears to be ridge walking slightly out of the baseline plateau

where the flow over the flap is attached. Reviewing the results of table 6.12, it is seen that none of the C_l values coincide with values for a region of fully separated flow over the flap. Reviewing figure 6.16c, the optimizer appears to quickly converge in a maximum of three steps and then move around primarily under the influence of noise. The two trials of figure 6.16b are the repeated runs of figure 6.16a.

No convergence criteria were invoked in the optimizer routine in the interest of exploring the effects of noise in the optimum region. For example, premature indication of convergence would have terminated lengthy wind tunnel runs requiring restarts. The number of steps chosen was based on the length of a practical run (7-8 hours with MKS/Scanivalve, 3 hours PSI).

With the success of this proof of concept demonstration, it now seems feasible to invoke methods which provide for automatic determination of convergence. For instance, a simple criteria can be based on successive responses. If for a given number of steps (say 5) the lift coefficient remains within a tolerance (say ±0.01), the run is stopped. If this criteria is applied to the data of table 6.11, the runs would have been stopped after 8-9 iterations. Alternately, criteria could be based on flap position (x,y).

6.6 Blind Optimization

The optimization techniques under development are intended for eventual use in cases where the airfoil behavior is not known a priori. Therefore, a "blind" optimization was performed using a previously undocumented angle-of-attack of 12° with a flow modifier. The flap was fitted

with a 1%C Gurney flap located on the bottom surface at the trailing edge as shown in figure 6.17a, and the optimizer was demonstrated using a trial of two runs. The Gurney flap effectively changes the flap camber and rigging angle. Following these runs a baseline data set was obtained as before and the results were plotted together as figure 6.17b. Both the aft and forward starting point produced a ridge walking path which moved along the maximum region. The aft path clearly passed through the global maximum and the forward path was within 2% of the maximum and still progressing in a favorable direction when the optimizer was halted. The baseline data showed a global increase in C_l with values slightly greater than the baseline case for an angle-of-attack of 14°. This trend is in keeping with recent published results where Gurney flaps were used with multi-element airfoils to increase C_l [Papadakis, 1997; Ashby, 1996].

6.7 Lift Hysteresis Based on Flap Position - Experimental Evidence

Efficient use of optimizer methods requires some knowledge of the expected response to avoid problems. Typically, for example, noise must be quantified and the extents of the design space identified. In this case, an irreversible flow phenomenon was discovered which precluded operating the optimizer using continuous flow conditions. Clues to the existence of hysteresis in the response of lift coefficient to flap movement were found early on during the first attempts at testing using continuous flow. In section 6.2, the stall study indicated that the flap stalled at a more aft overhang setting and with a larger gap when the flow was left on during flap movement

(compare figures 6.3b and 6.4b for example). This finding led to an interest in identifying the shape and extent of the lift hysteresis "surface". Initially, overhang and vertical sweeps were conducted for a 14° case with both slat riggings, using free transition. The results of these tests are shown in a three-dimensional format in figure 6.18 with the detailed swept paths from the slat A case shown in figure 6.19. The baseline values of C_l were then plotted over the hysteresis paths in figure 6.19. A flap positional movement from a condition of maximum overhang or minimum vertical distance to a condition of minimum overhang or maximum vertical distance is defined as an *outgoing* path, and the same path reversed in direction is defined as the *return* path. All sweeps were conducted by moving the flap to the first point of the outgoing path, starting the tunnel, establishing the desired flow conditions, and then traversing the flap from point to point on the outgoing path stopping at each point to sample pressures. Then, without turning off the flow, the flap was traversed along the return path, stopped at the same points to sample pressures, and finally back to the start point (as described in section 5.5.2). For the six runs of figure 6.18, it was found that all of the measured baseline lift coefficients (flow off between runs) coincided with the return paths. This trend was identified in all the subsequent runs whether forced or free transition was invoked. Perhaps the most interesting and significant result of this whole study was first discovered in the data of figure 6.19: following an outgoing path on either a fixed x or y path, it appears that C_l actually increases to a value beyond the maximum found by traditional methods using

intermittent flow conditions. Since the increase was on the order of the perceived experimental error, it was decided to try and duplicate these initial findings in later trials. It was also noted, when comparing data from the trials with respect to differences due to the slat riggings (i.e. A versus B), no significant differences were noted in the shape or extent of the hysteresis loops.

These initial results sparked an interest in a detailed study with a dense spacing of hysteresis sweeps. Roughness elements were used to force boundary layer transition in an effort to eliminate any secondary effects caused by transition. A 3D plot of the results is shown in figure 6.20 and figure 6.21 shows the available lift increment due to hysteresis. In comparing the data to the initial free transition sweeps, no real differences were noted; the shape and extent of the hysteresis loops were comparable. Figures 6.22 and 6.23 contain the details of all the sweeps conducted in figure 6.20. While a formal comparison to the baseline data, using forced transition data was not possible, the trends clearly followed those of the free transition data. Again, an outgoing sweep showed an increase in C_l beyond the value found by using intermittent methods in all the cases where an overhang sweep was performed starting in a region of attached flow on the flap. A small hysteresis loop was observed for the Y=3.067%C and Y=3.345%C trials (figure 6.22) even though the start point was contained in a region where the flap was fully stalled. Vertical sweeps showed the same characteristic shape as found in the free transition case including the elevated C_l beyond the maximum

measured in intermittent flow. The vertical sweeps which started in the region where the flap was fully stalled did not exhibit hysteresis.

A limited study was performed using an 8° angle-of-attack and the A slat rigging with free transition. The two vertical and overhang sweeps are shown in figures 6.24 and 6.25. The previous trend which showed a continued increase in C_l above the intermittent baseline value was not evident in these trials suggesting that this phenomenon is dependent on angle-of-attack. The significance of the results and some of the potential implications to experimental and computational work are discussed in section 7.3.2.

Run	Mean	Std Dev	% Difference
1	3.272	0.008	0.051
2	3.293	0.027	0.7
3	3.271	0.005	0.015
4	3.285	0.023	0.446
5	3.284	0.007	0.426
6	3.289	0.006	0.595
7	3.251	0.013	0.582
8	3.273	0.011	0.09
9	3.259	0.015	0.323
10	3.267	0.008	0.103
11	3.276	0.011	0.194
12	3.254	0.009	0.478
13	3.288	0.007	0.546
14	3.275	0.004	0.155
15	3.282	0.01	0.358
16	3.254	0.006	0.489
17	3.25	0.016	0.613
18	3.285	0.01	0.454
19	3.256	0.003	0.432
20	3.272	0.015	0.066
21	3.262	0.016	0.258
22	3.309	0.007	1.188
23	3.277	0.007	0.22
24	3.266	0.016	0.111
25	3.26	0.024	0.291
26	3.274	0.013	0.125
27	3.234	0.034	1.111
28	3.259	0.01	0.335
29	3.297	0.016	0.84
30	3.289	0.005	0.587
average:	3.272	0.012	0.406
std dev:	0.016	0.007	0.294

Table 6.1 Variable-Size Simplex Simulation Run Summary, A-O-A = 14°, Gamma = 0.5, Start: x = 14.95, y = 0.35, Slat A

Run	Mean	Std Dev	% Difference
1	3.244	0.018	0.802
2	3.278	0.007	0.247
3	3.241	0.003	0.898
4	3.197	0.002	2.233
5	3.306	0.015	1.108
6	3.223	0.012	1.443
7	3.272	0.012	0.056
8	3.287	0.018	0.509
9	3.292	0.013	0.668
10	3.242	0.009	0.842
11	3.266	0.012	0.132
12	3.284	0.018	0.432
13	3.298	0.004	0.354
14	3.222	0.006	1.453
15	3.298	0.014	0.743
16	3.278	0.011	0.257
17	3.283	0.001	0.412
18	3.244	0.003	0.63
19	3.308	0.004	1.152
20	3.296	0.004	0.758
21	3.289	0.019	0.59
22	3.245	0.005	0.763
23	3.274	0.014	0.12
24	3.275	0.014	0.14
25	3.216	0.028	1.647
26	3.233	0.002	1.117
27	3.294	0.002	0.721
28	3.275	0.009	0.143
29	3.268	0.004	0.076
30	3.28	0.021	0.313
average:	3.267	0.010	0.692
std dev:	0.029	0.007	0.524

Table 6.2 Variable-Size Simplex Simulation Run Summary, A-O-A = 14°, Gamma = 0.5, Start: x = 14.55, y = 0.35, Slat A

Run	Mean	Std Dev	% Difference
1	2.761	0.006	0.156
2	2.759	0.007	0.063
3	2.775	0.003	0.658
4	2.768	0.008	0.39
5	2.756	0.008	0.025
6	2.763	0.003	0.219
7	2.753	0.007	0.139
8	2.774	0.005	0.61
9	2.749	0.012	0.306
10	2.766	0.008	0.311
11	2.738	0.002	0.675
12	2.769	0.007	0.431
13	2.777	0.016	0.742
14	2.772	0.004	0.534
15	2.753	0.008	0.128
16	2.748	0.022	0.318
17	2.765	0.012	0.292
18	2.744	0.007	0.455
19	2.782	0.011	0.91
20	2.763	0.012	0.222
21	2.77	0.005	0.461
22	2.747	0.009	0.351
23	2.755	0.019	0.071
24	2.774	0.019	0.616
25	2.734	0.013	0.832
26	2.767	0.009	0.371
27	2.769	0.008	0.418
28	2.77	0.005	0.459
29	2.773	0.004	0.569
30	2.767	0.012	0.357
average:	2.762	0.009	0.403
std dev:	0.012	0.005	0.229

Table 6.3 Variable-Size Simplex Simulation Run Summary, A-O-A = 8°, Gamma = 0.3, Start: x = 14.55, y = 0.35, Slat B

Run	Mean	Std Dev	% Difference
1	2.761	0.006	0.156
2	2.759	0.007	0.063
3	2.775	0.003	0.658
4	2.768	0.008	0.39
5	2.756	0.008	0.025
6	2.763	0.003	0.219
7	2.753	0.007	0.139
8	2.774	0.005	0.61
9	2.749	0.012	0.306
10	2.766	0.008	0.311
11	2.738	0.002	0.675
12	2.769	0.007	0.431
13	2.777	0.016	0.742
14	2.772	0.004	0.534
15	2.753	0.008	0.128
16	2.748	0.022	0.318
17	2.765	0.012	0.292
18	2.744	0.007	0.455
19	2.782	0.011	0.91
20	2.763	0.012	0.222
21	2.77	0.005	0.461
22	2.747	0.009	0.351
23	2.755	0.019	0.071
24	2.774	0.019	0.616
25	2.734	0.013	0.832
26	2.767	0.009	0.371
27	2.769	0.008	0.418
28	2.77	0.005	0.459
29	2.773	0.004	0.569
30	2.767	0.012	0.357
average:	2.762	0.009	0.403
std dev:	0.012	0.005	0.229

Table 6.4 Variable-Size Simplex Simulation Run Summary, A-O-A = 8°, Gamma = 0.3, Start: x = 14.85, y = 0.35, Slat B

Run	Mean	Std Dev	% Difference
1	3.203	0.02	2.035
2	3.283	0.012	0.388
3	3.213	0.006	1.745
4	3.278	0.007	0.234
5	3.204	0.007	2.023
6	3.192	0.007	2.372
7	3.283	0.002	0.382
8	3.292	0.008	0.666
9	3.251	0.023	0.588
10	failed		
11	3.196	0.007	2.272
12	3.291	0.007	0.643
13	3.209	0.016	1.852
14	3.204	0.005	2.023
15	3.286	0.007	0.482
16	3.199	0.01	2.163
17	3.302	0.02	0.991
18	3.209	0.008	1.864
19	3.269	0.016	0.031
20	3.278	0.008	2.38
21	3.277	0.007	0.215
22	3.27	0.009	0.01
23	3.254	0.014	0.478
24	failed		
25	3.252	0.005	0.552
26	3.268	0.005	0.054
27	3.221	0.011	1.487
28	3.207	0.003	1.941
29	3.279	0.001	0.286
30	3.204	0.011	2.004

Table 6.5 Variable-Size Simplex Simulation Run Summary, A-O-A = 14°, Gamma = 0.3, Start: x = 14.55, y = 0.35, Slat A

Run	Cl centroid	% Diff of Cl centroid	Last tri Mean	Last tri Std Dev	% Diff of Mean
1	3.268	0.053	3.226	0.029	1.349
2	3.265	0.15	3.242	0.027	0.848
3	3.291	0.632	3.239	0.018	0.953
4	3.276	0.199	3.24	0.024	0.915
5	3.273	0.105	3.214	0.022	1.727
6	3.248	0.687	3.248	0.042	0.664
7	3.236	1.04	3.224	0.022	1.411
8	3.265	0.145	3.204	0.04	2.027
9	3.28	0.294	3.2	0.024	2.133
10	3.253	0.507	3.23	0.031	1.236
11	3.292	0.681	3.241	0.029	0.873
12	3.291	0.639	3.23	0.027	1.17
13	3.267	0.105	3.22	0.039	1.481
14	3.266	0.127	3.244	0.021	0.8
15	3.274	0.121	3.196	0.03	2.27
16	3.266	0.109	3.24	0.032	0.903
17	3.271	0.036	3.205	0.044	1.978
18	3.29	0.6	3.246	0.019	0.745
19	3.293	0.692	3.255	0.026	0.451
20	3.27	0.011	3.257	0.01	0.391
21	3.283	0.408	3.231	0.006	1.184
22	3.241	0.888	3.207	0.032	1.918
23	3.298	0.853	3.227	0.016	1.317
24	3.278	0.239	3.208	0.04	1.901
25	3.259	0.344	3.219	0.04	1.554
26	3.26	0.304	3.238	0.02	0.979
27	3.275	0.15	3.229	0.01	1.243
28	3.255	0.459	3.225	0.017	1.375
29	3.266	0.124	3.241	0.022	0.894
30	3.274	0.113	3.217	0.052	1.607
average:	3.271	0.361	3.228	0.027	1.277
std dev:	0.015	0.292	0.016	0.011	0.504

Table 6.6 Steepest Ascent Simulation Run Summary, A-O-A = 14°, Start: x = 14.85, y = 0.35, Slat A

Run	CI centroid	% Diff of CI centroid	Last tri Mean	Last tri Std Dev	% Diff of Mean
1	3.261	0.264	3.225	0.031	1.388
2	3.261	0.277	3.217	0.025	1.609
3	3.239	0.956	3.235	0.038	1.071
4	3.262	0.275	3.203	0.062	2.041
5	3.269	0.027	3.181	0.046	2.721
6	3.246	0.737	3.205	0.056	1.995
7	3.238	0.972	3.193	0.042	2.3848
8	3.251	0.586	3.217	0.031	1.61
9	3.245	0.761	3.233	0.037	1.145
10	3.24	0.919	3.222	0.031	1.458
11	3.261	0.263	3.242	0.024	0.865
12	3.22	1.514	3.2	0.044	2.153
13	3.248	0.683	3.226	0.023	1.331
14	3.267	0.081	3.221	0.007	1.512
15	3.249	0.657	3.211	0.029	1.812
16	3.279	0.271	3.222	0.027	1.482
17	3.24	0.907	3.21	0.047	1.83
18	3.22	1.541	3.151	0.087	3.645
19	3.298	0.846	3.222	0.01	1.475
20	3.278	0.256	3.254	0.023	0.491
21	3.282	0.368	3.214	0.023	1.715
22	3.247	0.693	3.246	0.043	0.73
23	3.226	1.33	3.216	0.047	1.65
24	3.296	0.79	3.24	0.035	0.916
25	3.274	0.112	3.185	0.075	2.613
26	3.251	0.589	3.203	0.032	2.053
27	3.27	0.01	3.258	0.017	0.373
28	3.225	1.382	3.208	0.033	1.903
29	3.245	0.77	3.227	0.041	1.316
30	3.254	0.477	3.23	0.045	1.225
average:	3.255	0.644	3.217	0.037	1.617
std dev:	0.020	0.430	0.022	0.017	0.683

Table 6.7 Steepest Ascent Simulation Run Summary,
A-O-A = 14°, Start: x = 14.55, y = 0.35, Slat A

Run	Cl centroid	% Diff of Cl centroid	Last tri Mean	Last tri Std Dev	% Diff of Mean
1	2.754	0.032	2.74	0.008	0.531
2	2.72	1.267	2.734	0.028	0.757
3	2.724	1.118	2.735	0.013	0.729
4	2.787	1.152	2.735	0.014	0.711
5	2.715	1.462	2.738	0.013	0.617
6	2.734	0.765	2.717	0.014	1.388
7	2.762	0.244	2.742	0.023	0.461
8	2.72	1.258	2.74	0.015	0.536
9	2.742	0.479	2.75	0.009	0.165
10	2.729	0.947	2.738	0.006	0.607
11	2.773	0.668	2.738	0.009	0.63
12	2.737	0.65	2.733	0.02	0.794
13	2.735	0.718	2.74	0.012	0.53
14	2.766	0.402	2.744	0.021	0.407
15	2.754	0.051	2.7738	0.033	0.614
16	2.76	0.194	2.74	0.011	0.531
17	2.736	0.695	2.742	0.015	0.476
18	2.739	0.572	2.74	0.008	0.558
19	2.734	0.765	2.743	0.003	0.442
20	2.756	0.048	2.761	0.013	0.229
21	2.751	0.132	2.736	0.019	0.707
22	2.73	0.901	2.764	0.02	0.325
23	2.739	0.57	2.76	0.013	0.172
24	2.754	0.036	2.745	0.009	0.365
25	2.753	0.09	2.746	0.023	0.36
26	2.743	0.432	2.756	0.014	0.046
27	2.726	1.041	2.737	0.008	0.658
28	2.723	1.146	2.734	0.017	0.767
29	2.722	1.181	2.74	0.01	0.526
30	2.728	0.998	2.711	0.037	1.581
average:	2.742	0.667	2.742	0.015	0.574
std dev:	0.018	0.433	0.012	0.008	0.312

Table 6.8 Steepest Ascent Simulation Run Summary,
A-O-A = 8°, Start: x = 14.55, y = 0.35, Slat B

Run	CI centroid	% Diff of CI centroid	Last tri Mean	Last tri Std Dev	% Diff of Mean
1	2.738	0.608	2.738	0.007	0.634
2	2.734	0.752	2.74	0.006	0.541
3	2.75	0.176	2.744	0.017	0.401
4	2.737	0.653	2.726	0.009	1.039
5	2.775	0.722	2.746	0.003	0.34
6	2.752	0.124	2.742	0.021	0.476
7	2.741	0.519	2.737	0.018	0.656
8	2.701	1.944	2.733	0.015	0.79
9	2.77	0.552	0.016	0.016	0.076
10	2.772	0.623	2.76	0.008	0.172
11	2.753	0.071	2.744	0.004	0.386
12	2.785	1.095	2.736	0.019	0.674
13	2.737	0.655	2.732	0.012	0.821
14	2.714	1.482	2.755	0.009	0.348
15	2.748	0.253	2.746	0.014	0.32
16	2.729	0.939	2.74	0.006	0.54
17	2.728	0.979	2.741	0.028	0.514
18	2.752	0.124	2.735	0.018	0.732
19	2.741	0.494	2.748	0.008	0.241
20	2.767	0.444	2.744	0.021	0.417
21	2.74	0.551	2.763	0.01	0.287
22	2.728	0.978	2.737	0.003	0.661
23	2.724	1.127	2.745	0.015	0.377
24	2.767	0.421	2.738	0.006	0.626
25	2.756	0.041	2.735	0.014	0.72
26	2.762	0.24	2.739	0.011	0.563
27	2.738	0.61	2.732	0.003	0.832
28	2.749	0.23	2.738	0.025	0.619
29	2.735	0.733	2.724	0.022	1.123
30	2.701	1.966	2.725	0.023	1.071
average:	2.744	0.670	2.649	0.013	0.567
std dev:	0.020	0.491	0.497	0.007	0.258

Table 6.9 Steepest Ascent Simulation Run Summary,
A-O-A = 8°, Start: x = 14.85, y = 0.35, Slat B

	alpha = 14 x= 14.85 y= .35	alpha = 14 x= 14.55 y= .35	alpha = 8 x= 14.85 y= .35	alpha = 8 x= 14.55 y= .35
Steepest Ascent Ave % diff of centroid CI	0.361	0.644	0.67	0.667
Steepest Ascent Ave std dev of centroid CI	0.015	0.02	0.02	0.018
Sequential Simplex Ave % diff of mean	0.406	0.692	0.598	0.403
Sequential Simplex Ave std dev of mean CI	0.016	0.029	0.009	0.012

Table 6.10 Comparison of Simulation Results:
Variable-Size Sequential Simplex versus Steepest Ascent

Run 1					
N	x (in)	y (in)	CI	OH (%C)	Vert (%C)
0	14.550	0.250	2.55	2.245	3.345
1	14.498	0.297	2.61	2.532	3.083
2	14.509	0.333	2.70	2.474	2.883
3	14.525	0.365	2.74	2.387	2.706
4	14.537	0.389	2.76	2.317	2.572
5	14.555	0.403	2.78	2.215	2.493
6	14.560	0.420	2.78	2.189	2.399
7	14.565	0.438	2.79	2.161	2.302
8	14.580	0.426	2.77	2.078	2.366
9	14.588	0.444	2.79	2.032	2.268
10	14.589	0.425	2.80	2.029	2.374
11	14.585	0.423	2.81	2.052	2.384
12	14.579	0.434	2.79	2.086	2.325
13	14.593	0.428	2.79	2.007	2.359
14	14.599	0.414	2.78	1.972	2.433
15	14.610	0.425	2.80	1.914	2.376
16	14.625	0.420	2.79	1.828	2.403
17	14.617	0.423	2.81	1.872	2.384
18	14.631	0.415	2.80	1.793	2.427
19	14.651	0.419	2.81	1.686	2.406

Run 2					
N	x (in)	y (in)	CI	OH (%C)	Vert (%C)
0	14.950	0.350	2.06	0.023	2.789
1	14.892	0.390	2.72	0.343	2.569
2	14.873	0.406	2.76	0.448	2.480
3	14.863	0.415	2.77	0.506	2.427
4	14.849	0.425	2.81	0.586	2.374
5	14.839	0.431	2.80	0.642	2.341
6	14.834	0.424	2.78	0.668	2.378
7	14.824	0.427	2.80	0.721	2.359
8	14.815	0.421	2.79	0.773	2.395
9	14.807	0.432	2.80	0.820	2.337
10	14.815	0.432	2.78	0.771	2.334
11	14.804	0.435	2.81	0.832	2.316
12	14.788	0.436	2.80	0.921	2.313
13	14.771	0.441	2.79	1.015	2.282
14	14.758	0.440	2.81	1.088	2.292
15	14.744	0.429	2.80	1.169	2.349
16	14.738	0.442	2.82	1.200	2.279
17	14.727	0.436	2.81	1.261	2.311
18	14.717	0.427	2.83	1.319	2.364
19	14.713	0.417	2.81	1.341	2.419

Run 3					
N	x (in)	y (in)	CI	OH (%C)	Vert (%C)
0	14.850	0.250	2.08	0.578	3.345
1	14.820	0.313	2.72	0.747	2.994
2	14.809	0.392	2.75	0.809	2.554
3	14.806	0.413	2.79	0.821	2.439
4	14.799	0.428	2.80	0.862	2.356
5	14.784	0.441	2.80	0.944	2.282
6	14.774	0.443	2.82	0.998	2.272
7	14.780	0.434	2.80	0.966	2.326
8	14.767	0.435	2.82	1.038	2.318
9	14.776	0.446	2.82	0.992	2.256
10	14.759	0.449	2.80	1.086	2.242
11	14.754	0.436	2.81	1.112	2.314
12	14.753	0.431	2.80	1.119	2.338
13	14.753	0.426	2.80	1.118	2.365
14	14.738	0.432	2.83	1.203	2.334
15	14.730	0.442	2.81	1.246	2.281
16	14.723	0.440	2.81	1.283	2.289
17	14.709	0.439	2.79	1.364	2.297
18	14.712	0.449	2.79	1.344	2.242
19	14.712	0.440	2.81	1.346	2.292

Table 6.11 Convergence History from Optimizer Paths of Figure 6.15a

Convergence History from Optimizer Paths of Figure 6.16a

Run 1

N	x (in)	y (in)	Cl	OH (%C)	Vert (%C)
0	14.800	0.350	2.59	0.856	2.789
1	14.797	0.450	3.29	0.872	2.234
2	14.758	0.473	3.23	1.092	2.105
3	14.770	0.461	3.28	1.024	2.174
4	14.776	0.456	3.28	0.991	2.198
5	14.784	0.447	3.30	0.945	2.251
6	14.743	0.471	3.28	1.171	2.120
7	14.753	0.464	3.31	1.115	2.155

Run 2

N	x (in)	y (in)	Cl	OH (%C)	Vert (%C)
0	14.950	0.450	2.55	0.023	2.234
1	14.910	0.480	2.68	0.244	2.066
2	14.904	0.530	3.32	0.279	1.791
3	14.908	0.517	3.32	0.256	1.863

Run 3

N	x (in)	y (in)	Cl	OH (%C)	Vert (%C)
0	14.950	0.450	2.56	0.023	2.234
1	14.914	0.485	2.68	0.223	2.041
2	14.910	0.524	3.35	0.247	1.821
3	14.895	0.531	3.32	0.327	1.787
4	14.900	0.521	3.32	0.298	1.842
5	14.909	0.520	3.32	0.248	1.845
6	14.897	0.523	3.34	0.318	1.828

Convergence History from Optimizer Paths of Figure 6.16b

Run 1

N	x (in)	y (in)	Cl	OH (%C)	Vert (%C)
0	14.800	0.350	2.66	0.856	2.789
1	14.782	0.396	2.77	0.959	2.532
2	14.778	0.446	3.41	0.978	2.254
3	14.790	0.434	3.39	0.909	2.322
4	14.749	0.458	3.36	1.142	2.191
5	14.761	0.453	3.35	1.074	2.219
6	14.766	0.439	3.38	1.047	2.295
7	14.752	0.443	3.35	1.123	2.274
8	14.752	0.431	3.38	1.122	2.342

Run 2

N	x (in)	y (in)	Cl	OH (%C)	Vert (%C)
0	14.950	0.450	2.62	0.023	2.234
1	14.927	0.494	3.37	0.151	1.987
2	14.883	0.518	3.37	0.395	1.856
3	14.891	0.511	3.38	0.349	1.896
4	14.895	0.502	3.37	0.328	1.943
5	14.896	0.491	3.39	0.322	2.007
6	14.855	0.514	3.38	0.549	1.877
7	14.863	0.506	3.37	0.508	1.924
8	14.872	0.504	3.38	0.454	1.933

Table 6.12 Convergence History from Optimizer Paths of Figure 6.16

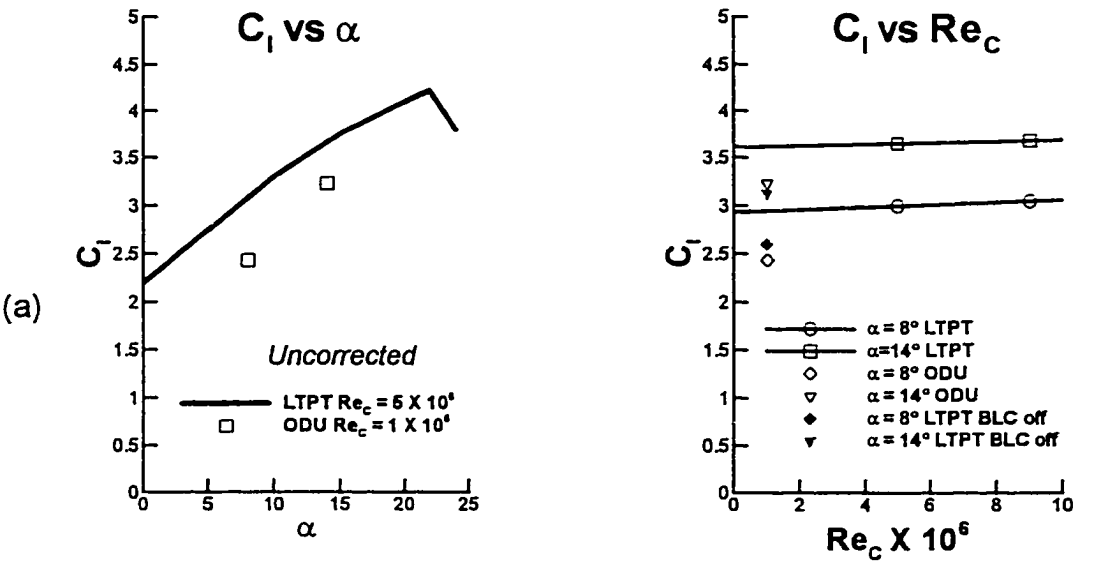

Note: LTPT Data interpolated from 12° and 16° data

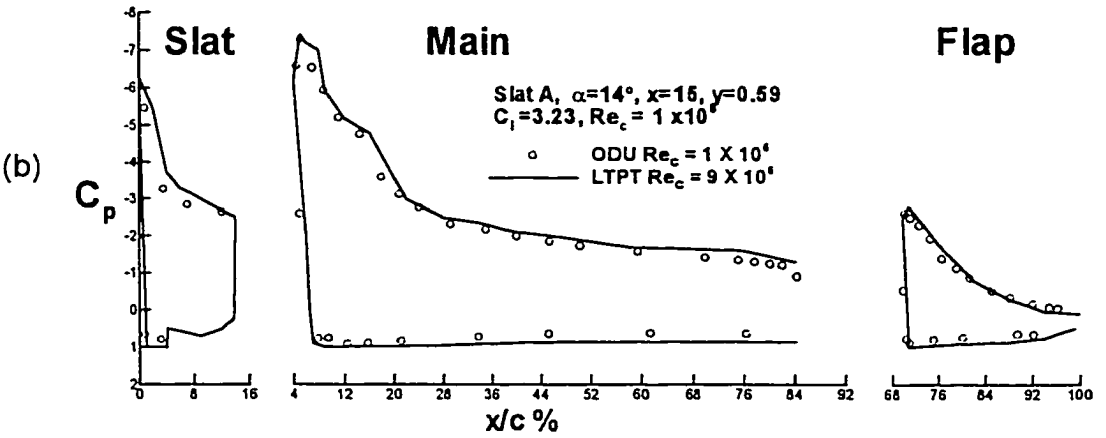

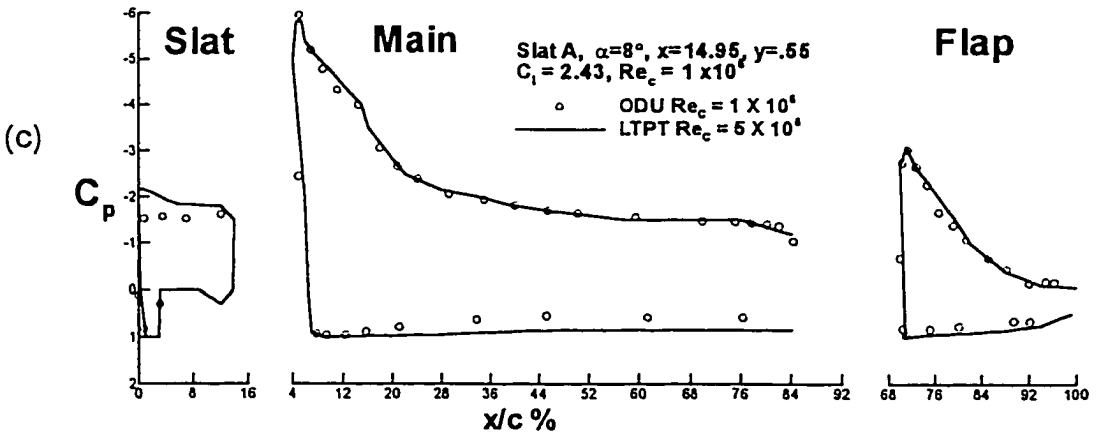

Figure 6.1 Comparisons to Reference Data

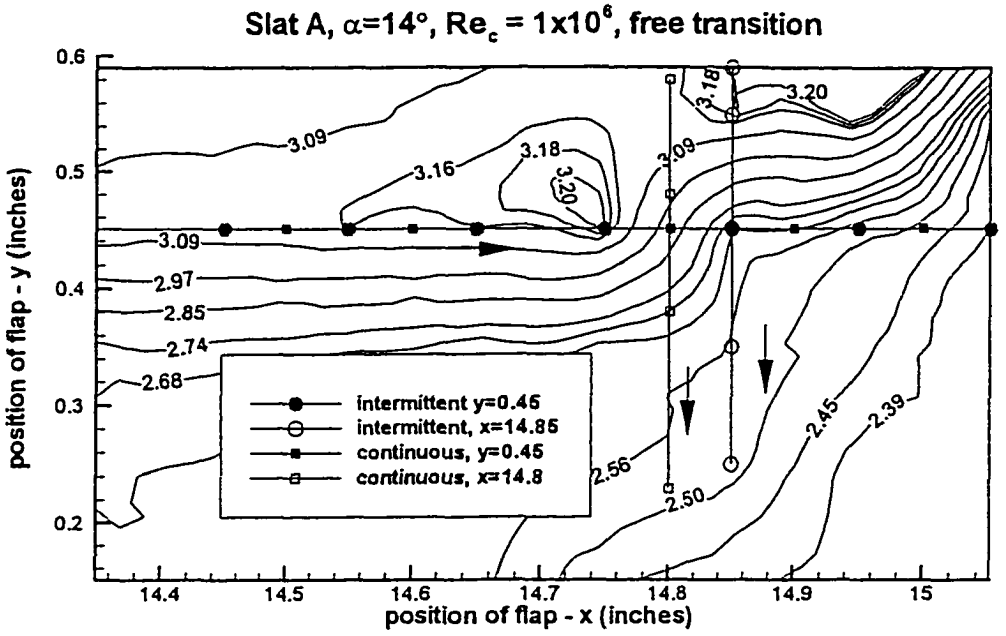

Figure 6.2a Paths Used For Stall Progression Study

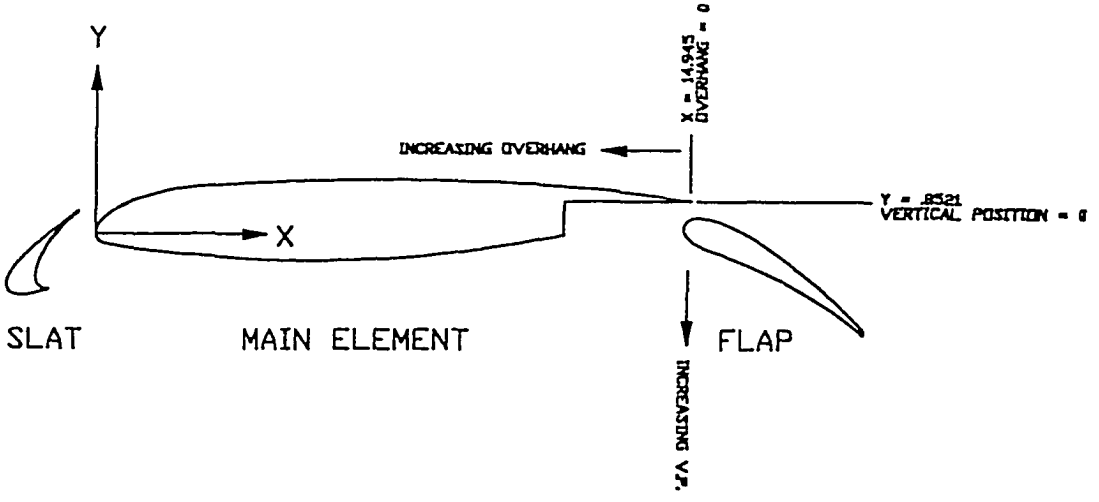

Figure 6.2b Nomenclature For Flap Position

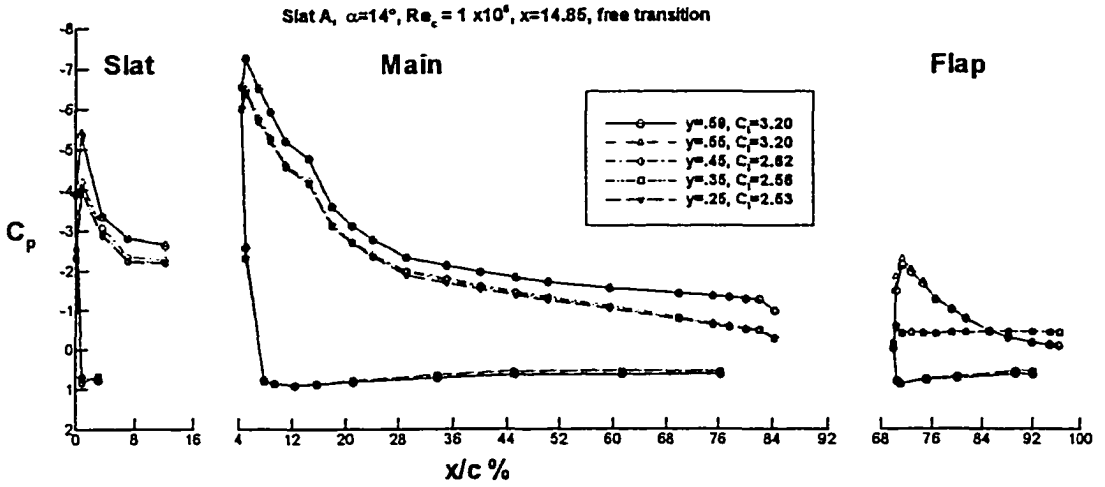

Figure 6.3a Stall Progression due to Flap Motion in the Vertical Direction - Intermittent Flow

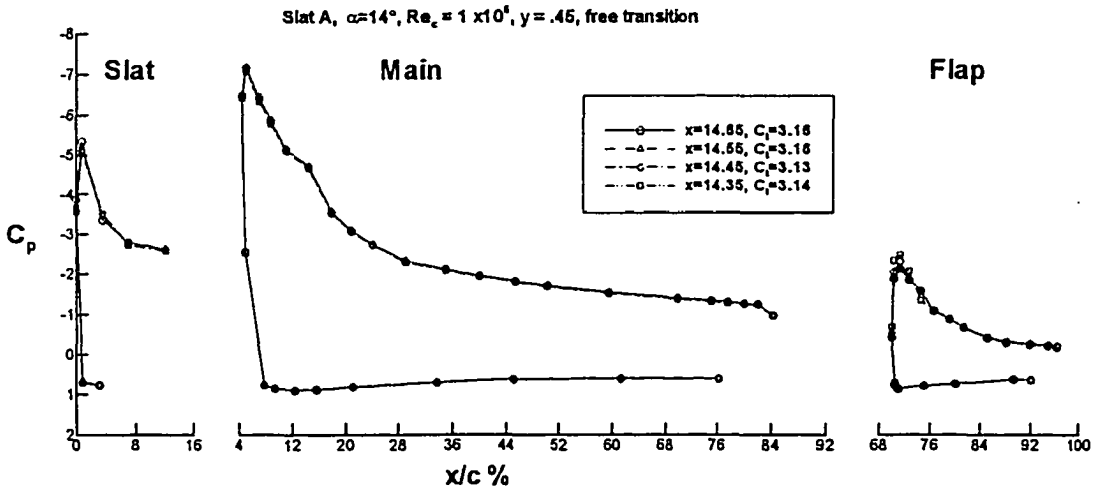

Figure 6.3b Stall Progression due to Flap Motion in the Horizontal Direction - Intermittent Flow

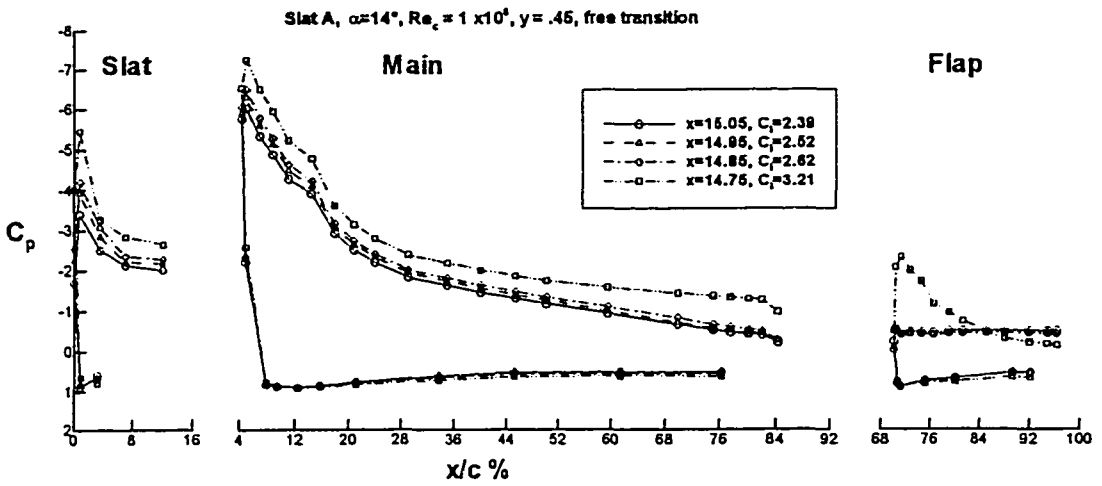

Figure 6.3b Concluded

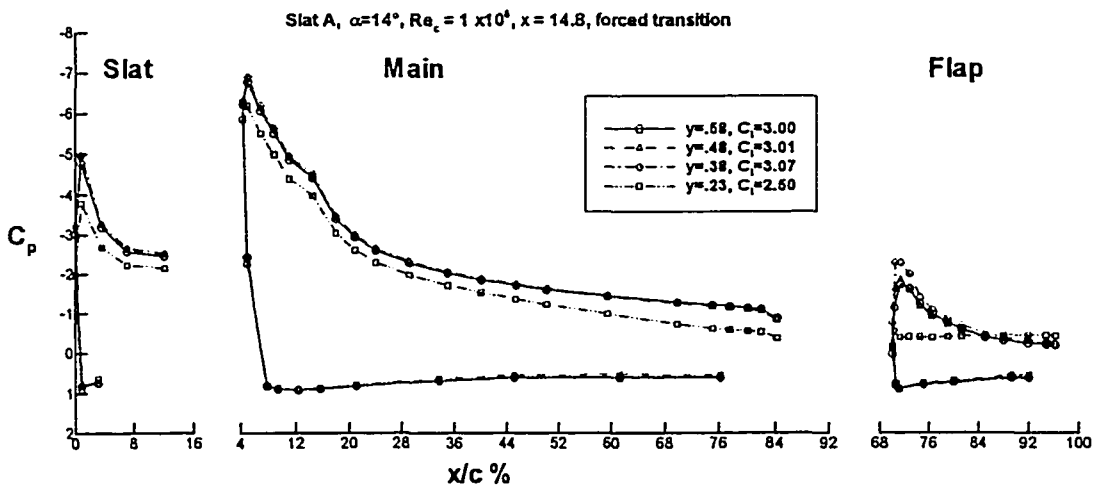

Figure 6.4a Stall Progression due to Flap Motion in the Vertical Direction - Continuous Flow

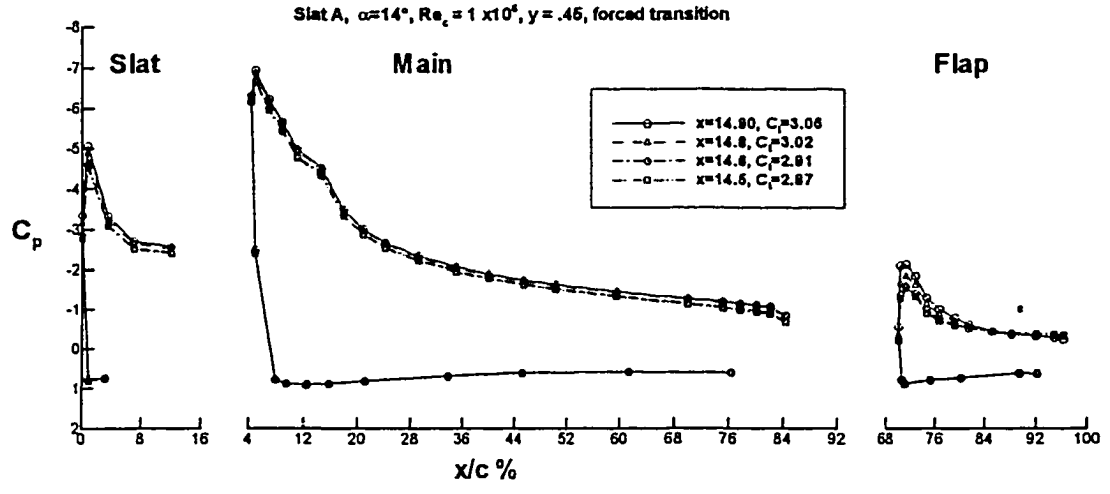

Figure 6.4b Stall Progression due to Flap Motion in the Horizontal Direction - Continuous Flow

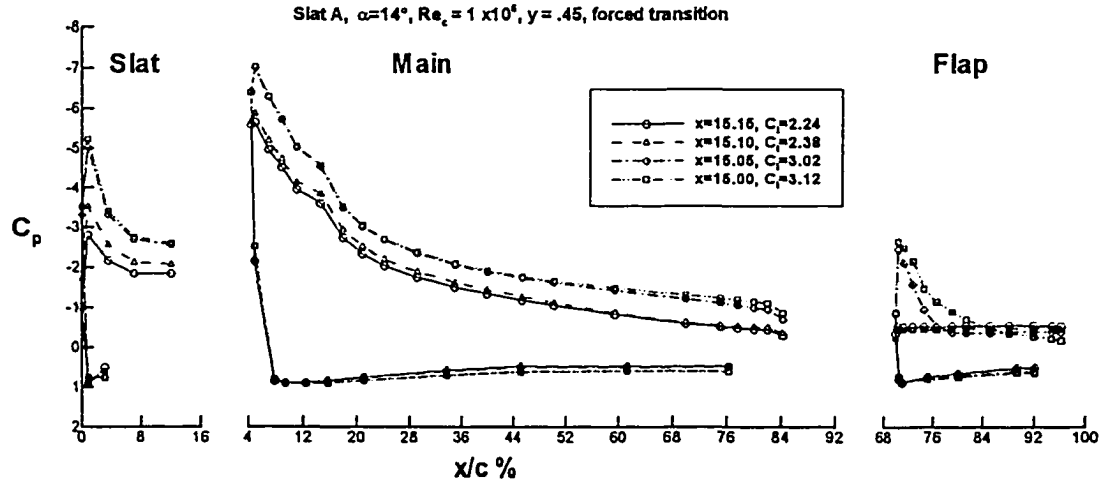

Figure 6.4b Concluded

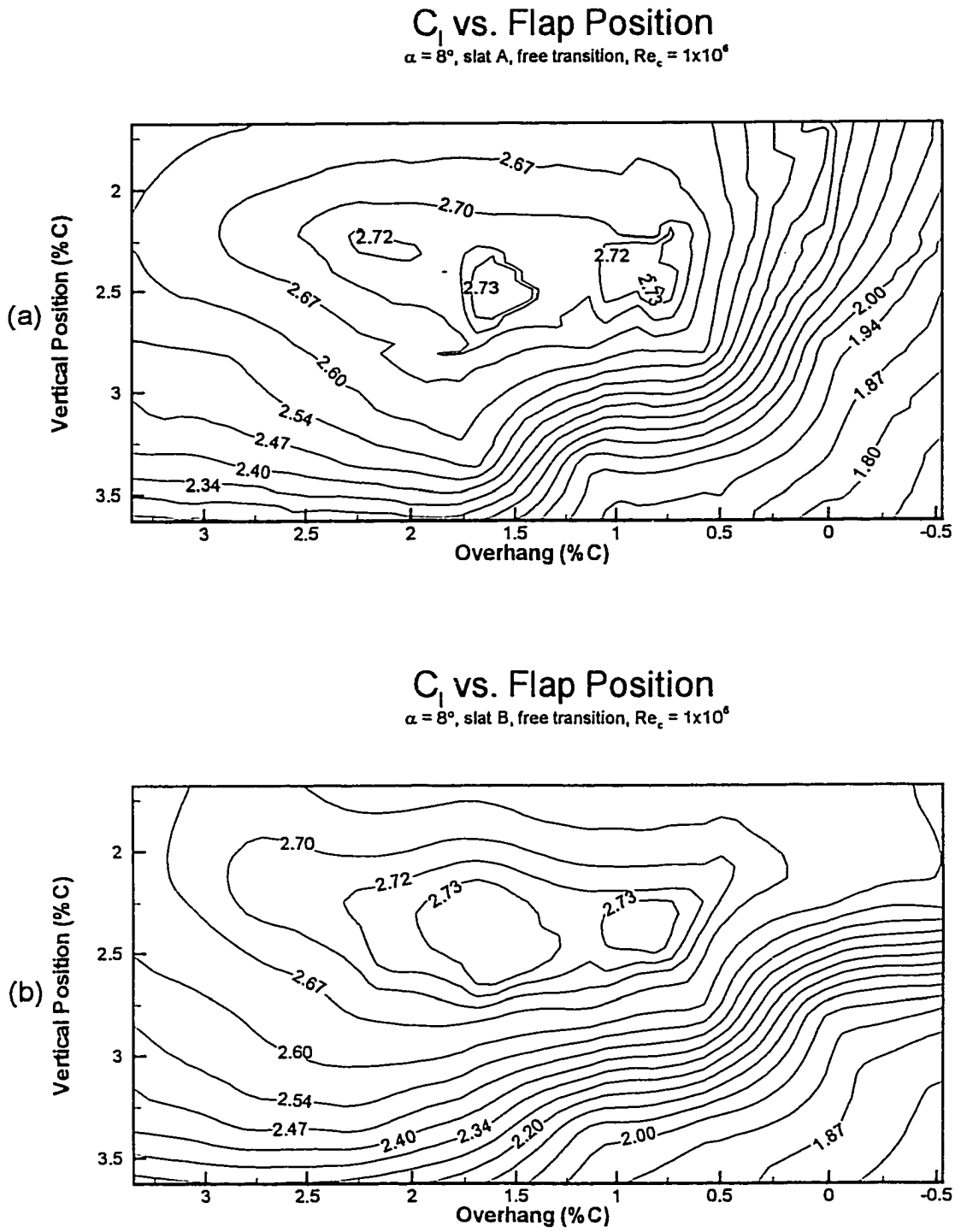

Figure 6.5 Lift Coefficient versus Flap Position, Baseline for A-O-A = 8°

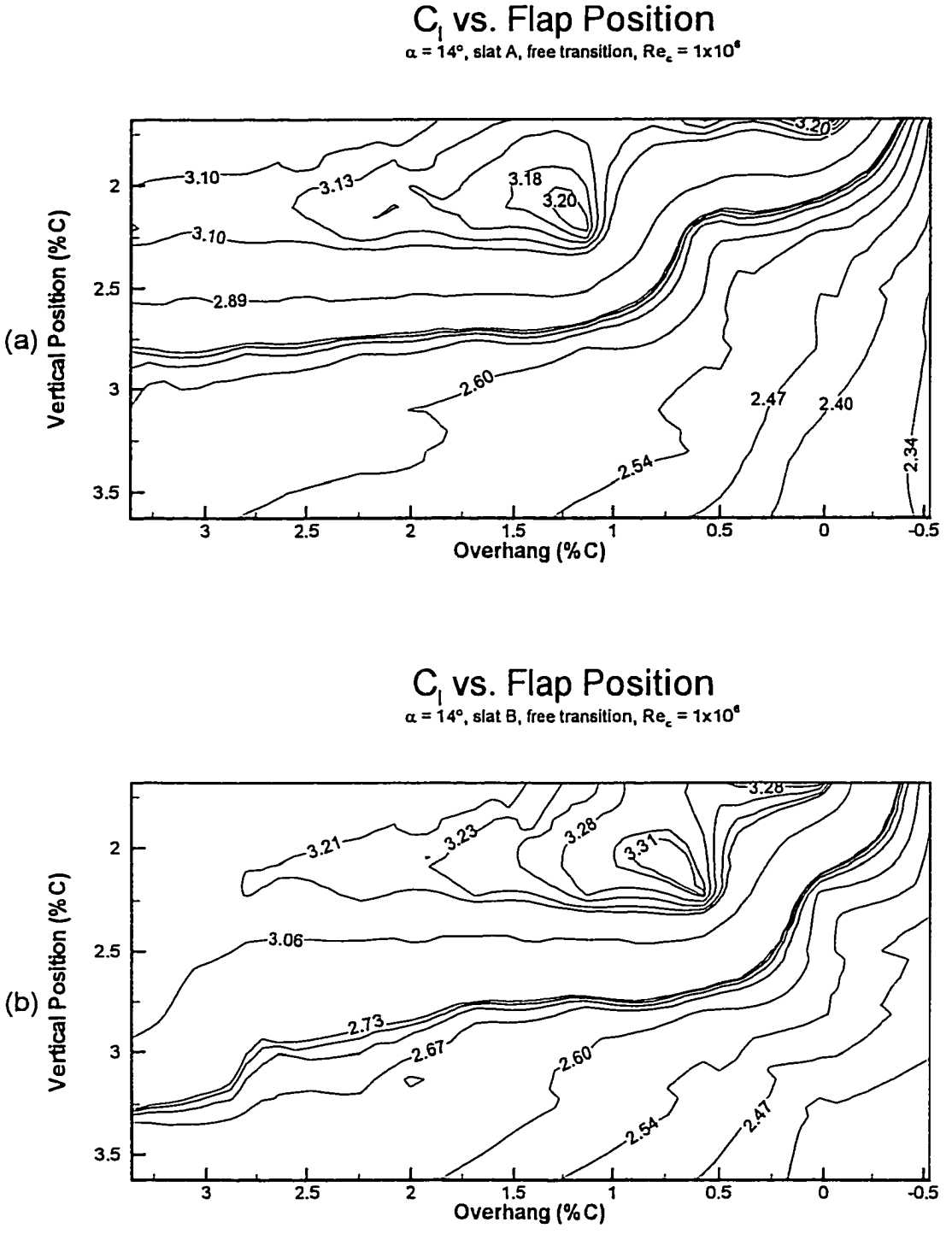

Figure 6.6 Lift Coefficient versus Flap Position, Baseline for A-O-A = 14°

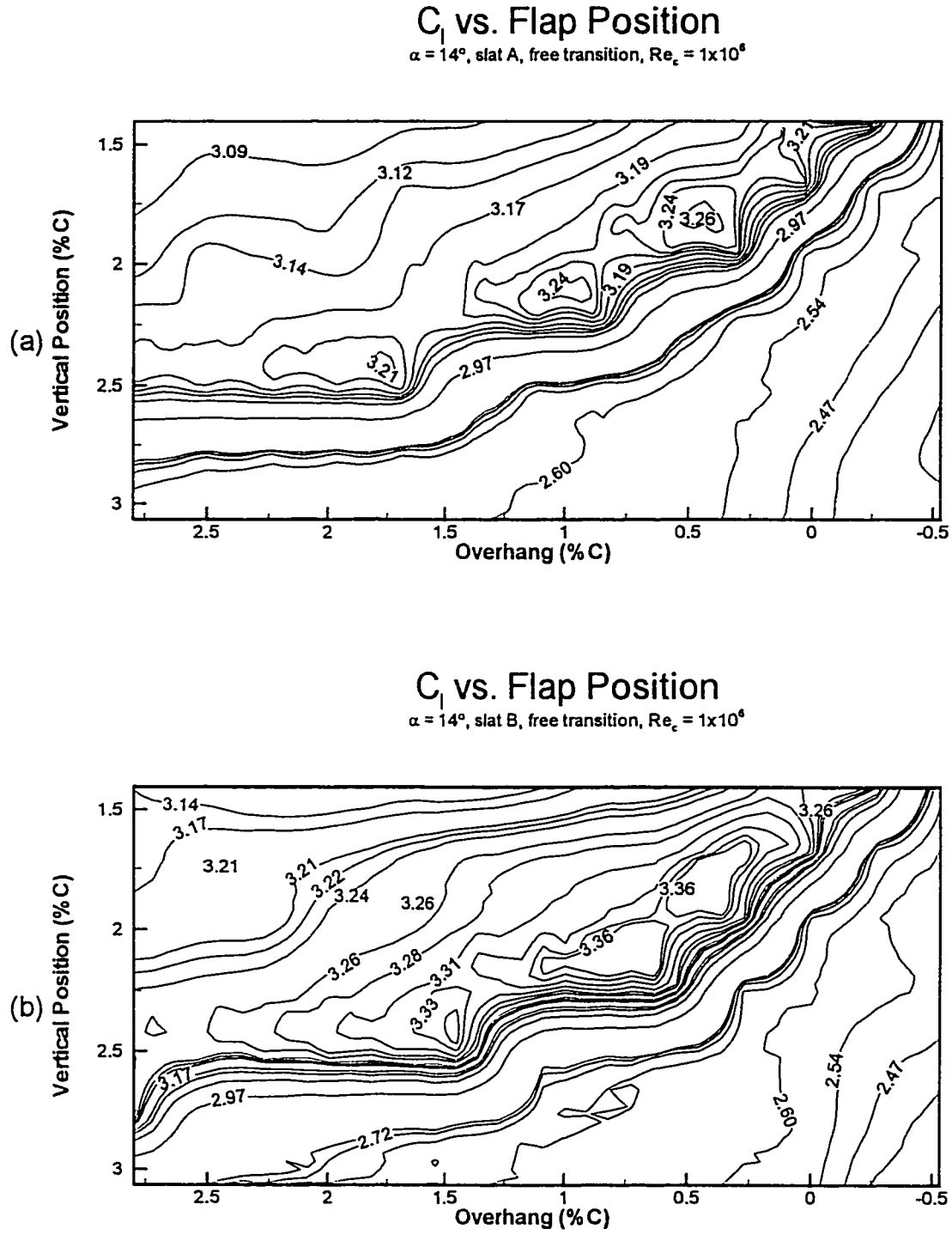

Figure 6.7 Lift Coefficient versus Flap Position, Dense Grid, Baseline for A-O-A = 14°

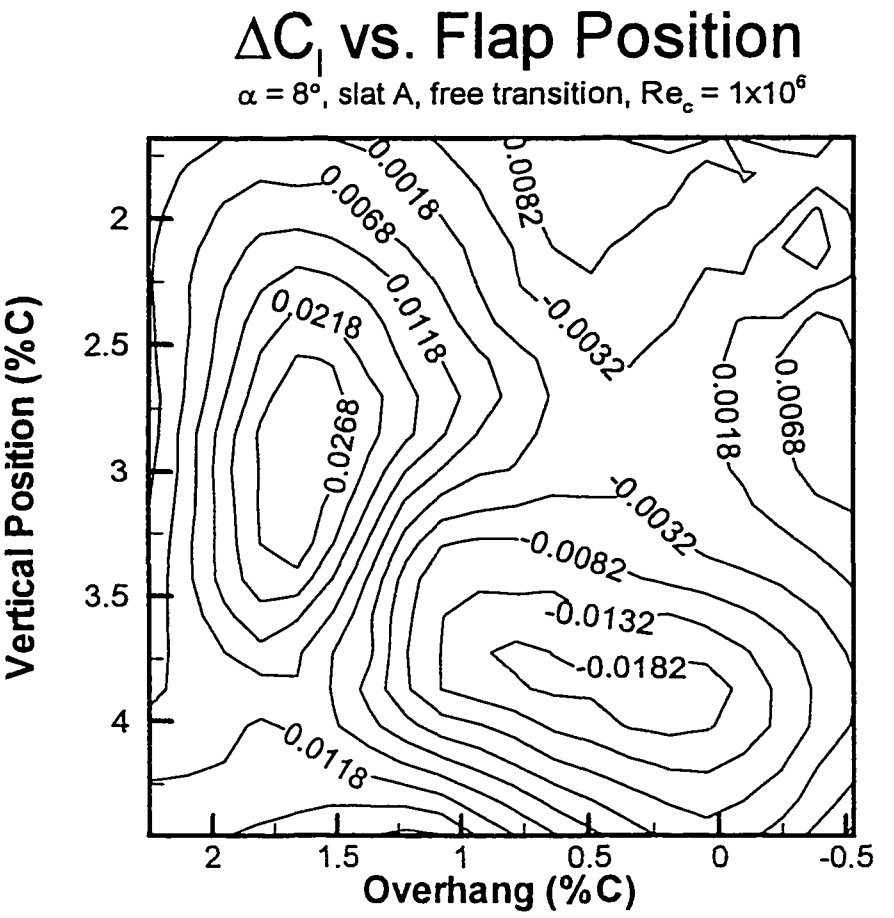

Figure 6.7c Lift Coefficient versus Flap Position, Error in Surface Fitting

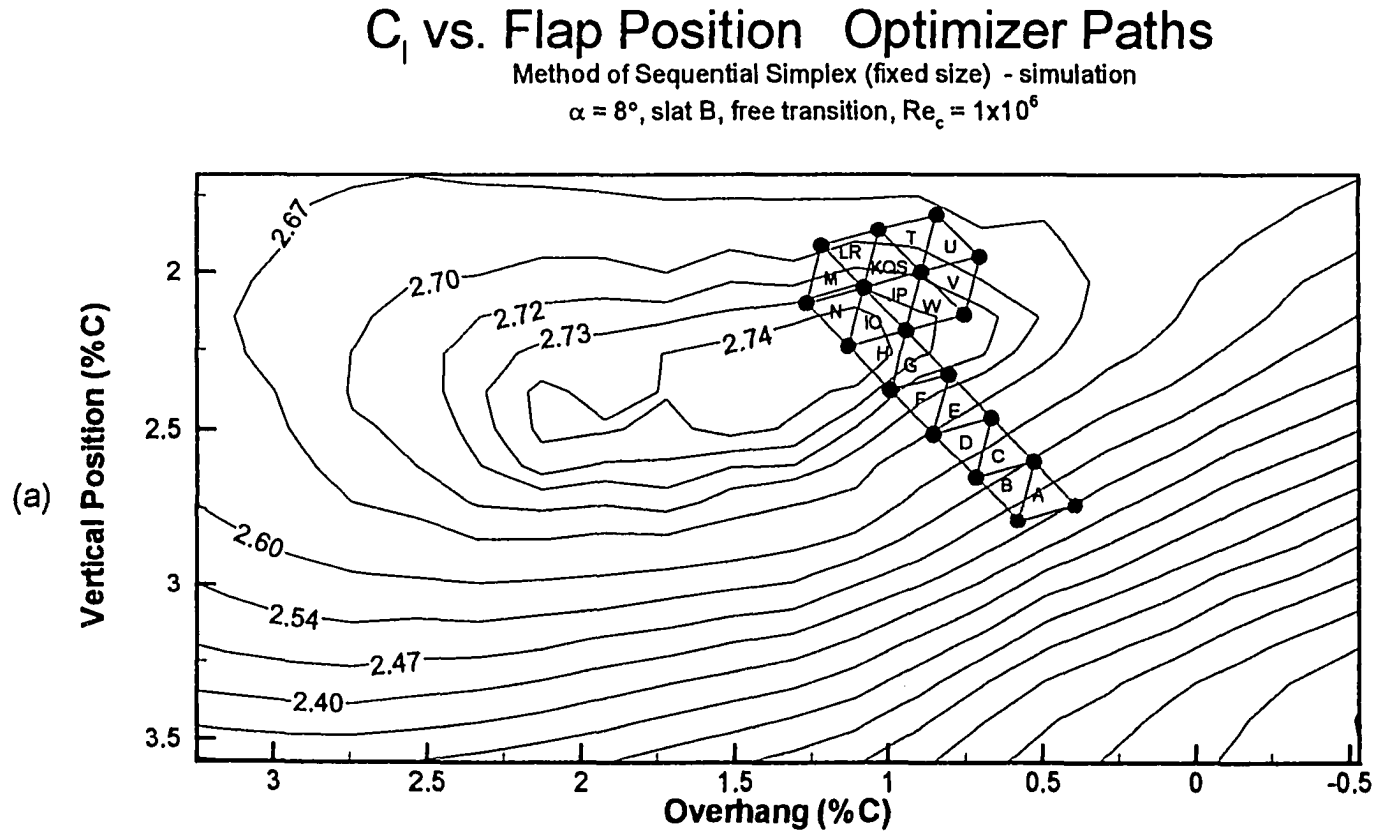

Figure 6.8 Fixed-Size Sequential Simplex Simulations, A-O-A = 8°

(b)

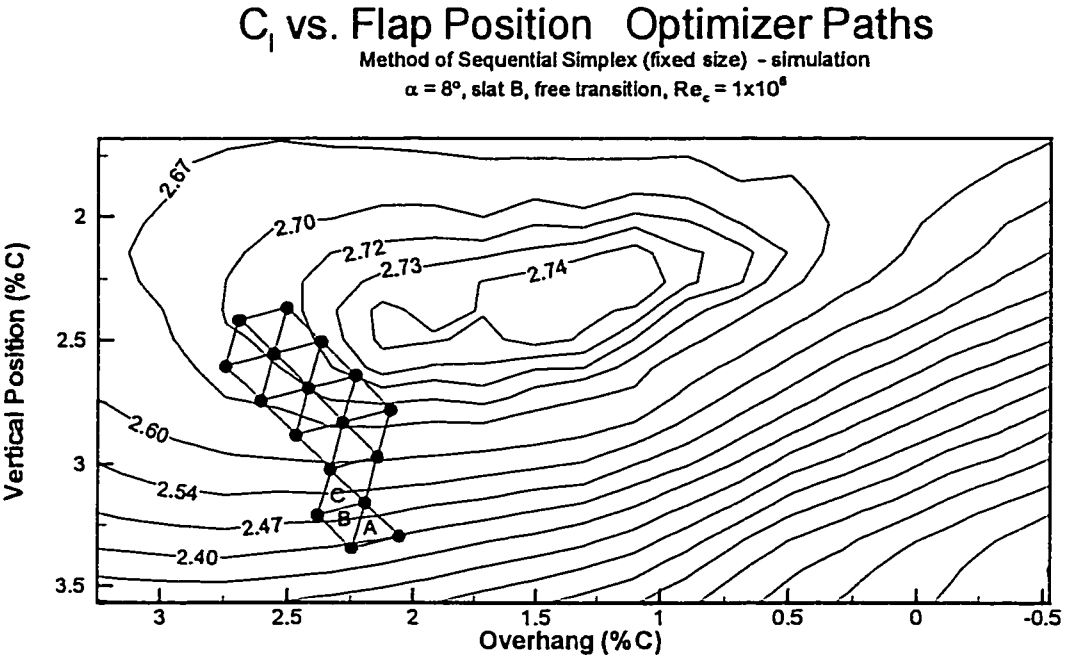

(c)

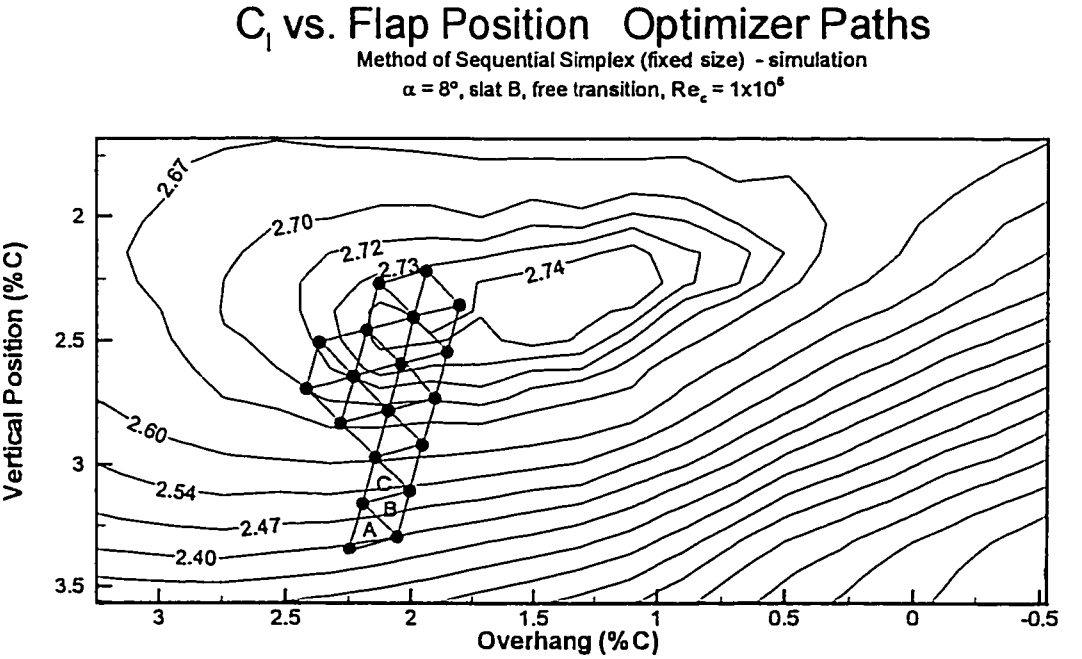

Figure 6.8 Concluded

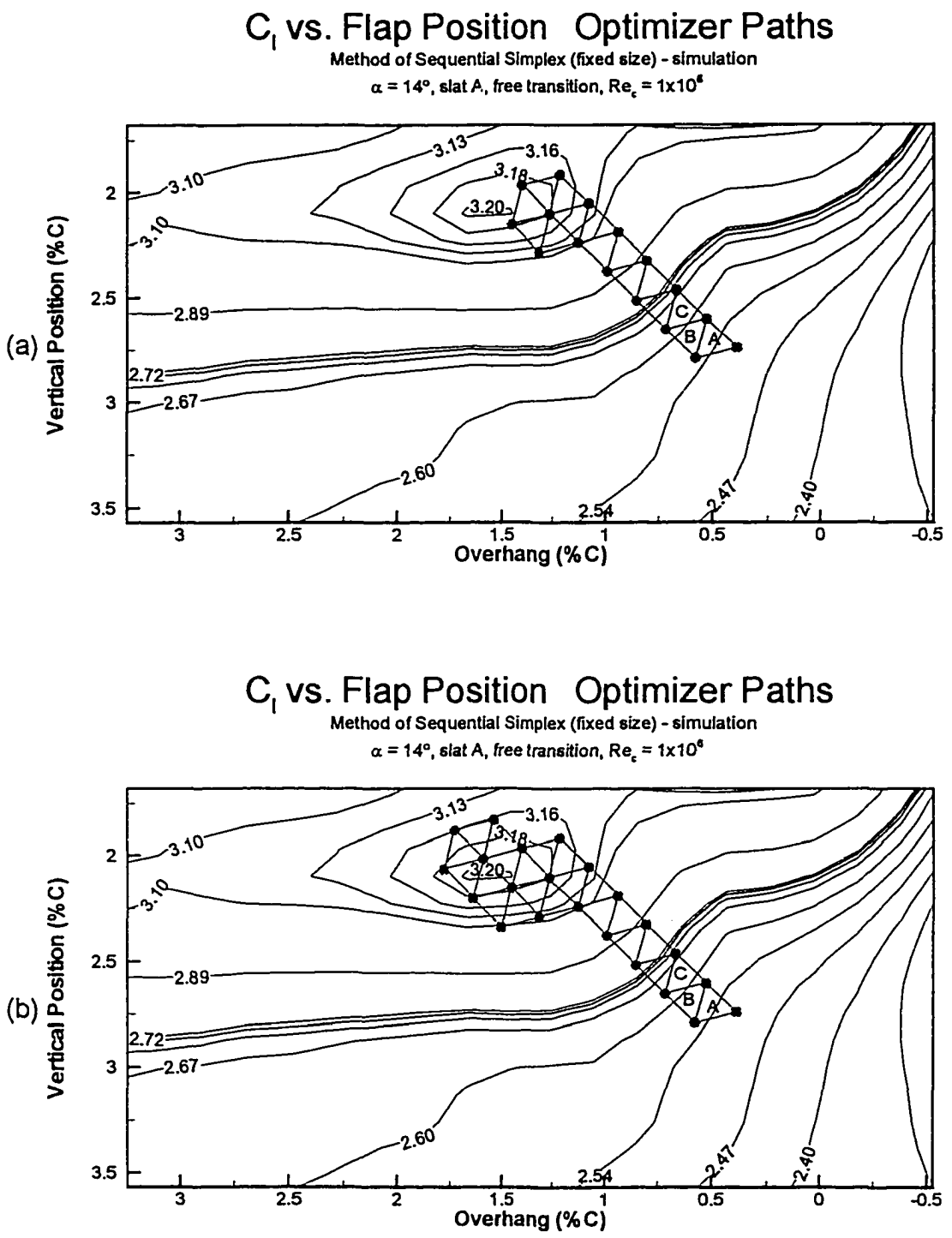

Figure 6.9 Fixed-Size Sequential Simplex Simulations, A-O-A = 14°

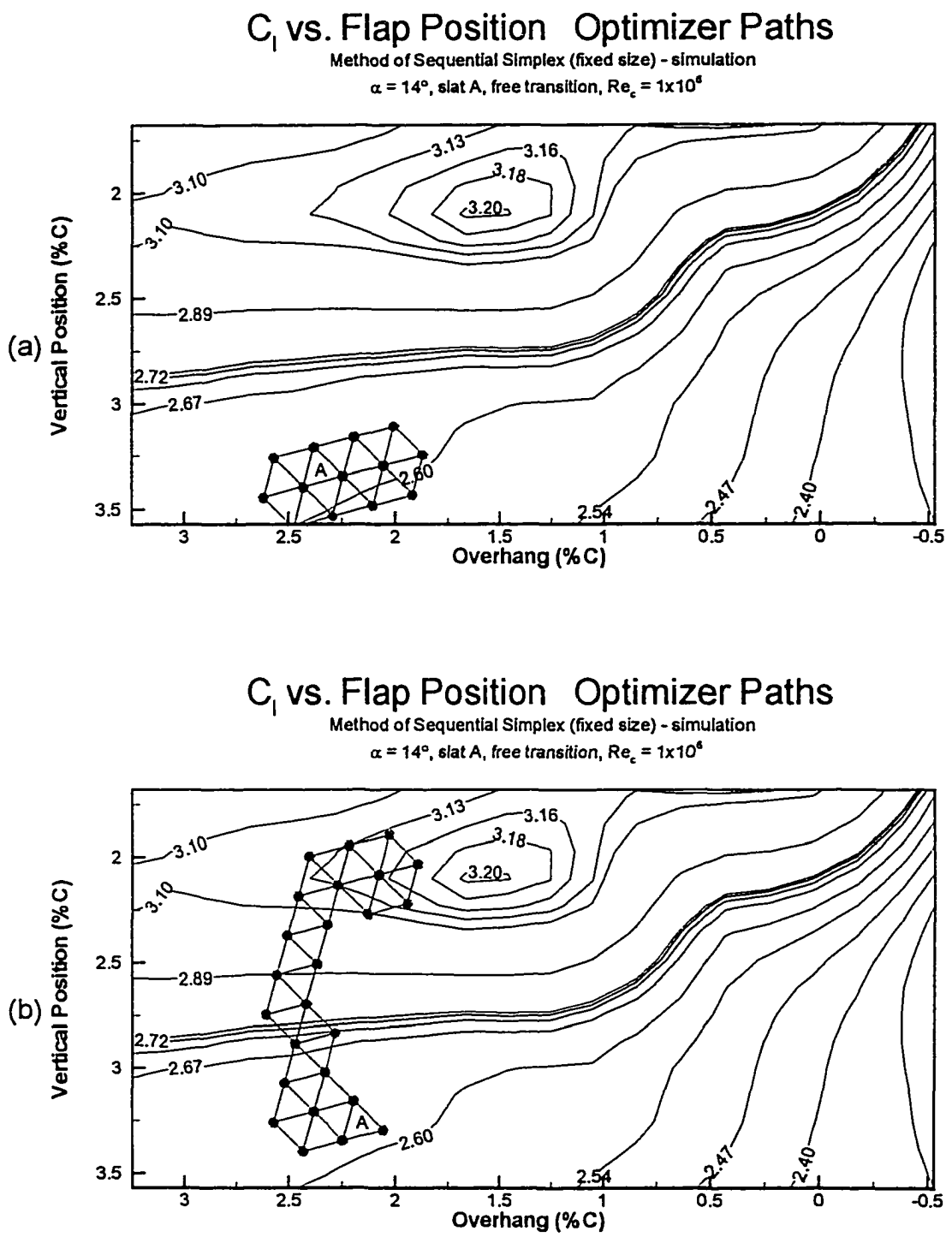

Figure 6.10 Fixed-Size Sequential Simplex Simulations, A-O-A = 14°, Examples of Poor Performance

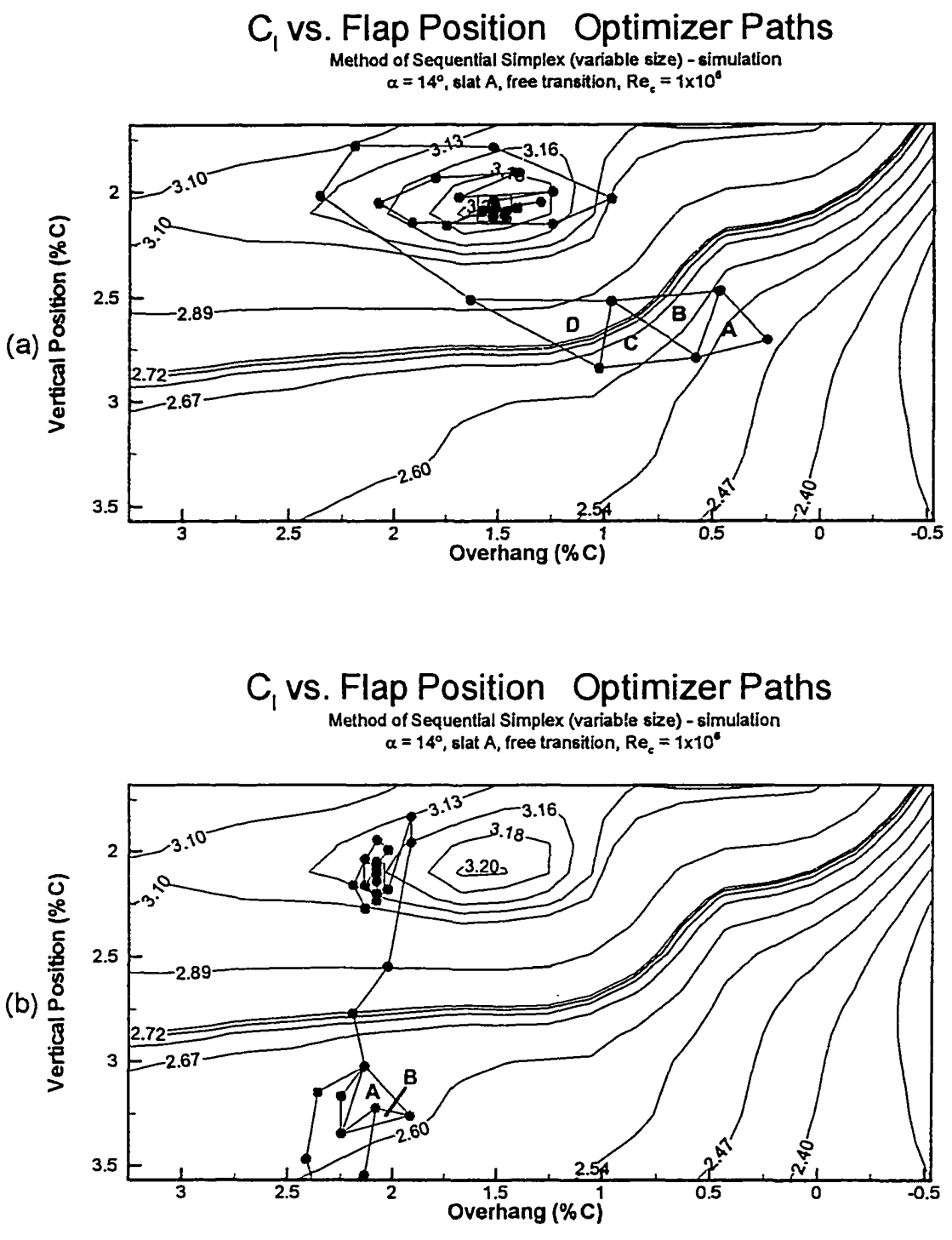

Figure 6.11 Variable-Size Sequential Simplex Simulations, A-O-A = 14°,

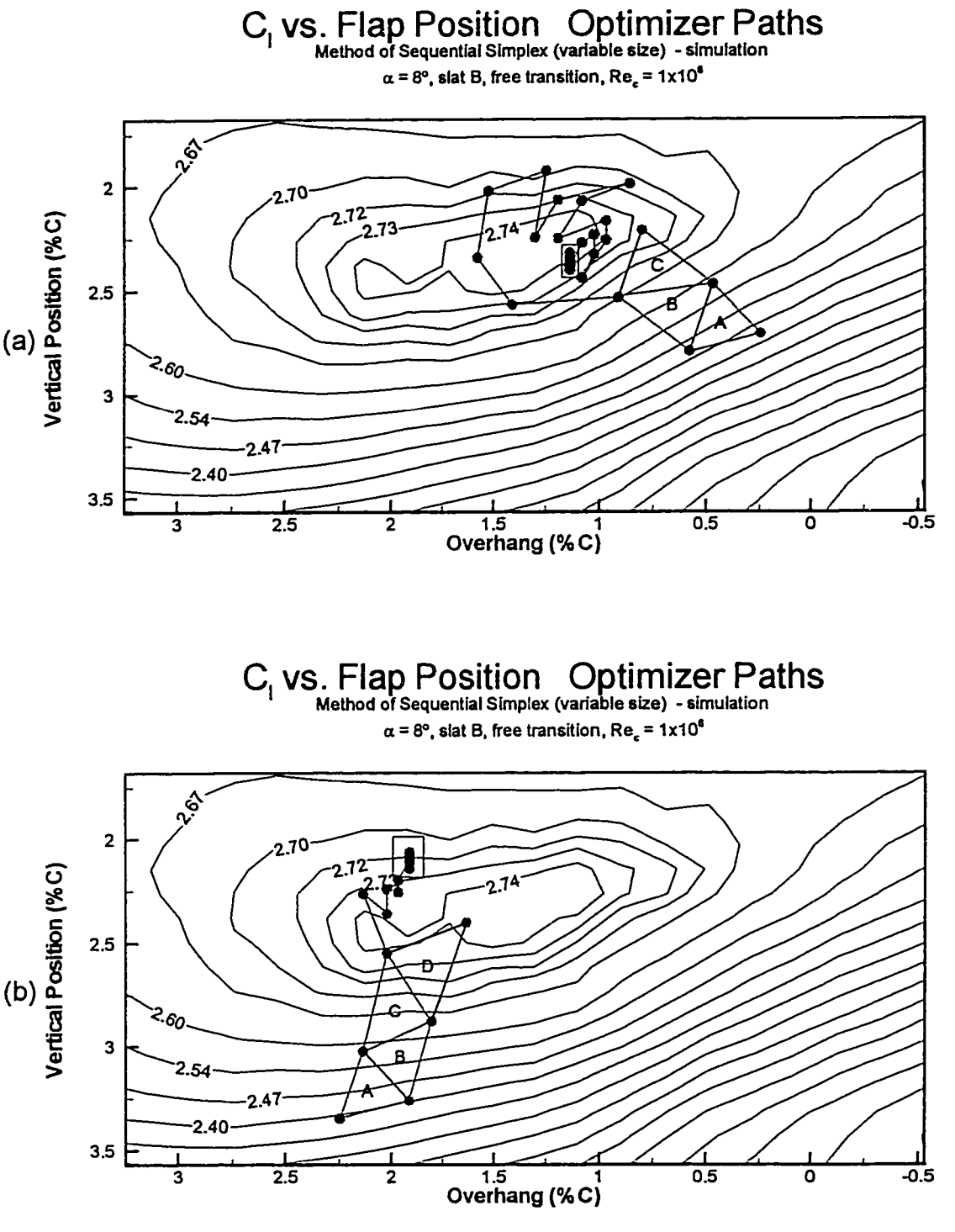

Figure 6.12 Variable-Size Sequential Simplex Simulations, A-O-A = 8°

(a)

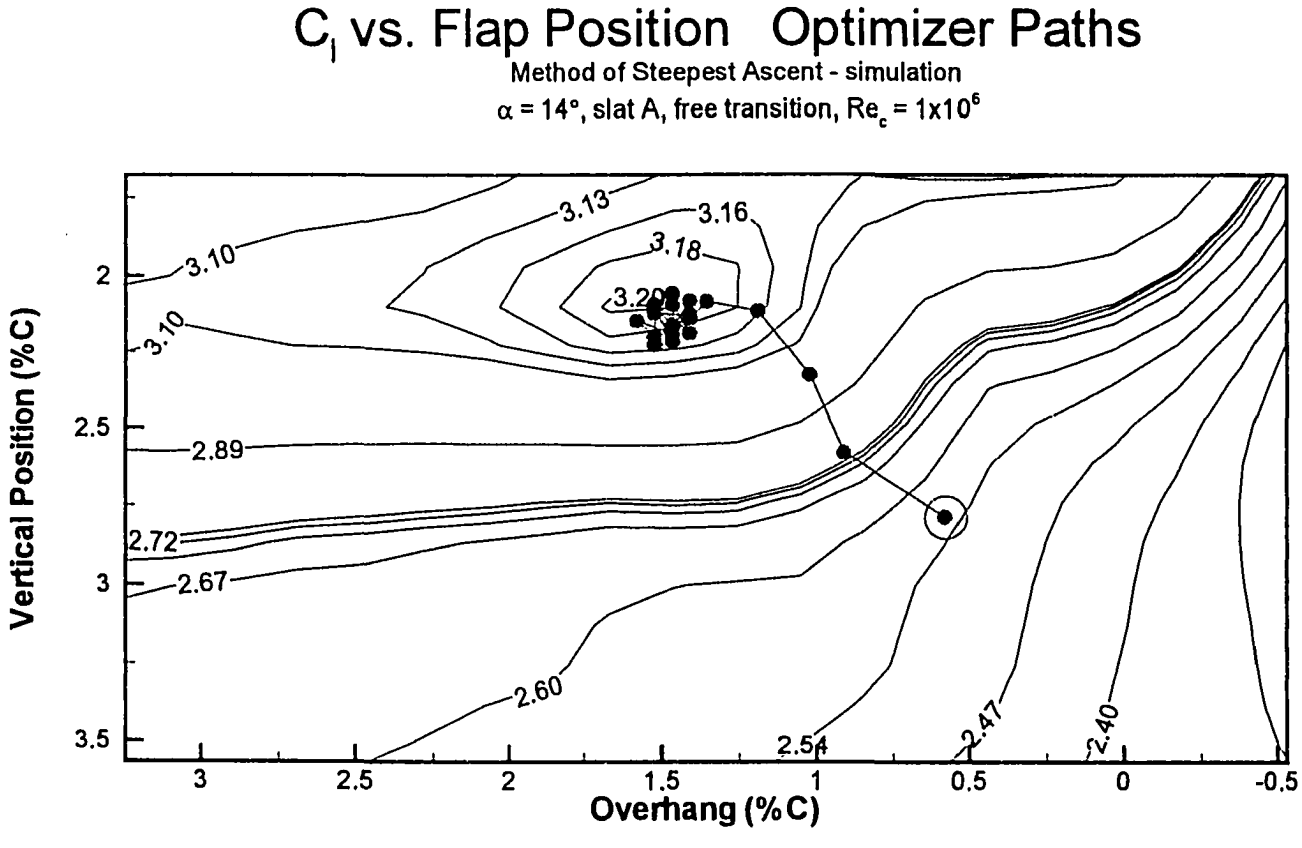

Figure 6.13 Steepest Ascent Simulations, A-O-A = 14°

(b)

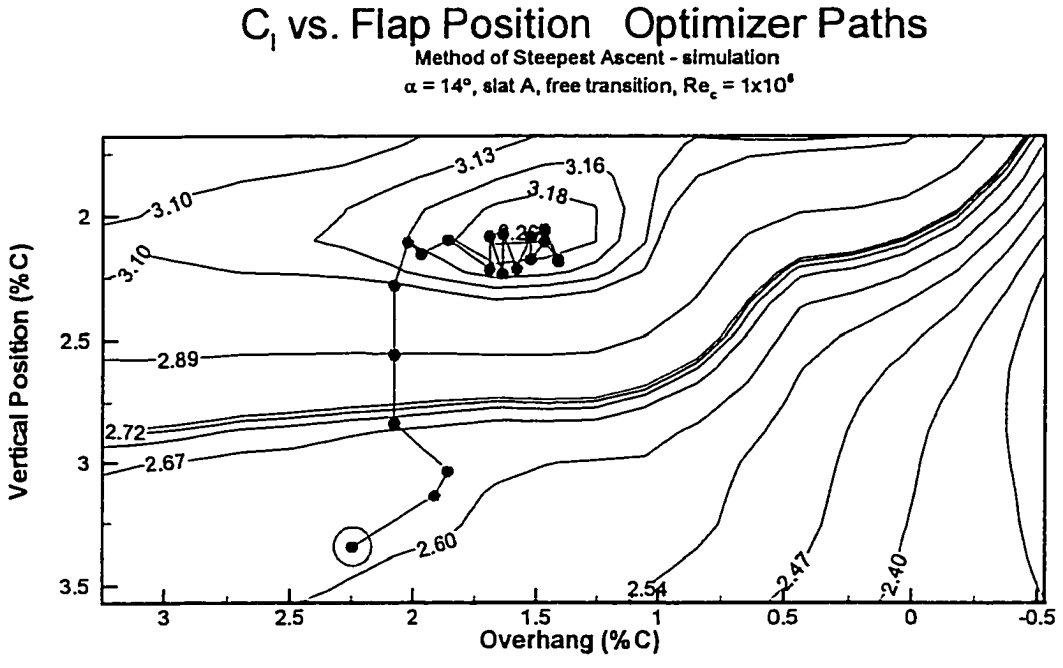

(c)

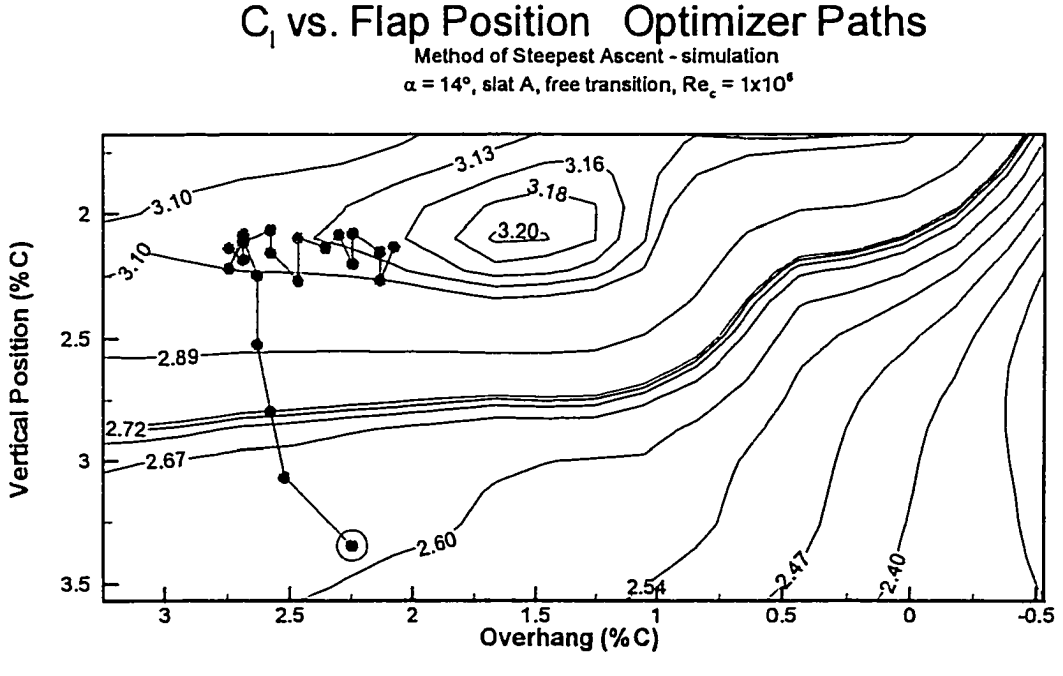

Figure 6.13 Concluded

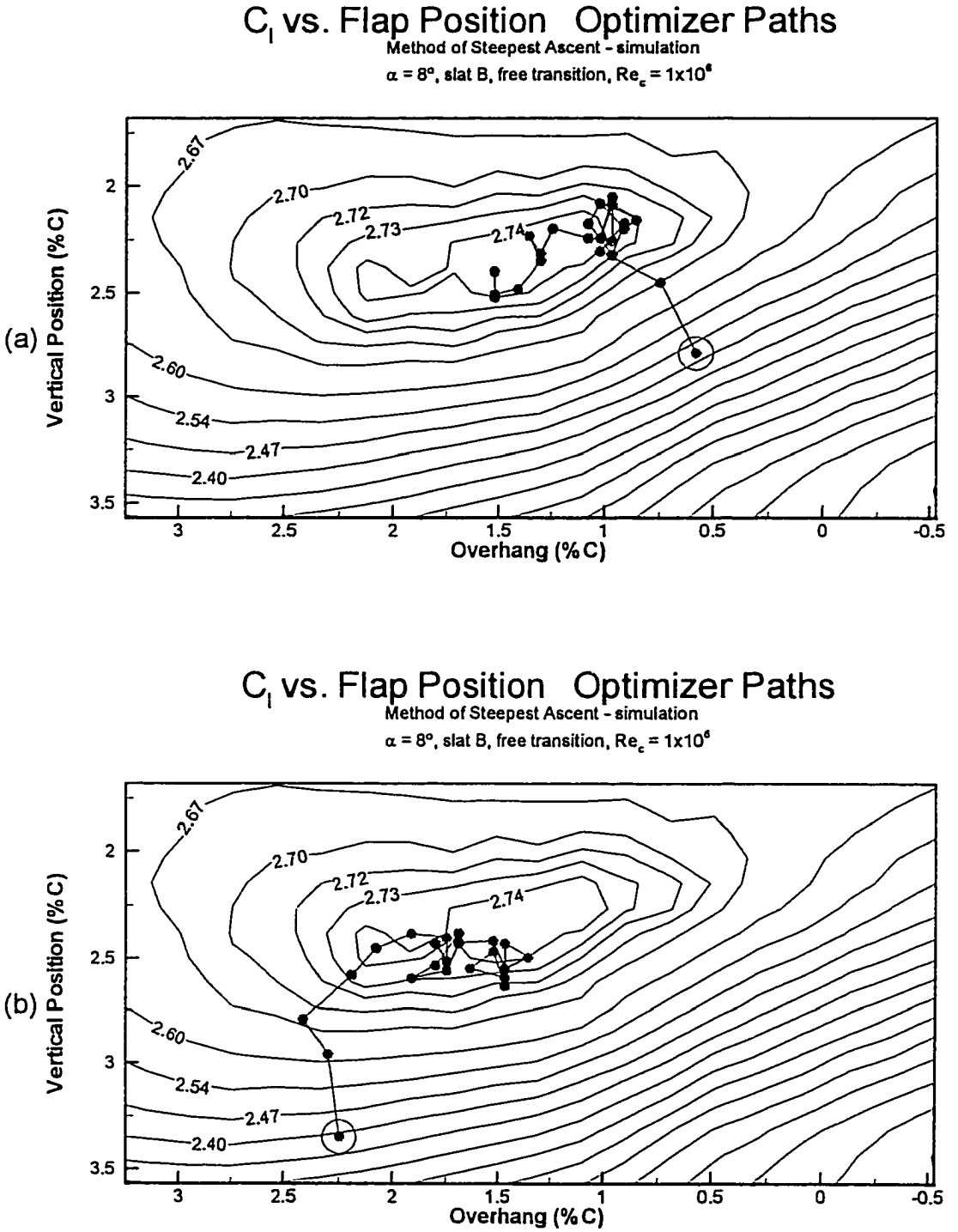

Figure 6.14 Steepest Ascent Simulations, A-O-A = 8°

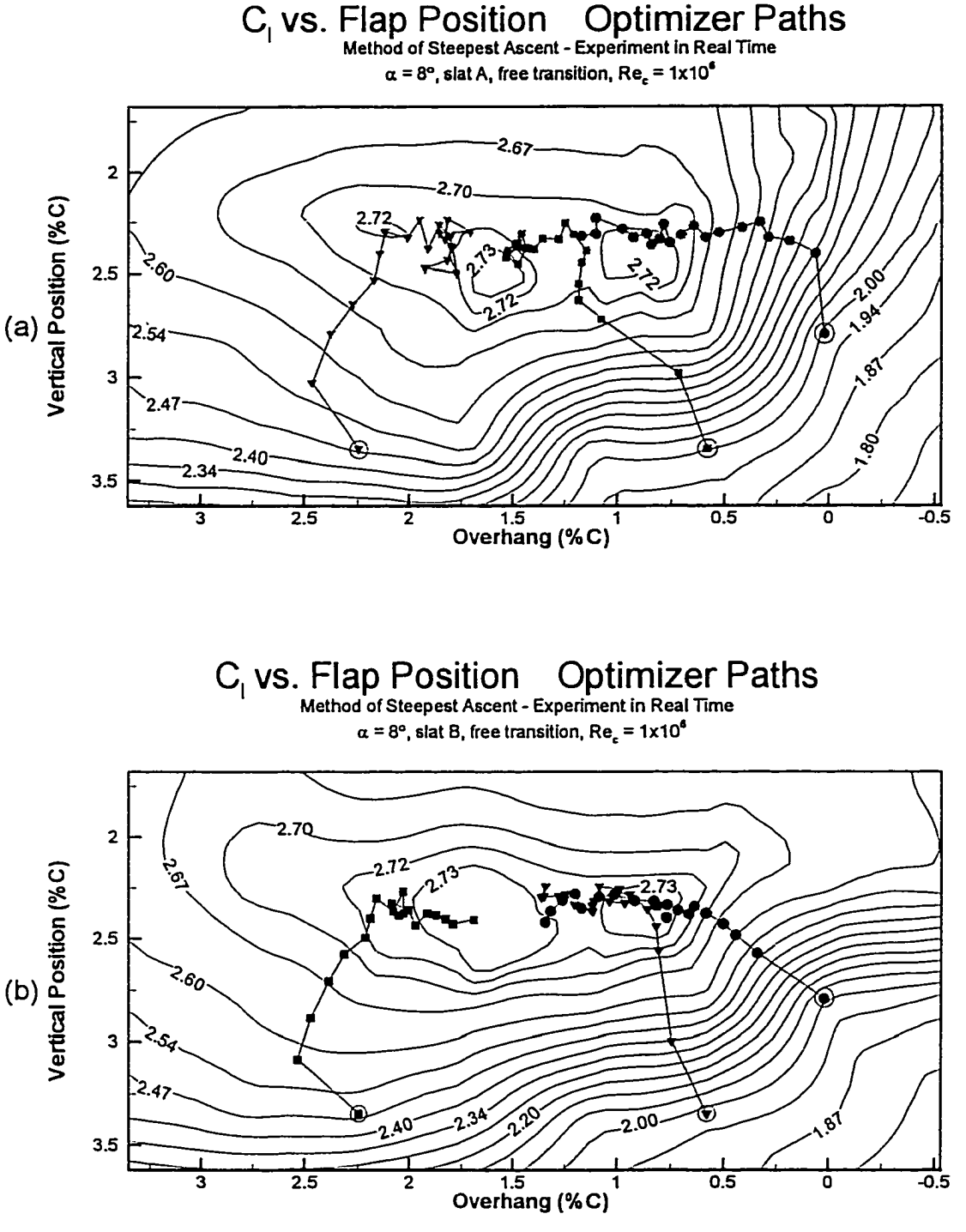

Figure 6.15 Steepest Ascent Experiments, A-O-A = 8°

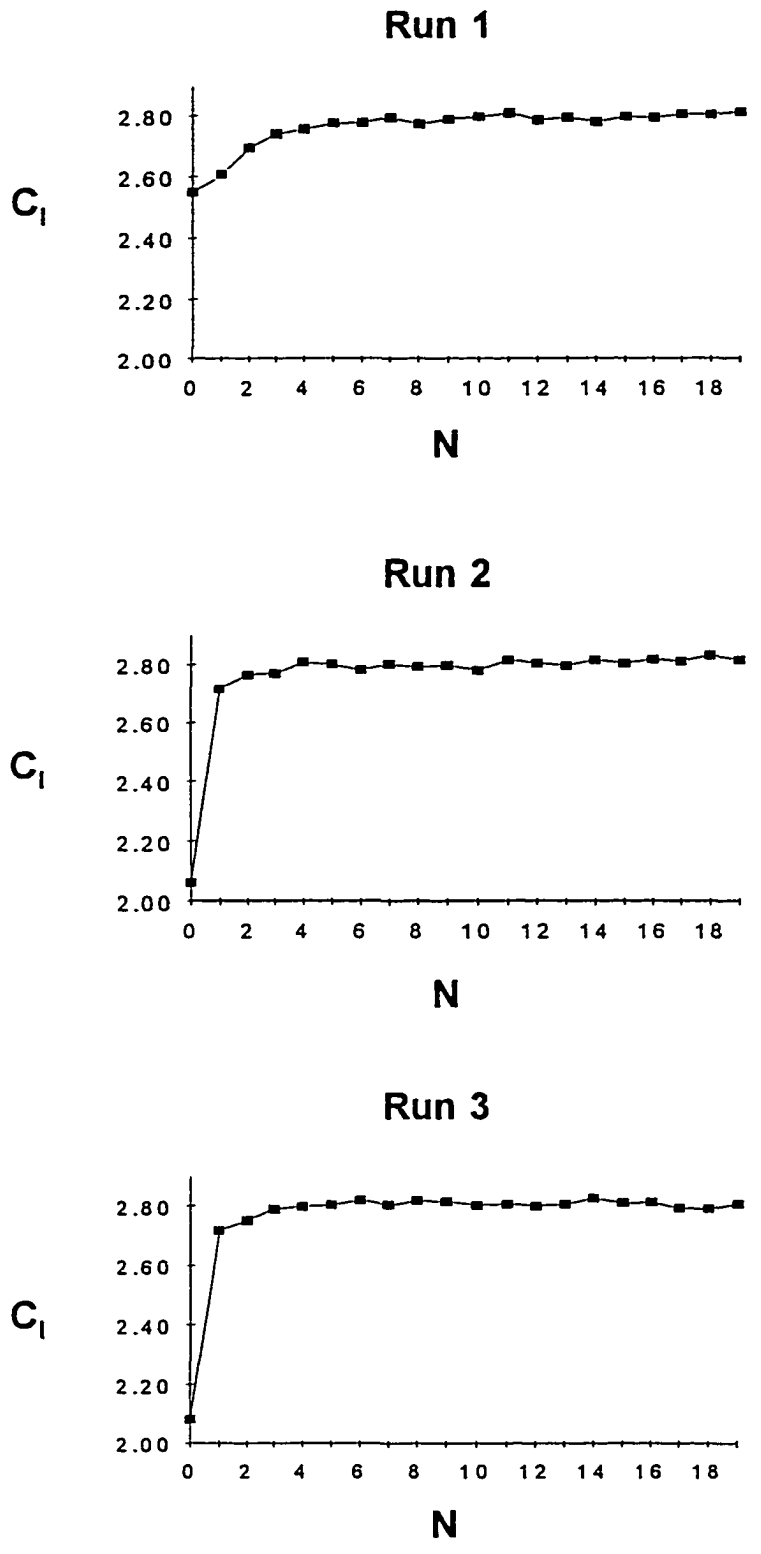

Figure 6.15c Convergence History from Optimizer Paths of Figure 6.15a

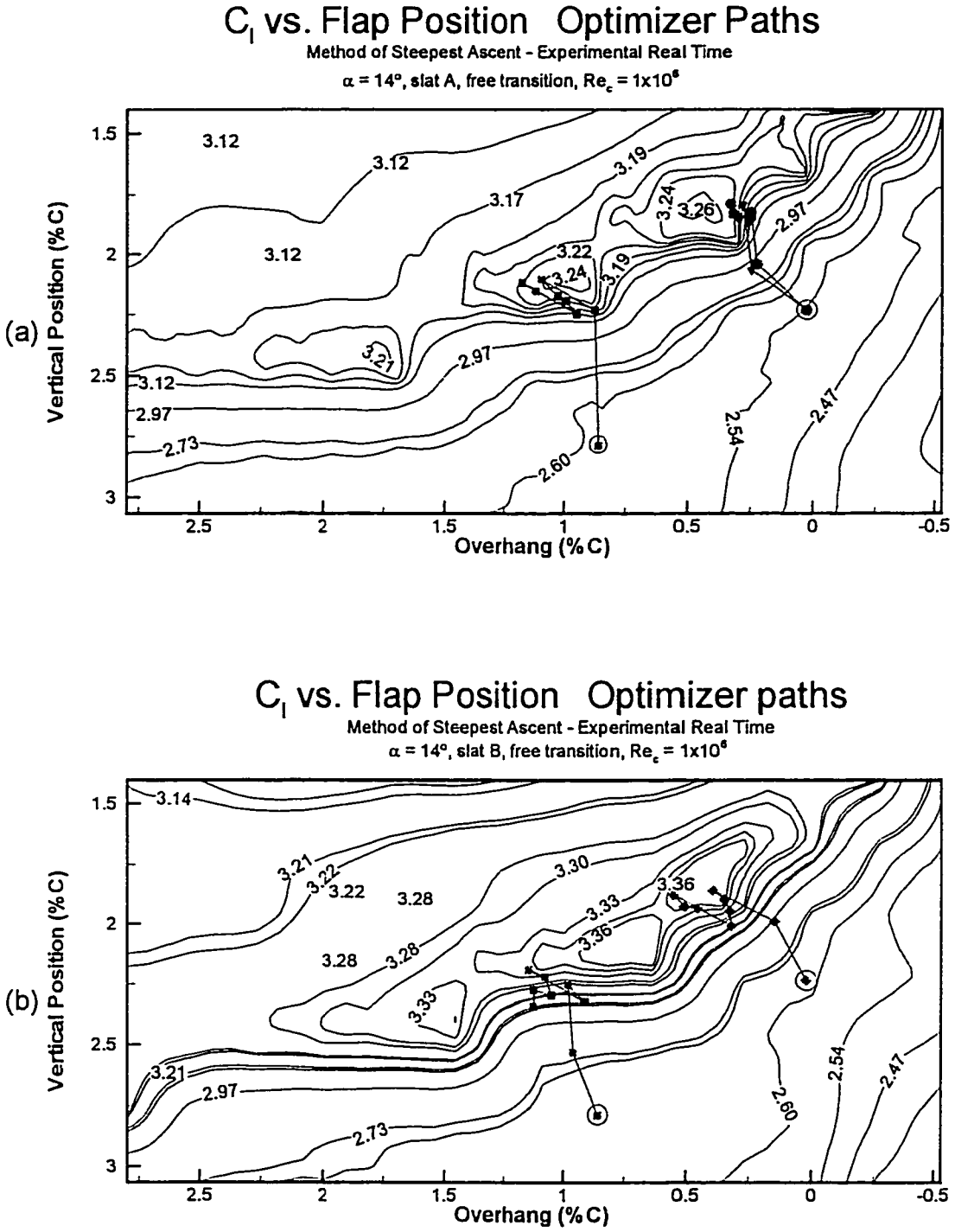

Figure 6.16 Steepest Ascent Experiments, A-O-A = 14°

Convergence History from Optimizer Paths of Figure 6.16a

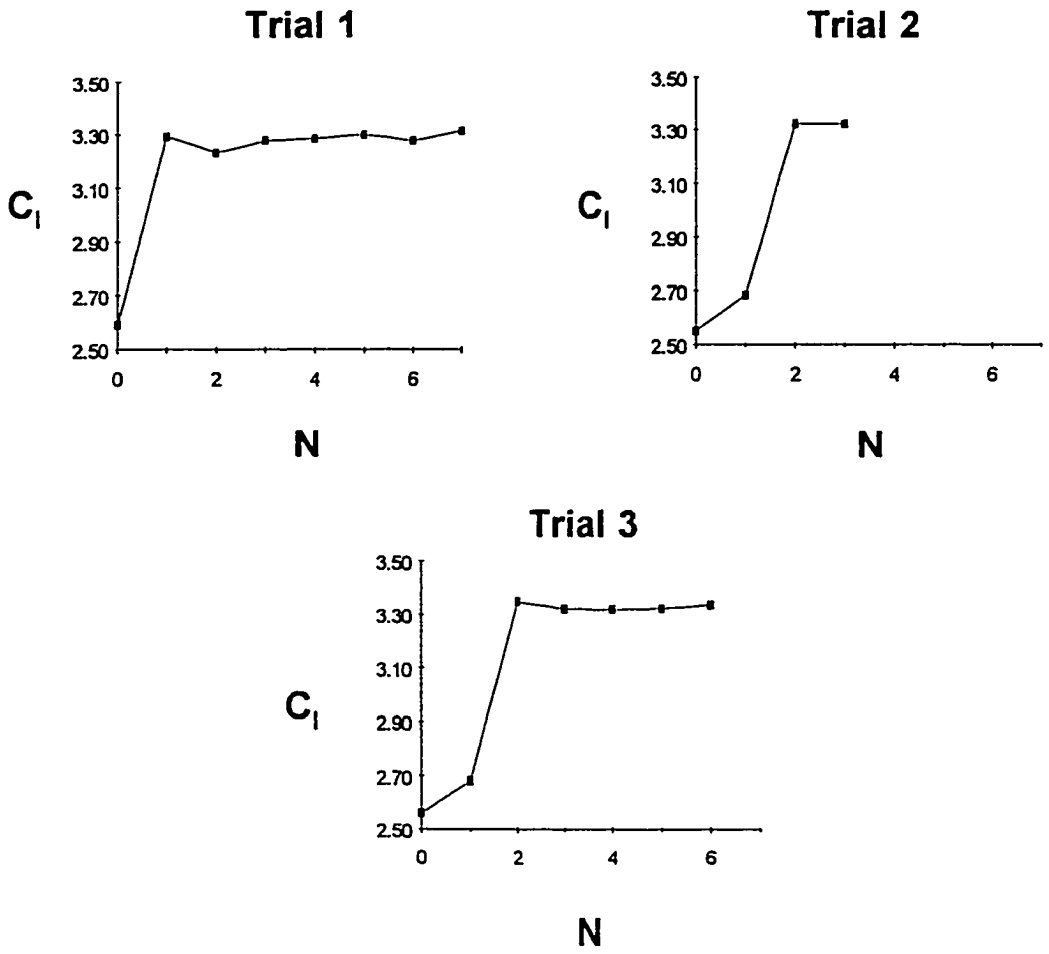

Convergence History from Optimizer Paths of Figure 6.16b

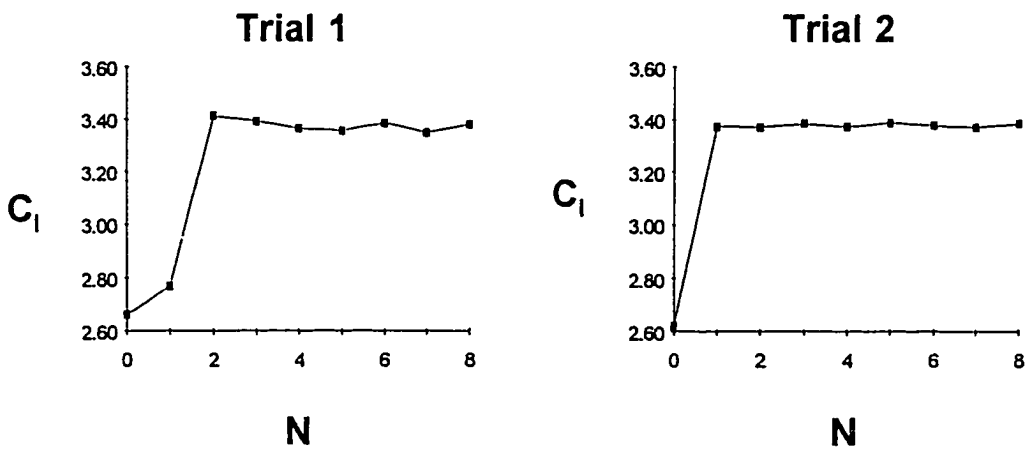

Figure 6.16c Convergence History from Optimizer Paths of Figure 6.16

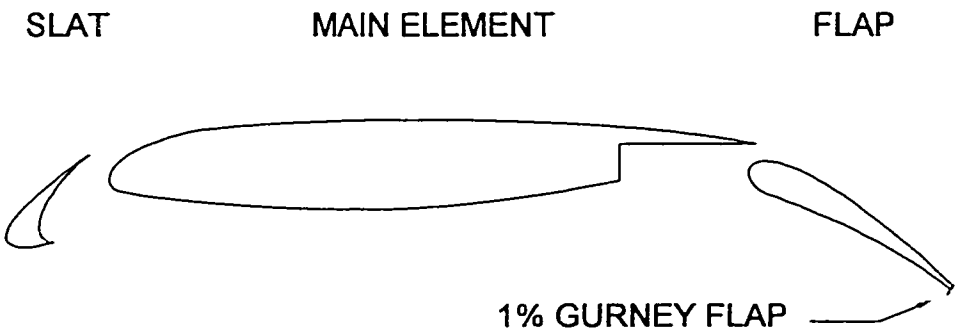

Figure 6.17a Model Configuration for Blind Optimization

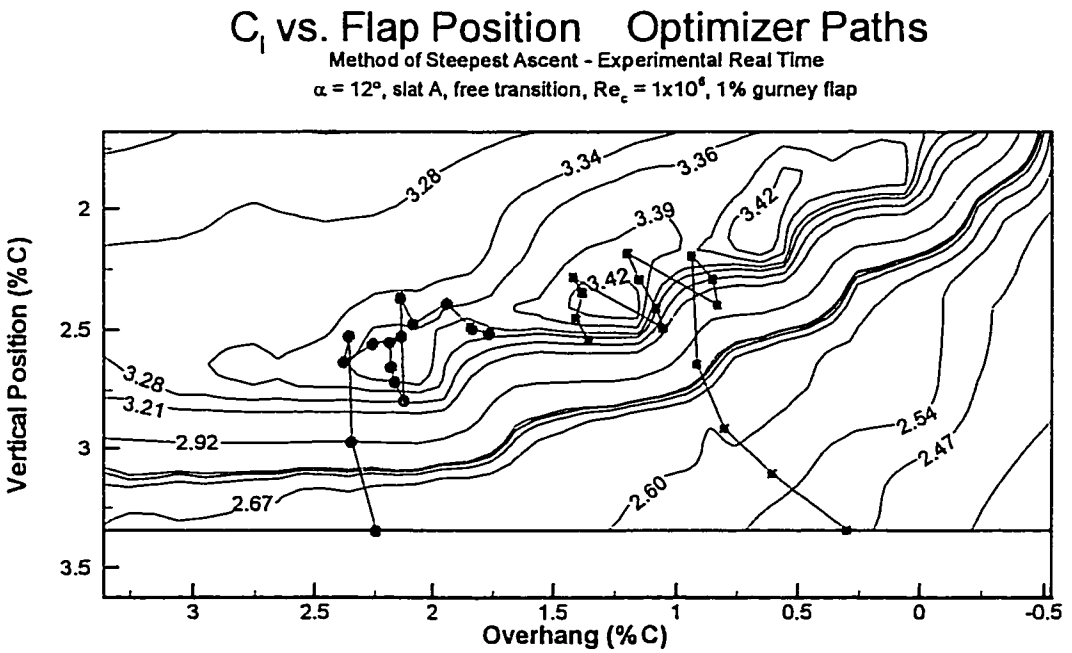

Figure 6.17b Optimizer Paths for Blind Optimization

(a)

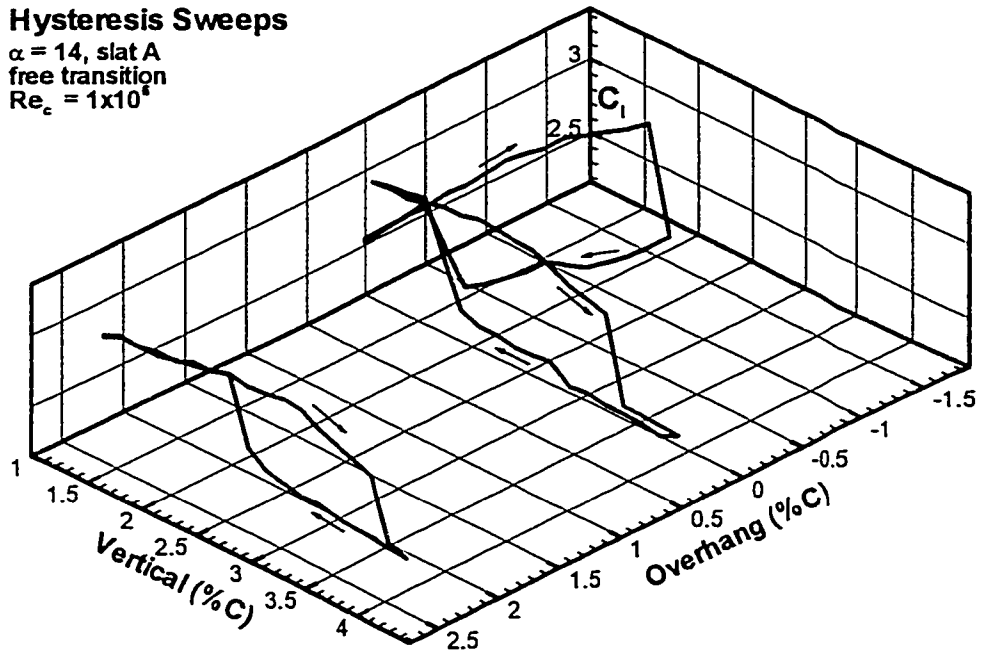

(b)

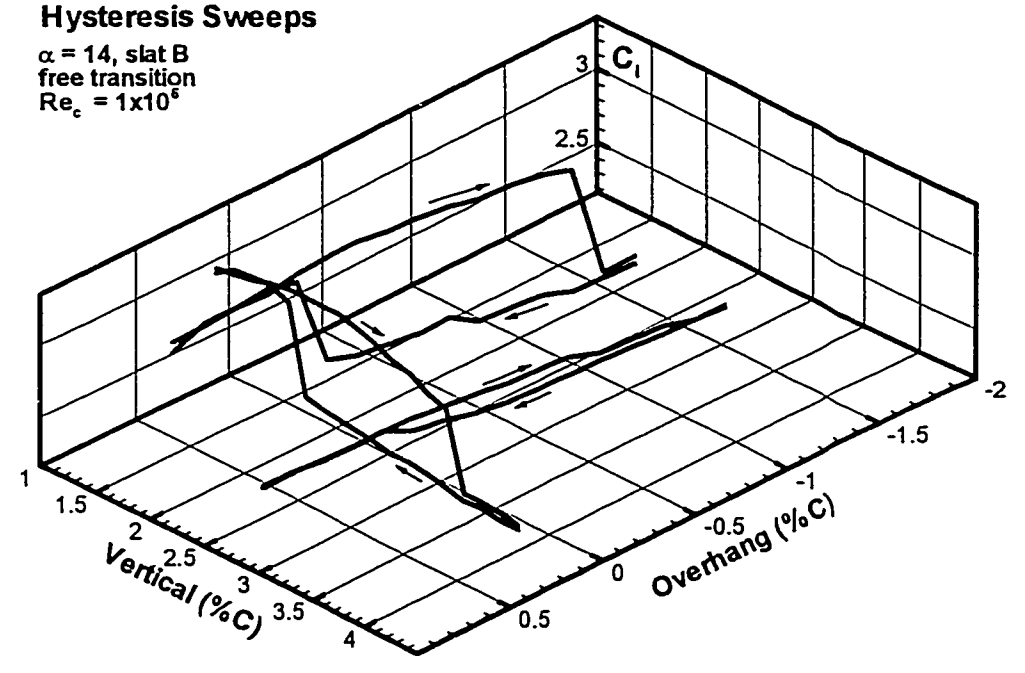

Figure 6.18 Hysteresis Sweep Study, A-O-A = 14°, Free Transition

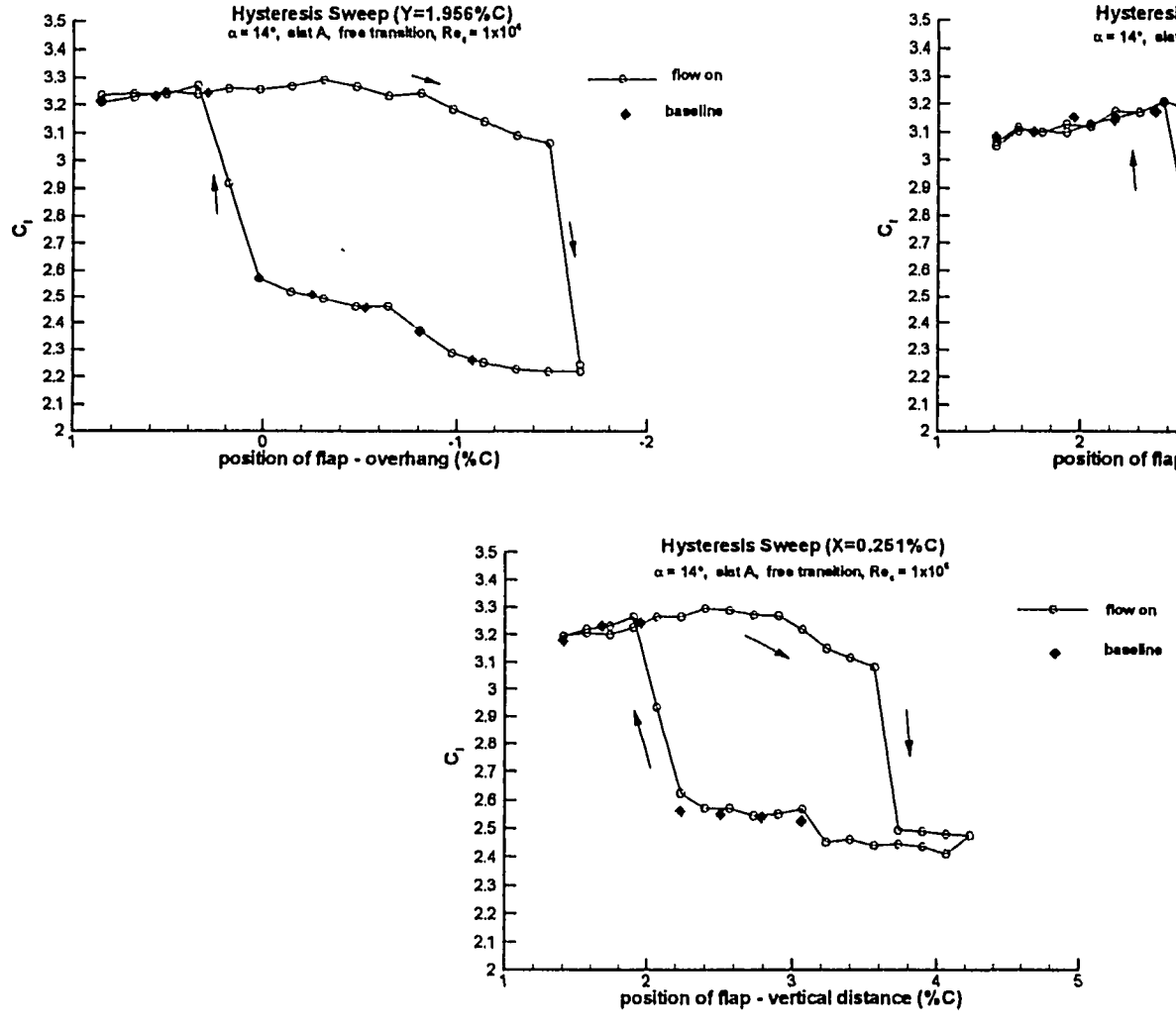

Figure 6.19 Hysteresis Sweeps of Figure 6.18a with Baseline

(a)

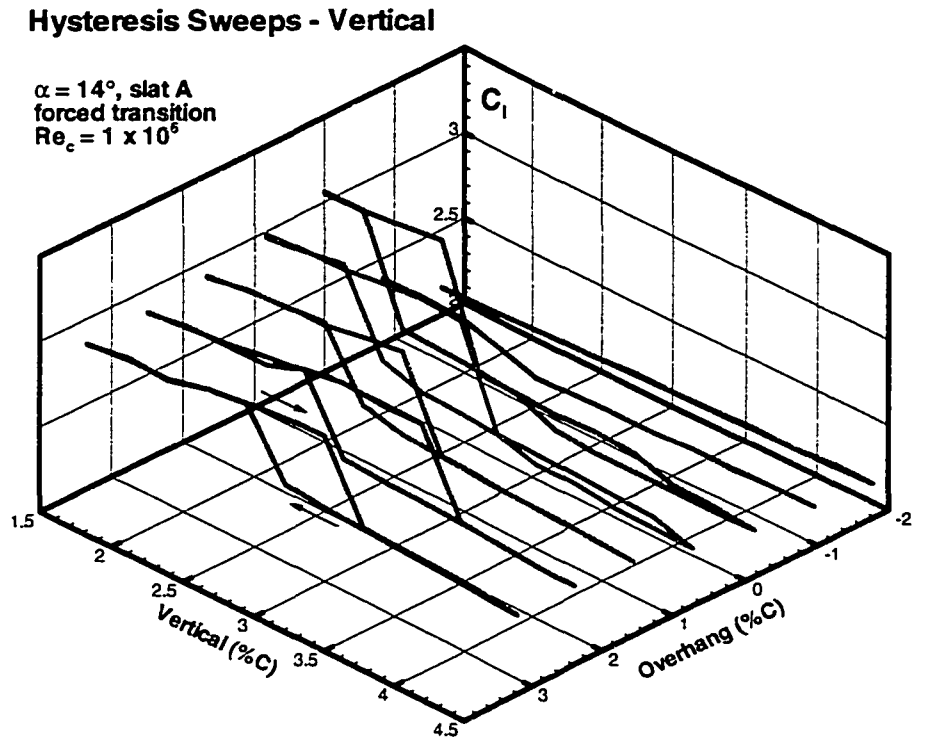

(b)

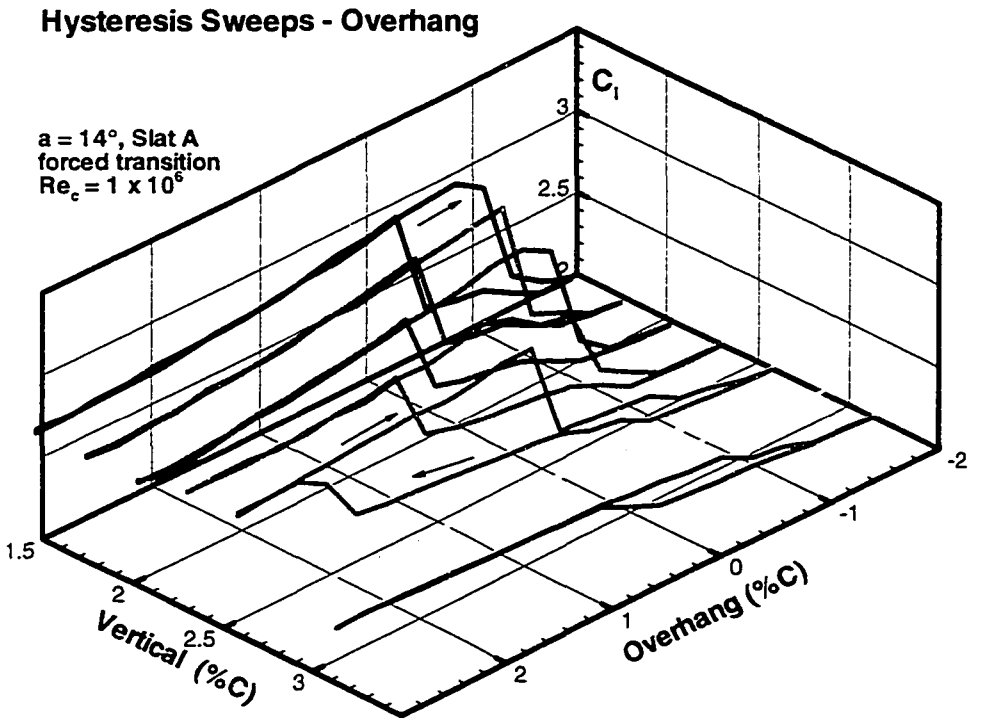

Figure 6.20 Hysteresis Sweep Study, A-O-A = 14°, Forced Transition

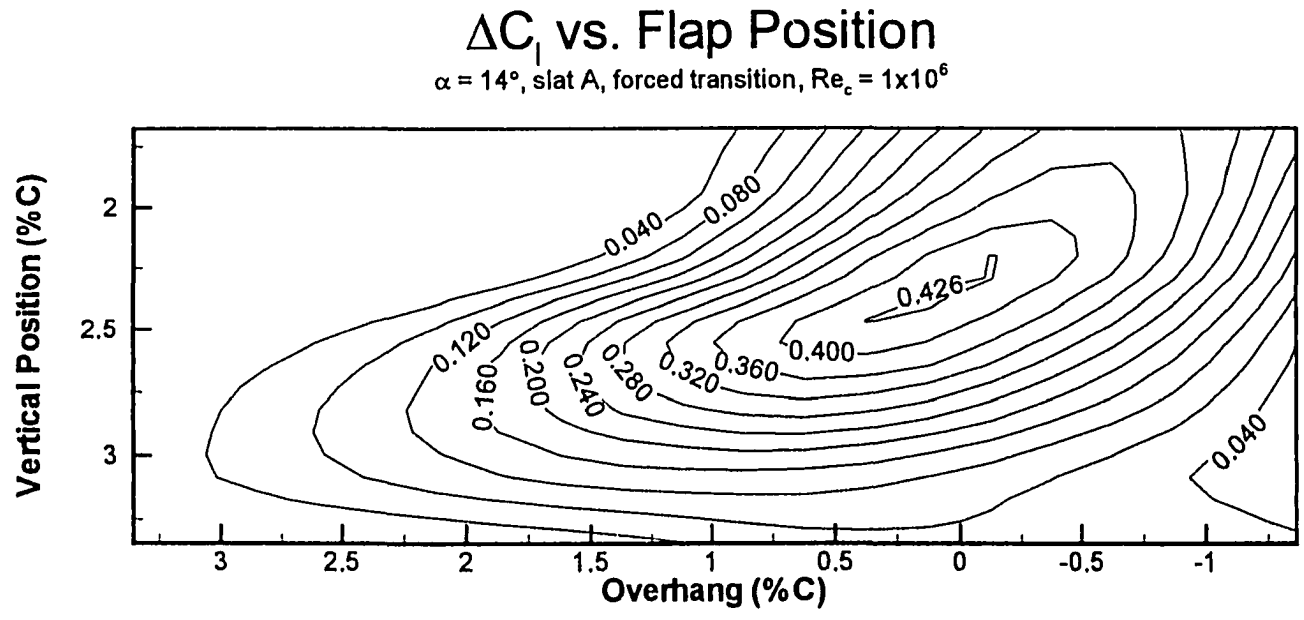

Figure 6.21 Lift Increment due to Hysteresis, Data of Figure 6.20b

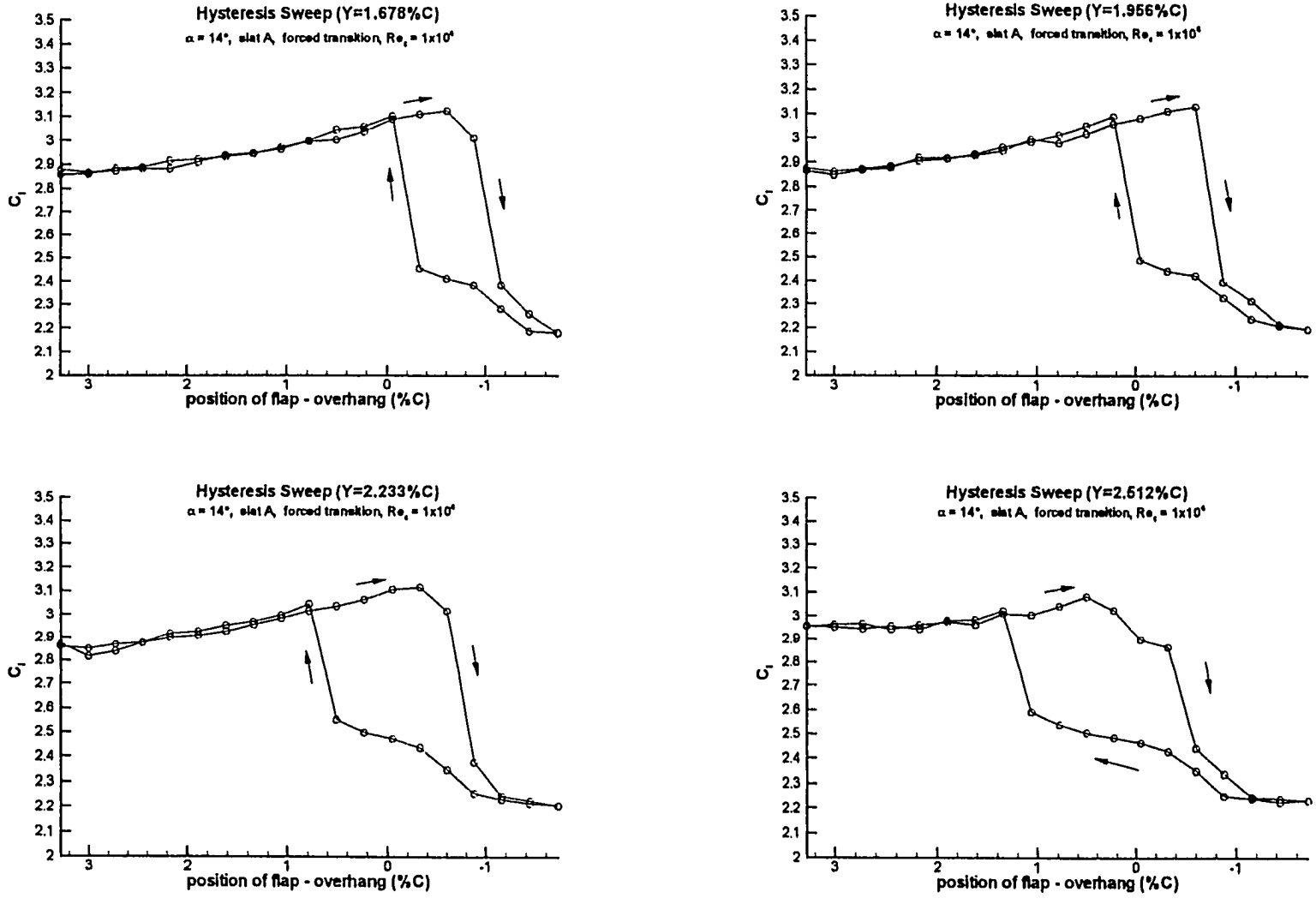

Figure 6.22 Hysteresis Sweeps of Figure 6.20b

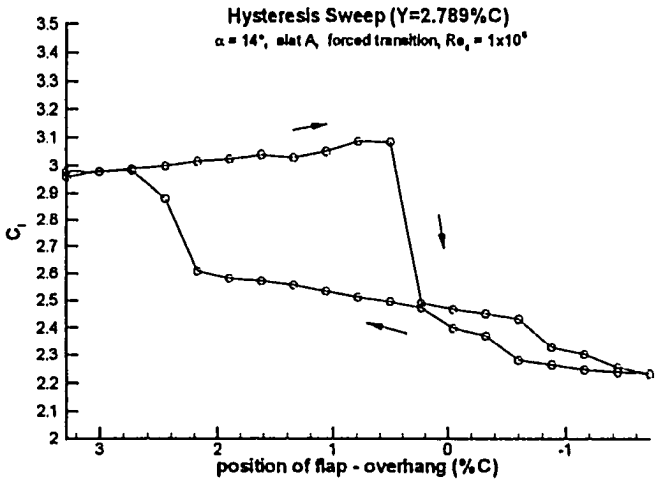

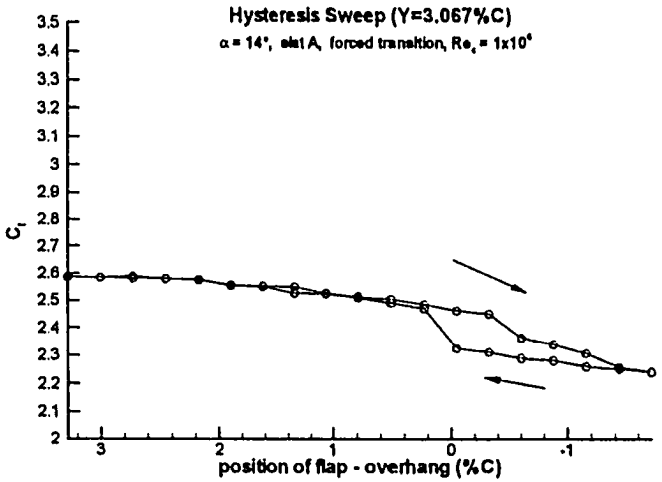

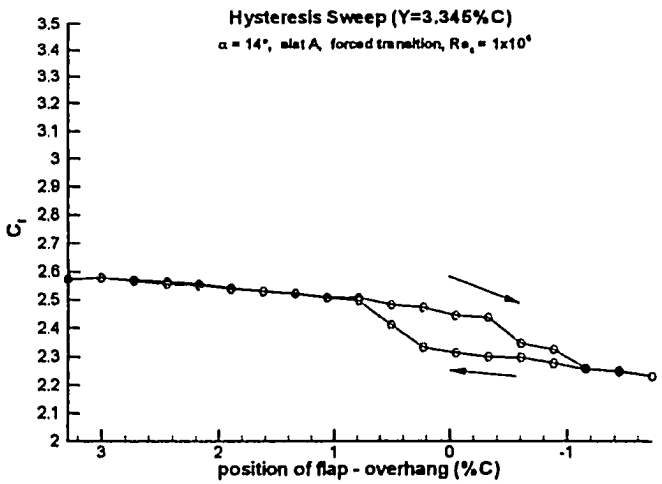

Figure 6.22 Concluded

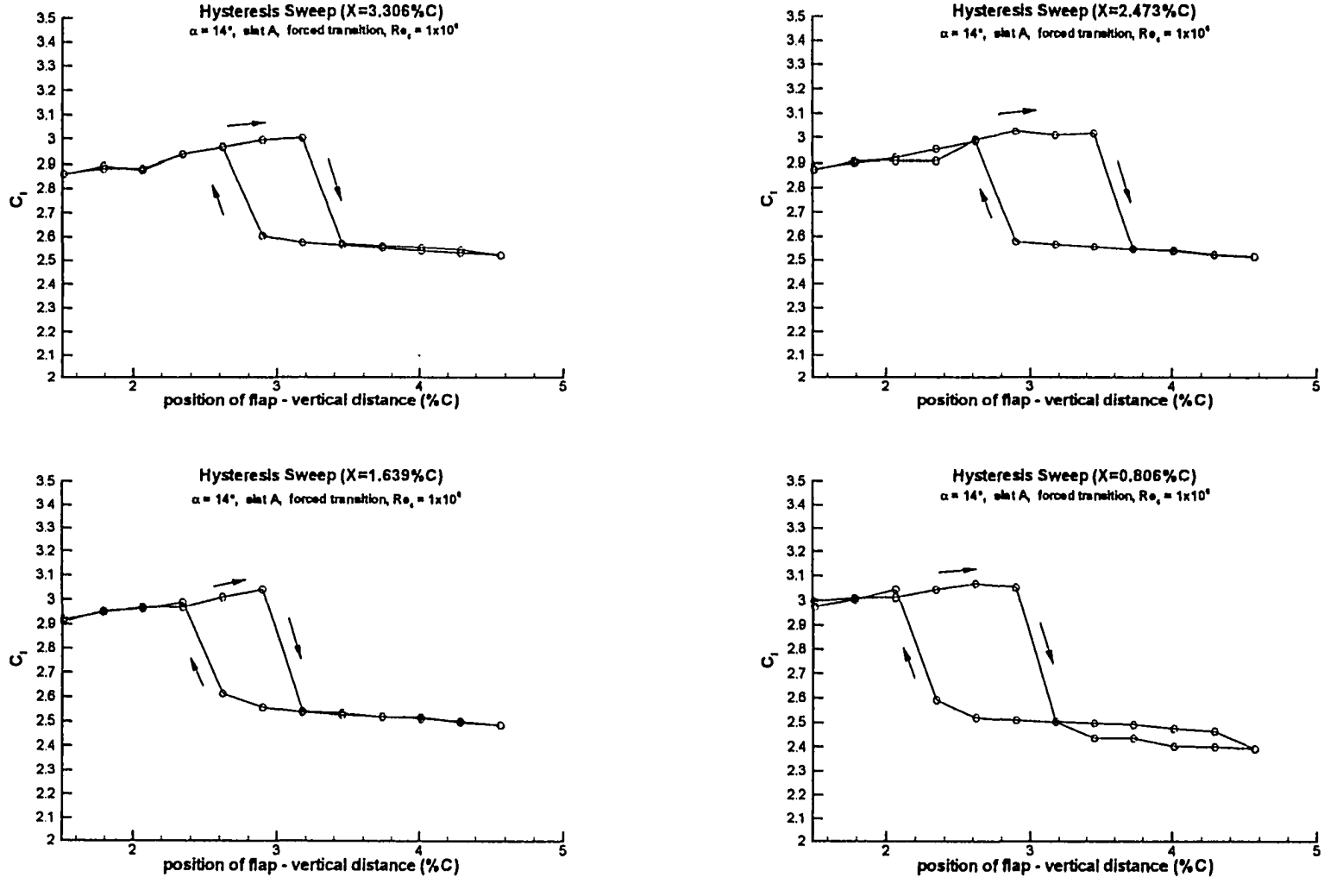

Figure 6.23 Hysteresis Sweeps of Figure 6.20a

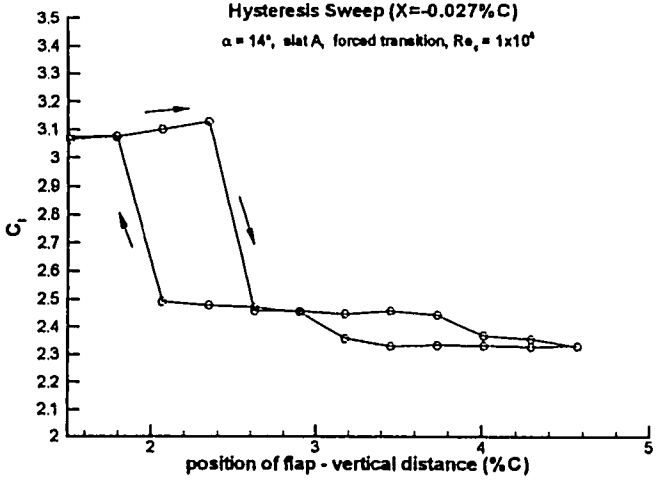

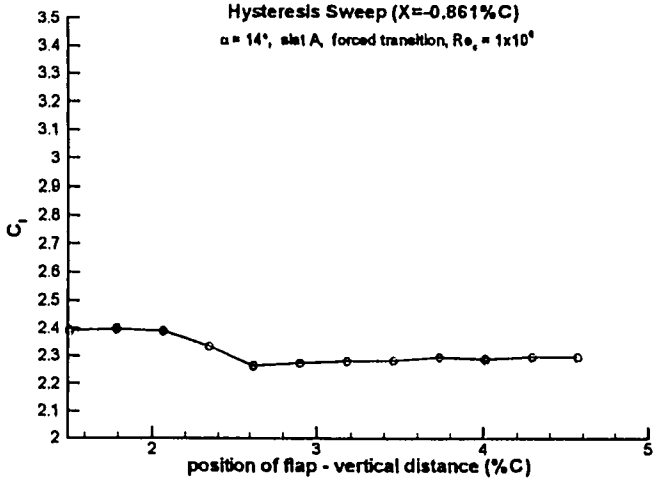

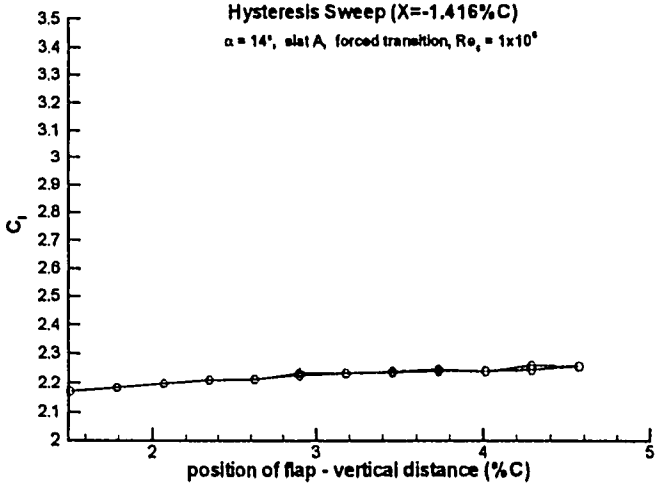

Figure 6.23 Concluded

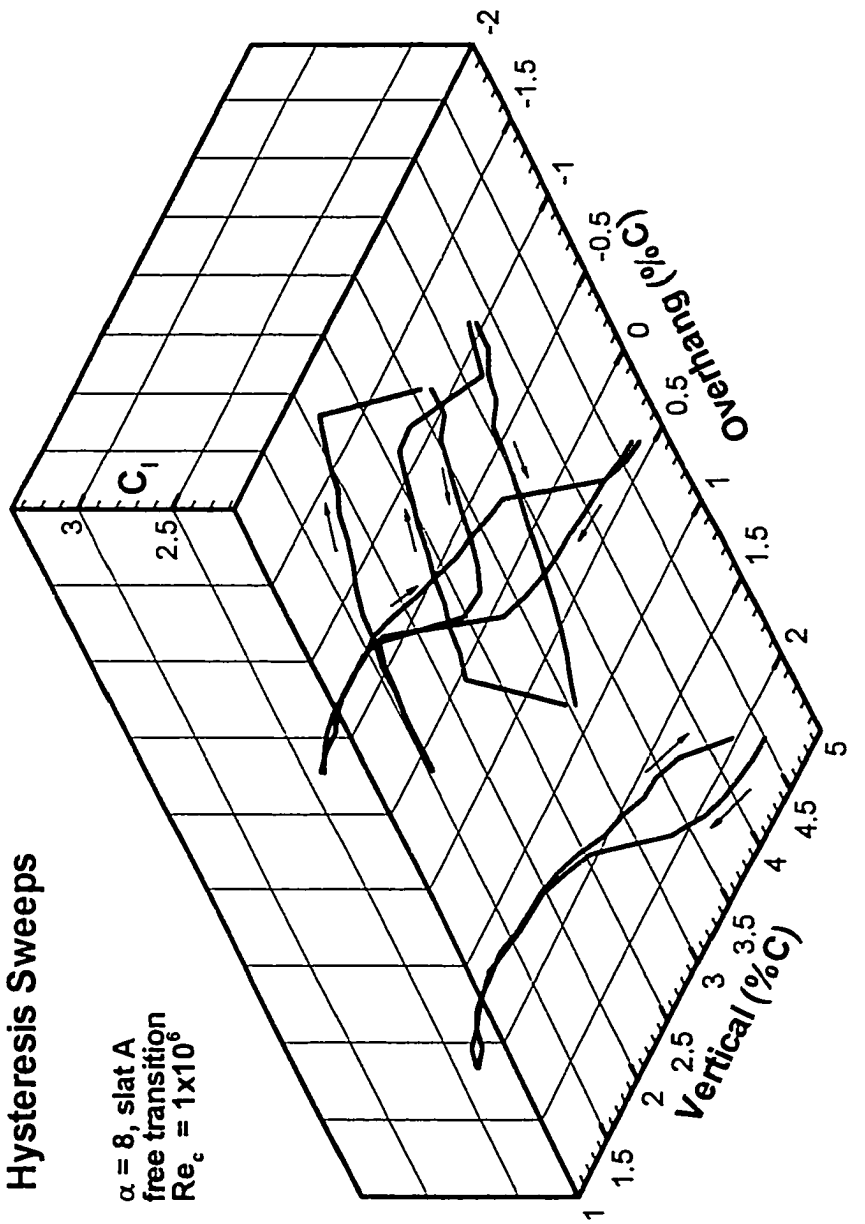

Figure 6.24 Hysteresis Sweep Study, A-O-A = 8°

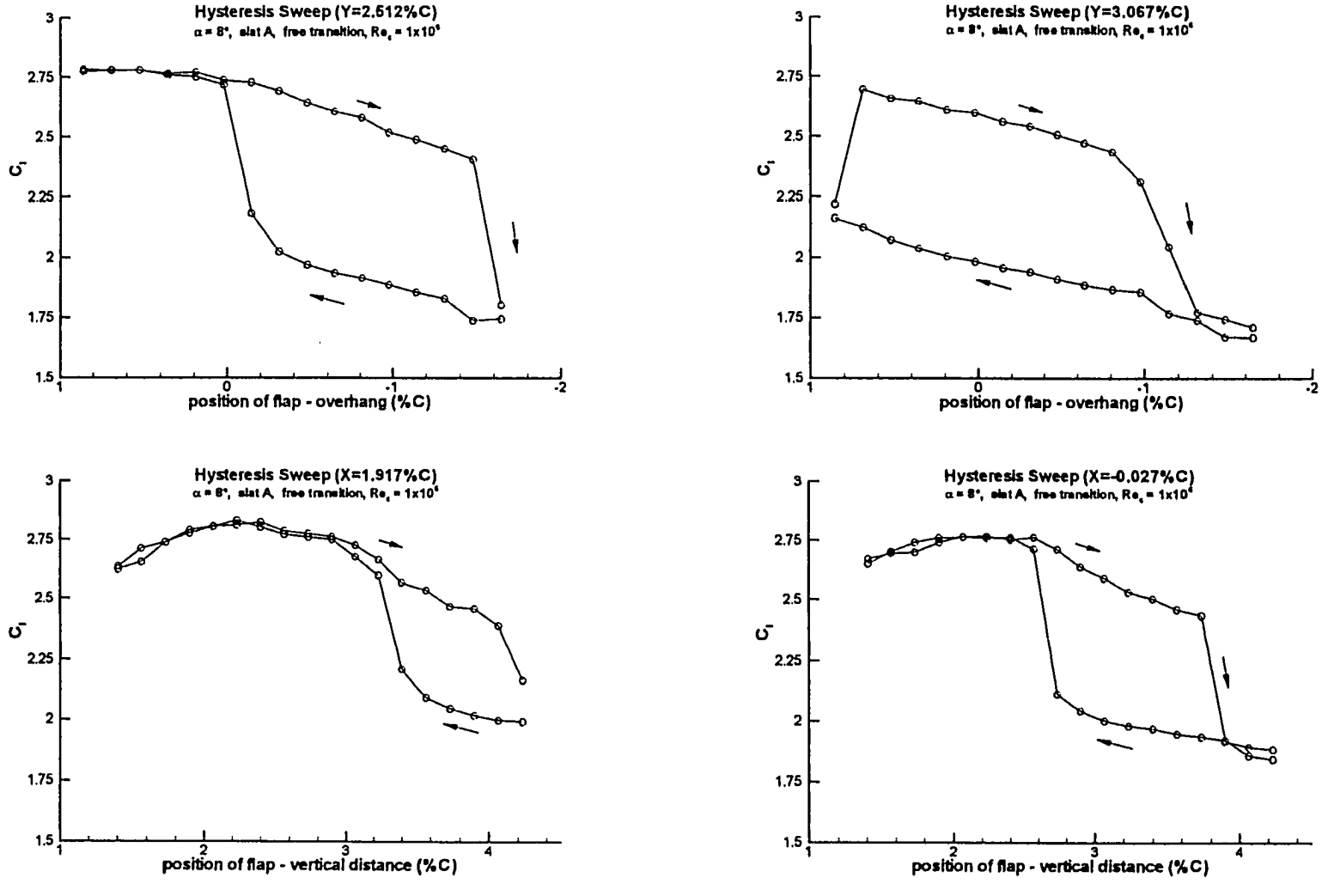

Figure 6.25 Hysteresis Sweeps of Figure 6.24

7 DISCUSSION OF RESULTS

7.1 Summary of Significant Results

Experimental geometry optimization techniques for a modern three-element airfoil model with a remotely actuated flap were demonstrated in this study. Internal actuators, located inside the main element, were designed which provided two degrees of freedom to a trailing-edge flap: vertical and horizontal translation. Automated wind tunnel test methods were presented which determined optimal flap position based on lift. Lift forces on all three elements were determined by integration of surface pressures, and flap location was determined by monitoring servomotor encoder counts. Software was developed to run on a personal computer to coordinate lift measurements, wind tunnel control, and flap position and later to invoke an optimization routine. All measurements were made at a Reynolds number of one million, both allowing free transition of boundary layers and using roughness elements to force transition.

Detailed results for lift coefficient versus flap vertical and horizontal position were presented using two different slat riggings and two airfoil angle-of-attack settings: 8 and 14 degrees. The 8-degree case, chosen as representative of an aircraft approach angle-of-attack, showed a broad optimal area for flap position when compared to the 14-degree case, which was chosen as the reasonable limit for uniform flow qualities for this experimental setup. The shape of the optimal area was relatively insensitive

to changes in slat rigging (gap and overhang), however overall lift coefficient values were affected.

Initial experimental data were used to construct a response surface using a multivariate regression. Experimental values of lift coefficient versus flap position were simulated using a random error routine in conjunction with the response surface. Optimizers using the method of steepest ascent, a fixed-size sequential simplex method, and a variable-size sequential simplex method were demonstrated using the simulated experimental data. Results of the simulations showed that all the methods would work. The method of steepest ascent was seen to have two distinct advantages compared to the variable-size simplex method: (1) initial faster convergence, and (2) freedom from adjustment of scaling parameters.

An on-line optimizer, using the method of steepest ascent, was demonstrated with the wind tunnel model, automatically locating the region of optimum lift as a function of flap position. Optimizer paths were compared to the baseline data using the same configurations. Results for the 8-degree case were extremely convincing with the optimizer working successfully for all six attempts. Trials using the optimizer for the 14-degree case, while fraught with hardware problems, proved that the optimizer was viable. A blind optimization was conducted using a configuration without a baseline study: a Gurney flap affixed to the trailing-edge flap with an overall angle-of-attack of 12 degrees. The optimizer paths compared favorably to the baseline data measured later.

7.2 Extension to Three-Dimensional Testing

7.2.1 Actuator Design

Internal flap actuators, located inside the main element of a two-dimensional model have been demonstrated to work well with the loads associated with a low Mach and low Reynolds number flow condition. There is an opportunity to extend this technology directly to three-dimensional models under similar flow condition; however, as was shown in section 2.2.3, it is ineffective to optimize element gap and overhang at conditions that are vastly lower in Reynolds and Mach number than flight conditions. Unfortunately, lift loads at near flight conditions are extremely high, causing leading-edge and trailing-edge elements to deflect (see section 4.3), and challenging the model designer to create a powerful actuator which is compact enough to reside in the wing. It is conceivable to create electro-mechanical actuators, with larger gear reduction drives than used in the present study, capable of working in parallel translation stages, which could afford sufficient power to move a flap under near flight flow conditions. With minimal additional flow interference a third degree of freedom could be added, providing adjustable flap deflection. It stands to reason that multiple sets of flaps (i.e. inboard and outboard), common to subsonic transport aircraft further complicate automated model design.

7.2.2 Optimizer Algorithm

The steepest ascent optimizer presented in this work is equally valid for both two-dimensional and three-dimensional testing. The objective

function of a 3D model is still lift coefficient, albeit for the full wing. If parallel actuator stages are fitted to the model, the design variables, flap gap and overhang, can be specified at a given spanwise station and the problem is now mathematically identical to the 2D case. Incidentally, if the combined main element, slat, and flap form a straight taper wing planform, the gap and overhang in terms of percent of local nested chord will remain constant along the flap span, completely analogous to the 2D case. Additional degrees of freedom such as flap deflection angle can be readily incoporated into the gradient based optimizer algorithm.

7.3 Lift Hysteresis as a Function of Flap Position

7.3.1 A Hypothesis for the Flow Physics of Lift Hysteresis

Lift hysteresis as a function of angle-of-attack has been reported for a two-element airfoil by Biber and Zumwalt [Biber and Zumwalt, 1993]. In their study, they found that an airfoil and flap configured for high lift exhibited a hysteresis loop in the lift curve when the 2D model was cycled in pitch from zero lift to complete stall (both elements). Several configurations, including optimal, large, and small gaps, were tested and in each case the flap stalled first. The mechanism for stall was described in the same way as discussed in section 6.2. It was found that the interaction of the potential jet flow in the slot with the main element wake controlled the nature of the separation on the flap upper surface. In addition, the authors described the turbulent mixing between the wing wake and the flap boundary layer that takes place when the flap stalls as being responsible for the irreversibility in the lift curve.

With this scenario in mind and the results of the stall progression study and hysteresis sweeps, a hypothesis has been developed to describe the lift hysteresis due to flap motion. Consider an overhang sweep (vertical position constant) where the starting point is well forward. As the flap progresses aft, the gap is initially constant, and as a result the pressure distribution remains relatively unchanged as shown in figure 6.3b and described in section 6.2. As the flap continues to move aft, the flap gap begins to widen and the size and influence of the potential jet flow region increases, providing a more favorable pressure gradient over the upper surface of the flap which promotes a thin, laminar boundary layer. The slot flow centerline tends to follow the flap curvature under the influence of the strong pressure gradients of the wing wake [Biber and Zumwalt, 1993; Nelson, 1995; Nakayama, 1990; Olson and Orloff, 1981]. The more powerful wing wake pushes the flap boundary layer downward (toward the surface), limiting separation. This beneficial interaction continues until the gap reaches a critical width at which time the point of separation on the flap begins to move forward from the trailing edge [Brune and McMasters, 1990]. This is understood to be a result of the now reduced jet flow velocity with its accompanying increasingly adverse pressure gradient. The separation point on the flap upper surface travels forward with increasing gap until the main element wake and flap boundary layer begin mixing [Biber and Zumwalt, 1993]. Once the flap shear layer is separated there is a bubble-shaped region downstream of the separation point defined by the flap surface and the point where the shear layer eventually joins the separating streamline

of the flap. As the flap is moved further aft, more mixing occurs in the combined turbulent wakes of the flap and main element and eventually the flap is fully stalled [Biber and Zumwalt, 1993]. As the flap now begins to traverse the return path, the turbulent mixing is well established. The high momentum carried in the main element wake (including the slat wake) mixes with the lower momentum of the flap boundary layer keeping the flow over the flap separated (seen in the constant pressure distributions on the flap upper surface) until the slot flow is well established again and mixing begins to subside.

The fact that the flap stalls at a further aft position under continuous flow conditions than under intermittent conditions can be attributed to the establishment of a favorable slot flow and flap boundary layer. When continuous conditions are used for testing, the slot flow and flap boundary layer are well established while the flap gap is small. The flap can then be moved to a position where under intermittent testing conditions, the gap will produce a stalled flap. This difference can be accounted for by considering that during intermittent testing, the boundary layer on the flap will develop with the rising tunnel freestream velocity. It will therefore progress from a condition established by low Reynolds numbers, which are known to be susceptible to separation, to the test condition. If the flap boundary layer initially separates and begins to mix with the wake of the main element while the flow accelerates, the effects are irreversible.

7.3.2 Optimization with Hysteresis Present

If wind tunnel productivity for high-lift testing is to be maximized, optimization methods using automated models tested with continuous flow conditions represent the ultimate goal. Irreversibility in the form of lift hysteresis presents a formidable challenge to optimization algorithms. Experimental evidence has shown that while traversing the flap of a three-element airfoil to achieve maximum lift, an ideal configuration often occurs just prior to massive flow separation on the upper surface of the flap. If the direction of the search is reversed just after the flap has stalled, the irreversible nature of the flow precludes reattachment and the value for the lift coefficient found during the approach to the maximum is now much lower at the same point in the design space. Hence, the objective function is multi-valued and path dependent.

Consider an optimizer negotiating the paths of figure 6.22. Moving along any of the four outgoing paths other than the Y=1.956%C path with a small enough step size so as not to greatly overshoot the optimum should result in convergence. On the other hand, approaching the optimum of the Y=1.956%C path is more difficult due to the sudden stall resulting in almost no curvature in the path. As an alternative, intelligent algorithms could be employed, possibly using knowledge gained from an initial coarse baseline data set, which use unidirectional search patterns that retain a path history. Algorithm sensitivity to separated flow could be incorporated by monitoring top surface flap pressures, allowing identification of impending stall. CFD

methods may be able to predict this hysteretic phenomena and employ an optimizer using time accurate methods. At the time of this writing this approach is likely to be cost prohibitive.

7.4 Recommendations for Future Work

It is suggested that future research consider optimizations based on lift and drag including optimizing for best lift-to-drag ratio. Extending the study to higher angles-of-attack at or near maximum lift would be beneficial to aircraft designers but, requires the careful integration of a sidewall boundary layer control system.

This study demonstrated the practicality of in situ experimental geometry optimization but made little effort to optimize the efficiency of method. More sophisticated gradient and search methods should be evaluated as well as other methods including quasi-Newton methods which extract second order information from the available first order data.

Hysteresis in lift as a function of flap position was discovered when tests were conducted with continuous flow conditions. It was shown that optimal lift coefficients determined using continuous flow conditions exist over an extended range of flap positions when compared to those determined using intermittent (traditional) conditions. For a complete evaluation of the benefit of this lift increment to high-lift system efficiency, drag must be measured simultaneously.

Recommended future testing includes continuously measuring lift as the true flap trajectory is followed, requiring that a third degree of freedom,

flap deflection angle, be added to the actuators. Here again, drag must be measured in conjunction with lift to provide a complete picture of airfoil performance.

Extension of the current two-dimensional technology to higher Reynolds/Mach number facilities will require a redesign of the internal actuators to test at near flight conditions due to the higher loads. A suitable configuration may be a hybrid actuation system which draws on the superior power of actuators fitted just outside the tunnel sidewall, and a passive bracket system on the model which provides reaction forces and moments through bearing surfaces.

Regarding extension of the technology to three-dimensional testing, it appears plausible to install flap actuators in half-span models and eventually full three-dimensional models, which can be tested at near flight test conditions using the methods presented in this work.

8 CONCLUSIONS

A realistic two-dimensional three-element wind tunnel airfoil model was designed with internal servo actuators for adjusting flap position. This model was used to prove that internal actuators are practical for varying flap position during wind tunnel testing. Lift coefficients for a range of flap gap and overhang riggings were documented at two angles-of-attack using two slat riggings with the automated model.

The viability of on-line experimental geometry optimization of multi-element airfoils was demonstrated using the three-element automated airfoil model. Three optimization routines, suitable for use with the wind tunnel model, were demonstrated with an off-line simulation of a wind tunnel experiment. Two optimization search methods, a variable-size simplex and a fixed-size simplex routine, as well as a steepest ascent gradient method performed favorably during simulated on-line wind tunnel testing.

The steepest ascent method was chosen as the most robust and efficient for wind tunnel trials. The steepest ascent method was demonstrated on-line for four known configurations using two angles-of-attack; one angle was chosen as representative of a subsonic transport aircraft approach condition, and the other was chosen as the limiting angle-of-attack for maintenance of flow two-dimensionality for the wind tunnel setup. The steepest ascent optimizer was demonstrated successfully with an unknown configuration which employed a Gurney flap on the lower surface of

the model flap using a previously untested angle-of-attack. Extensions of the methods developed for use with three-dimensional testing were discussed.

Aerodynamic hysteresis was shown to be a critical issue when evaluating incremental lift measurements due to changes in flap position while the wind tunnel flow was kept on. Flow attachment on the upper surface of the flap was prolonged over an expanded range of gap and overhang settings using continuous flow conditions when compared to (traditional) intermittent flow conditions. In some cases, a favorable lift increment was shown to exist for these expanded gap and overhang settings.

REFERENCES

Abbott, I.H. and Von Doenhoff, A.E., "Theory of Wing Sections," Dover, 1959

Adair, D. and Horne, W.C., "Turbulent Separated Flow in the Vicinity of a Single-Slotted Airfoil Flap," AIAA 88-0613, January 1988

Adair, D. and Horne, W.C., "Characteristics of Merging Shear Layers and Turbulent Wakes of a Multi-Element Airfoil," NASA TM 100053, February 1988

Alcorn, C.W., "Boundary Layer Influences on the Subsonic Near-Wake of a Family of Three-Dimensional Bluff Bodies," Ph.D. Dissertation, Department of Mechanical Engineering and Mechanics, Old Dominion University, Norfolk, VA, 1993

Anderson, W.K. and Bonhaus, D.L., "Navier-Stokes Computations and Experimental Comparisons for Multielement Airfoil Configurations," AIAA 93-0645, 1993

Ashby, D.L., "Effects of Lift-Enhancing Tabs on a Two-Element Airfoil," Aerospace Engineering, pp. 31-37, April 1996

Backley, F., personal conversation, machinist and model builder, NASA Langley Research Center, Hampton, VA, January 1994

Baldwin, B.S. and Barth, T.J., "A One-Equation Turbulence Transport Model for High Reynolds Number Wall-Bounded Flows," NASA TM 102847, August 1990

Baldwin, B.S. and Lomax, H., "Thin Layer Approximation and Algebraic Model for Separated Flows," AIAA 78-0257, 1978

Banerjee, R. and Bhattacharyya, B.C., "Evolutionary Operation to Optimize Three-Dimensional Biological Experiments," Biotechnology and Bioengineering, Vol. 41, pp. 67-71, 1993

Barth, T.J. and Linton, S.W., "An Unstructured Mesh Newton Solver for Compressible Fluid Flow and Its Parallel Implementation," AIAA 95-0221, 1995

Bayard, D.S., Hadaegh, F.Y., and Meldrum, D.R., "Optimal Experiment Design for Identification of Large Space Structures," Automatica, Vol. 24, pp. 357-364, 1988

Beam, R. and Warming, R.F., "An Implicit Factored Scheme for Compressible Navier-Stokes Equations," AIAA Journal, Vol. 16, pp. 393-402, April 1978

Beck, J.V. and Arnold, K.J., "Parameter Estimation in Engineering and Science," John Wiley & Sons, 1977

Beer, F.P. and Johnston Jr., E.R., "Mechanics of Materials", McGraw-Hill Book Company, 1981

Benek, J.A. Buningg, P.G., and Steger, J.L., "A 3-D Chimera Grid Embedding Technique," AIAA 85-1523-CP, July 1985

Beveridge, S.G.G. and Schechter, R.S., "Optimization: Theory and Practice," McGraw-Hill Book Company, 1970

Biber, K. and Zumwalt, G.W., "Hysteresis Effects on Wind Tunnel Measurements of a Two-Element Airfoil," AIAA Journal, Vol. 31, No. 2, pp. 326-330, February 1993.

Biber, K. and Zumwalt, G.W., "Experimental Studies of a Two-Element Airfoil with Large Separation," AIAA 92-0267, 1992

Box, G.P. and Draper, N.R., "Empirical Model Building and Response Surfaces," John Wiley & Sons, 1987

Braden, J.A., Whipkey, R.R., Jones, G.S., and Lilley, D.E., "Experimental Study of the Separating Confluent Boundary-Layer," NASA CR-3655, 1983, also AIAA 86-0505, January 1986

Braslow, A.E., and Knox, E.C., "Simplified Method for Determination of Critical Height of Distributed Roughness Particles for Boundary-Layer Transition at Mach Numbers from 0 to 5," NACA TN 4363, September 1958

Brune, G.W. and McMasters, J.H., "Computational Aerodynamics Applied to High-Lift Systems," Applied Computational Aerodynamics, editor Henne, P.A., Progress in Astronautics and Aeronautics, AIAA, Vol. 125, pp. 389-433, 1990

Buning, P.G., Chan, W.M., Renze,K.J., Sondak,D., and Chiu,I.T., "OVERFLOW/F3D User's Manual, Version 1.6n," NASA Ames Research Center, Moffett Field, CA, October 1991

Butter, D.J., "Recent Progress on Development and Understanding of High Lift Systems," AGARD-CP-365, 1984

Cebeci, T., "An Interactive Boundary-Layer Approach to Multielement Airfoils at High Lift," Proceedings of The Fifth Numerical and Physical Aspects of Aerodynamic Flows, California State University, Long Beach, CA, pp. 1-12, 1992

Cebeci, T. and Smith, A.M.O., "Analysis for Turbulent Boundary Layers," Academic Press, 1974

Chan, W.M. and Steger, J.L., "A Generalized Scheme for Three-Dimensional Hyperbolic Grid Generation," AIAA 91-1586-CP, 1991

Cornell, J.A., "How to Apply Response Surface Methodology," American Society for Quality Control, Milwalkee, WI, 1990

Crowder, J.P., "Fluorescent Minitufts for Nonintrusive Flow Visualization," McDonnell Douglas Corporation, MDC J7374, February 1977

Dillner, B., May, F.W., and McMasters, J.H., "Aerodynamic Issues in the Design of High-Lift Systems for Transport Aircraft," AGARD-CP-365, 1984

Drela, M., "Design and Optimization Method for Multi-Element Airfoils," AIAA 93-0969, 1993

Drela, M., "Newton Solution of Coupled Viscous/Inviscid Multi-Element Airfoil Flows," AIAA 90-1470, 1990

Drela, M. and Giles, M.B., "Viscous-Inviscid Analysis of Transonic and Low Reynolds Number Airfoils," AIAA Journal, Vol. 25, No. 10, pp. 1347-1355, October 1987

Fletcher, R., and Reeves, C.M., "Function Minimization by Conjugate Gradients," Computer Journal, Vol. 7, pp. 149-154, 1964

Fox, R.L., "Optimization Methods for Engineering Design," Addison Wesley, 1971

Fox, R.T. and Lee, D., "Optimization of Metal Injection Molding: Experimental Design," International Journal of Powder Metallurgy, Vol. 26, No. 3, pp. 233-243, 1990

Garcia, S. and Scott, E.P., "Use of Genetic Algorithms in Optimal Experimental Designs," Proceedings of the 2nd International Conference on Inverse Problems in Engineering, eds. Delaunay, D., Raynand, M., and Woodbury, K., Engineering Foundation Conferences, New York, 1996

Gardner, T.P., "Optimization of Diesel Fuel Injection and Combustion System Parameters for Low Emissions Using Taguchi Methods," Proceedings of the 13th Annual Fall Technical Conference of the ASME Internal Combustion Engine Division - Fuels, Controls and Aftertreatment for Low Emissions Engines, ASME, 1991

Haftka, R.T., and Gürdal, Z., "Elements of Structural Optimization," 3rd Ed., Kluwer Academic Publishers, 1992

Hale, F. J., "Aircraft Performance Selection and Design," John Wiley and Sons, 1994

Hanson, P., personal communication, formerly assistant Division Chief, Dynamic Loads Division, Aeroelasticity Branch, NASA Langley Research Center, Hampton, VA, February 1998

Hoerner, S.F., "Fluid-Dynamic Lift," 2nd Ed., Hoerner Fluid Dynamics, Vancouver, WA, 1985

Holland, J.H., "Adaptation in Natural and Artificial Systems: An Introductory Analysis with Applications to Biology, Control, and Artificial Intelligence," University of Michigan Press, Ann Arbor, MI, 1975

Innes, F., Pearcey, H.H., and Sykes, D.M., "Improvements in the Performance of a Three Element High Lift System by the Application of Airjet Vortex Generators," The Aeronautical Journal, Vol. 99, No. 987, pp. 265-274, August/September 1995

Jacoby, S.L.S., Kowalik, J.S., and Pizzo, J.T., "Iterative Methods for Nonlinear Optimization Problems," Prentice-Hall, 1972

Johnson Jr., J.L. and Phelps III, J.L. , "Low-Speed Aerodynamics of the Upper-Surface Blown Jet Flap," SAE 740470, 1974

Karagounis, T., Maxworthy, T., and Spedding, G.R., "Generation and Control of Separated Vortices over a Delta Wing by Means of Leading Edge Flaps," AIAA 89-0997, 1989

Katz, J. and Plotkin, A., "Low Speed Aerodynamics: From Wing Theory to Panel Methods," McGraw-Hill Book Company, 1991

Kaufman, B.A. and Stone, D.H., "A Process Optimization Method for Lap Shear Bond Strength," Proceedings of the 32nd International SAMPE Symposium and Exhibition, eds. Carson, R., Burgg, M., Kjuller, K.J., and Riel, F.J., SAMPE, Covina, CA, Vol. 32, pp. 444-495, April 6-9, 1987

Khummongkol, D., Charoenkool, A., and Pongkum, N., "Experimental Optimization of Activated Carbon Synthesis by the Simplex Search Method," Applied Energy, Vol. 41, pp. 243-249, 1992

Klausmeyer, S.M. and Lin, J.C., "Comparative Results From a CFD Challenge Over a 2D Three-Element High Lift Airfoil", NASA TM 112858, May 1997

King, D.L. and Buck, M.E., "Experimental Optimization of an Anisotropic Etching Process for Random Texturization of Silicon Solar Cells," Proceedings, 22nd IEEE Photovoltaic Specialists Conference, IEEE, Vol. 1, pp. 303-308, 1991

Kobashi, Y.,Mochizuki, O., and Ogawara, K., "The Structure of Turbulence of a Corner Flow," Structure of Complex Turbulent Shear Flow: Proceedings of the Symposium, Marseille, France, pp. 356-365, August 31 - September 3, 1982

Kohlman, D.L., "Introduction to V/STOL Airplanes," The Iowa State University Press, 1981

Kornilov, V.I. and Kharitonov, A.M., "Investigation of Turbulent Flows in the Streamwise Asymmetric Corner Configurations," Experiments in Fluids, Vol. 2, No. 4, pp. 205-212, 1984

Krottmaier, J., "Optimizing Engineering Designs," McGraw-Hill Book Company, 1993

Kuethe, A. and Chow, C. Y., "Foundations of Aerodynamics," 4th Ed., John Wiley and Sons, 1986

Landman, D. and Britcher, C.P., "Advanced Experimental Methods for Multi-Element Airfoils," AIAA 95-1784, 1995

Landman, D. and Britcher, C.P., "Experimental Optimization Methods for Multi-Element Airfoils," AIAA 96-2264, 1996

Lewis, S.M., D'Argenio, D.Z., Bekey, G.A., and Mittman, C., "Optimal Inputs for Parameter Determination of Inert Gas Washout from the Lung," Respiration Physiology, Vol. 50, pp. 111-127, 1982

Lin, J.C., Robinson, S.K., McGhee, R.J., and Valarezo, W.O., "Separation Control on High Reynolds Number Multi-Element Airfoils," AIAA 92-2636, June 1992

Lin, J.C., personal communication, Engineer, Flow Modeling and Control Branch, NASA Langley Research Center, Hampton, VA, June 1993

Lin, J.C. and Dominik, C.J., "Optimization of an Advanced Design Three Element Airfoil at High Reynolds Numbers," AIAA 95-1858, 1995

Ljungström, B.L.G., "Development of a 2-Dim Wake Drag Evaluation System," FFA TN AU-860, 1973a

Ljungström, B.L.G., "2-D Wind Tunnel Experiments with Double and Triple Slotted Flaps," FFA TN AU-993, 1973b

Lynch, F.T., "Experimental Necessities for Subsonic Transport Configuration Development," AIAA 92-0158, January 1992

Marcum, D.L., "Generation of Unstructured Grids for Viscous Flow Applications," AIAA 95-0212, 1995

Mathsoft, "Mathcad User's Guide," Mathsoft Inc., 1995

McCormick, B.W., "Aerodynamics of V/STOL Flight," Academic Press, 1967

McCormick, B.W., "Aerodynamics, Aeronautics and Flight Mechanics," 2nd Ed., John Wiley and Sons, 1995

Meyers, J.F. and Hepner, T.E., "Velocity Vector Analysis of a Juncture Flow using a Three Component Laser Velocimeter," Presented at the Second International Symposium on Applications of Laser Anemometry to Fluid Dynamics, Lisbon, Portugal, July 2-4, 1984

Morgan, H.L., Ferris, J.C., and McGhee, R.J., "A study of High-Lift Airfoils at High Reynolds Numbers in the Langley Low Turbulence Pressure Tunnel," NASA TM-89125, July 1987

Mueller, T.J. and Batill, S.M., "Experimental Studies of Separation on a Two-Dimensional Airfoil at Low Reynolds Numbers," AIAA Journal, Vol. 20, No. 4, pp. 457-463, April 1982

Nakayama, A., Kreplin, H.-P., and Morgan, H.L., "Experimental Investigation of Flowfield About a Multielement Airfoil," AIAA Journal, Vol. 28, No. 1, pp. 14-21, January 1990

Nelder, J.A., and Mead, R., "A Simplex Method for Function Minimization," Computer Journal, Vol. 7, pp. 308-313, 1965

Nelson, R.C., "An Overview of High Lift Aerodynamics," AIAA Professional Studies Series, published short course notes, San Diego CA, June 23-24, 1995

Olson, L.E. and Orloff, K.L., "On the Structure of Turbulent Wakes and Merging Shear Layers of Multielement Airfoils," AIAA 81-1248, June 1981

Otto, J.C., Paraschivoiu, M., Yesilyurt, S., and Patera, A.T., "Bayesian-Validated Computer-Simulation Surrogates for Optimization and Design," Proceedings of the ICASE Workshop on Multidisciplinary Design Optimization, Hampton, VA, March 1995

Otto, J.C., Landman, D., and Patera, A.T., "A Surrogate Approach to the Experimental Optimization of Multi-Element Airfoils," AIAA 96-4138, 1996

Pankhurst, R.C. and Holder, D.W., "Wind Tunnel Technique," Revised Ed., Sir Issac Pitman & Sons, 1965

Papadakis, M., Myose, R.Y., and Matallana, S., "Experimental Investigation of Gurney Flaps on a Two Element General Aviation Airfoil," AIAA 97-0728, 1997

Partlett, L.P., "Free-Flight Wind-Tunnel Investigation of a Four-Engine Sweptwing Upper-Surface Blown Transport Configuration," NASA TN D-8479, 1977

Paschal, K., Goodman, W., McGhee, R., Walker, B., and Wilcox, P.A., "Evaluation of Tunnel Sidewall Boundary-Layer-Control Systems for High-Lift Airfoil Testing," AIAA 91-3243, 1991

Phadke, M. S., "Quality Engineering Using Robust Design," Prentice-Hall, 1989

Phelps, A.E., personal communication, president of Prestec, Inc. (formerly assistant Branch Head for Subsonic Aerodynamics Branch, NASA Langley Research Center, Hampton, VA), December 1997

Pope, A. and Goin, K.L., "High Speed Wind Tunnel Testing," John Wiley and Sons, 1978

Rae, W.H. and Pope, A., "Low Speed Wind Tunnel Testing," John Wiley and Sons, 1984

Renze, K.J., Buning, P.G., and Rajagopalan, R.G., "A Comparative Study of Turbulence Models for Overset Grids," AIAA 92-0437, 1992

Scheiman, J. and Kubendran, L.R., "Laser Velocimeter Measurements in a Wing-Fuselage Type Juncture," NASA TM-100588, April 1988

Scott, E.P. and Haftka, R.T., "Optimization and Experiments," AIAA 95-0121, 1995

Selig, M.S., Guglielmo, J.J., Broeren, A.P., and Giguère, P., "Experiments on Airfoils at Low Reynolds Numbers", AIAA 96-0062, 1996

Semones, G. B. and Lim, H.C., "Experimental Multivariate Adaptive Optimization of the Steady-State Cellular Productivity of a Continuous Baker's Yeast Culture," Biotechnology and Bioengineering, Vol. 33, pp. 16-25, 1989

Shenk, A, "Calculus and Analytic Geometry," 2nd Ed., Goodyear Publishing Company, 1979

Smith, A.M.O., "High-Lift Aerodynamics," AIAA 74-939, 1974

Spalart, P.R. and Allmaras, S.R., "A One-Equation Turbulence Model for Aerodynamic Flows," AIAA 92-0439, 1992

Spendley, W., Hext, G.R., and Himsworth, F.R., "Sequential Application of Simplex Designs in Optimisation and Evolutionary Operation," Technometrics, Vol. 4, No. 4, pp. 441-461, November 1962

Stainback, C.P., McGghee, R.J., Beasley, W.D., and Morgan Jr., H.R., "The Langley Research Center's Low-Turbulence Pressure Tunnel," AIAA 86-0762, 1986

Valarezo, W.O., Dominik, C.J., McGhee, R.J., Goodman, W.L., and Paschal, K.B., "Multi-Element Airfoil Optimization for Maximum Lift at High Reynolds Numbers," AIAA 91-3332-CP, 1991

Valarezo, W.O., Dominik, C.J., and McGhee, R.J., "Multielement Airfoil Performance Due to Reynolds and Mach Number Variations," AIAA Journal of Aircraft, Vol. 30, No. 5, pp. 689-694, September - October 1993

Valarezo, W.O. and Mavriplis, D.J., "Navier-Stokes Applications to High-Lift Airfoil Analysis," AIAA 93-3534, 1993

van Gelder, P.A., "Design of an Integrated Control System for Flutter Margin Augmentation and Gust Load Alleviation, Tested on a Dynamic Windtunnel Model," NLR MP 86034 U, 1986

Vatsa, V.N., Sanetrick, M.D., Parlette, E.B., Eiseman, P., "Multi-Block Structured Grid Approach for Solving Flows Over Complex Aerodynamic Configurations," AIAA 94-0655, 1994

Villén J., Señoráns, F.J., Herraiz, M., Reglero, G., and Tabera, J., "Experimental Design Optimization of Large Volume Sampling in a Programmed Temperature Vaporizer. Application in Food Analysis," Journal of Chromatographic Science, Vol. 30, pp. 261-266, 1992

Walker, B., personal conversation, mathematician, Low Turbulence Pressure Tunnel, NASA Langley Research Center, Hampton, VA, December 1994

Walters, F.H., Parker Jr., L.R., Morgan, S.L., and Deming, S.L., "Sequential Simplex Optimization," CRC Press, 1991

Wedderspoon, J. R., "The High Lift Development of the A320 Aircraft," ICAS-86-2.3.2, 1986

Wentz, W.H., "Wind Tunnel Tests of the GA(W) - 2 Airfoil with 20% Aileron, 25% Slotted Flap, 30% Fowler Flap, and 10% Slot-Lip Spoiler," NASA CR-145139, 1976

Woods, W. A., "Visualized Flow," Pergamon Press, The Japan Society of Mechanical Engineers, 1988

Woodward, D.S., "Some Types of Scale Effect in Low-Speed, High-Lift Flows," ICAS-88-4.9.3, pp. 1402-1416, 1988

Yesilyurt, S., Ghaddar, C.K., Cruz, M.E., and Patera, A.T., "Bayesian-Validated Surrogates for Noisy Computer Simulations; Application to Random Media," SIAM Journal on Scientific Computing, to appear

Yesilyurt, S. and Patera, A.T., "Surrogates for Numerical Simulations; Optimization of Eddy-Promoter Heat Exchangers," Computer Methods in Applied Mechanics and Engineering, Vol. 121, pp. 231-257, 1995

APPENDIX A: ENGINEERING CALCULATIONS

A.1 Roughness Particle Size Calculations

For a fully turbulent boundary layer to be generated downstream of the roughness strip a Reynolds number R_k based on roughness particle height should be slightly larger than 600 [Braslow and Knox, 1958]. In order to pick a roughness height, first the velocity at the location of the transition strip must be estimated. Choosing this location as 5% of local chord on the top surface of each element [Rae and Pope, 1984; Papadakis et al., 1997] the velocity at this point is found by assuming incompressible inviscid flow outside the boundary layer. Using the well know relation for the pressure coefficient [Kuethe and Chow, 1986]:

$C_p = 1 - (u/U)^2$; u is the desired local velocity, U is the freestream velocity

Average C_p measured at 5% chord for the slat ≈ -5
Average C_p measured at 5% chord for the main ≈ -5
Average C_p measured at 5% chord for the flap ≈ - 3

U ≈ 30 m/s for the Reynolds number of 1,000,000

for the slat and main:	$-5 = 1 - (u/U)^2$	→ $u/U = 2.45$	$u = 74$ m/s
for the flap:	$-3 = 1 - (u/U)^2$	→ $u/U = 2$	$u = 60$ m/s

The 5% chord location in meters for the roughness strip is:

for the flap:	x = .05(5.4 in)(m/39.37 in) = 0.0069 m
for the slat:	x = .05(2.6 in)(m/39.37 in) = 0.0033 m
for the main:	x = .05(14.9 in)(m/39.37 in) = 0.019 m

To find the non-dimensional roughness height, first calculate $R_k / (R_x)^{1/2}$ where R_x is the Reynolds number based on location x from the leading edge to the roughness station (5% chord here).

$$R_x = \frac{\rho U x}{\mu}$$

$$\frac{R_k}{\sqrt{R_{x\,slat}}} = \frac{600}{\sqrt{\frac{(1.2)(30)(.0033)}{1.78 \times 10^6}}} = \frac{600}{81.7} = 7.34$$

All units are SI, and the corresponding result for the main element is 3.06. Using figure 4 of TN 4363 [Braslow and Knox, 1958] with freestream Mach number M = U/a = 30/340 = 0.088 ≈ 0 (the speed of sound is near standard conditions) the non-dimensional roughness height is found to be η≈1.66 for the main element and η≈ 3.5 for the slat. Now using the definition of non-dimensional roughness height, calculate the roughness height:

$$\eta_k = \frac{k}{2x}\sqrt{R_x} \rightarrow k = \frac{2x\eta_k}{\sqrt{R_x}} \rightarrow k_{slat} \approx \frac{2(.0033)(3.5)}{81.7} = .00028\,m \approx .01\,inches$$

A similar calculation for the main element gives a particle height of 0.012 inches. These two values represent the minimum and maximum particle sizes required. Choosing the largest size will allow the use of one particle size on all elements. An additional caveat should be borne in mind: if the station Reynolds number is less than 100,000 then the minimum value for R_k is 1000 [Rae and Pope, 1984]. Reviewing, the slat and main station Reynolds numbers are about 6,670 and 38,000. Reworking the calculations as shown

before, and choosing again the largest particle size (i.e. that of the main element), k = 0.019". The closest grit size is found to be #30 to err on the large side. This diameter is approximately 0.028 inches and was used for all elements. A roughness strip width of approximately 3/16 inch was chosen [Rae and Pope, 1984]. Number 30-grit carborundum particles were distributed on a masked strip which had been sprayed with an adhesive.

A.2 Determination of Lift Coefficient for 3 Element Airfoil from Surface Pressure Data

If the pressure coefficient (C_p) is known for each surface pressure tap location, the lift force may be calculated by integrating the pressures. Consider first the main element of the 3 element system. The pressure acting on the surface may be resolved into forces acting normal (lift) and parallel (drag) to the freestream. Let c be the chordwise position and C the chord length of the airfoil; the lift force is L.

Figure 1

Main Element

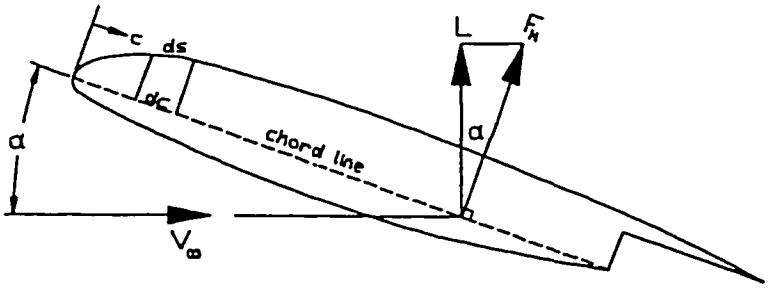

F_N is the force acting normal to the airfoil chordline. The incremental normal force may be calculated for a unit depth of span, as the pressure acting over the projected area dc along the chord line, where ΔP is the difference in pressures between the upper and lower surfaces:

$$\Delta P = P_{upper} - P_{lower} \qquad \text{(A.2-1)}$$

$$F_N = -\int_0^C \Delta P \, dc \qquad \text{(A.2-2)}$$

The lift force as shown in figure 1 is the component of the normal force which is perpendicular to the freestream direction.

$$L = F_N \cos\alpha \tag{A.2-3}$$

Recall the definition for pressure coefficient (C_p), where q is the dynamic pressure and, P_∞ is the freestream pressure.

$$C_p = \frac{P - P_\infty}{q} \tag{A.2-4}$$

The lift force can be written as:

$$L = q \cos\alpha \int_0^c (C_{P_{lower}} - C_{P_{upper}}) \, dc \tag{A.2-5}$$

Using the definition of lift coefficient (C_l), where the area per unit depth is the chord length C, write:

$$C_l = \frac{L}{q S} = \frac{\cos\alpha}{C} \int_0^c (C_{P_{lower}} - C_{P_{upper}}) \, dc \tag{A.2-6}$$

For a 3-element airfoil the component forces must be added to give the whole system lift. The lift of the slat and flap can be resolved normal to the freestream direction so that the system total lift is simply the sum of the component lift. For flap and slat deflection angles δ_f and δ_s respectively the individual lift coefficients are given as:

$$C_{l_{slat}} = \frac{\cos(\delta_s - \alpha)}{C_{slat}} \int_0^{C_{slat}} (C_{P_{lower}} - C_{P_{upper}})\, dc \qquad \text{(A.2-7)}$$

$$C_{l_{flap}} = \frac{\cos(\delta_f + \alpha)}{C_{flap}} \int_0^{C_{flap}} (C_{P_{lower}} - C_{P_{upper}})\, dc \qquad \text{(A.2-8)}$$

For convenience in obtaining the system lift coefficient, the stowed chord length for the cruise configuration airfoil is used as a reference chord length for the calculation of each coefficient. Calculation of the system lift coefficient is now an algebraic sum of the individual lift coefficients:

$$C_{l_{system}} = (C_{l_{main}} + C_{l_{slat}} + C_{l_{flap}})_{C_{stowed}} \qquad \text{(A.2-9)}$$

The trapezoidal rule is used for numerically integrating the pressure coefficients.

Appendix A.3 Flap Deflection at Full Scale Reynolds Numbers

This calculation was done using a MathCad worksheet. The drawing below depicts a two dimensional flap model of 36" span with restoring end moments applied through forces R1 at distance a. The problem can be simplified by noting the symmetry about the midspan of the flap. The dimensions are representative of a 3 element, 22" nested, 2D high lift model.

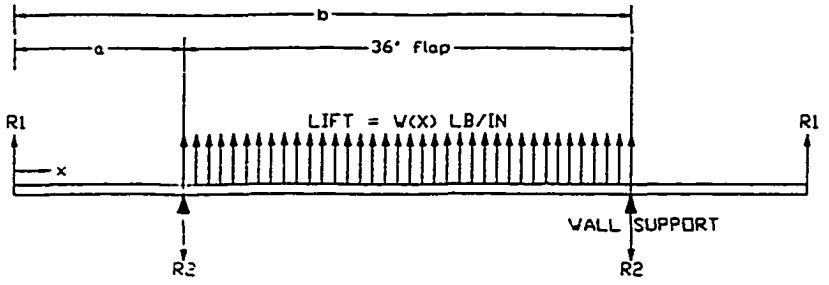

Choosing a total lift of 3000 lbs as representative of a load at full scale Reynolds numbers and distributing the load over the whole span we can solve for the moment in the flap by considering a section with positive moment M as shown.

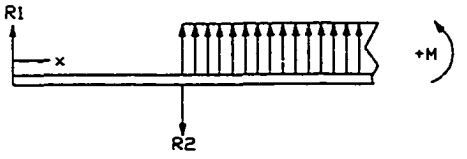

Choose R1 such that the deflection at midspan is zero	$R1 := 800$ lbs
Modulus of elasticity for typical steels	$E := 30000000$ psi
Moment of inertia of flap (based on 30% flap)	$I := .094$ in^4
Choose typical moment arm distance	$a := 14$ $b := 36 + a$ in
Distributed lift load	$w := \frac{3000}{36}$
Statics using symmetry	$R2 := R1 + \frac{1}{2} \cdot w \cdot 36$
Moment equation considering section of the beam as shown above	$M(x) := R1 \cdot x - R2 \cdot (x - a) + \frac{w}{2} \cdot (x - a)^2$
Integrate M(x)dx twice, find deflection equation using	$y(x) = \frac{1}{EI} \cdot \int \int M(x)\, dx\, dx$
Resulting equation for deflection between a and b	$y(x) = \frac{1}{EI} \cdot (F(x) + C_1 \cdot x + C_0)$

Where $F(x) := \frac{R1}{6}\cdot x^3 - \left[\frac{R2}{6}\cdot(x-a)^3\right] + \frac{w}{24}\cdot(x-a)^4$

Boundary conditions due to wall supports $y(a)=y(b)=0$

Solve for constants of integration using linear algebra $A := \begin{pmatrix} a & 1 \\ b & 1 \end{pmatrix}$ $b := \begin{pmatrix} -F(a) \\ -F(b) \end{pmatrix}$ $C := A^{-1}\cdot b$

Solve for deflection in flap and plot

$i := 14..50$ $x_i := i$ $y_i := \frac{1}{E\cdot I}\cdot\left(F(x_i) + C_0\cdot x_i + C_1\right)$ $xf_i := x_i - 14$

Midspan deflection $y_{32} = 0.0029$ in

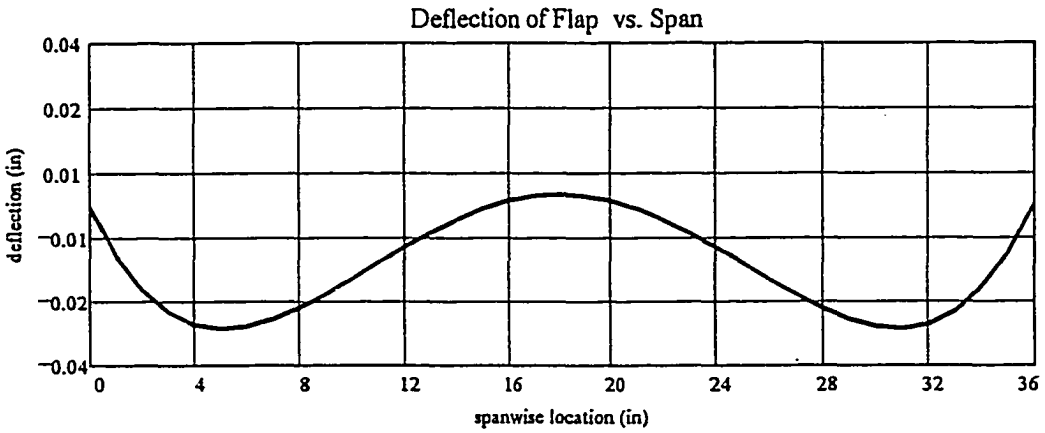

Compare maximum deflection using pinned ends no restoring end moments) $ymax := \frac{-5\cdot(-w)\cdot 36^4}{384\cdot E\cdot I}$ $ymax = 0.6463$

Check normal stress level in flap (psi) $c := .6$ $\sigma_i := \frac{M(x_i)\cdot c}{I}$

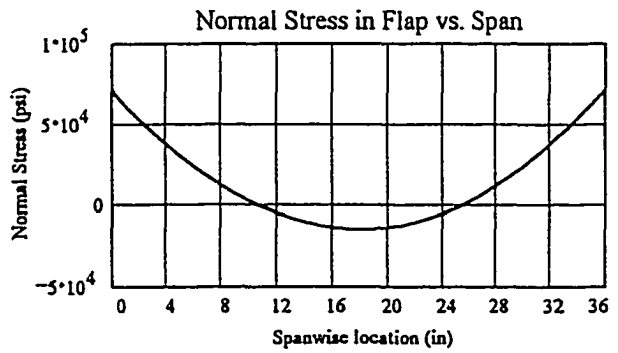

stress at wall

$\sigma_{14} = 7.1489\cdot 10^4$ psi

stress at midspan

$\sigma_{32} = -1.4681\cdot 10^4$ psi

Compare the previous results now to a conservative calculation (assumes pinned connections at brackets) for a model with a flap supported by 2 brackets. The same two dimensional flap model is used with a 36" span, but brackets are added, located 9" from the ends. The dimensions are representative of a 3 element, 22" nested, 2D high lift model.

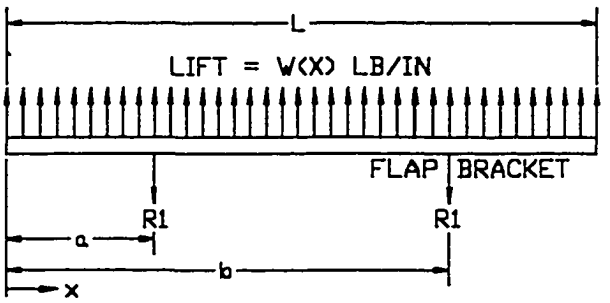

Length of flap

$$L := 36$$

Modulus of elasticity for typical steels

$$E := 30000000 \text{ psi}$$

Moment of inertia of flap (based on 30% flap)

$$I := .094 \quad \text{in}^4$$

Bracket locations at a and b, left to right using the same notation as previously

$$a := 9 \quad b := L - 9 \text{ in}$$

Distributed lift load

$$w := \frac{3000}{36}$$

Statics using symmetry, identical reactions at each bracket

$$R1 := \frac{1}{2} \cdot w \cdot 36$$

Moment equation, a<x<b

$$M2(x) := -R1 \cdot (x - a) + \frac{w}{2} \cdot x^2$$

Moment equation, x<a

$$M1(x) := \frac{w}{2} \cdot x^2$$

$$M(x) := \text{if}(x < a, M1(x), M2(x))$$

Integrate M(x)dx twice, find deflection equation using

$$y(x) := \frac{1}{EI} \cdot \int \int M(x)\, dx\, dx$$

Resulting equation for deflection between left side and center span

$$y(x) := \frac{1}{EI} \cdot \left(F(x) + C_0 \cdot x + C_1\right)$$

$$F2(x) := -\frac{Rl}{6}\cdot(x-a)^3 + \frac{w}{24}\cdot x^4$$

Again functions for the deflection equation for regions a<x<b and x<a respectively

$$F1(x) := \frac{w}{24}\cdot x^4$$

$$F(x) := \text{if}(x<a, F1(x), F2(x))$$

Boundary conditions due to flap brackets $y(a)=0$ $y(b)=0$

Solve for constants of integration a<x<b

$$A := \begin{pmatrix} a & 1 \\ b & 1 \end{pmatrix} \quad B := \begin{pmatrix} -F(a) \\ -F(b) \end{pmatrix} \quad C := A^{-1}\cdot B$$

Solve for range of deflection in flap and plot deflection vs span

$$i := 0..18 \qquad x_i := i \qquad y_i := \frac{1}{E\cdot I}\cdot\left(F(x_i) + C_0\cdot x_i + C_1\right)$$

maxy := max(y) maxy = 0.0565 miny := min(y) miny = −0.0081 range := maxy − miny

Range range = 0.0646 in

Midspan deflection $y_{18} = -0.0081$ in

$$j := 0..36 \qquad x_j := j$$

$$yp_j := \text{if}(j<19, y_j, y_{36-j})$$

Deflection at flap brackets (check to insure zero) $yp_9 = 0$ $yp_{27} = 0$

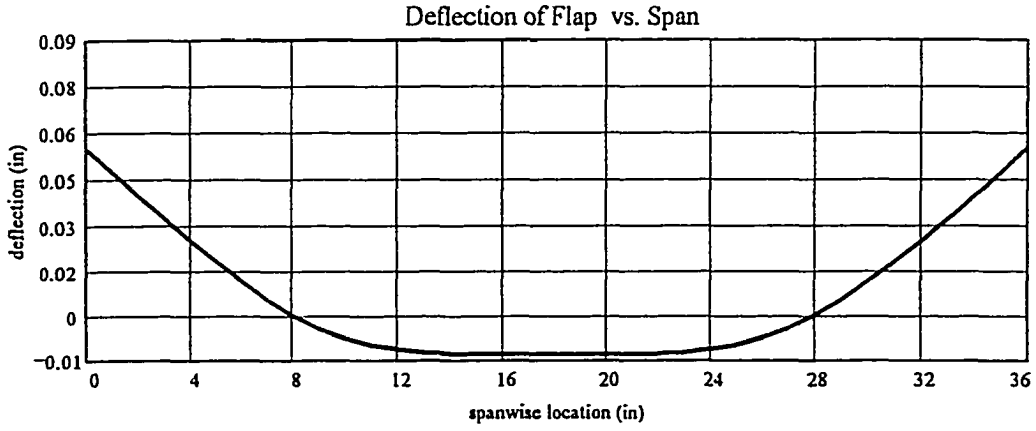

A.4 Standard Deviation of Measured Lift Coefficient

slat gap = 2.17% slat oh = -1.46% (slat B) A-O-A = 14

x=14.8, y=.3 (flap separated)	x=14.8, y=.5 (flap attached)	point number
2.6159	3.2801	1
2.6228	3.2776	2
2.6092	3.2899	3
2.626	3.3013	4
2.6093	3.298	5
2.6126	3.3034	6
2.6231	3.2885	7
2.6129	3.2599	8
2.6141	3.2735	9
2.6133	3.2725	10
2.6189	3.2772	11
2.622	3.2763	12
2.6186	3.2803	13
2.6174	3.2914	14
2.6123	3.3048	15
2.6155	3.305	16
2.6218	3.3047	17
2.6122	3.2926	18
2.6159	3.2878	19
2.6203	3.2799	20
2.618	3.301	21
2.6182	3.2809	22
2.6145	3.2701	23
2.6175	3.2903	24
2.6118	3.2825	25
2.615	3.2711	26
2.6169	3.296	27
2.6207	3.2851	28
2.6165	3.284	29
2.6178	3.2987	30
0.004071	0.011848	standard deviation
2.6167	3.286813	mean
0.155576	0.360483	% of mean

APPENDIX B: ENGINEERING DRAWINGS

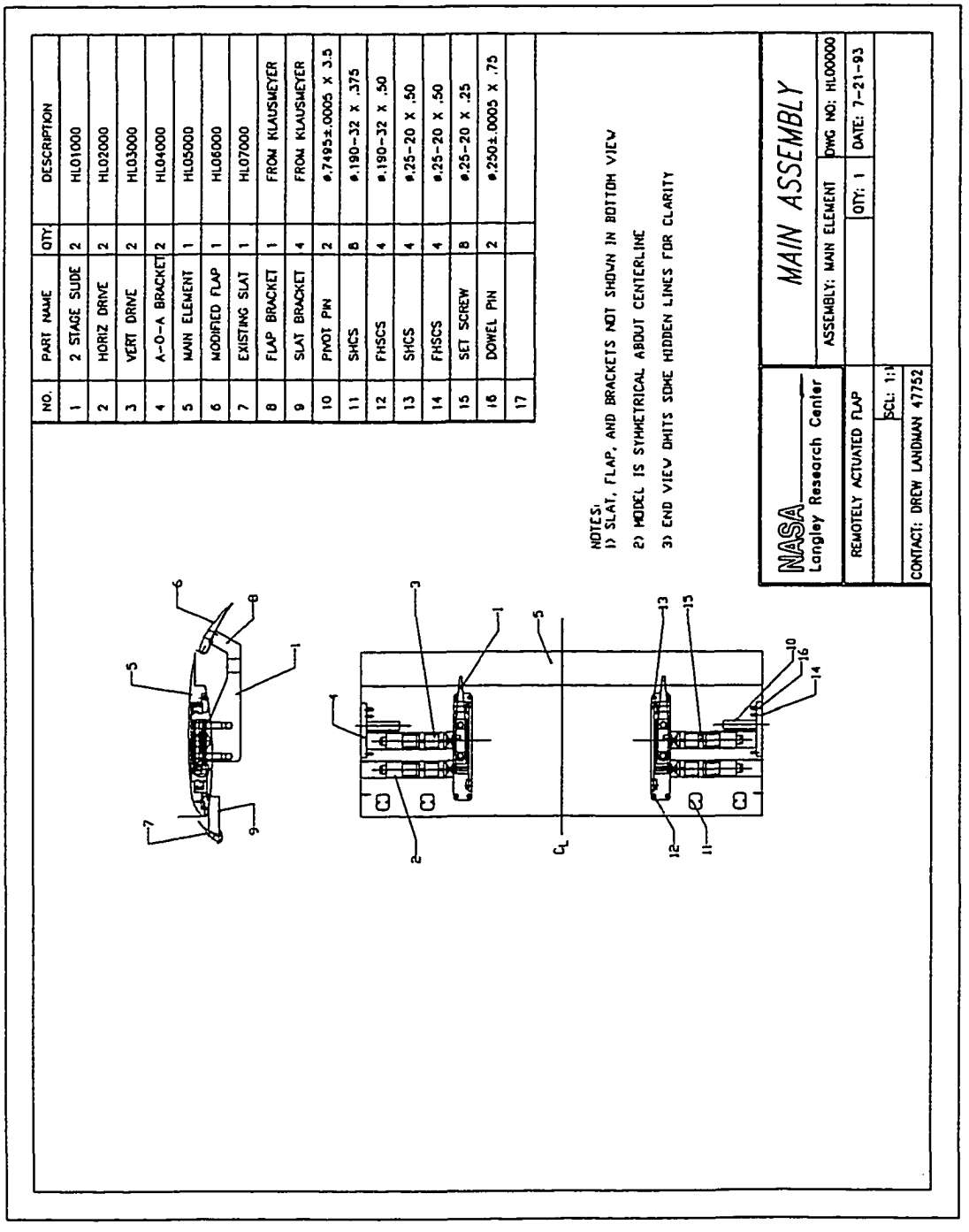

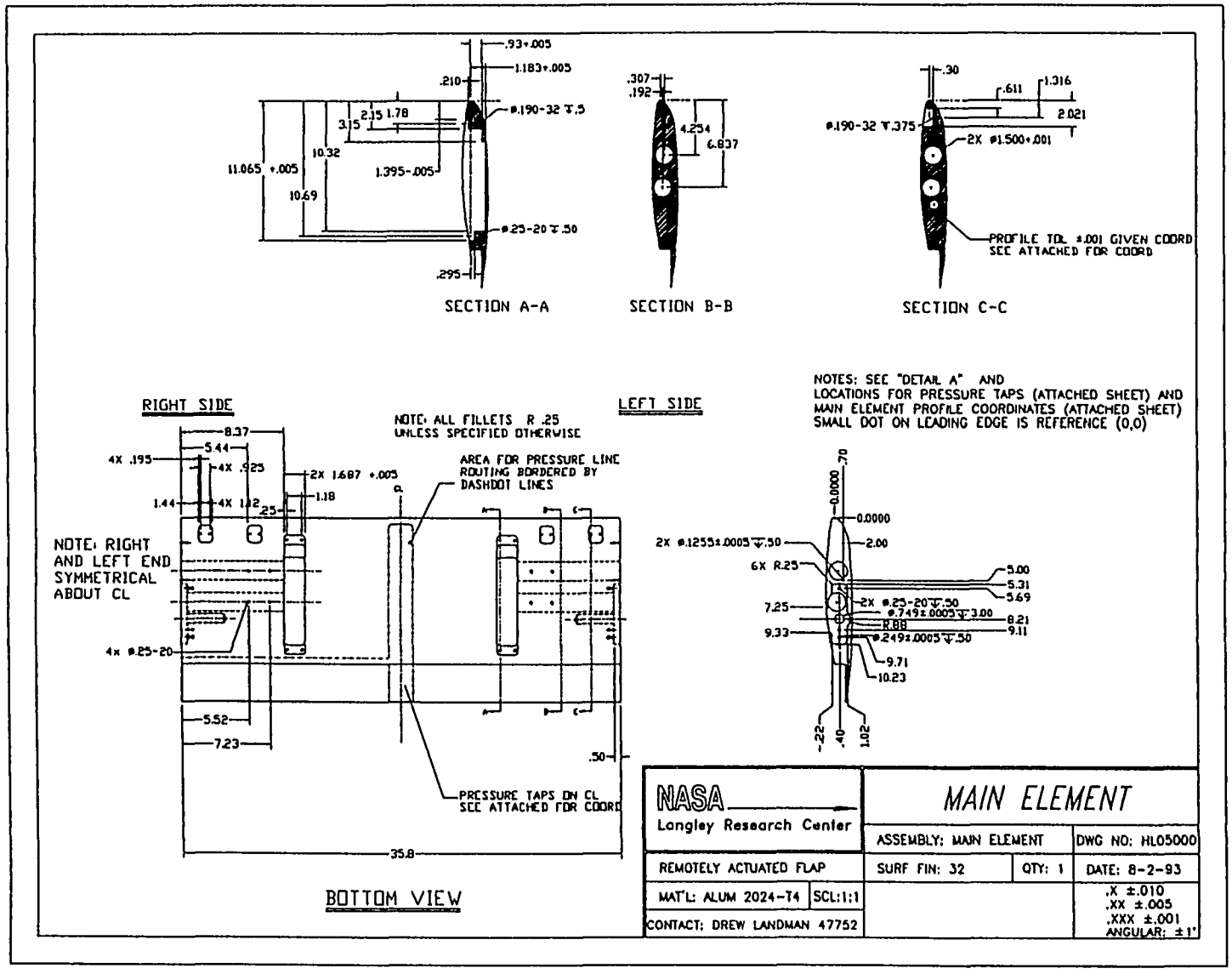

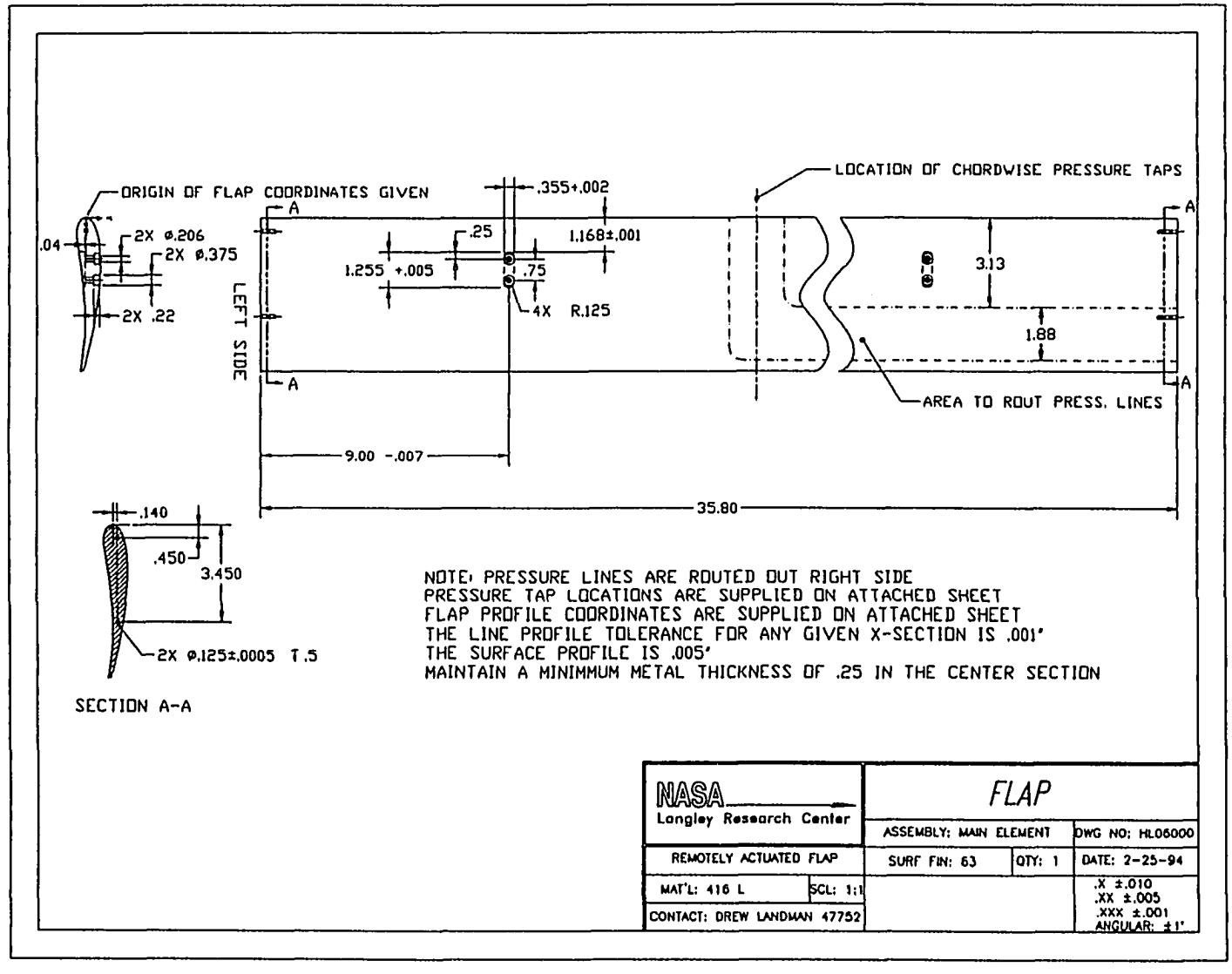

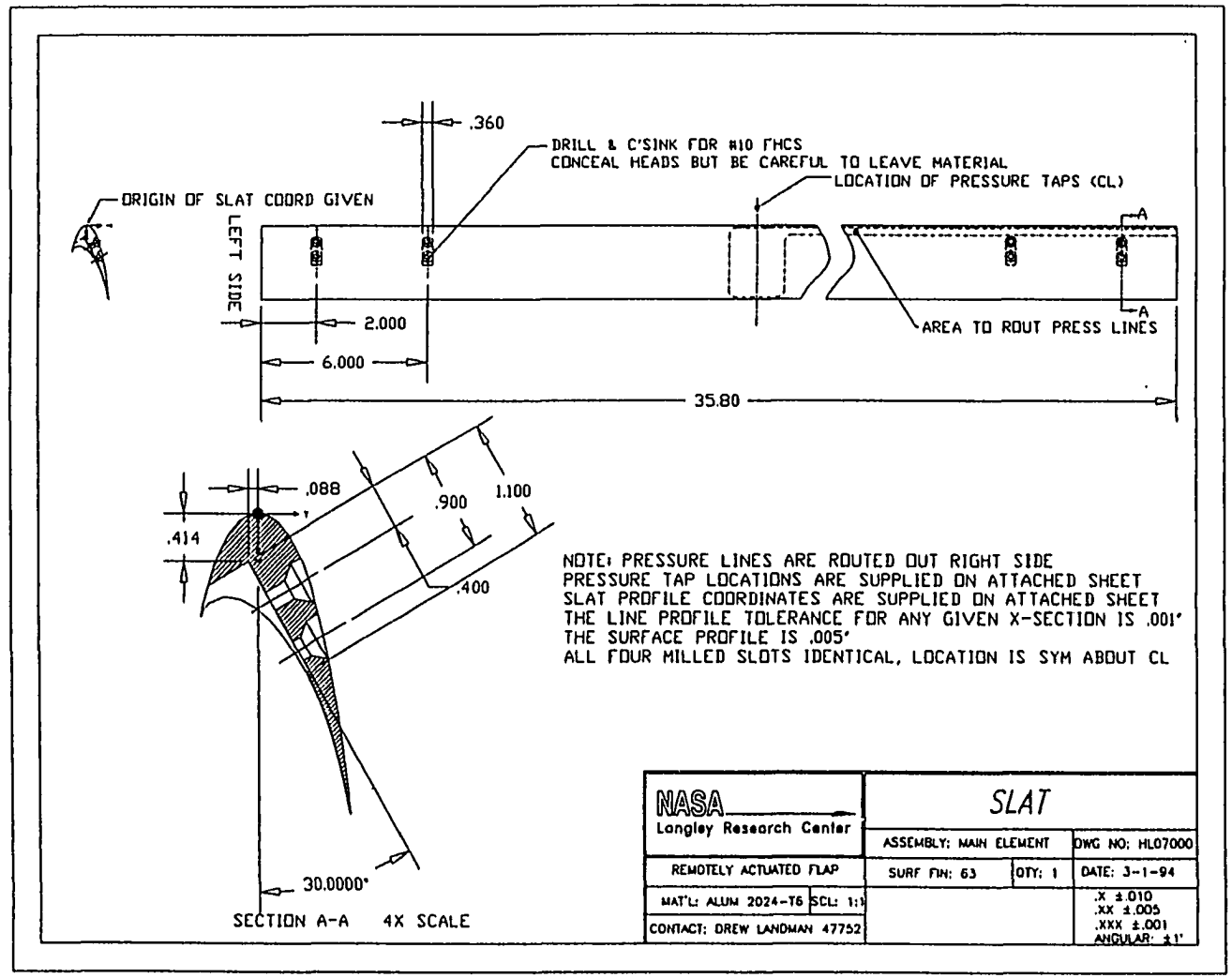

NOTE: LEFT ASSEMBLY SHOWN
(VIEWED FROM LEFT), R & L REQ'D,
PROFILE SHOWN FOR CLARITY ONLY

NO.	PART NAME	QTY.	DESCRIPTION
1	VERT SLIDE	1	DWG NO: HL01001
2	HORIZ SLIDE	1	DWG NO: HL01002
3	BASE, PLUG	1	DWG NO: HL01003
4	DOWEL PIN	2	ø.4999±.0001
5	LIMIT SWITCH	2	NEWARK 23F2296
6	CAP SCREWS	4	ø.086-56 X .375

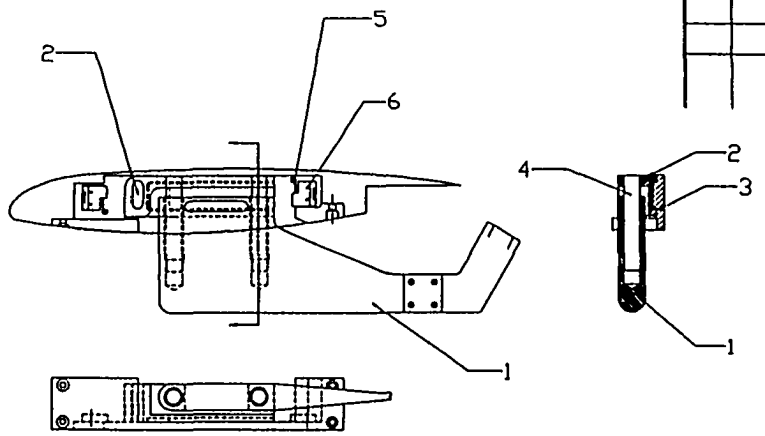

NASA Langley Research Center	2 STAGE SLIDE ASSBLY	
	ASSEMBLY: MAIN ELEMENT	DWG NO: HL01000
REMOTELY ACTUATED FLAP	SURF FIN: 63 QTY: 2	DATE: 6-29-93
SCL: 1:1	NOTES: 1 RIGHT, 1 LEFT	
CONTACT: DREW LANDMAN 47752		

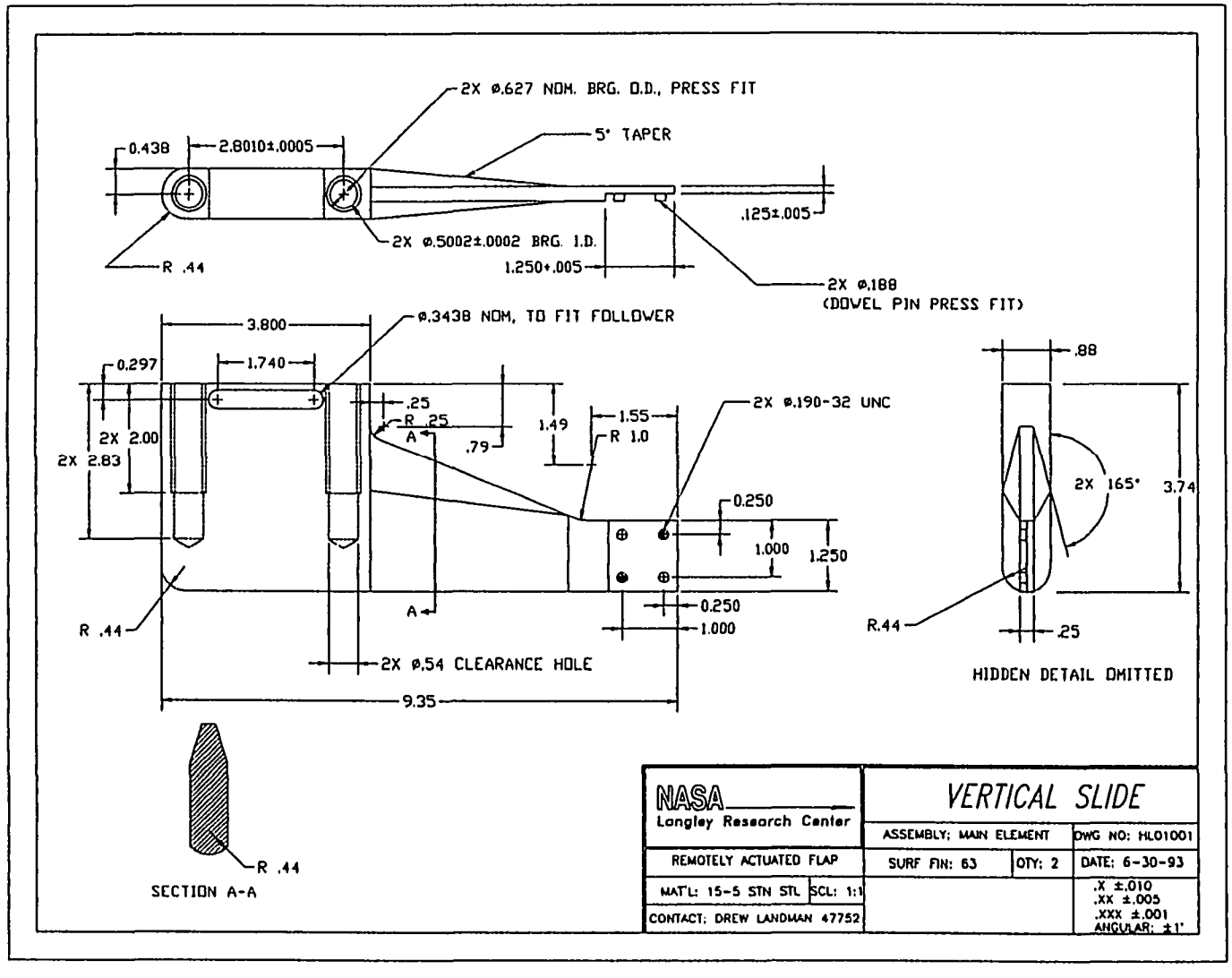

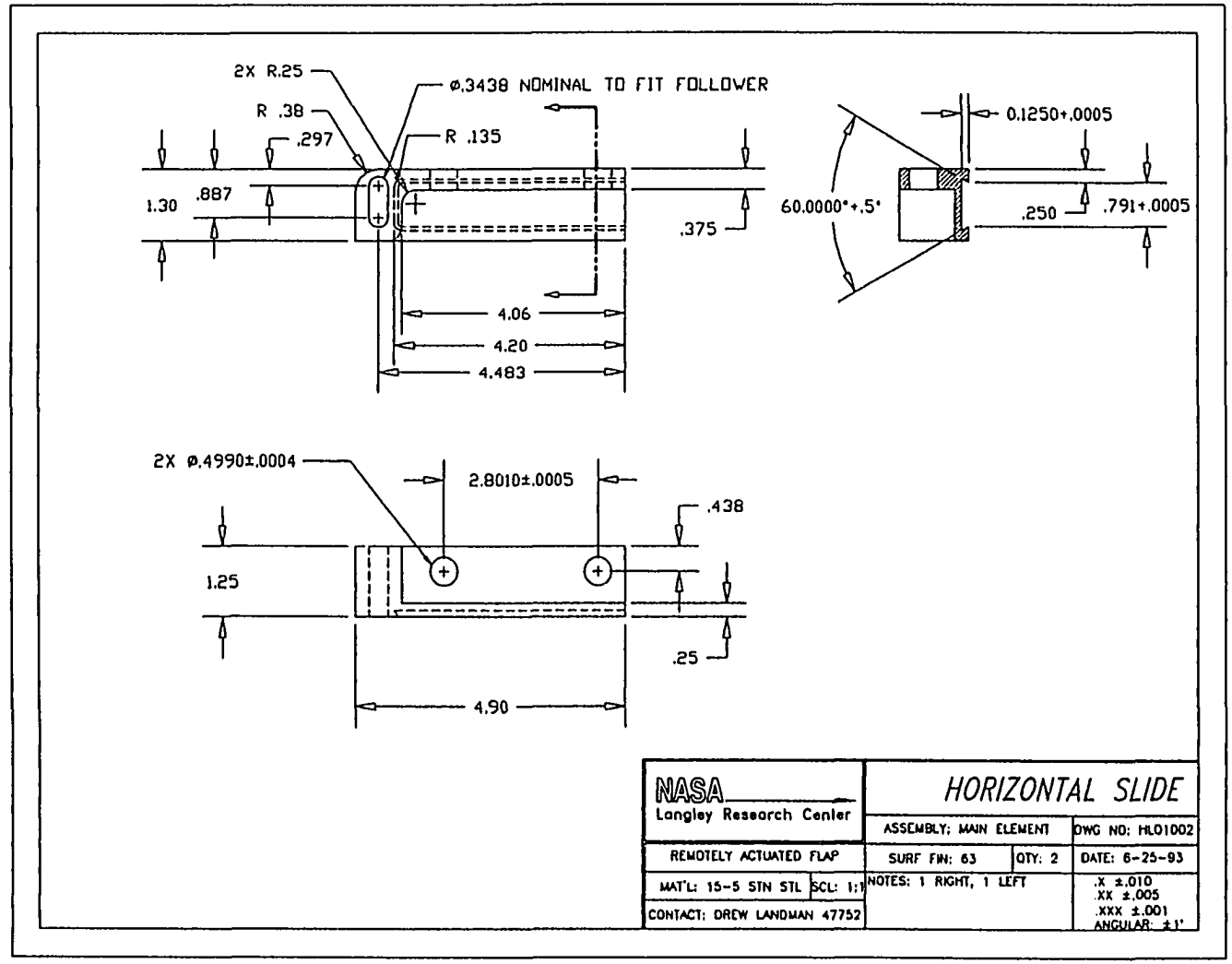

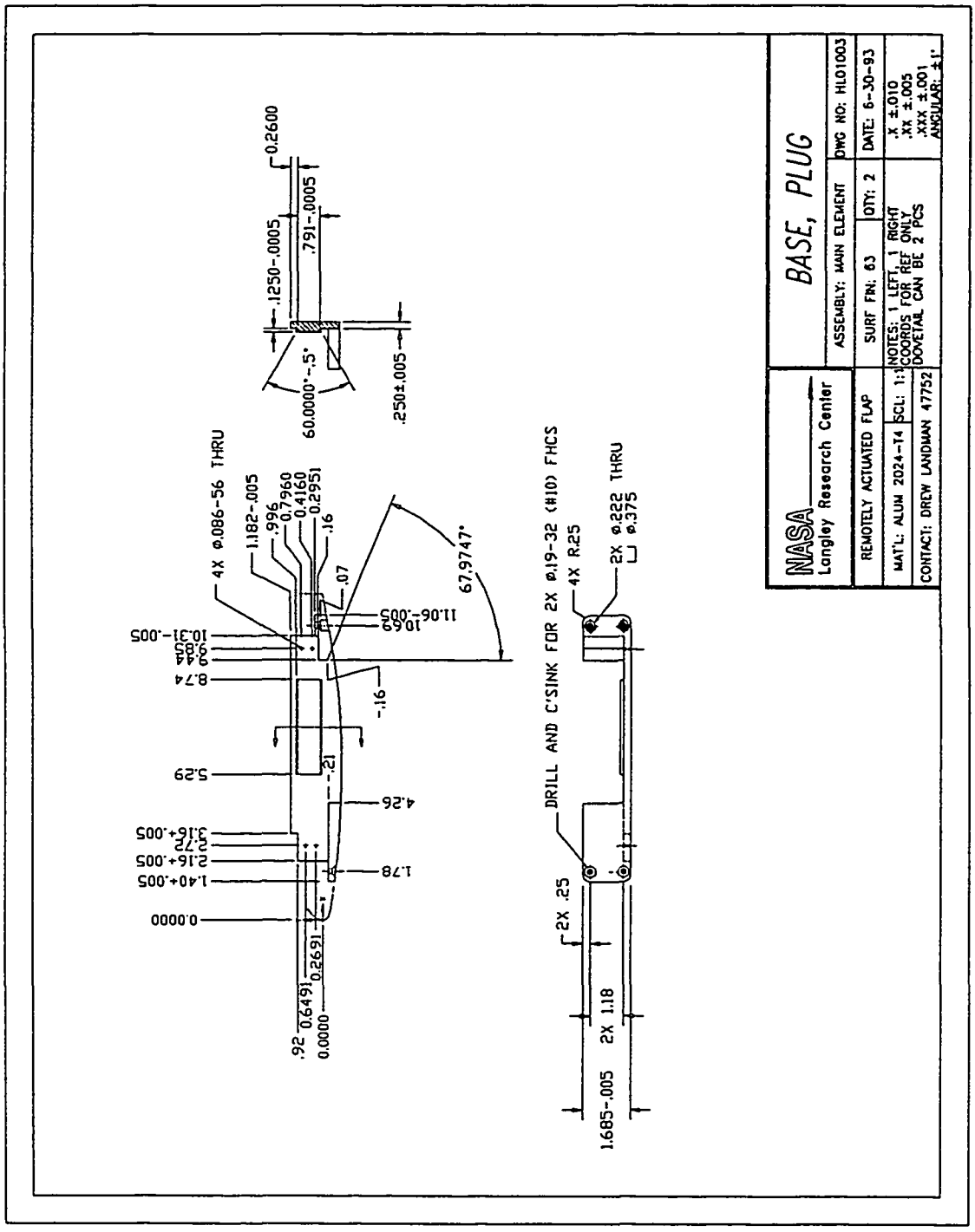

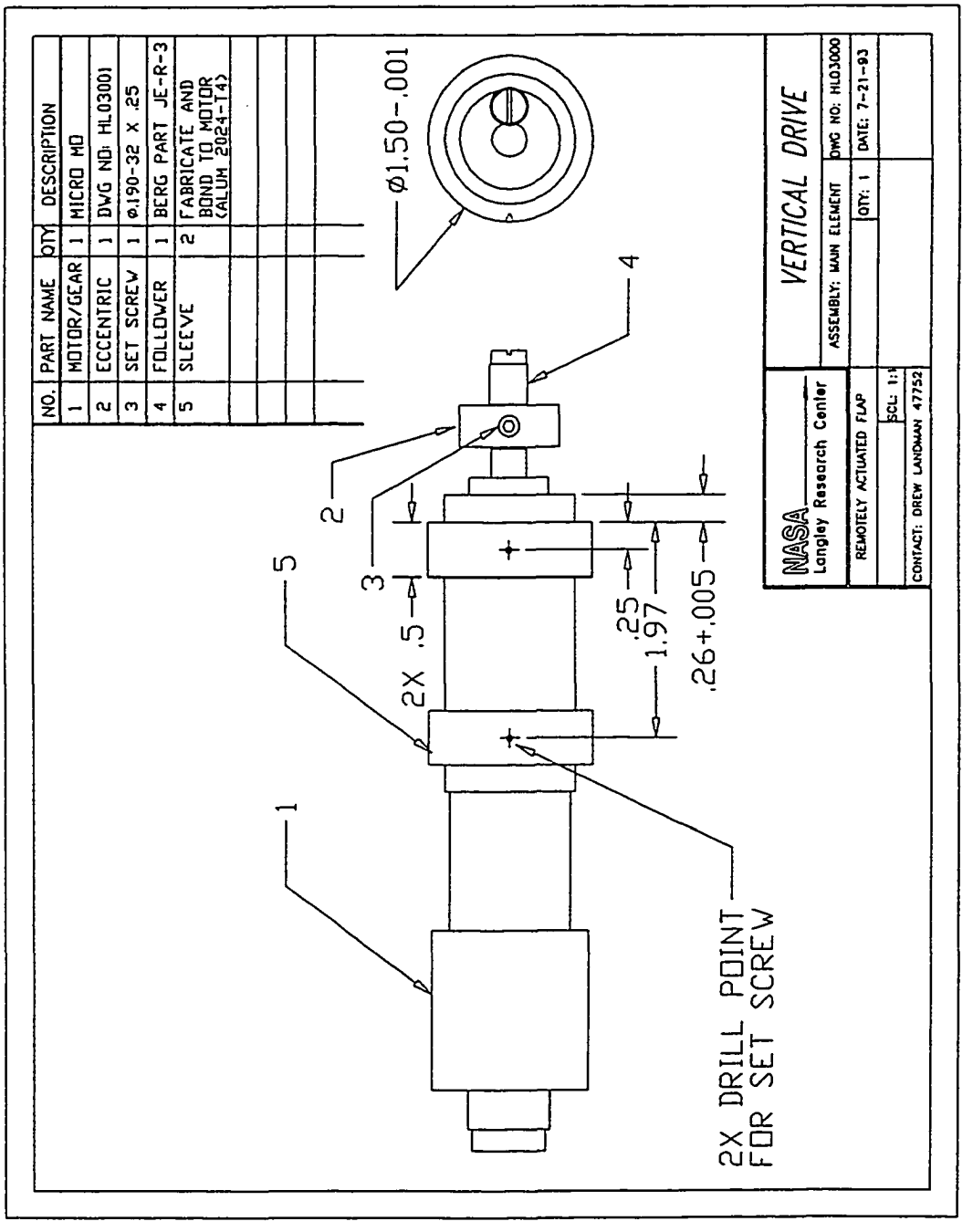

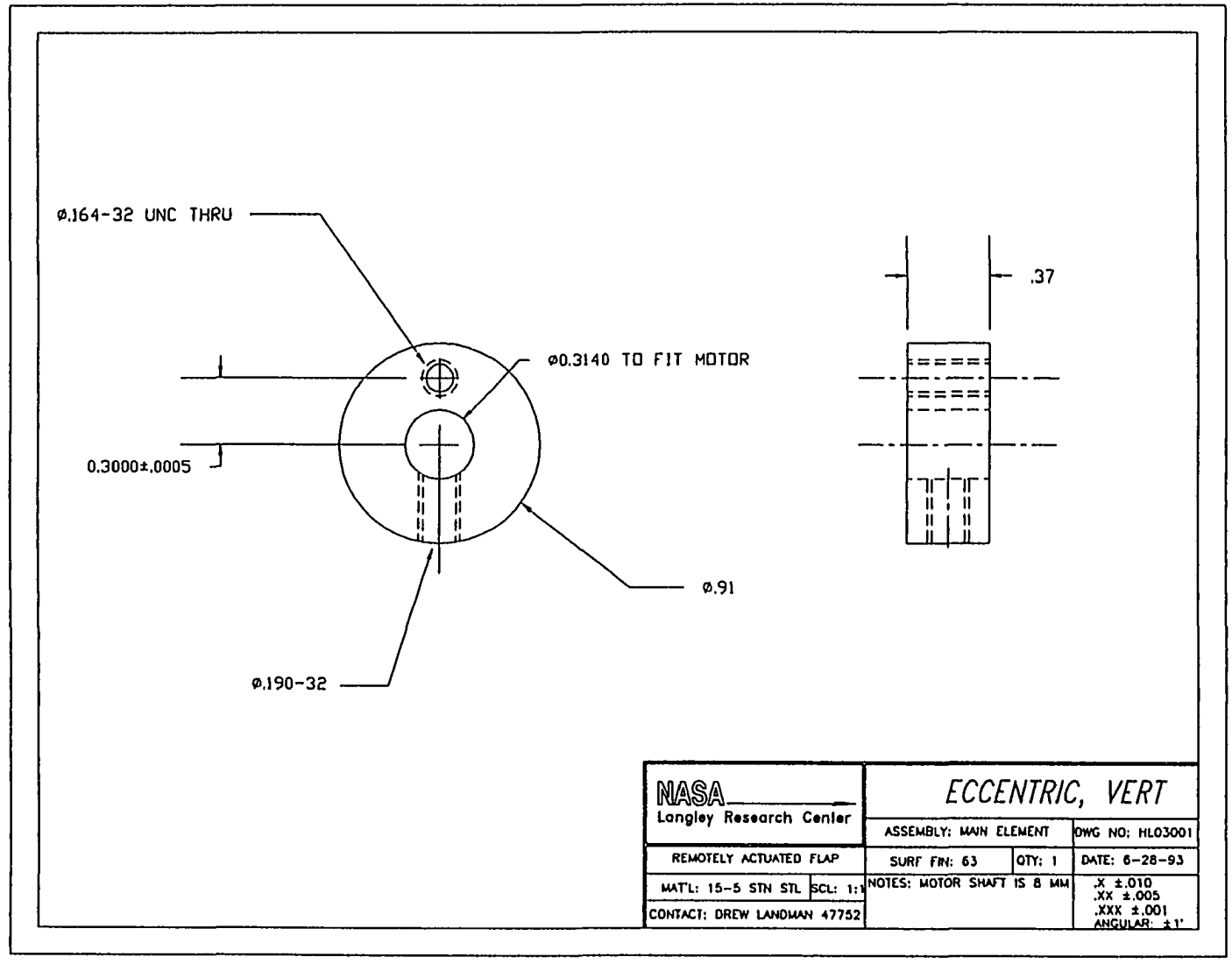

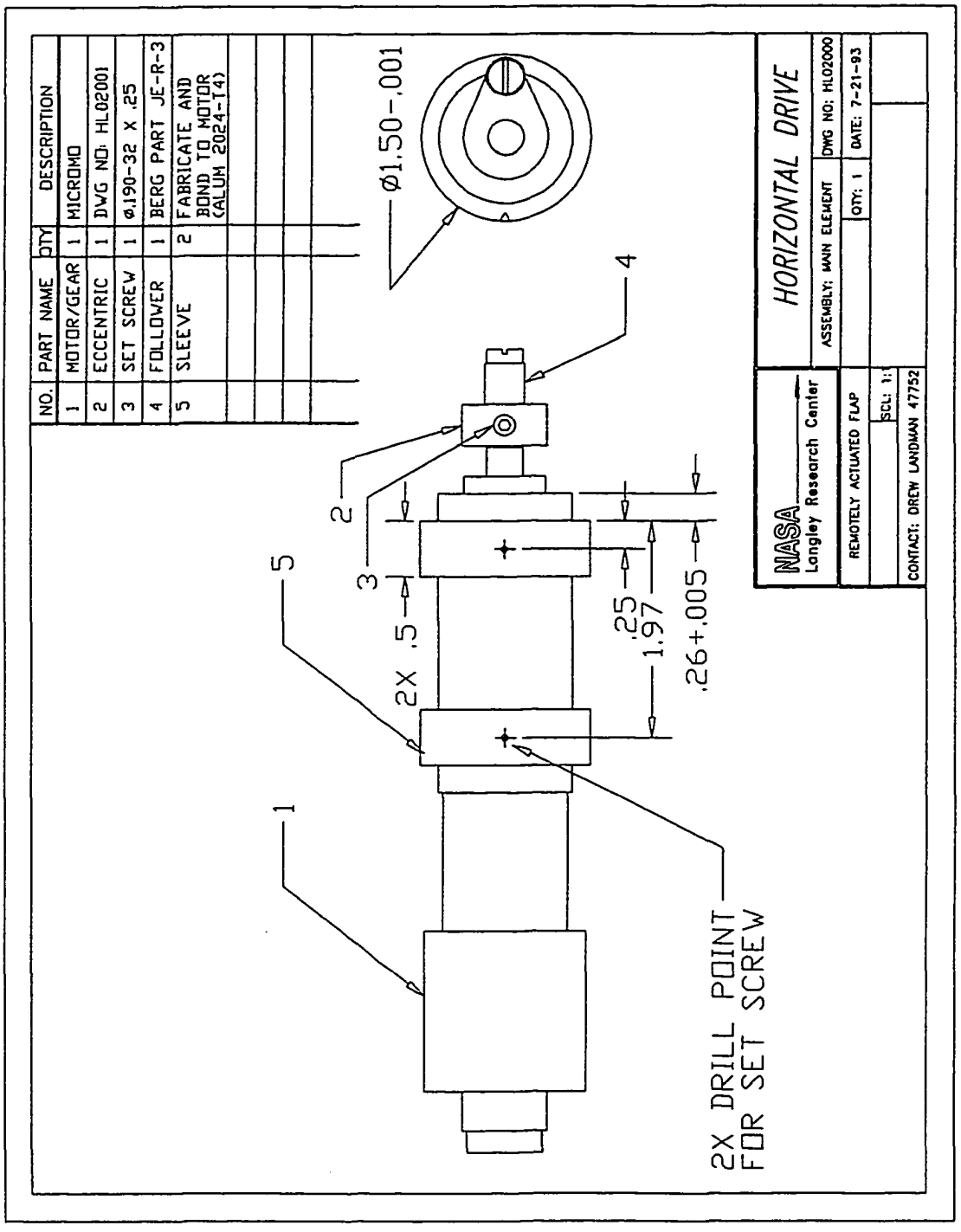

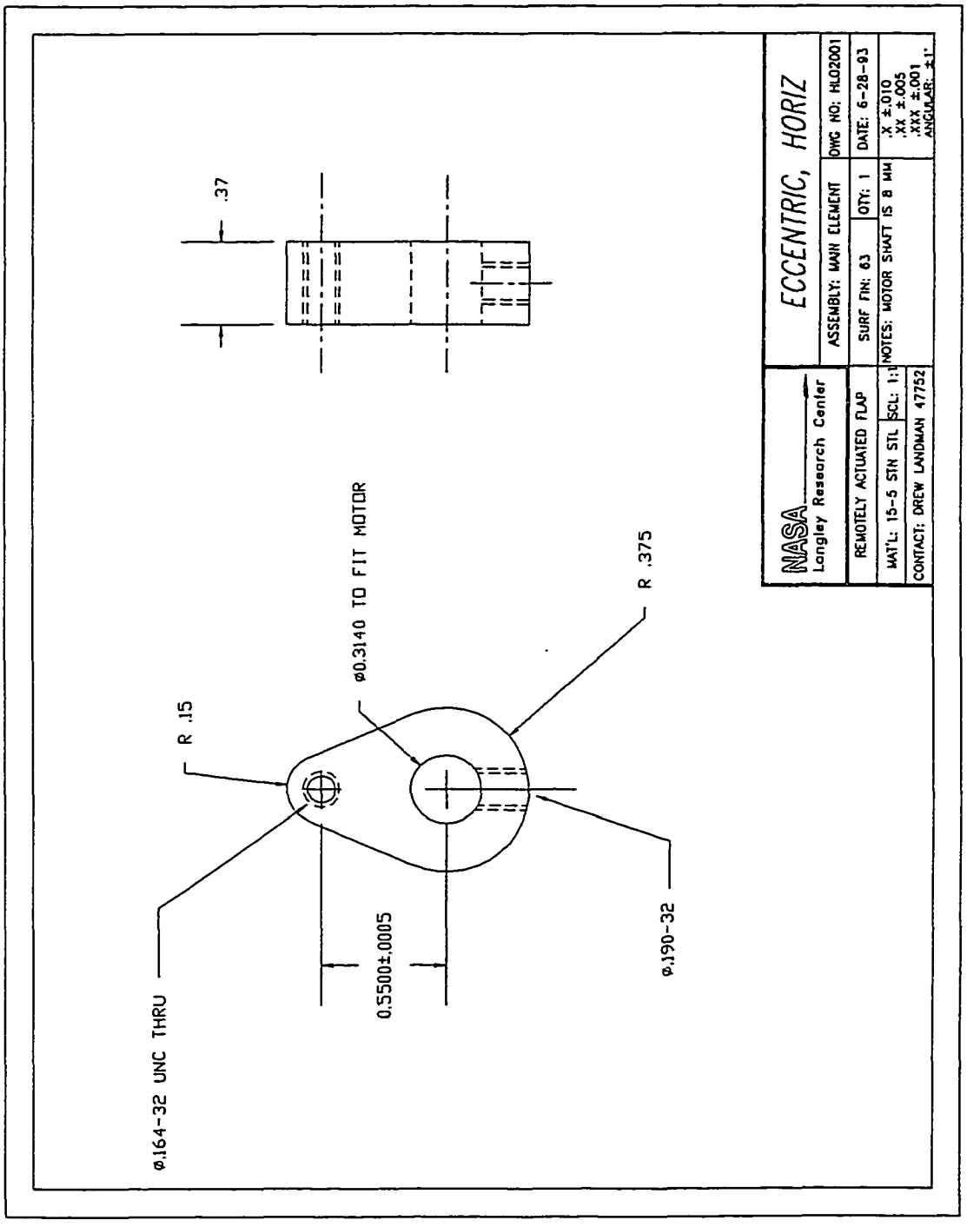

Flap Bracket

30 degree flap deflection
2 each - 1 left, 1 right

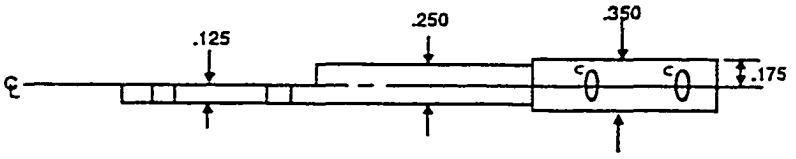

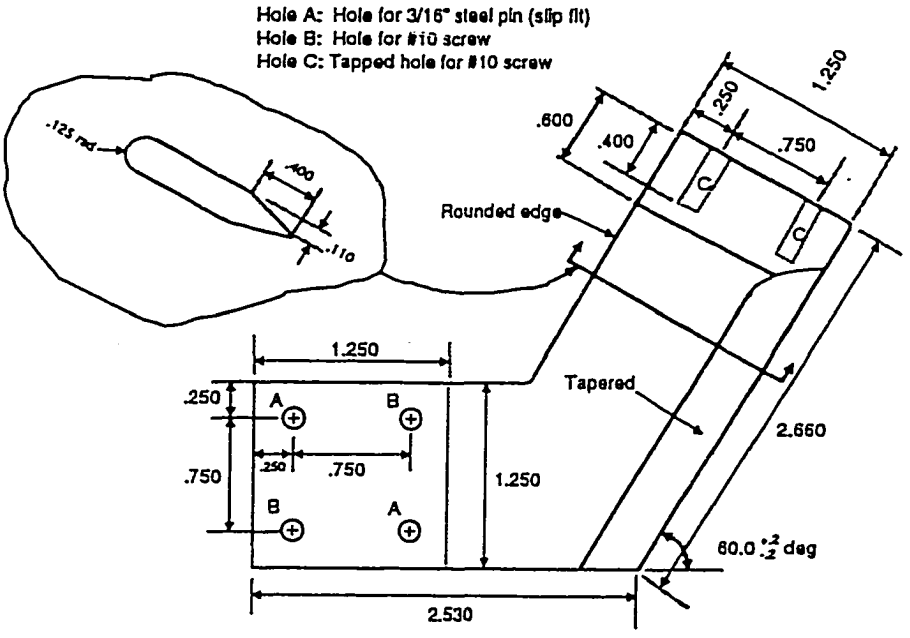

Material: 416 Stainless Steel
Dimensions in inches
Unless Spec'd, tol.:
.xx+-.010
.xxx +-.005

National Aeronautics and Space Administration
Langley Research Center
Hampton, VA

(Designer/Draftsman: Steve Klausmeyer)

Slat Bracket

(4 each)

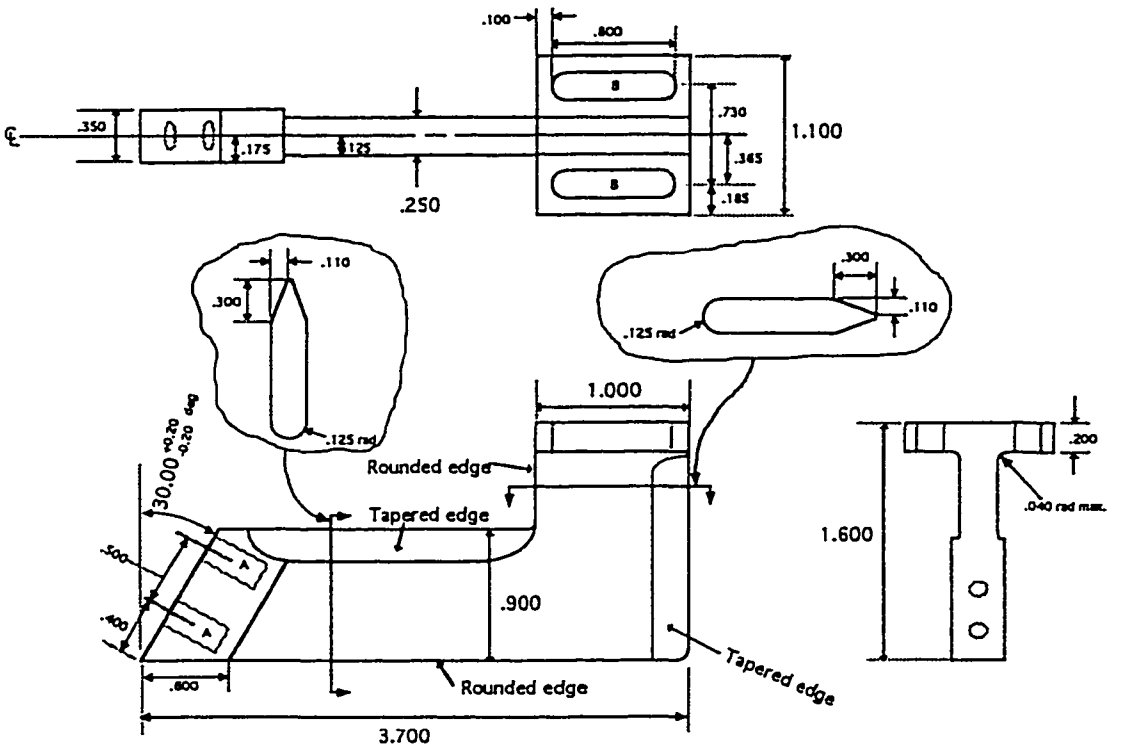

Hole A: Hole for #10 screw (.40" deep)
Slot B: Slot for #10 screw

Material: 416 Steel

Dimensions are in Inches

Unless otherwise
specified, tolerances are:
.xx +- .010
.xxx +- .005

National Aeronautics and Space Administration
Langley Research Center
Hampton, VA

(Designer/Draftsman: Steve Klausmeyer)

Pressure Tap Details

Pressure Taps - General Manufacturing Details

All centerline upper surface orifices are drilled through from the lower surface so that the upper surface is true to the profile. Taps on the lower surface are drilled into a removable cap which is screwed on to the element. All orifices have a diameter of 0.02" and are located within 0.005" of the given x location. All orifices are plumbed to (0.04" outside diameter) annealed stainless steel tubing which is routed to the right side of each element. Spanwise pressure taps are located on the upper surface, stainless tubing connects the orifices through milled channels on the lower surface which are filled with epoxy resin and re-profiled.

Pressure Tap Details - Main Element

There are a total of 37 pressure tap locations: 31 chordwise pressure tap locations on the midspan of the main element and 6 spanwise taps located at 12.73" from the leading edge. Spanwise taps are spaced 4 inches apart such that 3 are located left of the centerline and 3 right.

Pressure Tap Details - Flap

There are a total of 25 pressure tap locations: 19 chordwise pressure tap locations on the midspan of the main element and 6 spanwise taps located at 3.95" from the leading edge. The spanwise taps are spaced 4 inches apart such that 3 are located left of the centerline and 3 right.

Pressure Tap Details - Slat

There are a total of 8 chordwise pressure tap locations located on the midspan.

Chordwise Pressure Tap Locations (inches)

Main Element

x	y (approx)
12.9509	0.8657
10.2531	-0.2846
7.3433	-0.6238
5.2701	-0.6719
3.005	-0.5842
2.0258	-0.5028
1.4458	-0.4425
0.8973	-0.3653
0.6151	-0.3207
0.1002	-0.1933
0	-0.02
0.1128	0.3227
0.4618	0.6252
0.7915	0.8016
1.1973	0.9609
1.8217	1.1335
2.4319	1.213
2.9578	1.2592
3.5486	1.3423
4.4506	1.3546
5.503	1.3957
6.4057	1.14161
7.3678	1.4232
8.237	1.4165
9.9148	1.3676
11.7881	1.2535
12.7296	1.1678
13.1866	1.1183
13.6304	1.0647
13.9826	1.018
14.3795	0.9611

Flap

x	y (approx)
3.4779	-0.0283
1.816	-0.1563
0.9242	-0.2957
0.1926	-0.2774
0.0999	-0.2357
0	0.02
0.0541	0.1606
0.165	0.264
0.2266	0.3013
0.4907	0.4049
0.816	0.4764

Slat

x	y (approx)
0.5563	-0.4431
0.1501	-0.2534
0	-0.03
0.0296	0.1165
0.1403	0.2457
0.6318	0.4797
1.264	0.6349
2.1667	0.7815

APPENDIX C: SOFTWARE SAMPLE - EXPERIMENT SUPPORT

The program examples shown are coded in the LabView™ graphical instrumentation programming language and are known as Virtual Instruments (VI's). Each VI has a connector pane, to interface to other programs, a front panel, to display input-output information in the subprogram, and a block diagram, where the actual instructions are displayed by way of a data flow wire diagram. In this appendix the VI examples included are shown in the order: (1) connector pane, (2) front panel, (3) block diagram. There is a small written description of each program's function under the heading for each block diagram.

Connector Pane

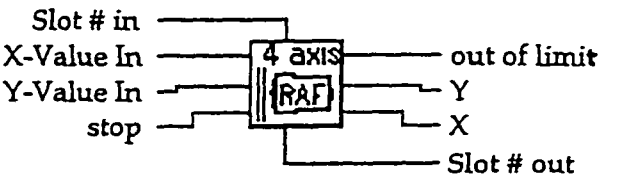

4AXISMOV.VI

Front Panel

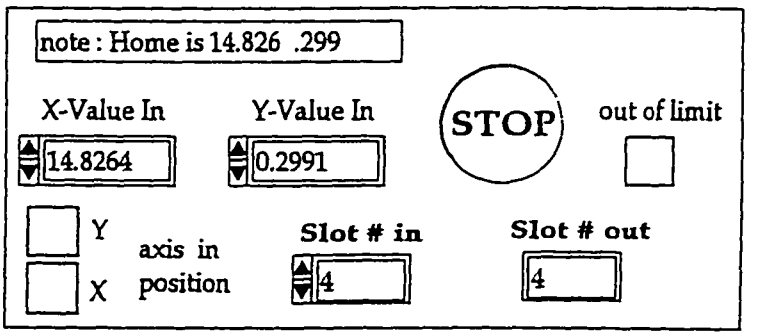

Block Diagram

This VI takes an input of flap position x, y and converts it to the required number of motor revolutions, calls each axis to move, and verifies the position is correct.

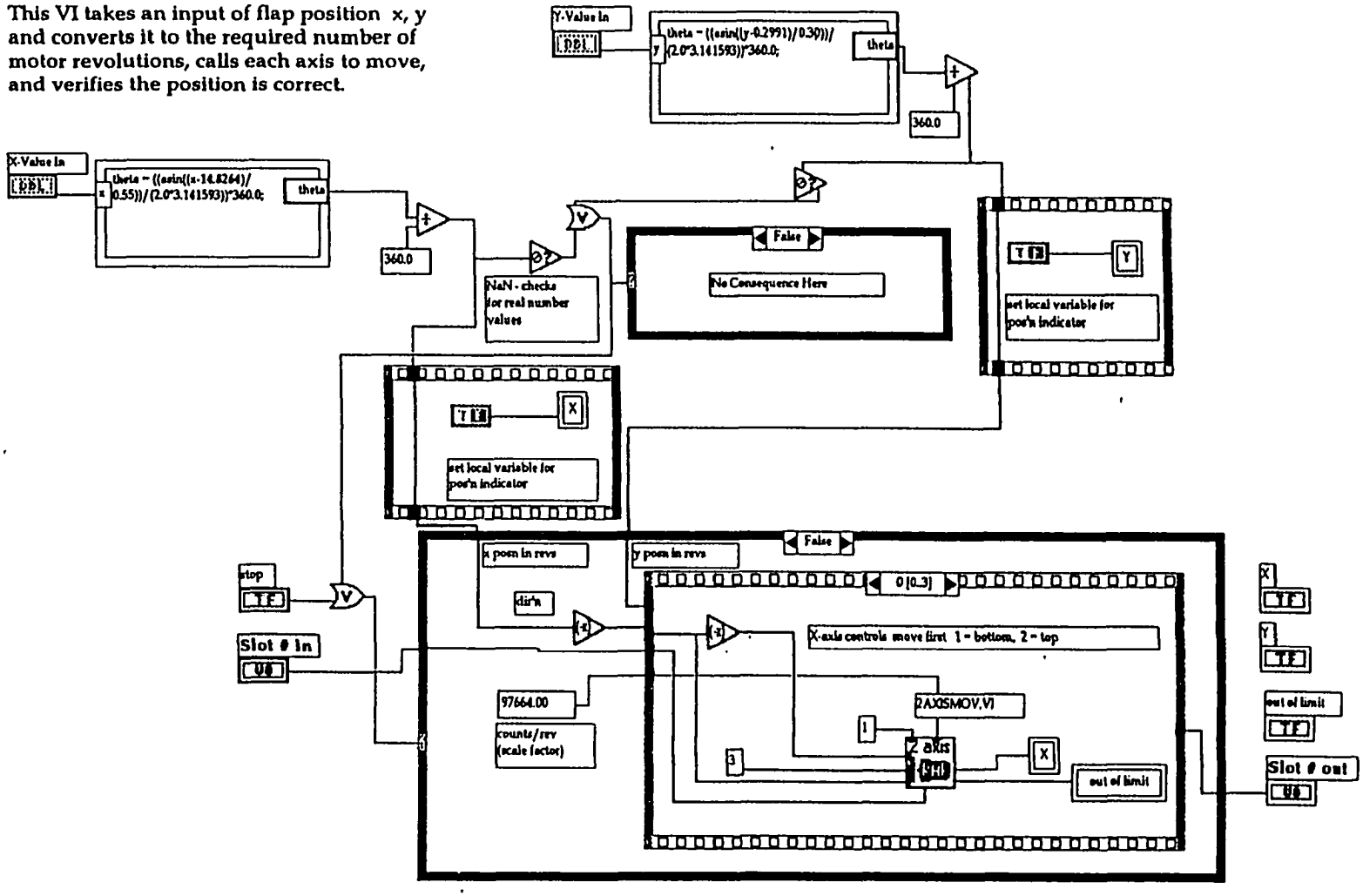

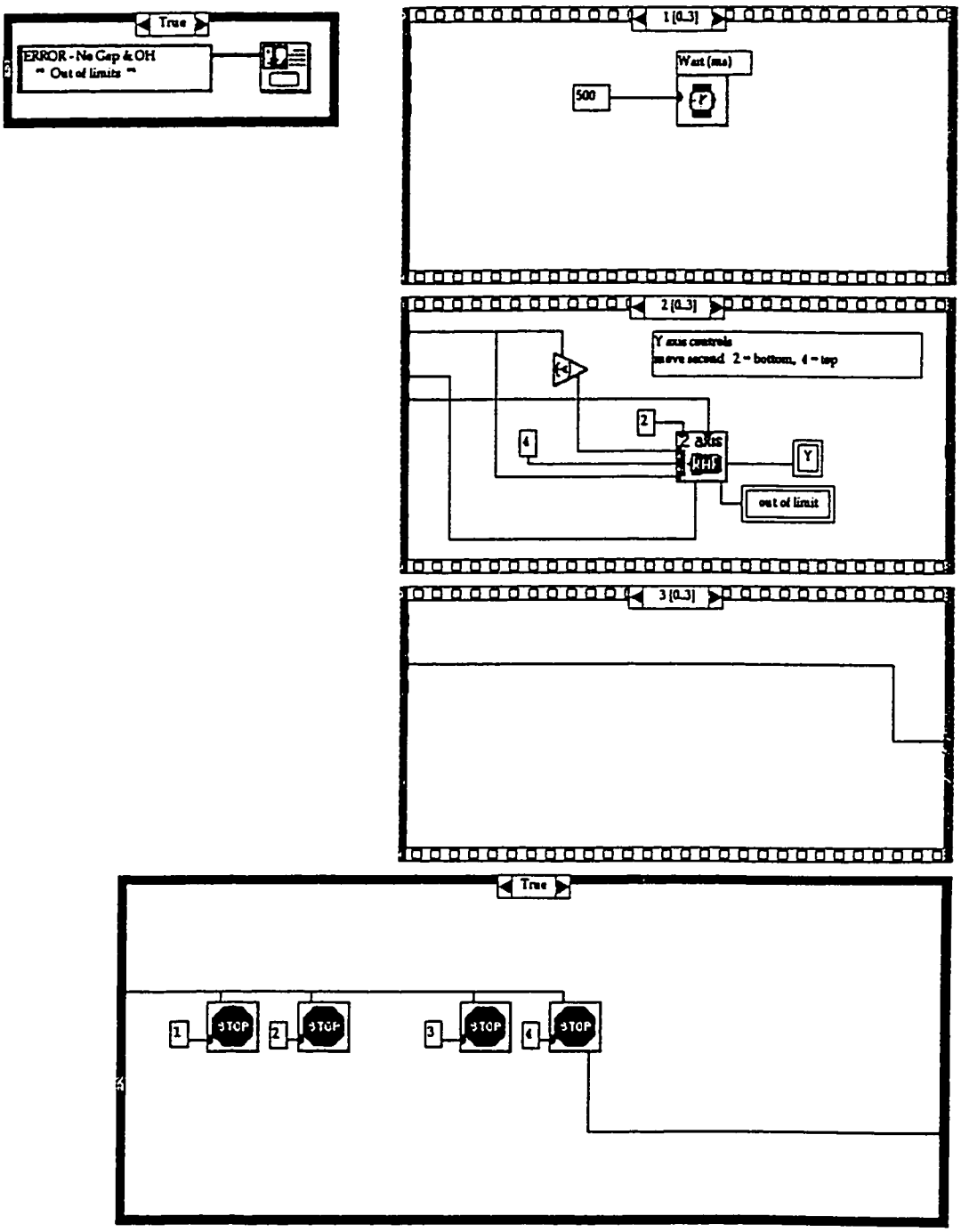

Connector Pane

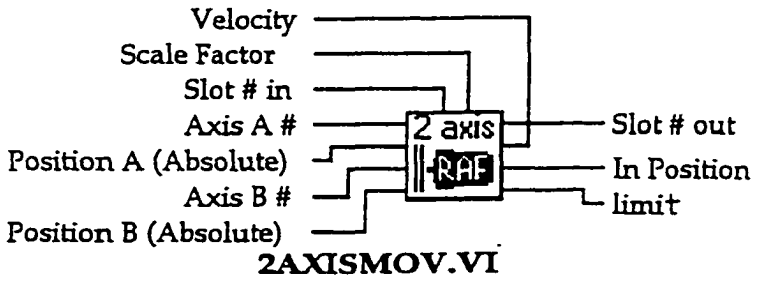

Front Panel

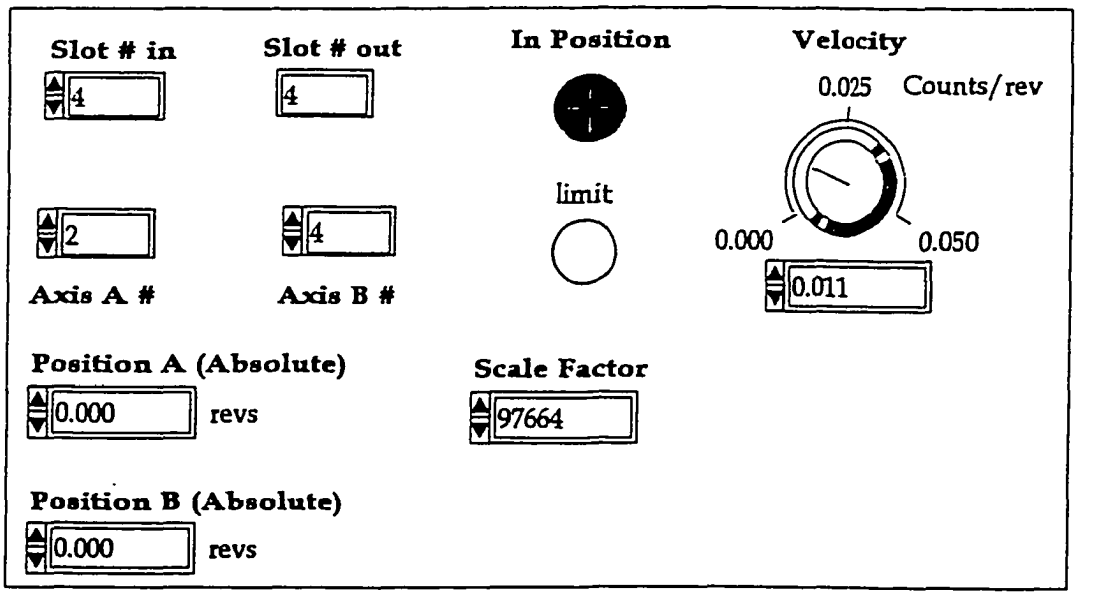

Block Diagram

This VI is used to move 2 axes in parallel either x or y

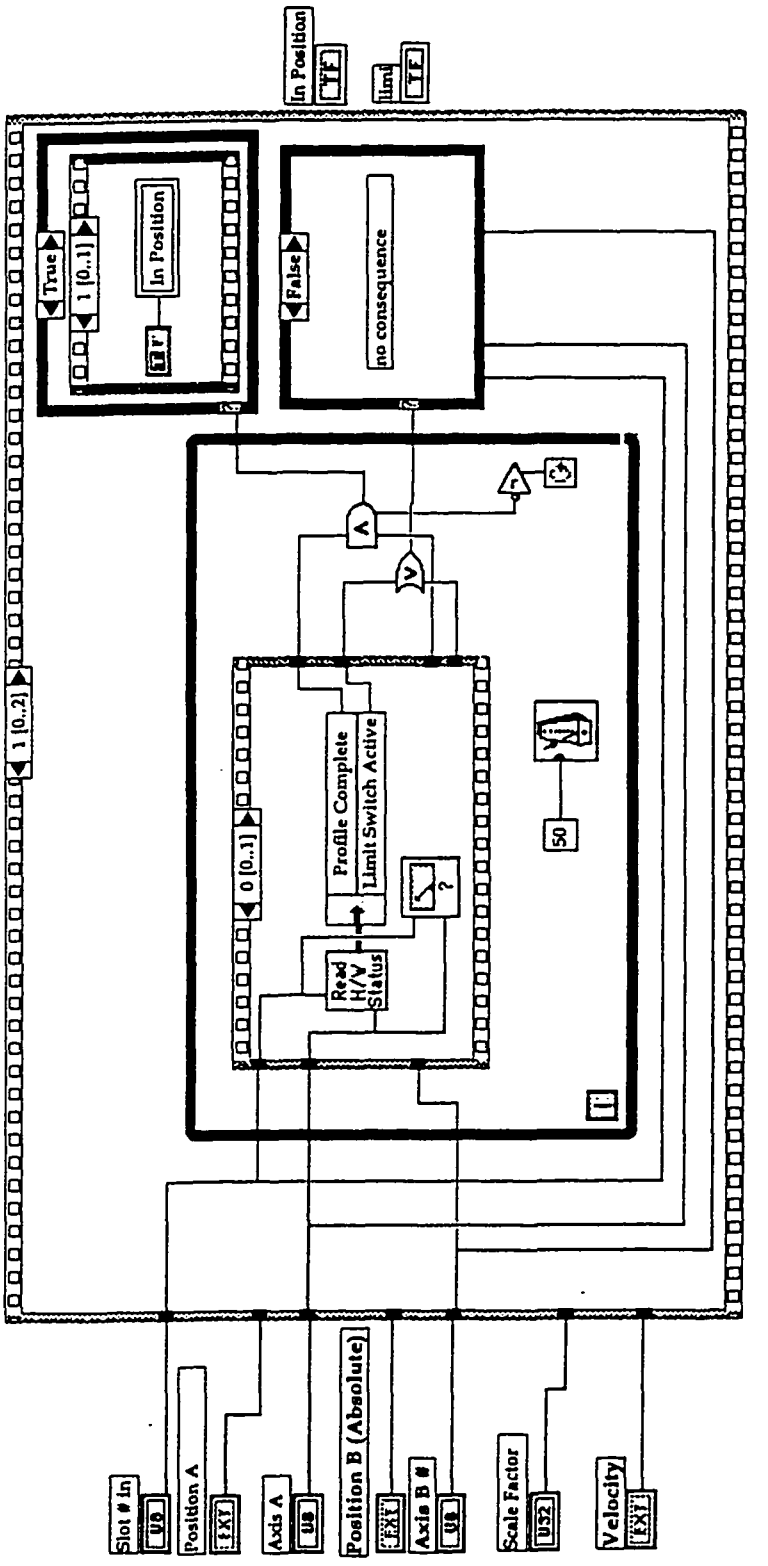

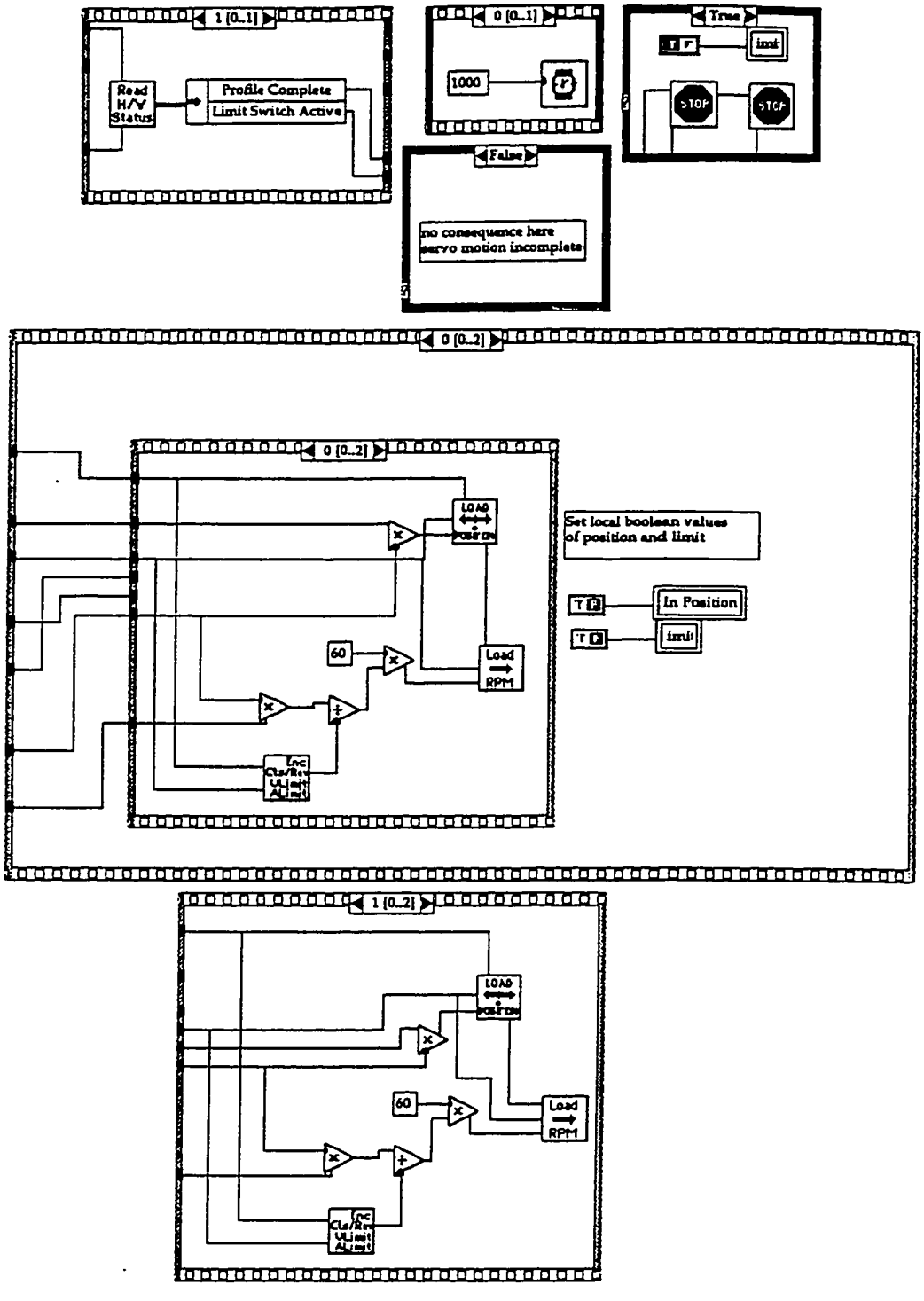

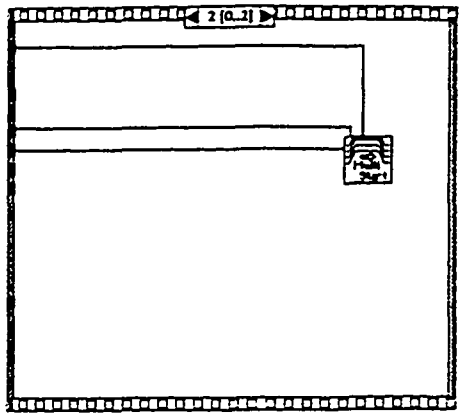

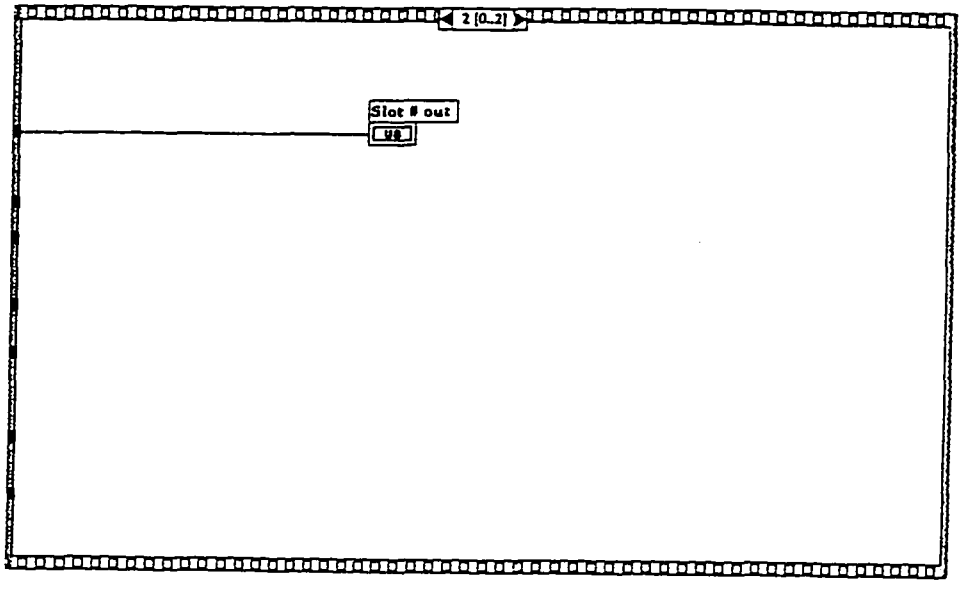

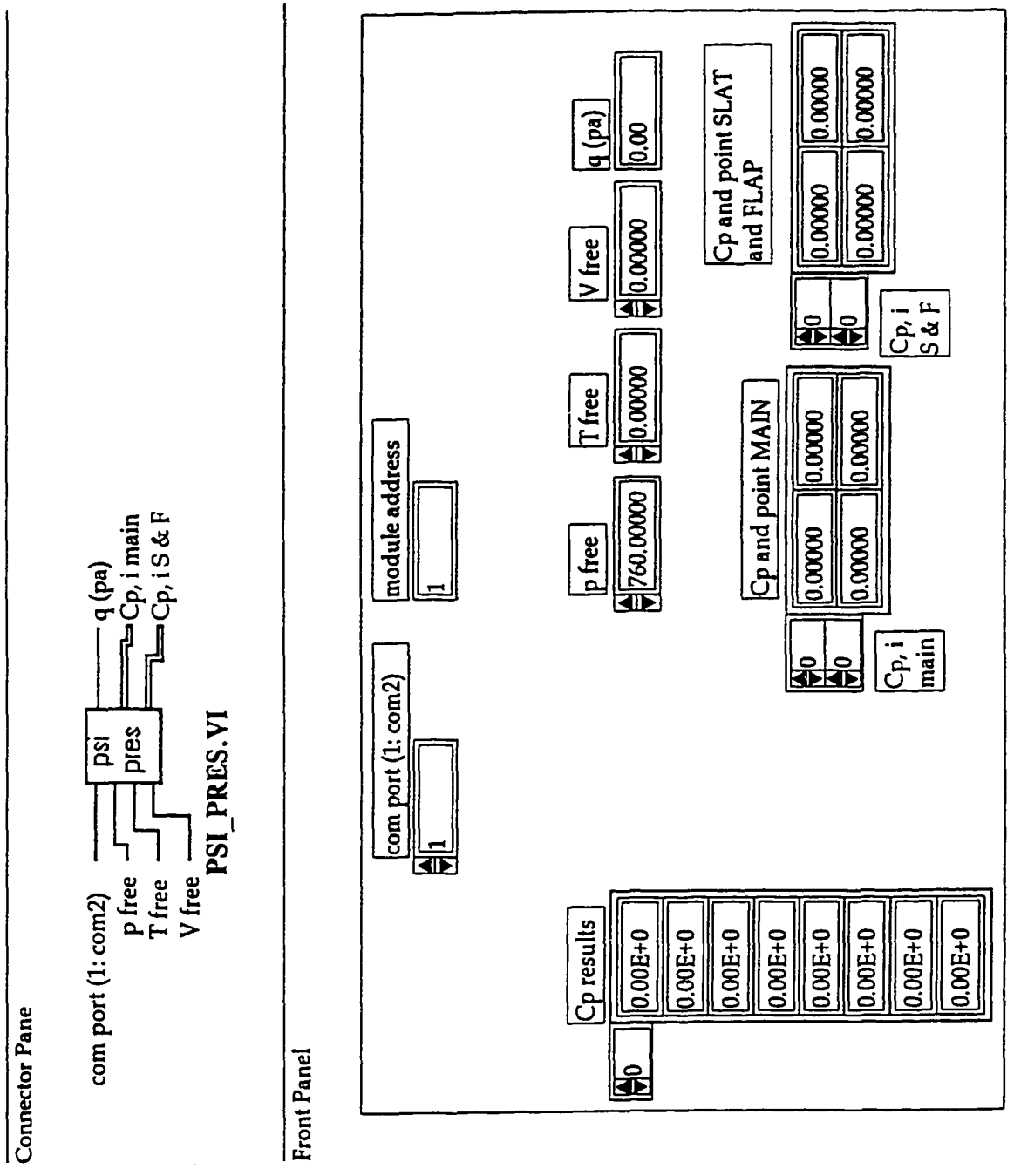

Block Diagram

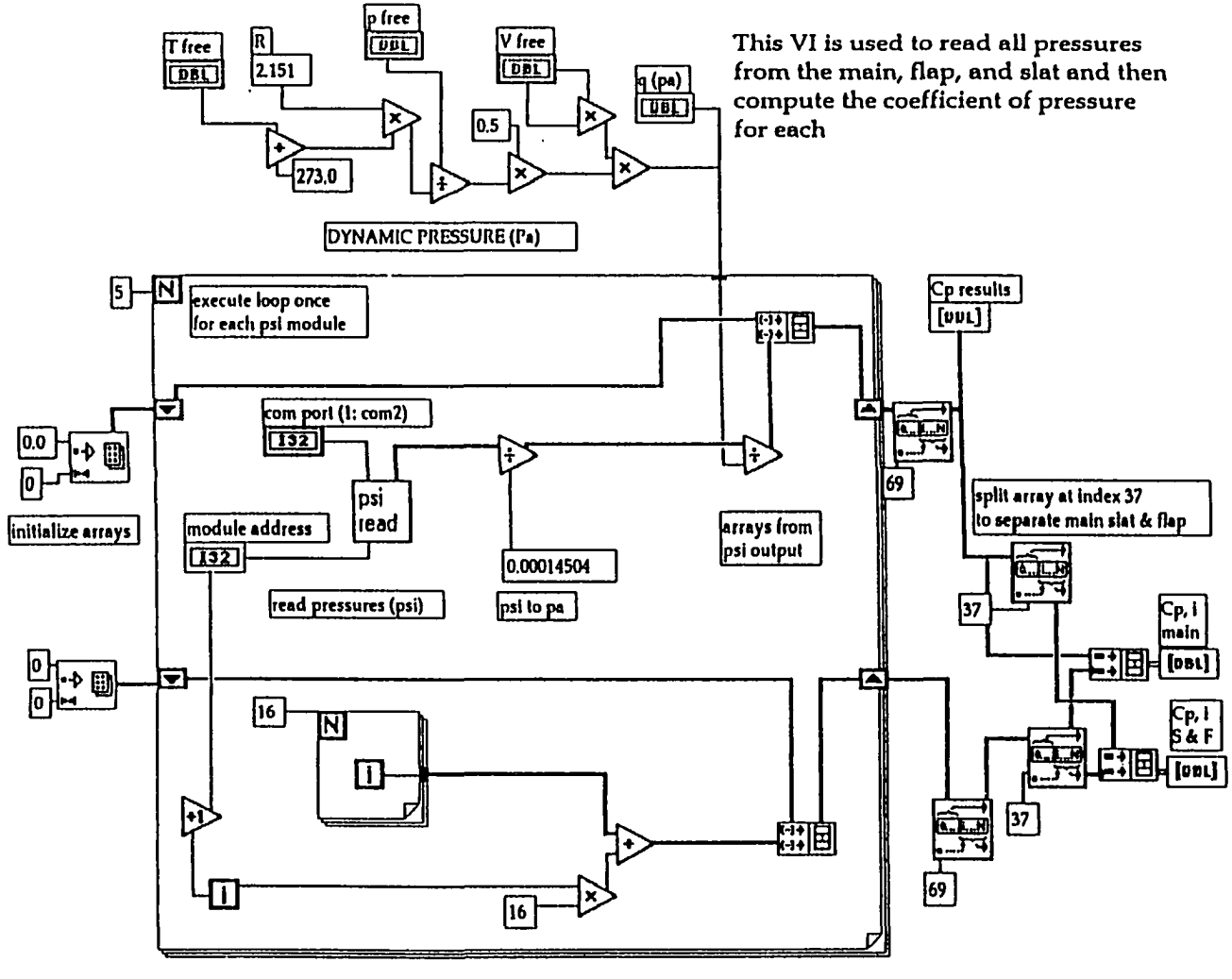

Connector Pane

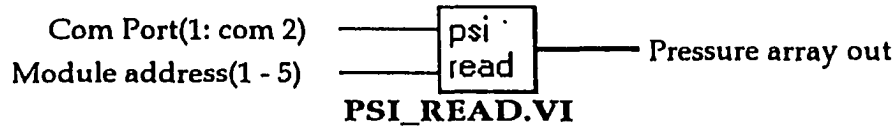

Front Panel

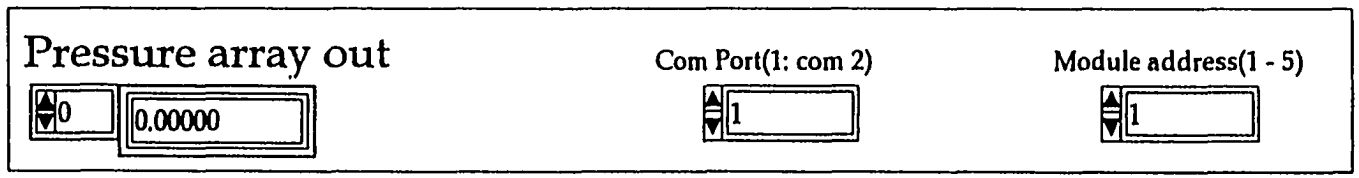

Block Diagram

This VI averages 10 samples (of the sampled burst) from 1 psi 9010 module

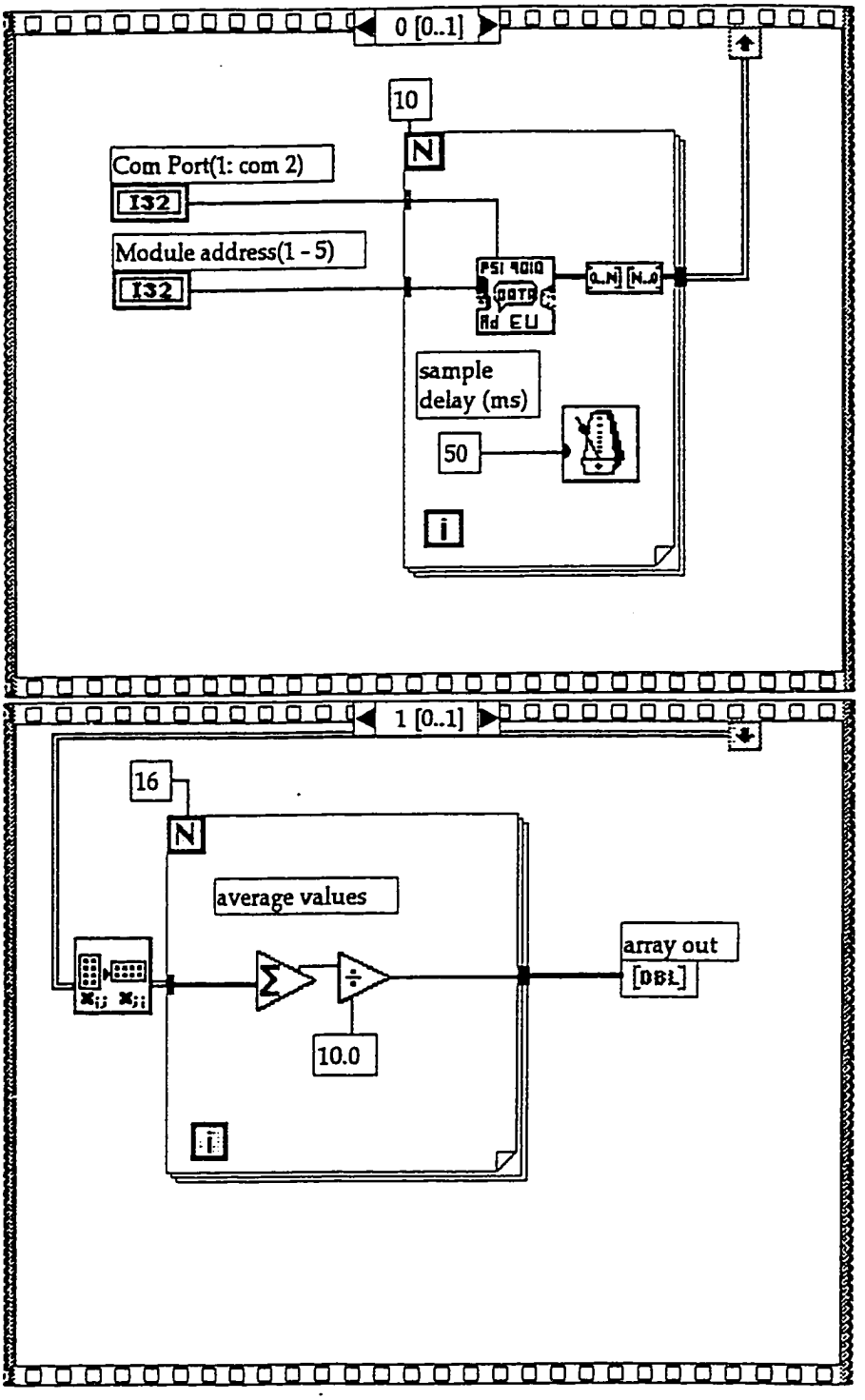

APPENDIX D: RAW DATA SAMPLE

Sample Raw Data File - Pressure Distribution

14.85	0.59	3.1959	(x, y, Cl)
26.0375	760	31.0415	(Temperature (C), Pressure (mmHg), Velocity (M/S))
14	30	30	(Angle of Attack, Flap Deflection, Slat Deflection)
2.4322	0.3012	0.4625	(Cl main, Clflap, Clslat,)
-0.9625	0		
-1.2532	1		
-1.2727	2		
-1.3174	3		
-1.3485	4		
-1.4068	5		(Cp's on main element 0-30)
-1.5491	6		
-1.7109	7		
-1.8252	8		
-1.9617	9		
-2.129	10		
-2.3312	11		
-2.7585	12		
-3.1075	13		
-3.5837	14		
-4.7631	15		
-5.1989	16		
-5.9204	17		
-6.5131	18		
-7.2659	19		
-6.5696	20		
-2.5799	21		
0.7834	22		
0.866	23		
0.921	24		
0.8934	25		
0.8338	26		
0.7273	27		
0.6399	28		
0.6398	29		
0.6391	30		
-1.2216	31		(Spanwise Cp's on main 31-36)
-1.3047	32		
-1.3453	33		
-1.2878	34		
-1.2194	35		
-1.1293	36		
-0.0756	37		(Cp's on flap 37-55)
-0.099	38		
-0.1601	39		
-0.2889	40		
-0.4506	41		
-0.7607	42		
-0.9881	43		
-1.2468	44		
-1.6538	45		
-1.9427	46		
-2.1266	47		
-1.4684	48		
-0.0083	49		
0.7867	50		
0.8809	51		
0.7841	52		
0.7345	53		
0.631	54		
0.6421	55		
-0.3182	56		(Spanwise Cp's on flap 56-61)
-0.2181	57		
-0.1523	58		
-0.148	59		
-0.1962	60		
-0.2397	61		
-2.6247	62		(Cp's on slat 62-68)
-2.8034	63		
-3.3486	64		
-5.3565	65		
-3.8856	66		
0.6889	67		
0.7862	68		

DATA FILE OF FIGURE 6.6A

X	Y	CI
15.05	0.55	2.44
14.95	0.55	3.26
14.85	0.55	3.2
14.75	0.55	3.15
14.65	0.55	3.12
14.55	0.55	3.07
14.45	0.55	3.04
14.35	0.55	3.02
15.05	0.45	2.39
14.95	0.45	2.52
14.85	0.45	2.62
14.75	0.45	3.21
14.65	0.45	3.16
14.55	0.45	3.16
14.45	0.45	3.13
14.35	0.45	3.14
15.05	0.35	2.33
14.95	0.35	2.47
14.85	0.35	2.56
14.75	0.35	2.6
14.65	0.35	2.64
14.55	0.35	2.68
14.45	0.35	2.71
14.35	0.35	2.72
15.05	0.25	2.33
14.95	0.25	2.36
14.85	0.25	2.53
14.75	0.25	2.57
14.65	0.25	2.59
14.55	0.25	2.61
14.45	0.25	2.62
14.35	0.25	2.64
15.05	0.15	2.34
14.95	0.15	2.37
14.85	0.15	2.4
14.75	0.15	2.46
14.65	0.15	2.58
14.55	0.15	2.57
14.45	0.15	2.59
14.35	0.15	2.6
15	0.59	3.23
14.9	0.59	3.21
14.85	0.59	3.2
14.8	0.59	3.14
14.75	0.59	3.11
14.7	0.59	3.1
14.65	0.59	3.08
14.55	0.59	3.05

DATA FILE OF FIGURE 6.7A

X	Y	CI
15.15	0.599	2.40
15.10	0.599	2.43
15.05	0.599	2.51
15.00	0.599	3.23
14.95	0.599	3.21
14.90	0.599	3.18
14.85	0.599	3.16
14.80	0.599	3.12
14.75	0.599	3.10
14.70	0.599	3.08
14.65	0.599	3.08
14.60	0.599	3.04
14.55	0.599	3.07
14.50	0.599	3.08
14.45	0.599	3.07
14.40	0.599	3.08
14.35	0.599	3.07
15.15	0.550	2.31
15.10	0.550	2.43
15.05	0.550	2.48
15.00	0.550	2.54
14.95	0.550	3.23
14.90	0.550	3.23
14.85	0.550	3.23
14.80	0.550	3.19
14.75	0.550	3.16
14.70	0.550	3.14
14.65	0.550	3.15
14.60	0.550	3.11
14.55	0.550	3.11
14.50	0.550	3.10
14.45	0.550	3.07
14.40	0.550	3.07
14.35	0.550	3.08
15.15	0.500	2.26
15.10	0.500	2.37
15.05	0.500	2.46
15.00	0.500	2.51
14.95	0.500	2.57
14.90	0.500	3.24
14.85	0.500	3.23
14.80	0.500	3.21
14.75	0.500	3.20
14.70	0.500	3.19
14.65	0.500	3.16
14.60	0.500	3.13
14.55	0.500	3.14
14.50	0.500	3.15
14.45	0.500	3.10
14.40	0.500	3.11
14.35	0.500	3.10
15.15	0.450	2.26
15.10	0.450	2.29
15.05	0.450	2.38
15.00	0.450	2.49
14.95	0.450	2.53
14.90	0.450	2.56
14.85	0.450	2.82
14.80	0.450	3.22
14.75	0.450	3.22
14.70	0.450	3.20
14.65	0.450	3.17
14.60	0.450	3.18
14.55	0.450	3.17
14.50	0.450	3.14
14.45	0.450	3.15
14.40	0.450	3.13
14.35	0.450	3.14
15.15	0.400	2.28
15.10	0.400	2.29
15.05	0.400	2.34
15.00	0.400	2.42
14.95	0.400	2.53
14.90	0.400	2.55
14.85	0.400	2.59
14.80	0.400	2.62
14.75	0.400	2.67
14.70	0.400	2.86
14.65	0.400	3.21
14.60	0.400	3.19
14.55	0.400	3.19
14.50	0.400	3.17
14.45	0.400	3.17
14.40	0.400	3.15
14.35	0.400	3.15
15.15	0.350	2.29
15.10	0.350	2.30
15.05	0.350	2.33
15.00	0.350	2.38
14.95	0.350	2.46
14.90	0.350	2.54
14.85	0.350	2.57
14.80	0.350	2.60
14.75	0.350	2.61
14.70	0.350	2.64
14.65	0.350	2.67
14.60	0.350	2.69
14.55	0.350	2.69
14.50	0.350	2.70
14.45	0.350	2.74
14.40	0.350	2.88
14.35	0.350	2.88
15.15	0.300	2.31
15.10	0.300	2.33
15.05	0.300	2.36
15.00	0.300	2.36
14.95	0.300	2.44
14.90	0.300	2.53
14.85	0.300	2.57
14.80	0.300	2.58
14.75	0.300	2.59
14.70	0.300	2.62
14.65	0.300	2.62
14.60	0.300	2.61
14.55	0.300	2.62
14.50	0.300	2.63
14.45	0.300	2.62
14.40	0.300	2.62
14.35	0.300	2.61

APPENDIX E: SOFTWARE LISTINGS FOR SIMULATIONS

Sequential Simplex - Remotely Actuated Flap Simulation for 14 degree angle of attack (fixed size simplex)

FN:ss_fix.mcd
Drew Landman
7/30/97

This MathCad worksheet models a simplex optimizer working with simulated experimental data for C_l=f(x,y). Noise is included for σ = .017 on C_l. Here the initial (j-1) vertex is discarded and the initial N vertex is forced to become the jth W vertex

read in a file that has x,y,Cl in 3 columns to generate response surface, data from α = 14 Slat A; experimental data it must be a FN.prn file in current directory (c:\data\mcad)

XYCL := READPRN(clxy1114)

xvec := $XYCL^{<0>}$ yvec := $XYCL^{<1>}$ CL := $XYCL^{<2>}$ Mxy := augment(xvec, yvec)

vs is a vector of 2nd order polynomials that best fit the Cl data in a small neighborhood controlled by span; any Cl can be found from a multivariable regression fit using Mathcad utilities

span := .25
vs := loess(Mxy, CL, span)

max(xvec) = 15.05 max(yvec) = 0.59
min(xvec) = 14.35 min(yvec) = 0.15

choose a starting point

xstart := .5 + min(xvec) ystart := .2 + min(yvec)
xstart = 14.85 ystart = 0.35

choose a scaling factor S

S := .035

calculate lengths for initial simplex n=2 for C_l = f(x,y) ref: Jacoby, S.L.S et. al. "Iterative Methods for NonLinear Optimization Problems", Prentice Hall 1972

$$n := 2 \quad pn := \frac{\sqrt{n+1} - 1 + n}{n\cdot\sqrt{2}}\cdot S \quad qn := \frac{\sqrt{n+1} - 1}{n\cdot\sqrt{2}}\cdot S$$

calculate simplex vertices X_0, X_1, X_2

$$X^{<0>} := \begin{pmatrix} xstart \\ ystart \end{pmatrix} \quad X^{<1>} := \begin{pmatrix} xstart + pn \\ ystart + qn \end{pmatrix}$$

$$X^{<2>} := \begin{pmatrix} xstart + qn \\ ystart + pn \end{pmatrix} \quad X^{<0>} = \begin{pmatrix} 14.85 \\ 0.35 \end{pmatrix} \quad X^{<1>} = \begin{pmatrix} 14.884 \\ 0.359 \end{pmatrix} \quad X^{<2>} = \begin{pmatrix} 14.859 \\ 0.384 \end{pmatrix}$$

Find Cl (response) at each vertex with random error, σ = .017 on C_l

i := 0..2

σ := .017

error := rnorm(3, 0, .017)

$CLcalc_i := interp(vs, Mxy, CL, X^{<i>}) + error_i$ CLcalc = $\begin{pmatrix} 2.528 \\ 2.489 \\ 2.535 \end{pmatrix}$

Define subroutines which find indices of vertex associated with the best (ib), worst (iw), and next best (in) response

findiw(CLsort, CLcalc) :=
k ← 0
while $CLsort_0 \neq CLcalc_k$
k ← k + 1
k

findin(CLsort , CLcalc) :=
k←0
while $CLsort_1 \neq CLcalc_k$
k←k + 1
k

input known optimum for data set:

opt := 3.27

findib(CLsort , CLcalc) :=
k←0
while $CLsort_2 \neq CLcalc_k$
k←k + 1
k

Begin Iteration N := 25

op(X , CLcalc , N , σ) :=
j←0
CLsort←sort(CLcalc)
iw←findiw(CLsort , CLcalc)
in←findin(CLsort , CLcalc)
ib←findib(CLsort , CLcalc)
for j ∈ 0..N
$xx \leftarrow \frac{X^{<ib>} + X^{<in>}}{2}$
$r_j \leftarrow 2 \cdot xx - X^{<iw>}$
errvect←rnorm(1 , 0 , σ)
error←$errvect_0$
$CLr_j \leftarrow interp(vs , Mxy , CL , r_j) + error$
$CLcalc_{iw} \leftarrow CLcalc_{in}$
$X^{<iw>} \leftarrow X^{<in>}$
$(CLcalc_{in} \leftarrow CLcalc_{ib}) \cdot (X^{<in>} \leftarrow X^{<ib>})$ if $CLr_j > CLcalc_{ib}$
$(CLcalc_{ib} \leftarrow CLr_j) \cdot (X^{<ib>} \leftarrow r_j)$ if $CLr_j > CLcalc_{ib}$
otherwise
$CLcalc_{in} \leftarrow CLr_j$
$X^{<in>} \leftarrow r_j$
μ←mean(CLcalc)
s←stdev(CLcalc)
$diff \leftarrow \left(\frac{opt - \mu}{opt}\right) \cdot 100$
$Xout \leftarrow augment(X^{<ib>} , augment(X^{<in>} , X^{<iw>}))$
$ansmat_{j,0} \leftarrow Xout_{0,0}$
ansmat Xout

$ansmat_{j,1} \leftarrow Xout_{1,0}$

$ansmat_{j,2} \leftarrow CLcalc_{ib}$

$ansmat_{j,3} \leftarrow Xout_{0,1}$

$ansmat_{j,4} \leftarrow Xout_{1,1}$

$ansmat_{j,5} \leftarrow CLcalc_{in}$

$ansmat_{j,6} \leftarrow Xout_{0,2}$

$ansmat_{j,7} \leftarrow Xout_{1,2}$

$ansmat_{j,8} \leftarrow CLcalc_{iw}$

$ansmat_{j,9} \leftarrow \mu$

$ansmat_{j,10} \leftarrow s$

$ansmat_{j,11} \leftarrow diff$

$ansmat_{j,12} \leftarrow j + 2$

$ans := op(X, CLcalc, N, \blacksquare)ansmat$

$j := 0..N$

$$init := \begin{pmatrix} X_{0,0} & X_{1,0} & CLcalc_0 \\ X_{0,1} & X_{1,1} & CLcalc_1 \\ X_{0,2} & X_{1,2} & CLcalc_2 \end{pmatrix}$$

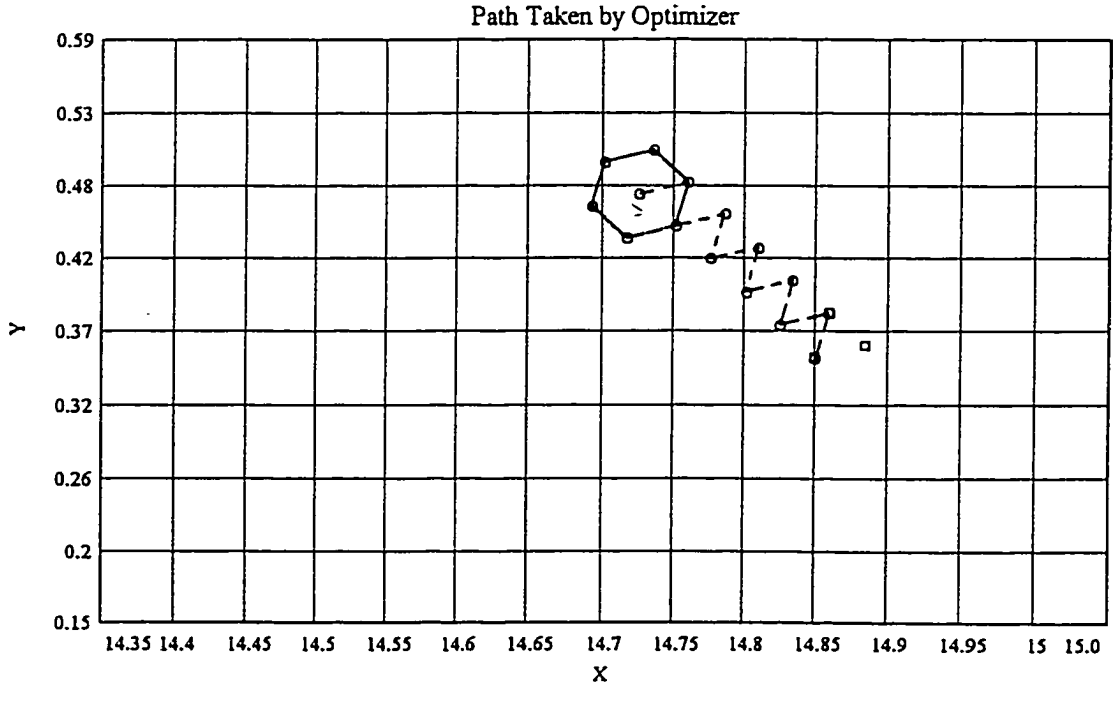

Note: first simplex vertices shown with square symbols

Summary of Run

start point: xstart = 14.85, ystart = 0.35

number of steps: N = 25

scaling factor: S = 0.035

Print results:

l := ans

initial simplex (x,y,Cl)

$$init = \begin{pmatrix} 14.85 & 0.35 & 2.528 \\ 14.884 & 0.359 & 2.489 \\ 14.859 & 0.384 & 2.535 \end{pmatrix}$$

subsequent reflections
(xb, yb, Clb, xn, yn, Cln, xw, yw, Clw, mean, standard deviation, % diff from opt, simplex num)

$$l = \begin{bmatrix}
14.825 & 0.375 & 2.584 & 14.859 & 0.384 & 2.535 & 14.85 & 0.35 & 2.528 & 2.549 & 0.025 & 22.04 \\
14.834 & 0.409 & 2.59 & 14.825 & 0.375 & 2.584 & 14.859 & 0.384 & 2.535 & 2.57 & 0.025 & 21.41 \\
14.801 & 0.399 & 2.738 & 14.834 & 0.409 & 2.59 & 14.825 & 0.375 & 2.584 & 2.637 & 0.071 & 19.35 \\
14.81 & 0.433 & 2.803 & 14.801 & 0.399 & 2.738 & 14.834 & 0.409 & 2.59 & 2.71 & 0.089 & 17.12 \\
14.776 & 0.424 & 2.978 & 14.81 & 0.433 & 2.803 & 14.801 & 0.399 & 2.738 & 2.839 & 0.101 & 13.16 \\
14.785 & 0.458 & 3.08 & 14.776 & 0.424 & 2.978 & 14.81 & 0.433 & 2.803 & 2.953 & 0.114 & 9.68 \\
14.751 & 0.449 & 3.191 & 14.785 & 0.458 & 3.08 & 14.776 & 0.424 & 2.978 & 3.083 & 0.087 & 5.721 \\
14.76 & 0.483 & 3.213 & 14.751 & 0.449 & 3.191 & 14.785 & 0.458 & 3.08 & 3.161 & 0.058 & 3.327 \\
14.726 & 0.474 & 3.27 & 14.76 & 0.483 & 3.213 & 14.751 & 0.449 & 3.191 & 3.225 & 0.033 & 1.391 \\
14.726 & 0.474 & 3.27 & 14.735 & 0.508 & 3.223 & 14.76 & 0.483 & 3.213 & 3.235 & 0.025 & 1.062 \\
14.726 & 0.474 & 3.27 & 14.702 & 0.498 & 3.246 & 14.735 & 0.508 & 3.223 & 3.246 & 0.019 & 0.725 \\
14.726 & 0.474 & 3.27 & 14.692 & 0.465 & 3.254 & 14.702 & 0.498 & 3.246 & 3.257 & 0.01 & 0.411 \\
14.726 & 0.474 & 3.27 & 14.717 & 0.44 & 3.202 & 14.692 & 0.465 & 3.254 & 3.242 & 0.029 & 0.863 \\
14.726 & 0.474 & 3.27 & 14.751 & 0.449 & 3.164 & 14.717 & 0.44 & 3.202 & 3.212 & 0.044 & 1.777 \\
14.726 & 0.474 & 3.27 & 14.76 & 0.483 & 3.208 & 14.751 & 0.449 & 3.164 & 3.214 & 0.043 & 1.712 \\
14.726 & 0.474 & 3.27 & 14.735 & 0.508 & 3.205 & 14.76 & 0.483 & 3.208 & 3.227 & 0.03 & 1.302 \\
14.726 & 0.474 & 3.27 & 14.702 & 0.498 & 3.224 & 14.735 & 0.508 & 3.205 & 3.233 & 0.027 & 1.144 \\
14.726 & 0.474 & 3.27 & 14.692 & 0.465 & 3.259 & 14.702 & 0.498 & 3.224 & 3.251 & 0.02 & 0.584 \\
14.726 & 0.474 & 3.27 & 14.717 & 0.44 & 3.192 & 14.692 & 0.465 & 3.259 & 3.24 & 0.035 & 0.909 \\
14.726 & 0.474 & 3.27 & 14.751 & 0.449 & 3.187 & 14.717 & 0.44 & 3.192 & 3.216 & 0.038 & 1.651 \\
14.726 & 0.474 & 3.27 & 14.76 & 0.483 & 3.192 & 14.751 & 0.449 & 3.187 & 3.216 & 0.038 & 1.648 \\
14.726 & 0.474 & 3.27 & 14.735 & 0.508 & 3.209 & 14.76 & 0.483 & 3.192 & 3.224 & 0.033 & 1.418 \\
14.726 & 0.474 & 3.27 & 14.702 & 0.498 & 3.256 & 14.735 & 0.508 & 3.209 & 3.245 & 0.026 & 0.767 \\
14.726 & 0.474 & 3.27 & 14.692 & 0.465 & 3.26 & 14.702 & 0.498 & 3.256 & 3.262 & 0.006 & 0.25 \\
14.726 & 0.474 & 3.27 & 14.717 & 0.44 & 3.201 & 14.692 & 0.465 & 3.26 & 3.243 & 0.031 & 0.816 \\
14.726 & 0.474 & 3.27 & 14.751 & 0.449 & 3.196 & 14.717 & 0.44 & 3.201 & 3.222 & 0.034 & 1.466
\end{bmatrix}$$

write results to file

ansout := stack(augment(init, zero), ans)
PRNCOLWIDTH := 12
PRNPRECISION := 6
WRITEPRN(SS5A) := ansout

$$zero := \begin{pmatrix} 0 & 0 & 0 & 0 & 0 & 0 & 0 & 0 & 0 & 0 \\ 0 & 0 & 0 & 0 & 0 & 0 & 0 & 0 & 0 & 0 \\ 0 & 0 & 0 & 0 & 0 & 0 & 0 & 0 & 0 & 0 \end{pmatrix}$$

Sequential Simplex - Remotely Actuated Flap Simulation for 14 degree angle of attack (variable size simplex)

FN:ss_var.mcd
Drew Landman
9/22/97

This MathCad worksheet models a variable size simplex optimizer working with simulated experimental data for C_l=f(x,y). The simplex may expand and contract in addition to reflecting. Noise is included for σ = .017 on C_l.

read in a file that has x,y,Cl in 3 columns to generate response surface, data from α = 14, Slat A; experimental data must be a FN.prn file in current directory (c:\data\mcad)

$XYCL := READPRN(clxy1114)$

$xvec := XYCL^{<0>}$ $yvec := XYCL^{<1>}$ $CL := XYCL^{<2>}$ $Mxy := augment(xvec, yvec)$

vs is a vector of 2nd order polynomials that best fit the Cl data in a small neighborhood controlled by span; any Cl can be found from a multivariable regression fit using Mathcad utilities

$span := .25$
$vs := loess(Mxy, CL, span)$

$max(xvec) = 15.05$ $max(yvec) = 0.59$
$min(xvec) = 14.35$ $min(yvec) = 0.15$

choose a starting point

$xstart := .2 + min(xvec)$ $xstart = 14.55$

$ystart := .2 + min(yvec)$ $ystart = 0.35$

choose a scaling factor S

$S := .06$

calculate lengths for initial simplex n=2 for $C_l = f(x,y)$ ref: Jacoby, S.L.S et. al. "Iterative Methods for NonLinear Optimization Problems", Prentice Hall 1972

$n := 2$ $pn := \frac{\sqrt{n+1} - 1 + n}{n \cdot \sqrt{2}} \cdot S$ $qn := \frac{\sqrt{n+1} - 1}{n \cdot \sqrt{2}} \cdot S$

calculate simplex vertices X_0, X_1, X_2

$X^{<0>} := \begin{pmatrix} xstart \\ ystart \end{pmatrix}$ $X^{<1>} := \begin{pmatrix} xstart + pn \\ ystart + qn \end{pmatrix}$

$X^{<2>} := \begin{pmatrix} xstart + qn \\ ystart + pn \end{pmatrix}$

$X^{<0>} = \begin{pmatrix} 14.55 \\ 0.35 \end{pmatrix}$ $X^{<1>} = \begin{pmatrix} 14.608 \\ 0.366 \end{pmatrix}$ $X^{<2>} = \begin{pmatrix} 14.566 \\ 0.408 \end{pmatrix}$

$i := 0..2$

Find Cl (response) at each vertex with random error, σ = .017 on C_l

$\sigma := .017$
$error := rnorm(3, 0, \sigma)$
$CLcalc_i := interp(vs, Mxy, CL, X^{<i>}) + error_i$ $CLcalc = \begin{pmatrix} 2.686 \\ 2.718 \\ 2.961 \end{pmatrix}$

Define subroutines which find Indices of vertex associated with the best (ib), worst (iw), and next best (in) response

$findiw(CLsort, CLcalc) :=$
k ← 0
while $CLsort_0 \neq CLcalc$
  k ← k + 1
k

findin(CLsort, CLcalc) :=
k ← 0
while $CLsort_1 \neq CLcalc_k$
  k ← k + 1
k

findib(CLsort, CLcalc) :=
k ← 0
while $CLsort_2 \neq CLcalc_k$
  k ← k + 1
k

define subroutine to]evaluate C_l (response) with added noise $\sigma = .017$

findCL(X) :=
errvect ← rnorm(1, 0, σ)
CLcalc ← interp(vs, Mxy, CL, X) + $errvect_0$
CLcalc

input known optimum for data set: opt := 3.27

Begin Iteration N := 25

op(X, CLcalc, N, σ) :=
γ ← .5
j ← 0
CLsort ← sort(CLcalc)
iw ← findiw(CLsort, CLcalc)
in ← findin(CLsort, CLcalc)
ib ← findib(CLsort, CLcalc)
for j ∈ 0..N
  $xx \leftarrow \frac{X^{<ib>} + X^{<in>}}{2}$
  $r_j \leftarrow 2 \cdot xx - X^{<iw>}$
  $CLr_j \leftarrow findCL(r_j)$
  $(CLcalc_{iw} \leftarrow CLr_j) \cdot (X^{<iw>} \leftarrow r_j)$ if $CLcalc_{in} \le CLr_j \le CLcalc_{ib}$
  $xe \leftarrow r_j + \gamma \cdot xx - (X^{<iw>}) \cdot \gamma$ if $CLr_j > CLcalc_{ib}$
  $CLxe \leftarrow findCL(xe)$ if $CLr_j > CLcalc_{ib}$
  otherwise
    $xc \leftarrow xx + .5 \cdot (xx - X^{<iw>})$ if $(CLr_j < CLcalc_{in}) \cdot (CLr_j \ge CLcal$
    $xc \leftarrow (xx + X^{<iw>}) \cdot .5$ if $(CLr_j < CLcalc_{in}) \cdot (CLr_j < CLcalc_{iw})$

$X^{\langle iw \rangle} \leftarrow xc$

$X^{\langle iw \rangle} \leftarrow xe \text{ if } (CLr_j > CLcalc_{ib}) \cdot (CLxe \geq CLcalc_{ib})$

$CLcalc_{iw} \leftarrow CLxe \text{ if } (CLr_j > CLcalc_{ib}) \cdot (CLxe \geq CLcalc_{ib})$

$X^{\langle iw \rangle} \leftarrow r_j \text{ if } (CLr_j > CLcalc_{ib}) \cdot (CLxe < CLcalc_{ib})$

$CLcalc_{iw} \leftarrow CLr_j \text{ if } (CLr_j > CLcalc_{ib}) \cdot (CLxe < CLcalc_{ib})$

$xw \leftarrow X^{\langle iw \rangle}$

$xb \leftarrow X^{\langle ib \rangle}$

$xn \leftarrow X^{\langle in \rangle}$

$CLworst \leftarrow CLcalc_{iw}$

$CLbest \leftarrow CLcalc_{ib}$

$CLnext \leftarrow CLcalc_{in}$

$(CLcalc_{ib} \leftarrow CLworst) \cdot (X^{\langle ib \rangle} \leftarrow xw) \text{ if } CLbest < CLworst$

$(CLcalc_{in} \leftarrow CLbest) \cdot (X^{\langle in \rangle} \leftarrow xb) \text{ if } CLbest < CLworst$

otherwise

$X^{\langle in \rangle} \leftarrow xw$

$CLcalc_{in} \leftarrow CLworst$

$CLcalc_{iw} \leftarrow CLnext$

$X^{\langle iw \rangle} \leftarrow xn$

$\mu \leftarrow \text{mean}(CLcalc)$

$s \leftarrow \text{stdev}(CLcalc)$

$diff \leftarrow \left(\frac{opt - \mu}{opt}\right) \cdot 100$

$Xout \leftarrow \text{augment}(X^{\langle ib \rangle}, \text{augment}(X^{\langle in \rangle}, X^{\langle iw \rangle}))$

$ansmat_{j,0} \leftarrow Xout_{0,0}$

$ansmat_{j,1} \leftarrow Xout_{1,0}$

$ansmat_{j,2} \leftarrow CLcalc_{ib}$

$ansmat_{j,3} \leftarrow Xout_{0,1}$

$ansmat_{j,4} \leftarrow Xout_{1,1}$

$ansmat_{j,5} \leftarrow CLcalc_{in}$

$ansmat_{j,6} \leftarrow Xout_{0,2}$

$ansmat \cdot Xout$

$ansmat_{j,7} \leftarrow Xout_{1,2}$

$ansmat_{j,8} \leftarrow CLcalc_{iw}$

$ansmat_{j,9} \leftarrow \mu$

$ansmat_{j,10} \leftarrow s$

$ansmat_{j,11} \leftarrow diff$

$ansmat_{j,12} \leftarrow j + 2$

ansmat

$ans := op(X, CLcalc, N, \sigma)$ $\quad j := 0..N$

$l := ans$

$$init := \begin{pmatrix} X_{0,0} & X_{1,0} & CLcalc_0 \\ X_{0,1} & X_{1,1} & CLcalc_1 \\ X_{0,2} & X_{1,2} & CLcalc_2 \end{pmatrix}$$

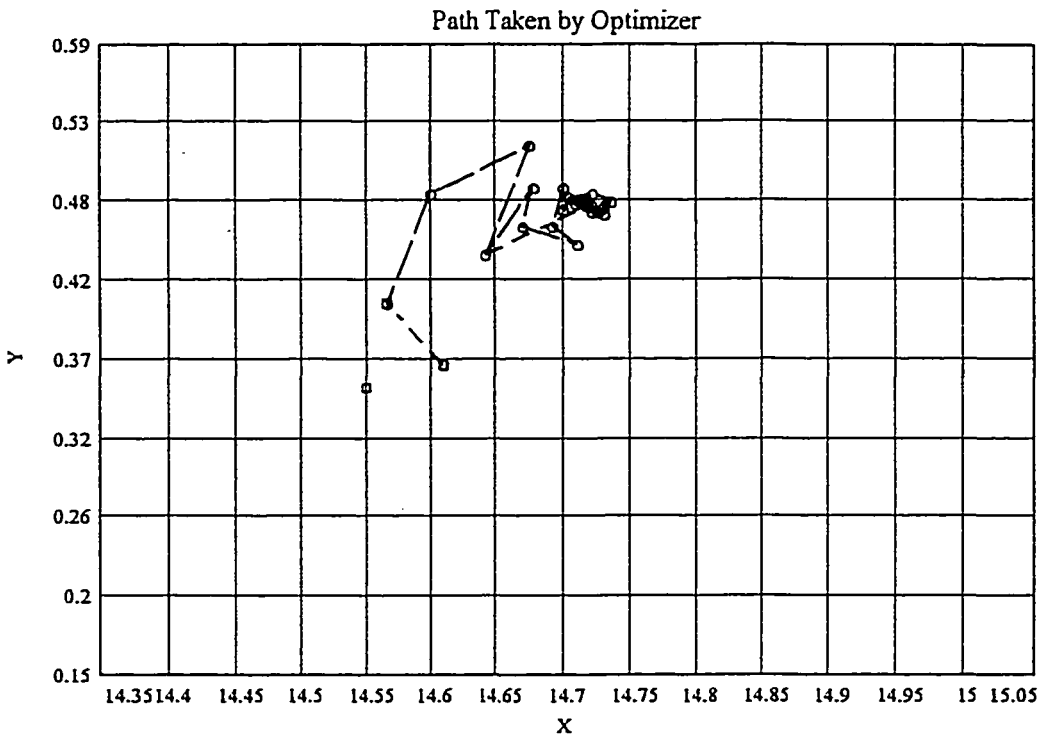

Note: first and last simplex vertices shown with square symbols

Method of Steepest Ascent - Remotely Actuated Flap Simulation for 8 degree angle of attack

FN:grat_asc.mcd
Drew Landman
3/19/95

This MathCad worksheet models a 1st order optimizer working with simulated experimental data for C_l=f(x,y). Noise is included for σ = .017 on C_l

read in a file that has x,y,Cl in 3 columns to generate response surface, data from α = 8, Slat A; experimental data must be a FN.prn file in current directory (c:\data\mcad)

XYCL := READPRN(xydata)

xvec := $XYCL^{<0>}$ yvec := $XYCL^{<1>}$ CL := $XYCL^{<2>}$ Mxy := augment(xvec, yvec)

vs is a vector of 2nd order polynomials that best fit the Cl data in a small neighborhood controlled by span; any Cl can be found from a multivariable regression fit using Mathcad utilities

span := .4
vs := loess(Mxy, CL, span)

max(xvec) = 15.05 max(yvec) = 0.55
min(xvec) = 14.35 min(yvec) = 0.15

set an increment for spacing 3 points: tol tol := .06 $h := \frac{\sqrt{3}}{2}\cdot tol$

scaling factor max, Smax: Smax := .05

1st point moving increment: S0 := .07

enter start point: xl := .5 + min(xvec) xstart := xl xstart = 14.85
yl := .2 + min(yvec) ystart := yl ystart = 0.35

i := 0..2

place points in equilateral triangle about centroidal point x1,y1

$$pt_0 := \begin{bmatrix} xl - \frac{tol}{2} \\ yl - \frac{h}{3} \end{bmatrix} \quad pt_1 := \begin{bmatrix} xl + \frac{tol}{2} \\ yl - \frac{h}{3} \end{bmatrix} \quad pt_2 := \begin{pmatrix} xl \\ yl + 2\cdot\frac{h}{3} \end{pmatrix} \quad pt_0 = \begin{pmatrix} 14.82 \\ 0.33268 \end{pmatrix}$$

calculate lift coefficient with random error at the 3 chosen points: pt_0, pt_1, pt_2

error := rnorm(3, 0, .017) $pt_1 = \begin{pmatrix} 14.88 \\ 0.33268 \end{pmatrix}$

$CLcalc_i := interp(vs, Mxy, CL, pt_i) + error_i$

$$A := \begin{bmatrix} 1 & xl - \frac{tol}{2} & yl - \frac{h}{3} \\ 1 & xl + \frac{tol}{2} & yl - \frac{h}{3} \\ 1 & xl & yl + 2\cdot\frac{h}{3} \end{bmatrix}$$

$pt_2 = \begin{pmatrix} 14.85 \\ 0.38464 \end{pmatrix}$

$CLcalc_i$

2.44216
2.30189
2.56688

calculate gradient on plane formed by 3 points, b gradient vector

$b := A^{-1} \cdot CLcalc \qquad b = \begin{pmatrix} 35.84085 \\ -2.3378 \\ 3.74997 \end{pmatrix} \qquad gradmag1 := \sqrt{(b_1)^2 + (b_2)^2}$

centroid of 3 points: $x0 := x1 \quad y0 := y1$

calculate new point to move to in direction of greatest slope of Cl(x,y)

$x1 := x0 + \frac{S0 \cdot b_1}{gradmag1} \quad y1 := y0 + \frac{S0 \cdot b_2}{gradmag1}$

set initial values for program: $x2 := x1 \quad xold := x0 \quad y2 := y1 \quad yold := y0$

input known optimum for data set: $opt := 2.755$

maximum number of moves, n: $n := 25$

Begin Iteration

$op(x1, y1, S0, Smax) :=$

$j \leftarrow 0$

for $j \in 0..n$

$pt_0 \leftarrow \begin{bmatrix} x1 - \frac{tol}{2} \\ y1 - \frac{h}{3} \end{bmatrix}$

$pt_1 \leftarrow \begin{bmatrix} x1 + \frac{tol}{2} \\ y1 - \frac{h}{3} \end{bmatrix}$

$pt_2 \leftarrow \begin{pmatrix} x1 \\ y1 + \frac{2 \cdot h}{3} \end{pmatrix}$

$error \leftarrow rnorm(3, 0, .017)$

for $i \in 0..2$

$CLcalc_i \leftarrow (interp(vs, Mxy, CL, pt_i))$

$A \leftarrow \begin{bmatrix} 1 & x1 - \frac{tol}{2} & y1 - \frac{h}{3} \\ 1 & x1 + \frac{tol}{2} & y1 - \frac{h}{3} \\ 1 & x1 & y1 + 2 \cdot \frac{h}{3} \end{bmatrix}$

$CLcalc \leftarrow CLcalc + error$

$b \leftarrow A^{-1} \cdot (CLcalc)$

$gradmag2 \leftarrow \sqrt{(b_1)^2 + (b_2)^2}$

$$\left(x0_j \leftarrow x1\right)\cdot\left(y0_j \leftarrow y1\right)$$

$$err \leftarrow rnorm(1, 0, .017)$$

$$CLcen_j \leftarrow \left[interp\left[vs, Mxy, CL, \begin{pmatrix} x0_j \\ y0_j \end{pmatrix} \right] + err_0 \right]$$

$$Stest \leftarrow \frac{gradmag2^{.5}}{gradmag1^{.5}} \cdot \sqrt{(x1 - xold)^2 + (y1 - yold)^2}$$

$$S1 \leftarrow if(Stest > Smax, Smax, Stest)$$

$$x1 \leftarrow x0_j + \frac{S1 \cdot b_1}{gradmag2}$$

$$y1 \leftarrow y0_j + \frac{S1 \cdot b_2}{gradmag2}$$

$$xold \leftarrow x0_j$$

$$yold \leftarrow y0_j$$

$$diff \leftarrow \left(\frac{opt - CLcen_j}{opt}\right) \cdot 100$$

$$\mu \leftarrow mean(CLcalc)$$

$$s \leftarrow stdev(CLcalc)$$

$$diffm \leftarrow \left(\frac{opt - \mu}{opt}\right) \cdot 100$$

$$gradmag1 \leftarrow gradmag2$$

$$ANSMAT_{j,0} \leftarrow x0_j$$

$$ANSMAT_{j,1} \leftarrow y0_j$$

$$ANSMAT_{j,2} \leftarrow CLcen_j$$

$$ANSMAT_{j,3} \leftarrow j + 2$$

$$ANSMAT_{j,4} \leftarrow S1$$

$$ANSMAT_{j,5} \leftarrow CLcalc_0$$

$$ANSMAT_{j,6} \leftarrow CLcalc_1$$

$$ANSMAT_{j,7} \leftarrow CLcalc_2$$

$$ANSMAT_{j,8} \leftarrow diff$$

$$ANSMAT_{j,9} \leftarrow \mu$$

$$ANSMAT_{j,10} \leftarrow s$$

$$ANSMAT_{j,11} \leftarrow diffm$$

ANSMAT

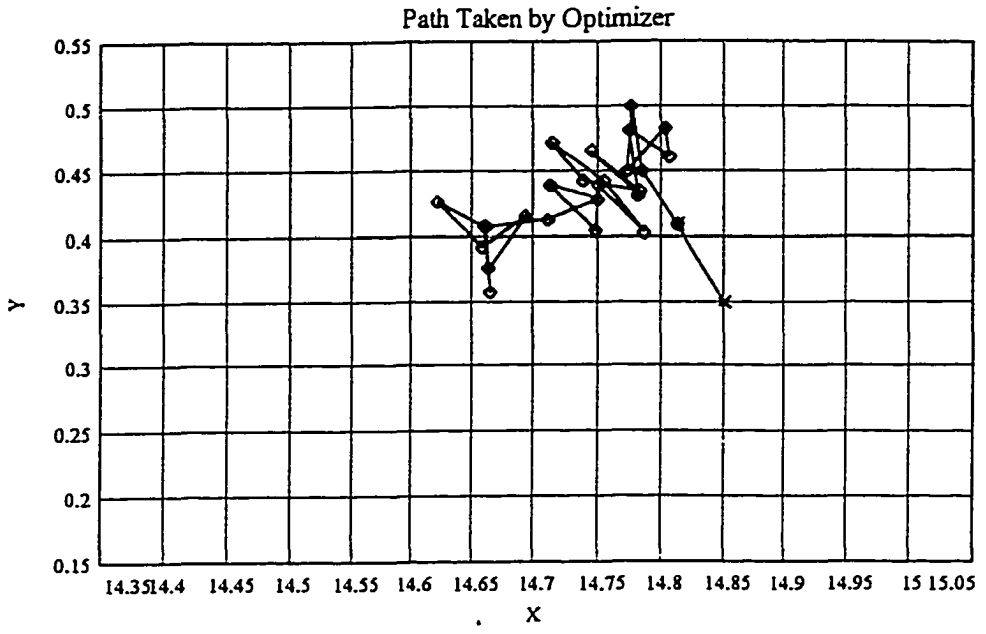

Summary of Run

increment for spacing 3 points tol: tol = 0.06

number of steps: n = 25

start point: xstart = 14.85
ystart = 0.35

scaling factors: Smax = 0.05
S0 = 0.07

end point: $ANS_{n,0}$ = 14.664 (x)
$ANS_{n,1}$ = 0.38 (y)

ANS := op(xl, yl, S0, Smax)

l := ANS

i := 0 .. n x := $ANS^{<0>}$ y := $ANS^{<1>}$

k := 0 .. l xplot := $\begin{pmatrix} xstart \\ x2 \end{pmatrix}$ yplot := $\begin{pmatrix} ystart \\ y2 \end{pmatrix}$

Print results:

x, y, Cl, j, S1, C_{l1}, C_{l2}, C_{l3}, %diff of Clcen from opt, mean, st dev, %diff from μ

l =

14.813	0.409	2.702	2	0.05	2.703	2.616	2.767	1.934	2.695	0.062	2.168
14.784	0.45	2.763	3	0.05	2.716	2.703	2.787	−0.297	2.735	0.037	0.722
14.777	0.5	2.701	4	0.05	2.741	2.733	2.656	1.944	2.71	0.038	1.628
14.773	0.45	2.764	5	0.045	2.728	2.75	2.761	−0.317	2.746	0.014	0.313
14.803	0.483	2.748	6	0.023	2.736	2.737	2.731	0.265	2.735	0.003	0.736
14.806	0.461	2.761	7	0.038	2.741	2.719	2.743	−0.223	2.734	0.011	0.754
14.774	0.481	2.735	8	0.05	2.748	2.755	2.713	0.743	2.739	0.019	0.596
14.782	0.432	2.768	9	0.05	2.741	2.676	2.758	−0.457	2.725	0.035	1.078
14.744	0.465	2.73	10	0.05	2.727	2.763	2.721	0.898	2.737	0.018	0.655
14.784	0.434	2.707	11	0.046	2.755	2.708	2.74	1.741	2.734	0.02	0.749
14.739	0.443	2.729	12	0.038	2.729	2.717	2.736	0.95	2.727	0.008	1.002
14.714	0.472	2.732	13	0.05	2.726	2.766	2.721	0.818	2.738	0.02	0.627
14.754	0.442	2.743	14	0.05	2.716	2.745	2.701	0.442	2.721	0.018	1.252
14.786	0.404	2.708	15	0.05	2.704	2.624	2.732	1.709	2.687	0.046	2.479
14.751	0.439	2.736	16	0.034	2.753	2.752	2.737	0.701	2.747	0.007	0.274
14.748	0.405	2.741	17	0.05	2.728	2.693	2.741	0.507	2.721	0.02	1.247
14.713	0.44	2.723	18	0.039	2.727	2.741	2.73	1.15	2.733	0.006	0.806
14.75	0.428	2.75	19	0.042	2.748	2.72	2.725	0.194	2.731	0.012	0.868
14.711	0.413	2.733	20	0.05	2.753	2.7	2.722	0.781	2.725	0.022	1.088
14.661	0.407	2.74	21	0.05	2.76	2.764	2.723	0.548	2.749	0.019	0.216
14.665	0.358	2.704	22	0.05	2.679	2.67	2.744	1.836	2.698	0.033	2.077
14.66	0.407	2.731	23	0.042	2.742	2.731	2.741	0.882	2.738	0.005	0.608
14.622	0.426	2.741	24	0.05	2.729	2.746	2.723	0.5	2.733	0.01	0.809
14.658	0.392	2.745	25	0.043	2.725	2.735	2.736	0.37	2.732	0.005	0.827
14.694	0.416	2.764	26	0.05	2.776	2.749	2.731	−0.323	2.752	0.018	0.122
14.664	0.376	2.716	27	0.05	2.745	2.689	2.766	1.415	2.733	0.033	0.782

AEROSPACE ACCESS
INFORMATION SERVICES FROM AIAA

March 19, 1998

Mr. D. Landman
Old Dominion University
Norfolk, VA

Dear Mr. Landman:

In response to your request of January 29, 1998:

First, AIAA Paper 88-0613, "TURBULENT SEPARATED FLOW IN THE VICINITY OF A SINGLE-SLOTTED AIRFOIL FLAP," by D. Adair et al, is a work of the U.S. Government and therefore in the public domain.;

The following documents are copyrighted by AIAA, but no copyright is asserted by AIAA in the United States. You may use these documents as you wish without violating copyright:

- "EVALUATION OF TUNNEL SIDEWALL BOUNDARY-LAYER-CONTROL SYSTEMS FOR HIGH-LIFT AIRFOIL TESTING," BY K. Paschal, et al.,
- "NAVIER-STOKES COMPUTATIONS AND EXPERIMENTAL COMPARISONS FOR MULTI ELEMENT AIRFOIL CONFIGURATIONS," by W. Anderson,et al,
- "MULTI-BLOCK STRUCTURED GRID APPROACH FOR SOLVING VISCOUS FLOWS OVER COMPLEX AERODYNAMIC CONFIGURATIONS," by V.N. Vatsa, et al,
- "A COMPARATIVE STUDY OF TURBULENCE MODELS FOR OVERSET GRIDS," by K.J. Renze, et al.

AIAA holds the copyright for the following documents:

- "MULTIELEMENT AIRFOIL PERFORMANCE DUE TO REYNOLDS AND MACH NUMBER VARIATIONS," by W.O. Valarezo, et al,
- "MULTI-ELEMENT AIRFOIL OPTIMIZATION FOR MAXIMUM LIFT AT HIGH REYNOLDS NUMBERS," by W.O. Valarezo, et al,
- "GENERATION OF UNSTRUCTURED GRIDS FOR VISCOUS FLOW APPLICATIONS," by D.L. Marcum,
- "NUMERICAL COMPUTATION OF VISCOUS FLOWFIELDS ABOUT MULTIPLE COMPONENT AIRFOILS," by D.M. Schuster,
- "EXPERIMENTAL INVESTIGATION OF FLOWFIELD ABOUT A MULTIELEMENT AIRFOIL," by A. Nakayama, et al.
- "GENERATION AND CONTROL OF SEPARATED VORTICES OVER A DELTA WING BY MEANS OF LEADING EDGE FLAPS," by T. Karagounis, et al,
- "HIGH-LIFT AERODYNAMICS - 37TH WRIGHT BROTHERS LECTURE," by A.M.O. Smith.

AIAA will grant permission for you to reprint the requested figures provided the following condition is accepted:

- Indicate directly beneath each figure "Copyright © ___ (fill in the appropriate year for each figure) AIAA - Reprinted with permission". Appropriate credit to our publication must appear on every copy of your work, either on the first page of the quoted text or in the figure legend.

AIAA Aerospace Database • International Aerospace Abstracts
85 John Street, 4th Floor • New York, NY 10038-2823 • 212/349-1120 • 800/348-7737 • Fax: 212/349-1283

Although it is not a condition for permission, we would appreciate a copy of your dissertation when completed. We will use the copy you provide for announcement in International Aerospace Abstracts and inclusion in the Aerospace Database. These tools provide announcement and retrieval mechanisms to scientists and engineers world-wide, thereby enhancing the awareness of and interest in your work.

Thank you for your inquiry.

Sincerely,

Steve Klimek

Steve Klimek
Business Operations

605 Third Avenue
New York, NY 10158-0012
212.850 6000
FAX 212.850.6088

John Wiley & Sons, Inc.
Publishers Since 1807

March 31, 1998

Drew Landman
Aerospace Engineering
Old Dominion University
VIA FAX ONLY: 757-864-7002

Dear Mr. Landman:

RE: Your letter dated March 18, 1998 requesting permission to reuse up to a maximum of 5 figures and/or 300 words in print media only from McCormick/AERODYNAMICS, AERONAUTICS, AND FLIGHT MECHANICS, 2nd Edition, (ISBN 0471-11037-6), a work published by John Wiley & Sons, Inc.

1. Permission is granted for this use, except that you must obtain authorization from the original source to use any material that appears in our work with credit to another source.
2. Permitted use is limited to the original edition of your forthcoming work described in your letter and does not extend to future editions of your work. In addition, permission does not include the right to grant others permission to photocopy or otherwise reproduce this material except for versions made by non-profit organizations for use by blind or physically handicapped persons.
3. Appropriate credit to our publication must appear on every copy of your work, either on the first page of the quoted text or in the figure legend. The following components must be included: Title, author(s) and /or editor(s), journal title (if applicable), Copyright © (year and owner). Reprinted by permission of John Wiley & Sons, Inc.
4. This permission is for non-exclusive world rights in the English language only. (For translation, please contact our Subsidiary Rights Department.)
5. This permission is for print rights only. If you wish permission for non-print media rights, please contact Judith Spreitzer, for requests for material from our books, and Neil Adams, for requests for material from our journals, when you have firm plans for publishing your book in a specific non-print medium.
6. If your published work contains more than 5 figures and/or 300 words from our title, this permission shall be void.

Sincerely,

Patrick Murphy
John Wiley & Sons, Inc.
Permissions Department

If you have any questions regarding permissions, please call (212) 850-6011.

VISIT OUR WEBSITE @ "HTTP://WWW.WILEY.COM" FOR PERMISSIONS INFORMATION AND REQUEST FORMS

pm331a8

VITA

Drew Landman holds a Bachelor of Science (1983) and a Master of Science (1984) in Mechanical Engineering from Lehigh University, Bethlehem, PA. He received his Professional Engineering registration in the state of Virginia in 1990. Mr. Landman currently lives in Norfolk, VA, and teaches in the Engineering Technology Department at Old Dominion University (ODU) where he is an Associate Professor. For the past two years he has served as the Chief Engineer for the ODU Langley Full-Scale Wind Tunnel where he has been involved in numerous facility upgrade projects including, specification of a new data acquisition system, writing software for data acquisition, mechanical design of an automobile force balance, and design of an automobile lift system. In addition Mr. Landman has served as test engineer for many race car wind tunnel entries. Mr. Landman enjoys flying and racing sailplanes in his spare time.